

AD/A-003 303

THE SHOCK AND VIBRATION BULLETIN. PART 2.
INVITED PAPERS, STRUCTURAL DYNAMICS

Naval Research Laboratory
Washington, D. C.

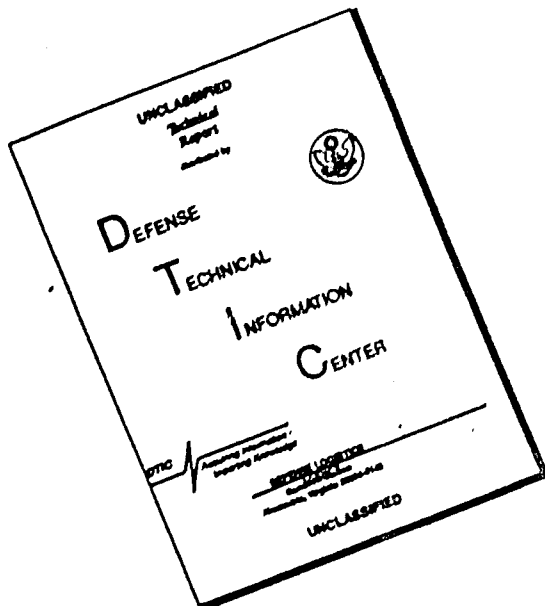
August 1974

DISTRIBUTED BY:



National Technical Information Service
U. S. DEPARTMENT OF COMMERCE

DISCLAIMER NOTICE



THIS DOCUMENT IS BEST
QUALITY AVAILABLE. THE COPY
FURNISHED TO DTIC CONTAINED
A SIGNIFICANT NUMBER OF
PAGES WHICH DO NOT
REPRODUCE LEGIBLY.

AD A 003303

023120

dc
Bulletin 44
(Part 2 of 5 Parts)

THE SHOCK AND VIBRATION BULLETIN

Part 2
Invited Papers, Structural Dynamics

AUGUST 1974

A Publication of
**THE SHOCK AND VIBRATION
INFORMATION CENTER**
Naval Research Laboratory, Washington, D.C.

Reproduced by
NATIONAL TECHNICAL
INFORMATION SERVICE
U S Department of Commerce
Springfield VA 22151

FOR INTERNAL ANNOUNCEMENT ONLY

NOT FOR GENERALIZED FOR SALE
OR GENERAL DISTRIBUTION

may
be purchased from

Shock and Vibration Information Center
Naval Research Laboratory, Code 6020
Washington, D. C. 20390



Office of
The Director of Defense
Research and Engineering

DDC
REFINED
JAN 21 1975
RECORDED
D

Approved for public release; distribution unlimited.

#1 AD-A003302

211

ACCESSION for	
NTIS	White Section <input checked="" type="checkbox"/>
DOC	Buff Section <input type="checkbox"/>
UNANNOUNCED	<input type="checkbox"/>
JUSTIFICATION	
BY	
DISTRIBUTION/AVAILABILITY CODES	
DISL	AVAIL AND OF SPECIAL
X	21

SYMPORIUM MANAGEMENT

THE SHOCK AND VIBRATION INFORMATION CENTER

Henry C. Pusey, Director
Edward H. Schell
Rudolph H. Volin
J. Gordan Showalter

Bulletin Production

Graphic Arts Branch, Technical Information Division,
Naval Research Laboratory

Bulletin 44
(Part 2 of 5 Parts)

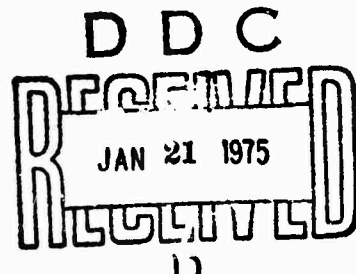
THE SHOCK AND VIBRATION BULLETIN

AUGUST 1974

**A Publication of
THE SHOCK AND VIBRATION
INFORMATION CENTER
Naval Research Laboratory, Washington, D.C.**

The 44th Symposium on Shock and Vibration was held at the Rice Hotel and Lyndon B. Johnson Space Center, Houston, Texas on 4-7 December 1973. The National Aeronautics and Space Administration was the host.

Office of
The Director of Defense
Research and Engineering



CONTENTS

PAPERS APPEARING IN PART 2

Invited Papers

SPACE SHUTTLE DYNAMICS	1
Mr. Robert F. Thompson, Manager, Space Shuttle Program, Lyndon B. Johnson, Space Center, Houston, Texas	
VIKING DYNAMICS — AN OVERVIEW	19
Dr. Richard E. Snyder, NASA Langley Research Center, Hampton, Virginia	
VIKING ORBITER — DYNAMICS OVERVIEW	25
Mr. Ben K. Wada, Jet Propulsion Laboratory, Pasadena, California	
VIKING LANDER DYNAMICS	41
Mr. Joseph C. Pohlen, Martin Marietta Aerospace, Denver, Colorado	

Structural Dynamics

PERFORMANCE OF STATISTICAL ENERGY ANALYSIS	47
R.F. Davis and D.E. Hines, McDonnell Douglas Astronautics Company, Huntington Beach, California	
PREDICTION OF SHOCK ENVIRONMENTS BY TRANSFER FUNCTION MEASUREMENT TECHNIQUES	65
G.C. Kao, J.M. Cantril, G.D. Shipway, Wyle Laboratories, Huntsville, Alabama, and M.A. Boyd, U.S. Army Corps of Engineers, Huntsville, Alabama	
DETERMINATION OF GUIDEWAY ROUGHNESS FROM CONSTRUCTION TOLERANCES	83
B.J. Brock, Vought Systems Division LTV Aerospace Corporation, Dallas, Texas	
SELECTED SYSTEM MODES USING THE DYNAMIC TRANSFORMATION WITH MODAL SYNTHESIS	91
E.J. Kuhar, General Electric Company, Philadelphia, Pennsylvania	
STRUCTURAL DYNAMICS COMPUTATIONS USING AN APPROXIMATE TRANSFORMATION	103
C.S. O'Hearne and J.W. Shipley, Martin Marietta Aerospace, Orlando, Florida	

LINEAR LUMPED-MASS MODELING TECHNIQUES FOR BLAST LOADED STRUCTURES	111
W.J. Liss, Jr. and N.J. DeCapua, Bell Laboratories, Whippny, New Jersey	
DEVELOPMENT AND CORRELATION: VIKING ORBITER ANALYTICAL DYNAMIC MODEL WITH MODAL TEST	125
B.K. Wada, J.A. Garba and J.C. Chen, Jet Propulsion Laboratory, Pasadena, California	
MODAL TEST RESULTS OF THE VIKING ORBITER	165
E.L. Leppert, B.K. Wada, Jet Propulsion Laboratory, Pasadena, California, and R. Miyakawa, Martin-Marietta Aerospace, Denver, Colorado (assigned to the Jet Propulsion Laboratory)	
IMPLEMENTATION OF INTERACTIVE GRAPHICS TO A TRANSIENT RESPONSE RING CODE	177
R.W. Buchanan, T.N. Vogel and P.G. Underwood, Lockheed Missiles and Space Company, Sunnyvale, California	
COMPUTER GENERATED DISPLAYS OF STRUCTURES IN VIBRATION	185
H.N. Christiansen, Brigham Young University, Provo, Utah	
VIBRATION REDUCTION BY USING BOTH THE FINITE ELEMENT STRAIN ENERGY DISTRIBUTION AND MOBILITY TECHNIQUES	193
J. J. Sciarra, Boeing Vertol Company, Philadelphia, Pennsylvania	
INFLUENCE OF ELASTIC SUPPORTS ON NATURAL FREQUENCIES OF CANTILEVER BEAMS	201
R.F. Solberg, Jr., Southwest Research Institute, San Antonio, Texas	

PAPERS APPEARING IN PART 1

Summaries of Papers Presented at 44th Symposium

PAPERS APPEARING IN PART 3

Shock Testing

DIGITALLY CONTROLLED TRANSIENT WAVEFORM TESTING — ALTERNATE METHOD TO SLOW SINE SWEEP	
B.K. Kim, Jet Propulsion Laboratory, Pasadena, California	

COMPARISON OF SHOCK SPECTRUM TECHNIQUES AND THE METHOD OF LEAST FAVORABLE RESPONSE	
A.F. Witte and R.J. Wolf, Kaman Sciences Corporation, Colorado Springs, Colorado	

APPLICATION OF LEAST FAVORABLE RESPONSE TECHNIQUES INCORPORATING FIELD DATA FOURIER TRANSFORM PHASE ANGLE
R.J. Wolf and A.F. Witte, Kaman Sciences Corporation, Colorado Springs, Colorado

MATCHING SHOCK SPECTRA WITH SUMS OF DECAYING SINUSOIDS COMPENSATED FOR SHAKER VELOCITY AND DISPLACEMENT LIMITATIONS
D.O. Smallwood and A.R. Nord, Sandia Laboratories, Albuquerque, New Mexico

A CASE FOR DAMPED OSCILLATORY EXCITATION AS A NATURAL PYROTECHNIC SHOCK SIMULATION
D.B. Nelson and P.H. Prasthofer, Sandia Laboratories, Livermore, California

DEVELOPMENT OF A PYROTECHNIC SHOCK TEST FACILITY
D.R. Powers, McDonnell Douglas Astronautics Company, Santa Monica, California

STUDY OF AN EXPERIMENTAL TECHNIQUE FOR APPLICATION TO STRUCTURAL DYNAMIC PROBLEMS
R.F. Snell, McDonnell Douglas Astronautics Company, Huntington Beach, California

TIMEWISE OUTPUT OF PYROTECHNIC BOLTS
V.H. Neubert, The Pennsylvania State University, University Park, Pennsylvania and R.P. Parker, Uniroyal Research Center, Middlebury, Connecticut

PYROTECHNIC SHOCK REDUCTION
S.N. Prescott, Jet Propulsion Laboratory, Pasadena, California

IMPACT TESTING WITH THE 35-FOOT CENTRIFUGE
J.V. Otts, Sandia Laboratories, Albuquerque, New Mexico

FRAGMENT VELOCITIES FROM EXPLODING LIQUID PROPELLANT TANKS
R.L. Bessey, Southwest Research Institute, San Antonio, Texas

Shock Analysis

PIPING DESIGN FOR HYDRAULIC TRANSIENT PRESSURE
C.C. Huang, R.J. Bradshaw, Jr., U.S. Army Engineer Division, Huntsville, Alabama and H.H. Yen, Sperry-Rand Corporation, Huntsville, Alabama

POPPING MOTOR DOME SHOCK DURING FIRST STAGE SEPARATION ON POSEIDON MISSILE FLIGHTS
L.R. Pendleton and R.L. Henrikson, Lockheed Missiles and Space Company, Sunnyvale, California

SCALING OF WATER IMPACT DATA FOR SPACE SHUTTLE SOLID ROCKET BOOSTER
R. Madden, H.A. Wright, Bolt Beranek and Newman, Inc., Cambridge, Massachusetts and D.A. Kross, NASA Marshall Space Flight Center, Huntsville, Alabama

IDENTIFICATION OF AN OPTIMUM SET OF TRANSIENT SWEEP PARAMETERS
FOR GENERATING SPECIFIED RESPONSE SPECTRA

R.C. Rountree, The Aerospace Corporation, El Segundo, California and
C.R. Freberg, University of Southern California, Los Angeles, California

ANALYSIS OF OPEN CELL POLYURETHANE FOAM UNDER
IMPACT LOADING

V. Sepcenko, Boeing Aerospace Company, Seattle, Washington

MEASUREMENT OF PEAK PRESSURES PRODUCED AT THE GROUND SURFACE
BY SHALLOW BURIED EXPLOSIVES

B.L. Morris, U.S. Army Mobility Equipment Research and Development
Center, Fort Belvoir, Virginia

PAPERS APPEARING IN PART 4

Underwater Problems

APPLICATION OF MECHANICAL IMPEDANCE CONCEPTS TO THE COUPLING
PROBLEM OF STRUCTURES IN SHOCK ENVIRONMENT

R. Aquilina and L. Gaudriot, Center D-Etudes et de Recherches Techniques
Sous-Marines, Direction Des Constructions Et Armes Navales, Toulon, France

THE NAVY LARGE FLOATING SHOCK PLATFORM-PART I: PHYSICAL
DESCRIPTION AND CAPABILITIES

C.G. Schrader, West Coast Shock Facility, San Francisco, California

THE NAVY LARGE FLOATING SHOCK PLATFORM-PART II: SHOCK
CHARACTERISTICS

E.W. Clements, Naval Research Laboratory, Washington, D.C.

THE EFFECT OF UNIFORM EXTERNAL PRESSURIZATION ON THE DYNAMIC
RESPONSE OF ISOTROPIC CYLINDRICAL SHELLS

F.J. Dziale, University of Massachusetts, Amherst, Massachusetts

ON DEFINING TIME DOMAINS FOR RADIATION DAMPING AND ADDED MASS
EFFECTS IN FLUID-STRUCTURAL INTERACTION

A.V. Clark Jr., Naval Research Laboratory, Washington, D.C.

Environments and Measurements

HARPOON MISSILE FLIGHT ENVIRONMENTAL MEASUREMENT PROGRAM

V.S. Noonan, J.L. Gubser and R.D. Harmening, McDonnell Douglas Astro-
nautics Company, St. Louis, Missouri

NARROW BAND TIME HISTORY ANALYSIS OF TRANSPORT AIRCRAFT
VIBRATION DATA

R.E. Thaller and J. Pearson, Air Force Flight Dynamics Laboratory, Wright-
Patterson AFB, Ohio

PRELIMINARY MEASUREMENT AND ANALYSIS OF THE VIBRATION ENVIRONMENT OF COMMON MOTOR CARRIERS

W.N. Sharpe, T.J. Kusza, F.W. Sherman and J.W. Goff, School of Packaging,
Michigan State University, East Lansing, Michigan

THE DYNAMIC ENVIRONMENT OF LANDING CRAFT

M.B. Gens, Sandia Laboratories, Albuquerque, New Mexico

A RESONANCE-TYPE BACK-TO-BACK CALIBRATOR FOR ACCELEROMETERS

J.A. Macinante, N.H. Clark, B.H. Cresswell, CSIRO, Division of Applied
Physics, National Standards Laboratory, Sydney, Australia

A NEW TRANSVERSE CALIBRATOR FOR ACCELEROMETERS

J.A. Macinante, N.H. Clark, and B.H. Cresswell, CSIRO, Division of Applied
Physics, National Standards Laboratory, Sydney, Australia

PAPERS APPEARING IN PART 5

Isolation and Damping

DESIGN OF CONSTRAINED LAYER TREATMENTS FOR BROAD TEMPERATURE DAMPING

D.I.G. Jones, Air Force Materials Laboratory, Wright-Patterson AFB, Ohio

**REDUCTION OF INTERIOR CABIN NOISE LEVELS IN A HELICOPTER
THROUGH ADDITIVE DAMPING**

J.P. Henderson, Air Force Materials Laboratory, Wright-Patterson AFB, Ohio
and A.D. Nashif, University of Dayton, Dayton, Ohio

**VIBRATION DAMPING AND ISOLATION WITH ENERGY ABSORBING
COMPOSITES**

J. Nunes, Brunswick Corporation, Skokie, Illinois

**SUPPRESSION OF TORSIONAL VIBRATION WITH ZERO TORSIONAL
STIFFNESS COUPLINGS**

J.M. Vance, University of Florida, Gainesville, Florida and R.A. Brown, E.I.
du Pont de Nemours and Company, Inc., Wilmington, Delaware

Vibration Testing and Analysis

DEVELOPMENT OF SAM-D MISSILE RANDOM VIBRATION RESPONSE LOADS

P.G. Hahn, Martin Marietta Aerospace, Orlando, Florida

**EVALUATION OF BLOCKED ACOUSTIC PRESSURE ON STIFFENED
CYLINDRICAL SHELLS**

V.M. Conticelli, Aeritalia S.p.A., Naples, Italy, and G.C. Kao, Wyle
Laboratories, Huntsville, Alabama

**REDUCTION OF HULL NOISE AND VIBRATION BY CENTER OF PERCUSSION
ROADARM DESIGN**

D.D. Ustick, U.S. Army Tank-Automotive Command, Warren, Michigan

SYNCHRONIZATION AND PHASE ANGLE OF TWO UNBALANCED ROTORS

M. Paz, University of Louisville, Louisville, Kentucky, P.H. Schrader and
R. Blackmon, Vibrating Equipment Division, Rexnord, Inc., Louisville, Kentucky

**EXPERIMENTAL INVESTIGATION OF THE DYNAMIC RESPONSE OF
CANTILEVER ANISOTROPIC PLATES**

R.L. Sierakowski, University of Florida, Gainesville, Florida and C.T. Sun,
Iowa State University, Ames, Iowa

SPACECRAFT VIBRATION TEST LEVEL COST OPTIMIZATION STUDY

J.P. Young, NASA Goddard Space Flight Center, Greenbelt, Maryland

FLIGHT QUALIFICATION OF SPECIAL EQUIPMENT

J. Pearson and R.E. Thaller, Air Force Flight Dynamics Laboratory, Wright-
Patterson AFB, Ohio

THE USE OF LISSAJOUS FIGURES IN VIBRATION TESTING

J.D. Ray, Memphis State University, Memphis, Tennessee and C.W. Bert,
University of Oklahoma, Norman, Oklahoma

STRUCTURAL DYNAMIC RESPONSE ANALYSIS OF ROCKET TEST SLEDS

T.N. Gardner, Mechanics Research Incorporated, Los Angeles, California

CONSIDERATION OF THE RESPONSE OF A SLED BORNE MISSILE

A.R. Glaser, Rockwell International, Columbus, Ohio and L.C. Mixon,
6585th Test Group, Holloman AFB, New Mexico

**FLOW-INDUCED VIBRATIONS OF A GLASS-REINFORCED PLASTIC
SONAR DOME**

D.A. King, Rockwell International Corporation, Anaheim, California

**AERO-ACOUSTIC ENVIRONMENT OF A RECTANGULAR CAVITY WITH A
LENGTH TO DEPTH RATIO OF FOUR**

L.L. Shaw and D.L. Smith, Air Force Flight Dynamics Laboratory, Wright-
Patterson AFB, Ohio

**RESPONSE OF LINEAR DYNAMICAL SYSTEMS UNDER NONSTATIONARY
RANDOM EXCITATIONS**

T.S. Sankar and D. Doan, Sir George Williams University, Montreal, Canada

**MEANS OF CONTROLLING THE DYNAMIC MOTION OF BOTTOM MOORED
MINE CASES EXPOSED TO HIGH CURRENT**

J.J. O'Neill, J. Berezow and J.E. Goeller, Naval Ordnance Laboratory, Silver
Spring, Maryland

INVITED PAPERS

SPACE SHUTTLE DYNAMICS

Mr. Robert Thompson
Lyndon B. Johnson Space Center
Houston, Texas

I would like to outline the Shuttle as we see it at this time, and to point out to you some of the features and the characteristics of the shuttle vehicle that will be of particular interest to you in your speciality area. As Dr. Faget pointed out in his welcoming remarks, we feel that the Shuttle is fairly fertile ground for those interested in shock and vibration.

In looking through some of your literature it was my understanding that one of the principal formats for the opening session was to have the host agency describe some of its current program activities, and to point out where in those program activities interest in the field of shock and vibration might be found. We are at a very critical time in the design and development phase of the Space Shuttle program. This program has been underway for nearly four years. The first few years were spent in developing the basic concept of the Shuttle and advancing some of the technology required to be applied to the shuttle. For the last two years, we have been very active in moving into preliminary design. The configuration that is described is fairly stable and sufficiently mature to the point where it can be expected to endure. The detailed type of shock and vibration considerations that I point out will be the real problems that we will be working with in the next few years.

Figure 1 provides background for those who aren't particularly familiar with the Shuttle, and it gives you an overview of what we are trying to achieve with the Shuttle system. As the country came through its first 10 or 15 years of space flight activity, as depicted on the bottom part of Figure 1, we developed a family of launch vehicles unique for the various missions in both our manned and unmanned programs. In the late sixties it became apparent to all that the Apollo objectives were to be achieved, and the Skylab program, which is currently flying, would effectively utilize the remainder of Apollo hardware. Thus it became necessary for the country to decide what it would like to do in space in order to have a space capability in the 1980 time period. So after many studies it was generally felt that the development of a general purpose launch

system, or a general purpose space transportation system, was the correct next step. We looked at many alternates, such as continuing exploration of the planets, large space station programs, and many other things all of which were attractive and had a great deal of future potential. We felt that the most important priority was the development of an economic space transportation system, and in so doing we had to balance the development cost against the operation cost. We were very conscious of the development funding that would be required over a period of four or five years to bring the Shuttle system into being, and we were particularly eager to assure that the developed system could operate to and from earth orbit in an economical manner. This dictated a number of characteristics, and we looked at many configurations. We have settled on the one depicted in Figure 2, and we are well underway in our design and development activities for it.

Some of the physical features and characteristics of the Shuttle are depicted in an artist's concept of the vehicle in its launch configuration; there are three major elements, the Orbiter element which is the delta-wing-airplane-like module, the External Tank-the large body in the center which carries the liquid hydrogen and liquid oxygen for the rocket engines in the base of the orbiter, and on either side of the tank the Solid Rocket Boosters. So these are the bodies, the masses, the springs, and the rocket propulsion forces that we will be dealing with in the system in the launch environment.

Figure 3 shows some of the overall system sizes and characteristics. The overall system weight is slightly in excess of 4 million lbs at lift off. We are able to carry a maximum of 65,000 lbs payload if we were flying a due east orbit, and the payload would be as low as 32,000 lbs for a retrograde orbit. The delta wing in the orbiter configuration has a span under 80 ft. The payload bay is 15 ft in diameter and 60 ft in overall length, and is located in the central part of the vehicle. The delta wing is sized to give a capability of flying approximately 1100 miles cross track during reentry and then achieving an acceptable landing velocity for a tangential landing on

the runway in an airplane type mode. The Orbiter has three liquid-propellant rocket engines located in the base and each engine has about 470,000 lbs of thrust in vacuum. We have approximately 1,200,000 lbs of thrust pushing on the back end of the Orbiter.

The other propulsion systems in the Orbiter are the two orbital maneuvering system engines; each of these 6,000-lbs thrust engines are ignited in the late launch part of the trajectory that pushes the Orbiter into orbit. These engines are used to attain orbit because the main engines are cut off just prior to going into orbit. They are also used for maneuvers while in orbit and for the retrograde maneuver prior to reentry into the atmosphere. We have a large number of RCS (reaction control systems) engines located in pods on either side of the orbital maneuvering system, on the aft part of the vehicle, and located in the nose of the vehicle. These RCS engines are used for altitude control while on orbit and during the early part of reentry. Although the weight of the Orbiter is 150,000 lbs dry, it would weight in excess of 180,000 lbs at landing and could weight as much as 250,000 lbs for a full 65,000 lbs payload liftoff configuration. The total mass of the Orbiter is approximately 200,000 lbs.

The External Tank is 27 ft in diameter and 165 ft in overall length; it weighs 1,600,000 lbs at launch. Approximately 90% of that weight is in the liquid oxygen which is located in a tank in the forward end of the overall external tank. This mass is concentrated at the front end of the tank in consideration of the overall vehicle center of gravity relative to the thrust location on the Orbiter and the thrust vector of the combined vehicle. The Solid Rocket Boosters are attached 20 ft out from the centerline of the tank, and the principle axis of the Orbiter is 25 ft above the tank. Thus one can begin to visualize some of the forces, the masses, and the spring constants that are involved in this system. The main load path for the Orbiter to External Tank is through the aft-attachment where the Orbiter is attached to the tank through the three landing gear locations. The main 2,500,000 lbs thrust from each Solid Rocket Booster is taken out of the forward end of the tank and it feeds into the inner tank structure of the liquid hydrogen and liquid oxygen tanks.

Figure 4 shows the overall mission profile. The lower center part of the composite picture shows the vehicle in the vertical mode on the mobile launcher as it leaves the vehicle assembly building. We are using many of the ground support features of Saturn Apollo System; the vehicle on the pad would be supported by the two Solid Rocket Boosters, the External Tank would be supported between these two boosters and the Orbiter would be cantilevered on back of the External Tank. This view shows the vehicle on the launch pad nearby the service tower where we have the capability of onloading the payload while on the pad. After igniting the three engines at the aft end of the Orbiter

initially, we hold down the system while we build up the thrust on the Orbiter, and then we ignite the Solid Rocket Motors and release the hold downs of the Solid Rocket Motors so that all engines are burning in parallel at liftoff. We have thrust vector controls on both the solid and the Orbiter rocket engines. The vehicle lifts off in its parallel burn mode and the Solid Rocket Boosters burn for nearly two minutes (Fig. 4a). After the two minute burn, the solids have performed their mission, they burn out and are separated from the External Tank. During this separation maneuver the rockets on the Orbiter are still propelling; the Orbiter and the External Tank continue along the flight trajectory to just short of orbit. We shut down Orbiter engines 150 feet per second or so below orbital velocity and separate the External Tank from the Orbiter at that point. This puts the External Tank in a ballistic trajectory that will cause it to reenter and be destroyed by aerodynamic heating in the remote ocean region some 10,000 miles down range of the launch site.

We then ignite the orbital maneuvering engines and accelerate the Orbiter to orbital velocity where we can conduct a very wide range of missions. After a mission is completed, we ignite the orbital maneuvering engines again to slow the vehicle down to put it on a path to reenter the earth's atmosphere. We fly the vehicle through the early part of reentry at a relatively high angle of attack of approximately 35 degrees where we roll the vehicle about the lift vector in order to achieve the crossrange maneuvering. Once we get down to intermediate supersonic mach numbers, we transition the vehicle down to a more conventional angle of attack, in the 12 to 15 degree range, in order to come down through the atmosphere and maneuver into position to land tangentially on the runway. We expect to touch down on the runway somewhere in the range of 190 knots, depending on the conditions and payload. Incidentally we have runway touchdown and rollout problems in the shock and vibration area.

We are building the vehicle such that once the system matures, we will be able to turn the Orbiter around two weeks from the time it finishes one mission until it is ready to fly another one. We recover the spent Solid Rocket Booster cases from the ocean by parachute and recycle, reload, and reuse the spent cases. A great deal of the economy of the system comes from reusing the Orbiter and the Solid Rocket Boosters. It is important to focus on the various types of operations that we plan to conduct with the Orbiter. In the upper right of Figure 5 we have shown an artist's drawing depicting the placement, service, and the repair of satellites. The Orbiter is designed to operate in what might be called low earth orbit, or altitudes up to 600 nautical miles. One of the principal uses that we would expect of the vehicle is the implanting of satellites in various orbits from relatively low inclined orbits to the equator and polar or retrograde orbits. We would also expect to take propulsion

stages and satellites for higher energy orbits into the low earth orbit initially; they would be carried in the payload bay into lower earth orbit. Then the manipulator arm would move the payload and its "tug", or upper stage, out into the trajectory where the "tug" would be fired to transfer the satellite on into a higher energy orbit. People and experiments could be loaded in the payload bay of the Orbiter and go into orbit. The entire vehicle could be kept in orbit for periods of up to 30 days for various type of missions, either looking down at the earth or looking outward from earth in the astronomy type mode; various types of research activities, such as medical or manufacturing, where one would like to take advantage of the space environment.

The Orbiter is a natural for any future space station programs where one might want to take space station modules into orbit in a modular form. One can take modules anywhere up to the 15 ft by 60 ft size limitation and couple those modules together to build a large permanent space station. The Orbiter is also a natural for taking people to and from that space station. Furthermore, once the program has matured and we have as many as two Orbiters on hand, we will have a rescue capability.

Figures 6 and 7 depict the status of the program. We have been under way for just under 4 years, but for the last 2 to 2½ years we have had most of our industry people on board working on a final design. The first element of the system that we put under contract was the Orbiter engine; this contract was awarded in August of 1971 to the Rocketdyne Division of Rockwell International. The second element that we placed under contract was that for development of the Orbiter and for support of the government in an overall systems engineering role; that contract was let in July 1972 to the Martin Marietta Corporation. Then the last major element to go under contract was the Solid Rocket Motor, which was awarded to the Thiokol Chemical Corporation in November of 1973. Thus we have formed our major contractor team; they have been on board, some of them for as much as over 2 years. Figure 8 shows our overall program target schedule. The first horizontal flight of the system is expected to take place in 1976, our first vertical development flight is expected to occur in late 1978, and we would then plan to have the system in operation by the early 1980 time period. We have been through a number of our major early program milestones; our preliminary requirements reviews, our system requirement reviews and our preliminary design reviews. The critical design reviews are expected to take place in the 1975 time period.

Let us examine the vehicle to postulate and speculate on where we might encounter some of our concerns relative to shock and vibration, Figure 9. The vehicle has a number of fairly large masses, and we have to be able to separate these masses while in dynamic flight. Therefore, separation planes have to be carefully engineered

so that the masses will separate when we want them to and so that they will not separate when we don't want them to. One can afford to invest only a certain amount of stiffness in the interfaces between the major masses. We have many forces pushing on the vehicle as it flies; we have the thrust of the rocket engines, the thrust of both the Orbiter engines and the Solid Rocket Boosters, the gimbaling loads, and the thrust vectors in flight. Accordingly, many disturbing forces and moments are inherent in the vehicle are present as well as the external disturbing forces brought about by the disturbances of the atmosphere and the dynamic separation. Thus a fertile field exists to keep us on our toes in this overall area, and the overall structural dynamic characteristics of the vehicle has been one of the major concerns.

The artist's concept in Figure 10 depicts the vehicle sitting on the launch pad and the vehicle is supported by the two Solid Rocket Boosters. While on the launch pad we have to worry about the horizontal wind, the vortex shedding from nearby structures or from the vehicle itself. This vehicle, unlike some of our previous vehicles has wings on it so that the old bug-a-boo of "stop-sign" flutter and things of that nature will have to be considered while in the prelaunch configuration. Once we are ready to leave the launch pad, we ignite the rockets on the Orbiter initially; there is an upsetting moment because of the cantilever effect of the Orbiter. We hold the vehicle down while we build up thrust on the Orbiter. We have the capability, if we had any problem with the main propulsion system on the Orbiter coming up to thrust, of shutting down the engines and holding the vehicle in that configuration.

Once the two Solid Rocket Boosters are ignited, we are committed to launch, so we would leave the pad shortly after the ignition of these motors. We have dynamics involved in igniting the engines on the Orbiter and on the booster; after lift off and at the start of flight, there are the transient wind conditions that must be considered as sources of excitation. There are many sources of multipled body responses, from the masses involved, the elastic coupling between the Solid Rocket Booster and the tank and between the tank and the Orbiter; the disturbing forces and moments on the wing and on the vertical tail of the Orbiter are such sources, as well as sources for axial-lateral coupling. The asymmetry of the Shuttle configuration has been one of the things that has concerned us as compared with our previous vehicle (Saturn). The Titan, which has a similar arrangement of two solid rocket motors on either side of the tank, began to approach some of the asymmetry of the shuttle configuration, but we went one step further than the Titan by cantilevering the Orbiter on the back of the External Tank.

In addition the axial-lateral coupling potential of this vehicle is of some concern to us, and we are going to watch this very

carefully. Once we move into the higher speed region of flight, our maximum dynamic pressure is expected to be approximately 650 lbs/ft². This value is not extremely high for flight vehicles; many of our supersonic airplanes experience values that are considerably higher than that. However, we have to be careful in spending our weights and masses in this vehicle, so we can't afford to put too much stiffness in the structure and we have deliberately tried to hold the q down to 650 in concept and design of the vehicle. At that dynamic pressure we have the classical gust turbulence problems, and dynamic pressure will occur at transonic speeds producing both the aerodynamic interference and the mixed flow conditions inherent in transonic flight.

We expect fairly large lateral accelerations because we have wings and a vertical tail on the vehicle. The axial-lateral coupling manifest itself here strongly. During staging we are at a Mach number of approximately 6, and we are faced with the shutdown transients on the Solid Rocket Boosters. There is no way to shut down a solid rocket motor gracefully since it tails off fairly rapidly. Also it is necessary to consider the asymmetry in shut down and tail off of the solid rockets.

All through this flight we have the control system-coupling concern, the gimbaling of the rockets on the Orbiter as well as the Solid Rocket Boosters to fly the vehicle. We shut down the two Solid Rocket Boosters and separate those while the Orbiter continues to thrust. We have shown in Figure 9 that the q , when separating the External Tank from the Orbiter just prior to going into orbit, would be quite low. We don't expect any design load conditions in that area, but we must be prepared for the transients involved in shutting down the main engines on the Orbiter, separating the External Tank, and igniting the Orbiter maneuvering engines just prior to going into orbit. Following retrograde firing or entering the earth's atmosphere, the vehicle flies a Mach number spectrum of 25 down to 0, and fortunately we are through a good portion of the Mach number region before the dynamic pressure gets very high. The dynamic pressure of reentry never exceeds more than 225, and that is roughly 40% of what it is during launch. On landing we are planning to bring the Orbiter back unpowered, glide down through a fairly steep approach angle to the runway, and, as mentioned earlier, we will actually touch down on the runway at 190 knots. Touch-down dynamics on our runway runout area is certainly one of the concerns.

Figure 11 shows the vehicle in the launch configuration with the thrust of the rocket engines and the bodies involved. Figure 12 shows the vehicle configuration at max q . Figure 13 depicts staging where we separate the two Solid Rocket Boosters after their burn out and their transient shut down while the External Tank and the Orbiter are continuing on into orbit. Figure 14 shows the vehicle during the early

heating part of reentry, where it is at a high angle of attack, followed by a transition of a low angle of attack prior to landing. Figure 15 shows the vehicle in a fairly steep approach path to the runway for the airplane-type landing.

Figure 16 lists some of the unique features of potential instabilities of this configuration. First there is the classical coupling of the structure and the propulsion systems or "POGO". We bring the oxygen from the small tank located on the front of the External Tank down along the External Tank in 17-inch-diameter lines, about 100 ft long; then we have to turn that liquid oxygen and run laterally a few feet over into the aft end of the Orbiter where we feed the three rocket engines. There long liquid lines can have some closely spaced natural frequencies, and we are concerned about the overall coupling of the propulsion and structural systems. The lateral segment of this propellant line also enhances the axial-lateral coupling possibilities. There are some characteristics of the rocket engine that are different from previous designs. We are operating at a chamber pressure of 3000 psi; the chamber pressure on these hydrogen-oxygen engines is three times that of the engines in the upper stages of the Saturn launch vehicle. That means that the chamber pressure upstream in some of our ducts will get as high as 7000 lbs per square inch. In order to get our propellants up to those pressures, we have two different pumps, a low stage pump and a higher stage pump. As a result we have to be very concerned about the coupling in between these two pumps in our feed system.

We are also concerned about any possibility of coupling the propulsion-structural disturbing forces with our flight control forces. In fact, we are gimbaling our rocket engines close to the aft end of the Orbiter and the aft end of the Solid Rocket Booster.

We are concerned about normal classical lifting surface flutter although we have fairly stubby delta wings, and these are good structural configurations. However, we are fighting weight as we always do in any program, so we cannot afford to put excessive stiffness in our lifting surfaces. These wings are only useful during reentry and landing phase. We can't afford to carry too large a wing or too heavy a wing since it becomes too much a penalty on the overall system to be too generous in wing area or wing stiffness. Therefore, we have to be careful about classical wing-elevon flutter with such concerns as single degree of freedom flutter of the elevon.

In any rocket vehicle system, the possibility of control system induced instabilities must be considered. The large masses, the spring characteristics, the very high modal density of this vehicle makes it necessary that we be extremely careful in engineering and

designing our control system. Such care is needed in order that we can properly detune the system and not excite too many vibration modes in our flight control system. Inherent to the understanding of the overall structural dynamics of any vehicle is the understanding of the vibration modes and frequencies and the recognition of some of the potential problems that face us on the Shuttle. Figure 17 outlines a very aggressive program for understanding the vibration modes and frequencies of the vehicle from the very start. We have paid a great deal of attention to getting underway a broad base of a very comprehensive analytical activity where we use the best tools that are available to us today. The approach is to break the vehicle up into many many different elements and try to then understand the behavior of those elements. Concurrently with this analytical activity, as soon as we can mature various segments of the vehicle and once components have become available, we plan to schedule testing of those components. These would include static influence coefficient tests for each of the components, and we will also shake each component to understand its isolated vibration modes and frequencies. Once we have moved on to where we have combined these components into elements, such as the Orbiter the External Tank, the Solid Rocket Booster, we will individually test those elements, and we will feed back the results of these element tests into our analytical activity.

We are also starting very early to build a $\frac{1}{2}$ scale dynamic replica model. We deliberately chose a $\frac{1}{2}$ scale in order to get ourselves a sufficiently large vehicle that we felt could replicate the structure fairly accurately. We will bring this model along as soon as the design has matured to the point where the model can be built. We would use this model as a check against our analytical activity and our full scale activity as it matures.

Then as a sort of a graduation exercise, we currently have planned in the program some limited testing of the "all up" full scale Shuttle vehicle complete with a flight Orbiter once that element has become available. That is the building block approach we have underway to understand the vibration modes and frequencies that we are faced with in the overall configuration. The replica model, Figure 18, will replicate the Orbiter, the Solid Rocket Boosters, and the External Tank, and we will test several different fuel loadings in both the Solid Rocket Boosters and the External Tank. It will give us early confirmation of our analytical and full scale test activity work, and we will be able to perform parametric investigations of the effects of various propellant payloads. After we have finished our basic design phase, we want to use this model to study various effects of payload on the overall configurations; we can carry payloads of up to 65,000 lbs, and these payloads in themselves have their own set of dynamic characteristics. We have to be very concerned about the influence of the payload on the overall system in the dynamic launch

environment. We will use this model on into the operational phase of the program to check out the interactions between the model and the vehicle that are appropriate prior to committing the vehicle payload.

Figure 19 depicts the shuttle acoustic sources. Like any good launch vehicle, we have our share of problems facing us in this area, and we have several good noise generators. We have the liquid oxygen rockets in the aft end of the Orbiter at their high frequencies, and we expect energy content over a fairly high range of frequencies; coupled to that is the spectrum of the Solid Rocket Boosters which probably will fill out that part of the spectrum that the liquid rockets missed. Thus we might expect acoustic energy over a pretty broad range of frequencies. We have the reflection problems from the pad and nearby structure locations, so we expect to face fairly high acoustic levels over the aft end of the vehicle. The shuttle Orbiter is protected from the heat of reentry by a reusable external insulation. This might be classified as building a basic aluminum airplane and putting a light weight fire brick all over the surface of the airplane. We are concerned about the structural integrity of this light weight firebrick that we use for external insulation from the effects of the high acoustic environment that we face during the liftoff, launch, and reentry phases of flight.

During launch we also face the transonic and supersonic flow conditions, and we will also face the hypersonic flow regions that we will pick up during reentry. We are currently baselined to have the capability of adding air breathing engines to the orbiter for ferry missions, and these would be another acoustic source. We are concerned about the acoustic levels and their effects on the structure; specifically, these effects include the sonic fatigue of the structure, the thermal protection system integrity, and the environmental vibration in the payload. We intend to keep the environment in the payload acceptable to the payload people by adding reasonable attenuation to reduce the overall sound levels in the payload bay and in the cabin.

Figure 20 lists the dynamic environments and some of these have been enumerated in a discussion of the various mission phases. Some of the sources of the low frequency range of vibration are the lift off transients and staging (or separation) transients where large loads are suddenly released or where large structural forces in the rocket engine are shut down. Also there are the relatively low-frequency thrust oscillations that exist in any rocket engine. Aerodynamic buffet, landing, roll out, and taxi are all areas where shock and vibration specialities will be brought to bear in the design of the vehicle. The higher frequency vibration energy sources are the lift off noise, rough burning in the rocket engine, and aerodynamic noise. Some of the shock sources

include separation and staging since we have a number of pyros located on the vehicle, and currently most of our separation mechanisms are pyro oriented. We have small solid rocket motors for separating the Solid Rocket Boosters from the External Tank. The shock and vibration associated with igniting those rockets is contained in the exhaust that impinges on part of the structure and it imparts dynamic energy to the vehicle. We also have the landing shock as mentioned previously.

I don't want to sound too negative. I thought that one of the reasons people like to come to these type of meetings is to understand where others have problems. We fully expect to have some problems in this area, and we certainly didn't pick this particular vehicle configuration to make our vibration and structural dynamics job easier. We picked this shape of vehicle primarily for other considerations, such as low cost, reusability, overall size, and complexity of development. We realize we face a number of challenging areas in structural dynamics, but we don't see any show stoppers. If the tools that people such as yourselves have brought along through the years are applied intelligently, effective tests are conducted on the components, careful attention is paid to how we use our flight control system so that we use it in such a way that it helps to detune the vehicle rather than tune up the vehicle, then we can build a space Shuttle vehicle that can be flown safely and accurately. However, we have a lot of work ahead of us.

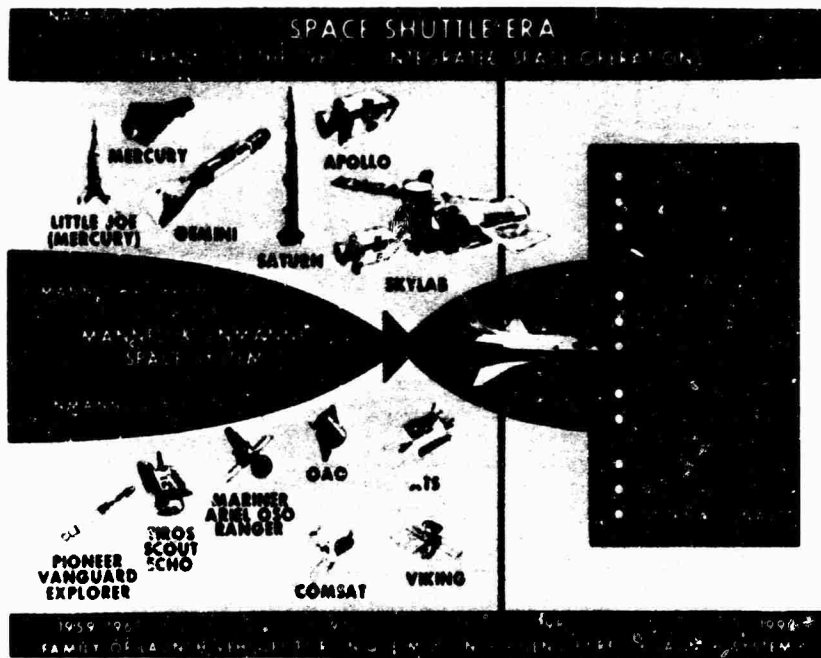


Figure 1



Figure 2

SPACE SHUTTLE SYSTEM

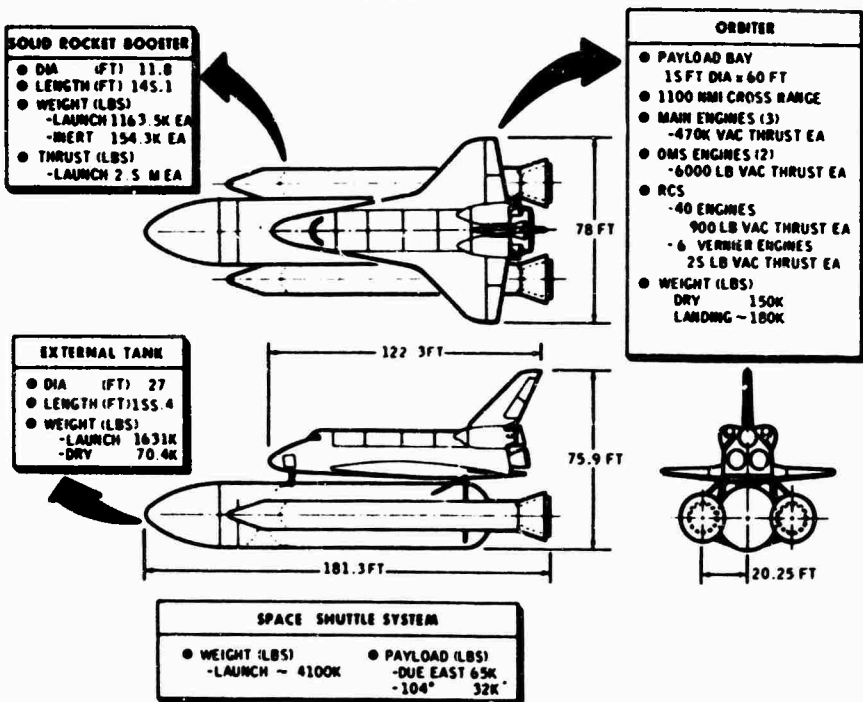


Figure 3

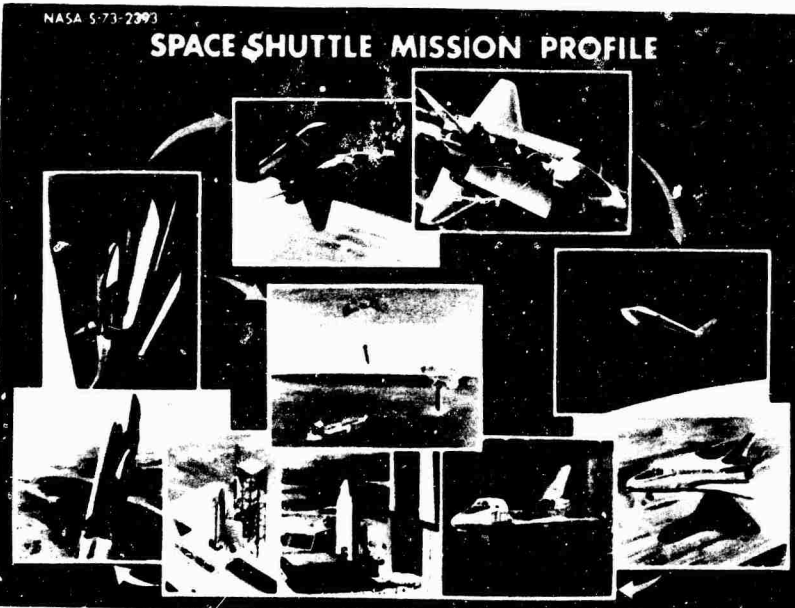


Figure 4

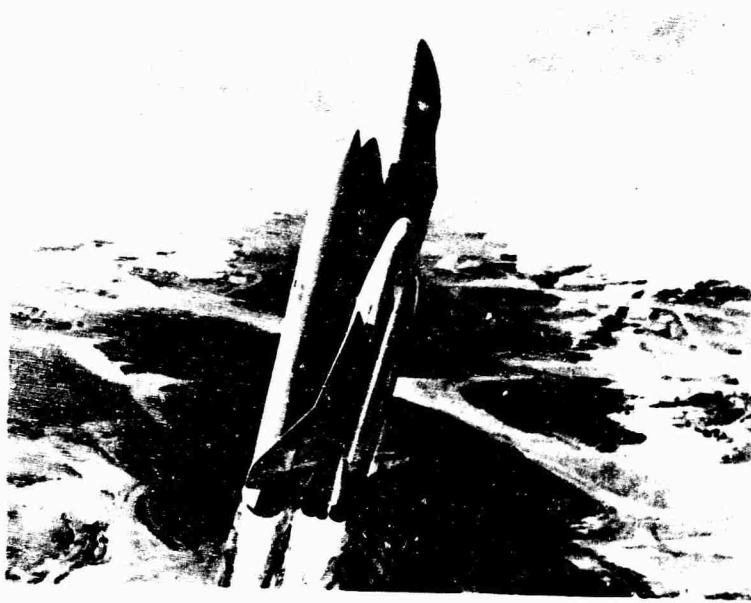


Figure 4a

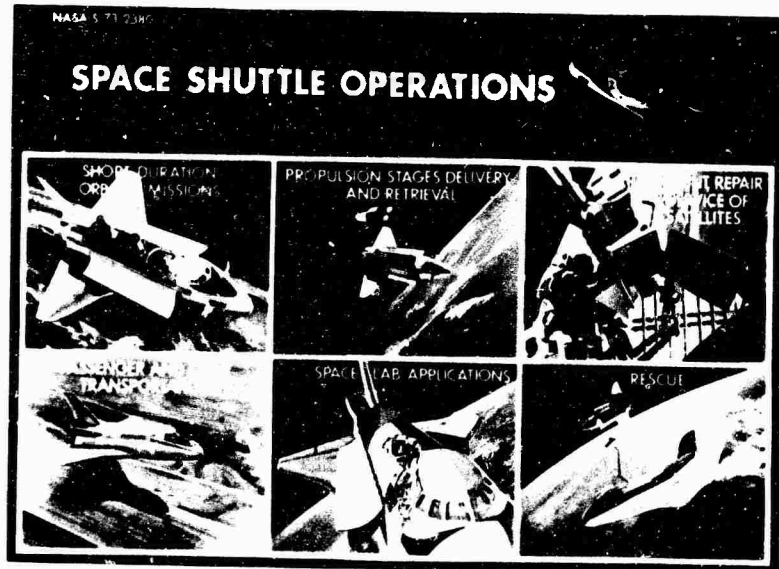


Figure 5

PROGRAM CONTRACT STATUS

MAIN ENGINE

- ROCKETDYNE DIVISION, NORTH AMERICAN
ROCKWELL CORP.* - CONTRACT AWARDED AUG 1971
- PRELIMINARY DESIGN REVIEW ACCOMPLISHED SEP 1972

ORBITER/INTEGRATION

- SPACE DIVISION, NORTH AMERICAN
ROCKWELL CORP.* - SELECTED AS CONTRACTOR JULY 1972
- PROGRAM REQUIREMENTS REVIEW COMPLETED NOV 1972
- SYSTEM REQUIREMENTS REVIEW ACCOMPLISHED AUG 1973

EXTERNAL TANK

- REQUEST FOR PROPOSAL ISSUED APR 1973
- CONTRACTOR SELECTED - MARTIN MARIETTA CORP. AUG 1973

SOLID ROCKET MOTORS

- REQUEST FOR PROPOSAL ISSUED JULY 1973
- CONTRACTOR SELECTED-WASATCH DIVISION,
THIOKOL CHEMICAL CORP. NOV 1973

*NOW ROCKWELL INTERNATIONAL CORPORATION

Figure 6

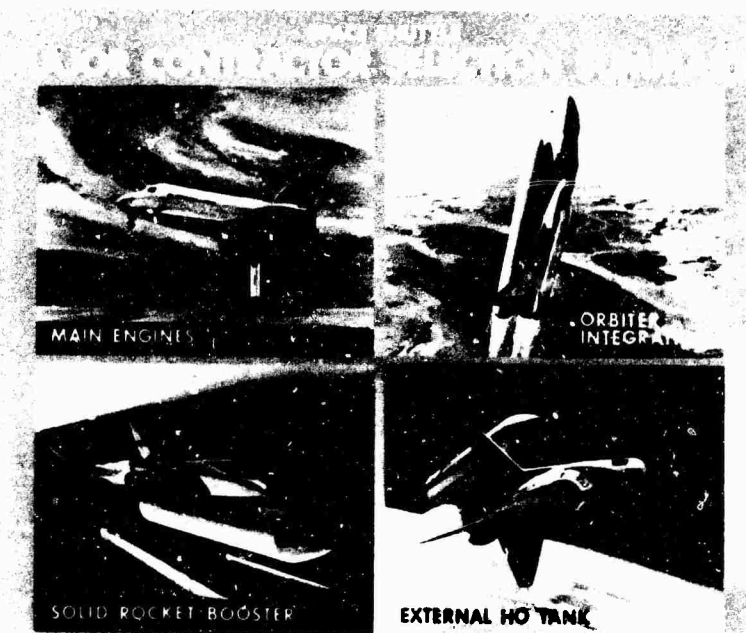


Figure 7

SPACE SHUTTLE SYSTEM PROGRAM TARGET SCHEDULE

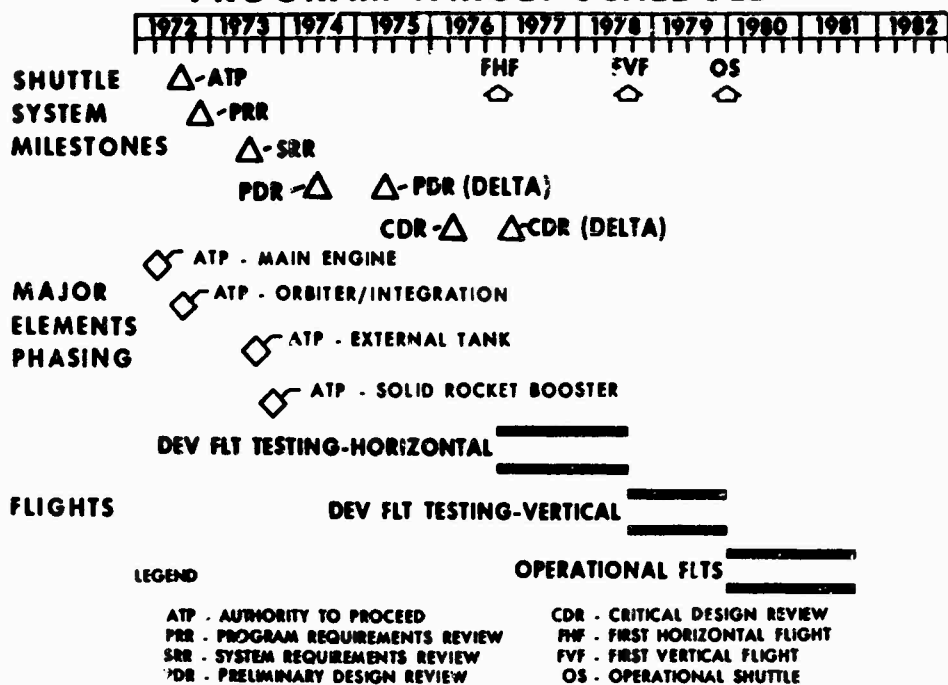


Figure 8

SPECTRUM OF SHUTTLE DYNAMIC LOADS

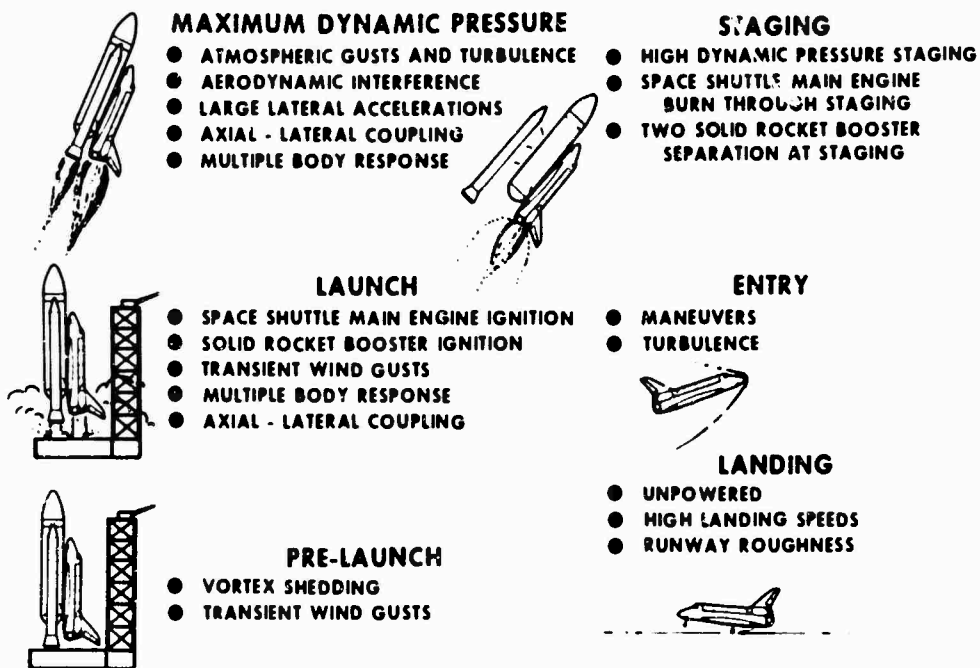


Figure 9

NASA-S-73-2412

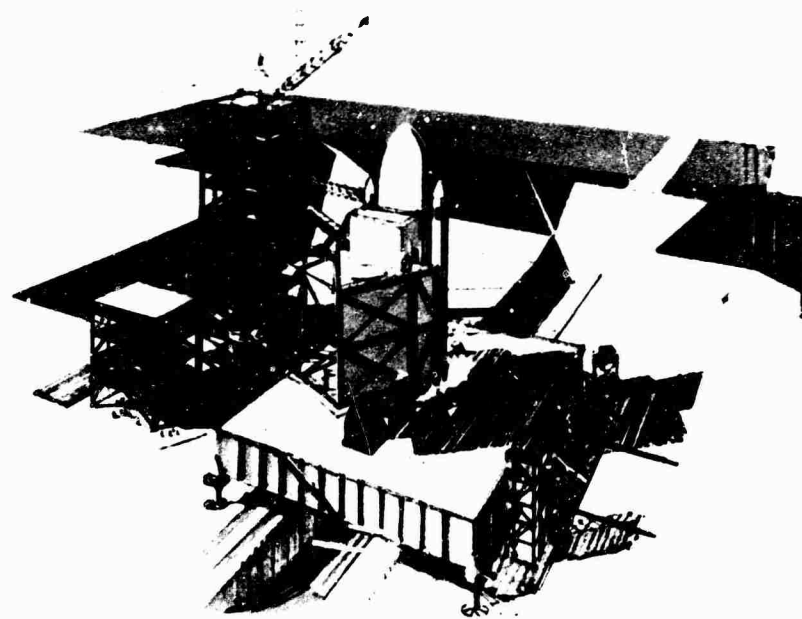


Figure 10

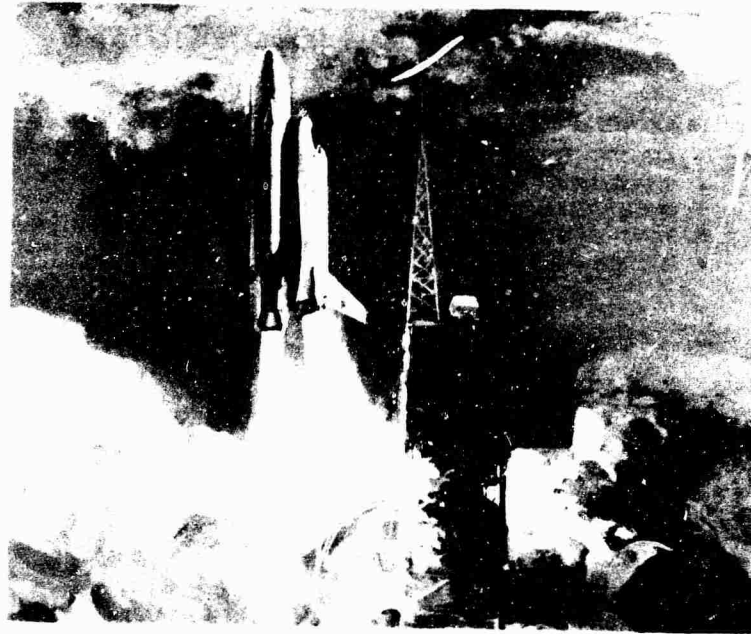


Figure 11

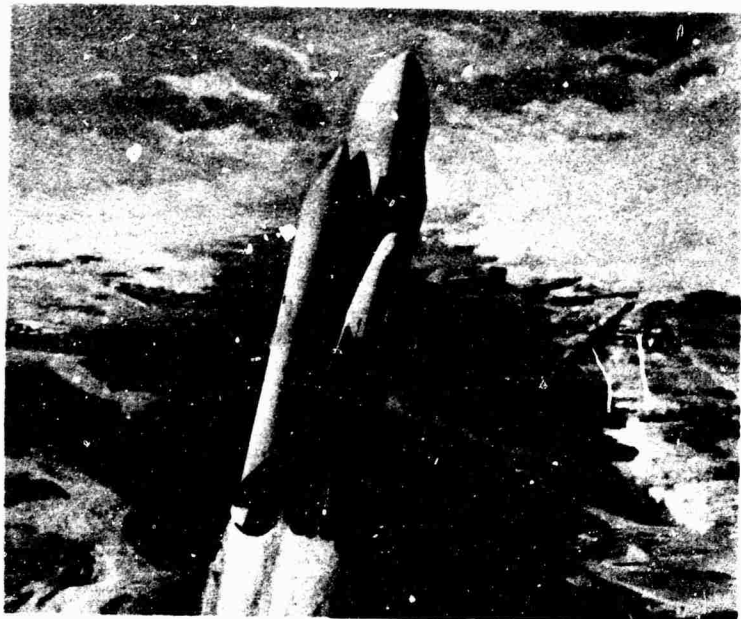


Figure 12

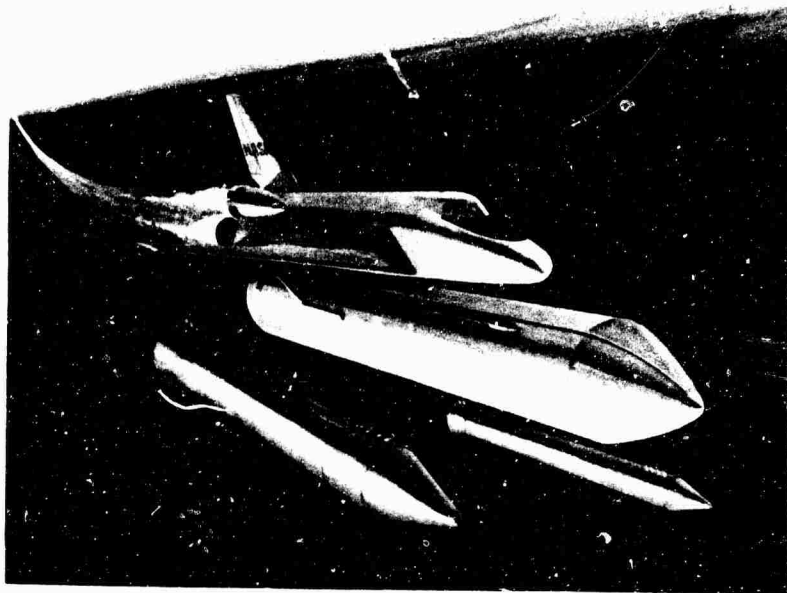


Figure 13

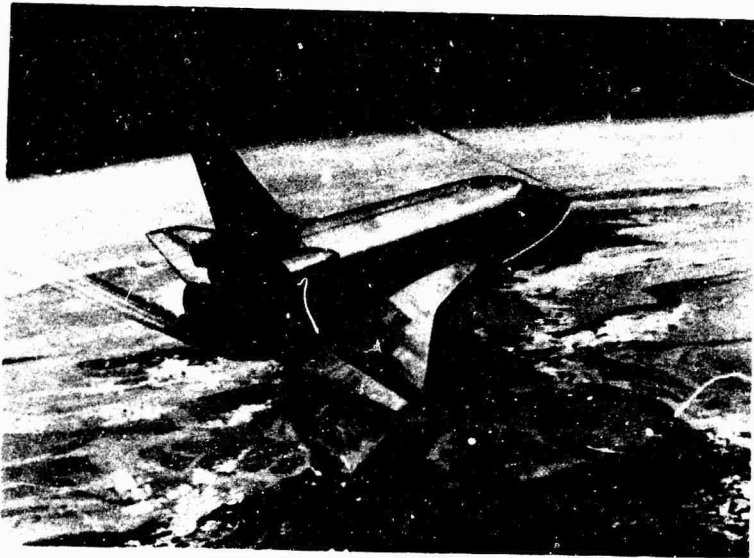


Figure 14

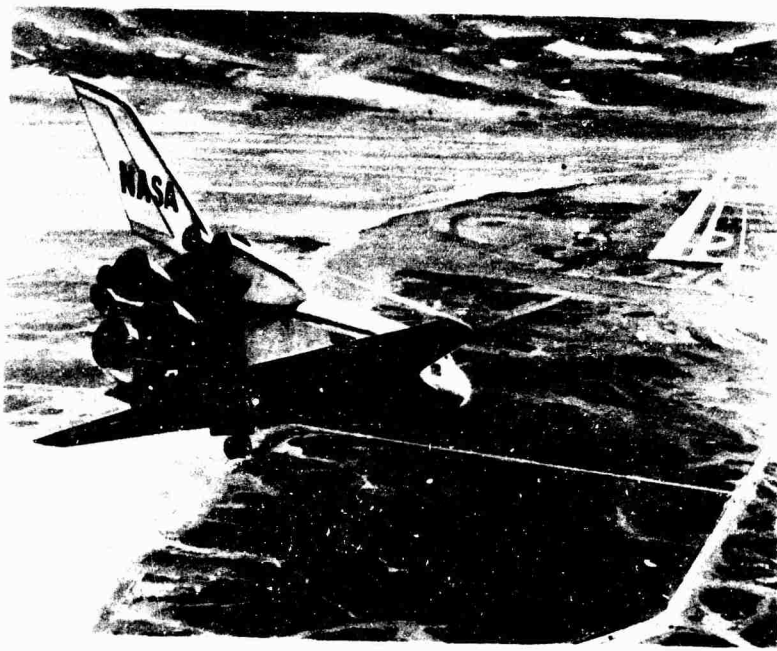


Figure 15

UNIQUE FEATURES OF POTENTIAL INSTABILITIES OF SHUTTLE

- PROPULSION/STRUCTURAL COUPLING (POGO)
 - AXIAL - LATERAL COUPLING DUE TO ASYMMETRY
 - LONG LIQUID OXYGEN LINES CAUSES CLOSELY SPACED LINE NATURAL FREQUENCIES
 - LATERAL SEGMENT OF PROPELLANT FEED LINE ENHANCES EFFECTS OF AXIAL - LATERAL COUPLING
 - HIGH CHAMBER PRESSURE, TWO STAGE PUMP MAIN ENGINES
 - POSSIBLE POGO/FLIGHT CONTROL COUPLING
- LIFTING SURFACE FLUTTER
 - AERODYNAMIC INTERFERENCE DUE TO MULTIPLE BODIES
- CONTROL SYSTEM STABILITY
 - AXIAL - LATERAL COUPLING DUE TO ASYMMETRY
 - HIGH MODAL DENSITY OF CONFIGURATION

Figure 16

'BUILDING BLOCK' APPROACH UNDERSTANDING OF SHUTTLE STRUCTURAL DYNAMICS

- EXAMPLE - VERIFICATION OF SHUTTLE STRUCTURAL DYNAMIC CHARACTERISTICS USED IN DYNAMIC STABILITY AND LOADS ANALYSES

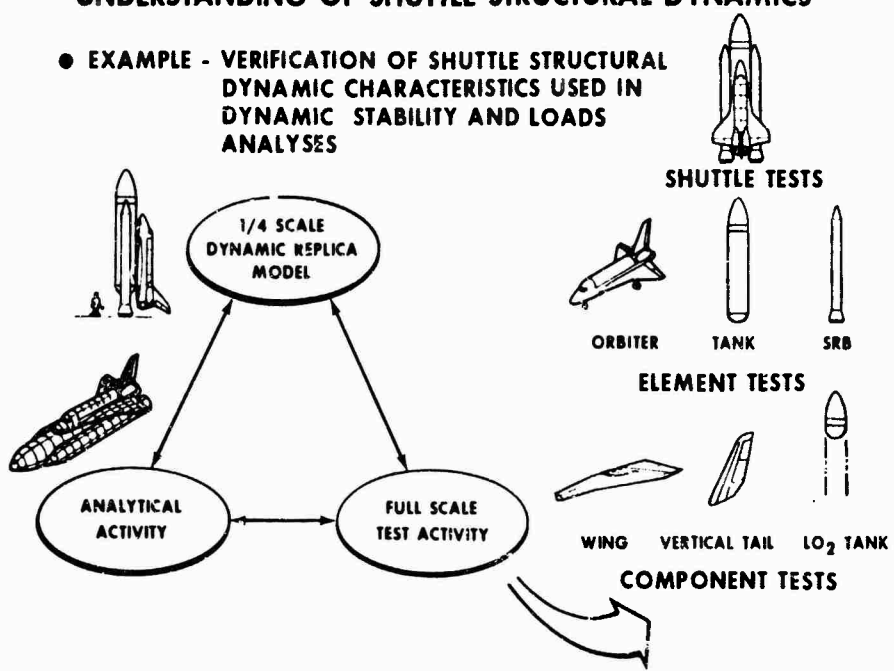


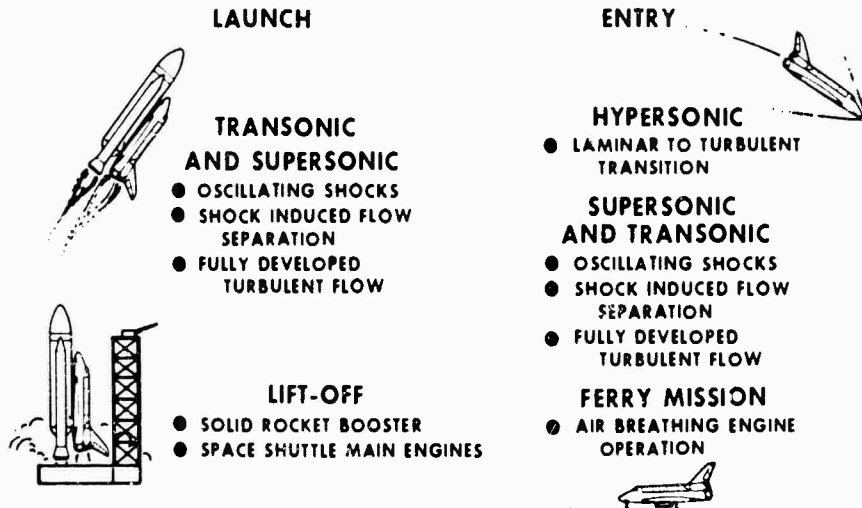
Figure 17

SPACE SHUTTLE DYNAMIC REPLICA MODEL

- 1/4 SCALE ORBITER, SOLID ROCKET BOOSTER AND EXTERNAL TANK
- PROVIDE EARLY CONFIRMATION OF SHUTTLE DYNAMIC CHARACTERISTICS
- PARAMETRIC INVESTIGATIONS OF PROPELLANT LOADING EFFECTS
- PARAMETRIC INVESTIGATIONS OF PAYLOAD EFFECTS
- UPDATE IF REQUIRED ON BASIS OF SUBASSEMBLY AND ELEMENT TEST RESULTS
- PAYLOAD INTEGRATION STUDIES DURING SHUTTLE OPERATIONAL PHASE

Figure 18

SHUTTLE ACOUSTIC SOURCES



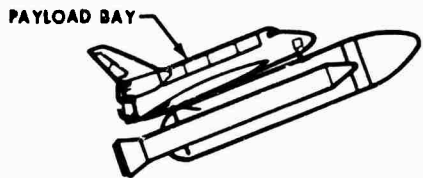
ACOUSTIC LEVELS PERTINENT TO:

- SONIC FATIGUE OF STRUCTURE
- THERMAL PROTECTION SYSTEM INTEGRITY
- ENVIRONMENTAL VIBRATION - EQUIPMENT AND PAYLOADS
- INTERNAL ACOUSTICS - CABIN AND PAYLOAD BAY

Figure 19

NASA-S-7J-2969

SPACE SHUTTLE PAYLOAD DYNAMIC ENVIRONMENTS



SOURCES

● VIBRATION:

- LOW FREQUENCY
 - LIFT-OFF TRANSIENTS
 - STAGING AND SEPARATION TRANSIENTS
 - ROCKET ENGINE THRUST OSCILLATION
 - AERODYNAMIC BUFFET
 - LANDING ROLL-OUT AND TAXI
- HIGH FREQUENCY
 - LIFT-OFF NOISE
 - ROCKET ENGINE ROUGH BURN
 - AERODYNAMIC NOISE

● SHOCK

- SEPARATION AND STAGING PYROS
- LANDING SHOCKS

PAYLOAD ENVIRONMENT CONTROL

● PAYLOAD ACCOMODATIONS

- ACOUSTIC TREATMENT
- VIBRATION CONTROL

Figure 20

VIKING DYNAMICS - AN OVERVIEW (U)

Richard E. Snyder
NASA Langley Research Center
Hampton, Virginia

(U) The Viking mission encompasses nearly all of the dynamic environments encountered in any NASA mission. These dynamic loading events include launch and boost, interplanetary cruise, orbit, entry, and landing. Design loads for these events are generated using transient loads analyses of modally coupled finite element models. Test programs are conducted to verify mathematical models and confirm loads analysis techniques.

INTRODUCTION

The Viking Project is a current NASA effort to explore Mars using two unmanned spacecraft during the 1975-1976 opportunity. The project is managed by the Viking Project Office at NASA's Langley Research Center. The objective of this project is to obtain scientific data which will significantly advance the knowledge of the planet Mars by direct measurements in the atmosphere and on the surface. Particular emphasis will be placed on obtaining information concerning biological, chemical, and environmental factors relevant to the existence of life on the planet. A detailed description of the Viking vehicle, mission, and scientific instruments is presented in Ref. [1].

The Viking mission encompasses nearly all of the dynamic environments encountered in any NASA mission. These dynamic loading events include launch and boost, interplanetary cruise, orbit, entry, and landing.

In this paper, the Viking Space Vehicle will be described and the structural configuration of the Viking spacecraft will be discussed. The significant dynamic events associated with the various mission phases will be identified. An overview of the analysis and test program which are used to determine loads and dynamic environments will be presented. This paper is part of a three-paper overview of the Viking dynamics. References [2,3] present details of the Orbiter and Lander dynamics, respectively.

VIKING SPACE VEHICLE

The launch vehicle for the Viking mission is the Titan III E/Centaur. Figure 1 shows the Viking Space Vehicle configuration. The spacecraft is mounted on top of the Centaur and enclosed in the new Centaur Standard Shroud. While both the Titan and the Centaur have been used in previous space missions, they have not previously been used in combination.

The Titan III E consists of two solid propellant rocket motors strapped on to liquid propellant core stages. The Centaur, which utilizes liquid oxygen and liquid hydrogen as propellants, is the high energy upper stage. The space vehicle weight at ignition is approximately 1.5 million pounds. The maximum thrust is approximately 2.3 million pounds. The spacecraft weighs 7,600 pounds.

VIKING SPACECRAFT

The Viking spacecraft in the cruise mode is shown in Fig. 2. The Orbiter and the Lander are the two basic elements. A bioshield to prevent recontamination after sterilization surrounds the Lander. The Lander is attached to the Orbiter "bus" by means of a three-point to four-point adapter.

VIKING ORBITER

The design of the Viking Orbiter is an extension of the Mariner '71. However, the

design is greatly influenced by the 3,500-pound propulsion subsystem which is attached to the "bus." The propulsion subsystem is a module consisting of two propellant tanks, a pressurant tank, and the engine. Much of the Orbiter science is contained in the scan platform.

VIKING LANDER

Figure 3 shows an exploded view of the Viking Lander capsule. The Lander capsule consists of a bioshield cap and base; the base cover, including the mortar and parachute system; the aeroshell; and the lander. The lander, aeroshell, and basecover are sterilized in order to prevent contamination of Mars with Earth organisms. The bioshield serves to prevent recontamination after sterilization. The basecover vent system controls the pressure equalization during the launch and entry phases of the mission. The disk-gap-band parachute is deployed by firing a mortar. The aeroshell is used for the initial aerodynamic deceleration and is covered with a lightweight ablator material.

The Lander in the landed configuration is shown in Fig. 4. The science and other operational subsystems are mounted to the Lander equipment mounting plate and side beams. The Lander is hexagonal in plan form and is fabricated primarily of aluminum and titanium. It is 58.8 inches wide and 18 inches deep. The landing gear consists of three inverted tripods. Each tripod consists of a main strut, an A-frame, and a foot pad. The landing gear absorbs most of the energy at impact by means of crushable aluminum honeycomb contained in the main strut. The A-frame is attached to the Lander body through short cantilevered beams which limit the loads by plastic deformation. In this configuration, the Lander weighs approximately 1,270 pounds.

SIGNIFICANT DYNAMIC EVENTS

Launch Phase

Figure 5 shows the space vehicle launch phase flight profile. The transient loading events associated with this mission phase govern the design of the Orbiter primary structure and a few areas of the Lander structure. The solid rocket motors burn for about 2 minutes and are jettisoned. Slightly before solid rocket motor burnout, the first stage engines are ignited. After separation, the second stage burns for 3-1/2 minutes. The Centaur Standard Shroud is separated during this burn. There are two Centaur burns prior to spacecraft separation.

Transient loads analyses of all of these events are accomplished using a modally coupled finite element mathematical model. Each cognizant organization is responsible for the development of a model of the structure for which they are responsible. These separate models are coupled modally to form the appropriate space vehicle configuration and transient response analyses are performed. Force time histories in spacecraft structural members are a part of analysis output.

Stage zero ignition, stage one shutdown, and the Centaur second engine cutoff are the controlling loading events for the spacecraft. The loads associated with stage zero ignition are generated using 21 pairs of flight-measured solid rocket motor thrust time histories. The resulting spacecraft internal member loads are each combined statistically to determine a "mean plus three sigma" load. Stage one shutdown is accomplished in a similar manner, using 27 flight-measured forcing functions. The Centaur second engine cutoff loads analysis uses a worse case shutdown profile.

The loads generated by these means are used to size structural members. Hence, this involves an iterative procedure. The advantage of this method of obtaining design loads is that it leads to minimum structural weight. The disadvantage is that it does require iterations which would result in redesign requirements.

Entry and Landing Phase

The entry and landing profile for a typical mission is shown in Fig. 6. This mission sequence produces the governing design loads for the Lander. The Lander enters the atmosphere at about 800,000 feet between 2 and 5 hours after separation from the Orbiter. The drag on the aeroshell produces the initial deceleration. The peak deceleration, which occurs between 80 - 100,000 feet, produces the highest steady state loading condition to which the Lander is subjected. The aeroshell and much of the Lander body are designed to meet this loading condition.

The mortar which deploys the parachute is fired at an altitude of about 21,000 feet above the surface. Shortly after the deployment of the parachute, the aeroshell is separated. This mission event is the designing condition for the mortar truss. The mortar fire also produces a high level dynamic environment for the components.

At 4,100 feet, the terminal propulsion engines are ignited and the parachute and base-cover are separated. The engines continue to fire until one of the legs contact the surface. The velocity at impact with the surface is approximately 8 feet per second.

The landing event produces loads which govern the design of the landing gear, portions of the Lander body side beams, the equipment mounting plate. A significant dynamic environment is also generated at component locations. The method of analysis used for the landing event is conceptually the same as that used for the stage zero ignition and stage one shutdown loading events. That is, transient loading analyses are conducted for a large number of randomly selected initial conditions, and statistical member and component loadings are generated. The frequency content of the responses at component locations are generated by shock spectra methods.

The stability of the Lander for the landing event is of critical importance. Stability analyses were carried out again using randomly selected initial conditions to determine the probability of a stable landing.

DYNAMIC TESTING

Modal surveys of both the Orbiter and Lander have been conducted to verify and correct the finite element math models which are used for the analysis of transient loading events. The final loads iteration for the launch phase of the mission is done using math models which have been confirmed by modal survey.

Component dynamic environments associated with the launch phase are derived from measurements made on full-scale dynamic models of the Orbiter and Lander during acoustic and sine wave tests. The sine wave and acoustic test levels were derived from expected flight environments. During the sine wave tests, the inputs are notched to prevent loads in primary structure from exceeding those computed for the launch phase of the mission.

Pyrotechnic shock levels for components have been established by measurements made on dynamic test models when actual pyrotechnics, including the mortar, were fired.

VIKING DYNAMIC SIMULATOR

Figure 7 shows the Viking Dynamic Simulator mounted on the Centaur. This spacecraft will be the payload on the proof flight of the Titan III E/Centaur. The purpose of this spacecraft is to acquire data which can be used to verify loads and loads analysis techniques associated with the launch phase of the Viking mission. The Viking Dynamic Simulator has mass, inertia, and center-of-gravity characteristics similar to those of the Viking spacecraft. It also has primary structural modal properties, below approximately 20 Hz, similar to the Viking spacecraft.

The Viking Dynamic Simulator consists of a rigid mass representing the Viking Lander, two rigid masses connected by a spring to represent the Viking Orbiter, a four-point to three-point adapter joining the Orbiter and Lander simulators, and a twelve-point to four-point adapter which joins the Orbiter simulator to the Centaur. The Viking Dynamic Simulator is instrumented with strain gages and accelerometers which will measure the structural responses associated with all transient loading events which occur during the launch phase of the mission. Acoustic measurements and spacecraft/shroud relative motion measurements will also be made. Post-flight loads analyses will be performed using the thrust time histories measured on the stage one engines during the shutdown of those engines. The computed load/time histories will be compared to those measured in flight. This will provide a quantitative evaluation of the degree of accuracy with which transient loads analyses can be accomplished. The math model of the spacecraft used in the loads analysis is in good agreement with a modal survey of the spacecraft.

CONCLUSION

This paper is part of a three-paper overview of the Viking dynamics. References [2,3] present details of the Orbiter and Lander dynamics, respectively.

The analysis and test programs which have been identified herein provide assurance that the Viking mission can be accomplished successfully with a lightweight structure.

REFERENCES

1. James S. Martin, Jr., and Charles W. Sibbers, "Project Viking," XXIII RD Congress of the International Federation, Vienna, Austria, October 9, 1972.
2. Ben K. Wada, "Viking Orbiter Dynamics," 44th Shock and Vibration Symposium, Houston, Texas, December 4-7, 1973.
3. Joe C. Pohlen, "Viking Lander Dynamics," 44th Shock and Vibration Symposium, Houston, Texas, December 4-7, 1973.

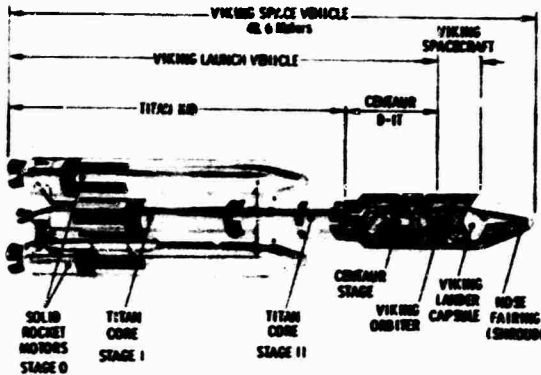


Figure 1. Viking space vehicle configuration.

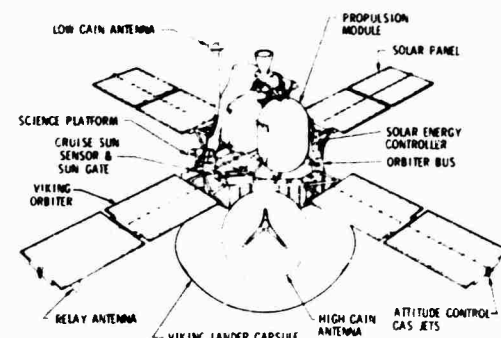


Figure 2. Spacecraft configuration in cruise mode (sunlit view).

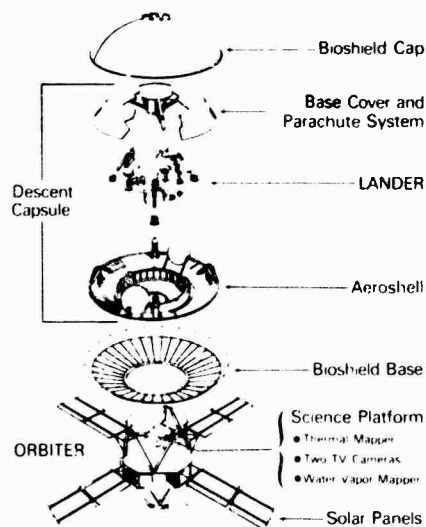


Figure 3. Exploded view of spacecraft.

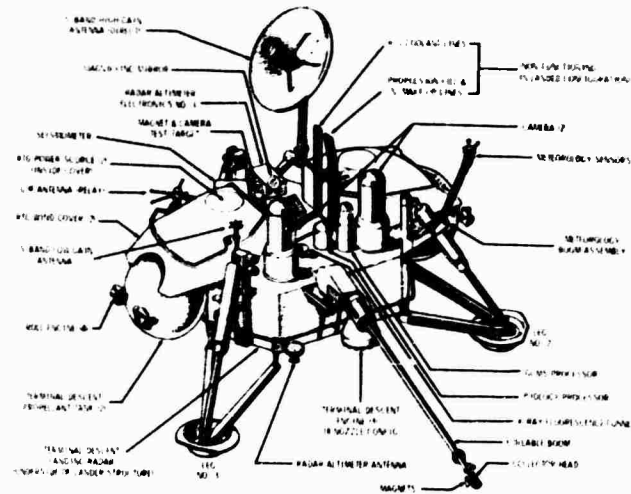


Figure 4. Landed configuration.

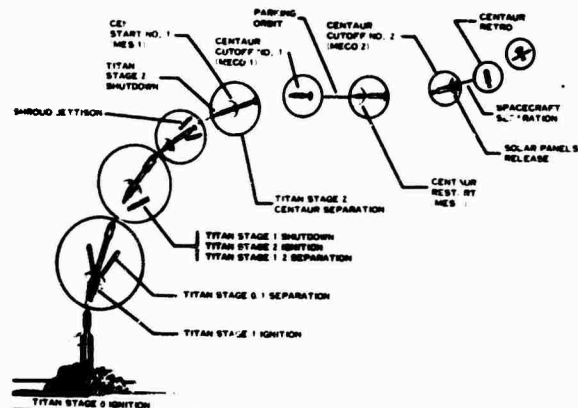


Figure 5. Launch phase flight profile.

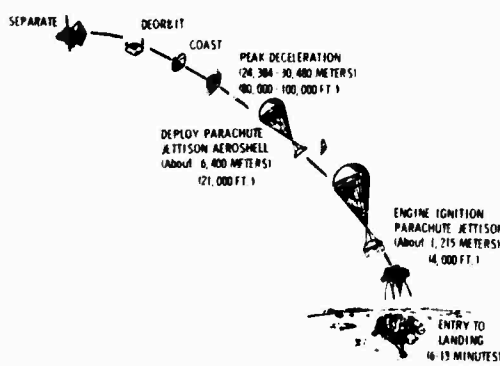


Figure 6. Entry and landing profile.

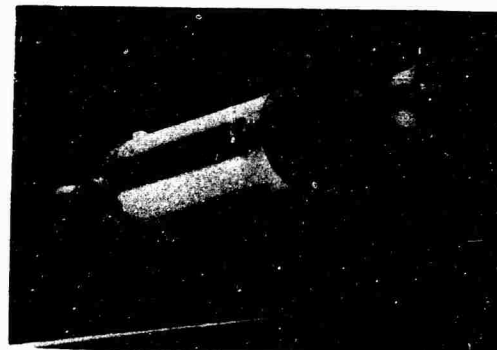


Figure 7. Centaur D-1T vehicle with Viking Dynamic Simulator.

VIKING ORBITER - DYNAMICS OVERVIEW*

Ben K. Wada
Jet Propulsion Laboratory
Pasadena, California

The Viking Spacecraft will be launched on a Titan III E/Centaur D-1T in August 1975 to conduct scientific studies of Mars. The Viking Orbiter part of the Viking spacecraft will conduct the experiments as it orbits Mars. An overview of the dynamics program of the Viking Orbiter is presented with emphasis on those aspects that differ from most NASA programs.

INTRODUCTION

The Jet Propulsion Laboratory is responsible for the Viking Orbiter System (VOS), which is part of the overall Viking Project managed by the Viking Project Office at Langley Research Center for NASA. Two Viking spacecraft (V-S/C) will be individually launched on a new Titan IIIIE/Centaur D-1T launch vehicle in August 1975.

This paper is an overview of the activities related to dynamics in the design, analysis, development tests and qualification tests of the Viking Orbiter System (VOS). This is one part of a series of three papers providing the dynamics overview of the Viking spacecraft. The other two papers are:

- (1) Viking Spacecraft - Dynamics Overview [1] by Dr. R. E. Snyder, Viking Project Office, Langley Research Center, and
- (2) Viking Lander Capsule - Dynamics Overview [2] by J. Pohlen, Martin Marietta Aerospace/Viking

The dynamics program was directly influenced by various Viking Project constraints and available data. The significant factors were:

- (1) Requirement for a lightweight structure
- (2) High reliability for a two V-S/C mission

- (3) A new launch vehicle consisting of a Titan IIIIE and Centaur D-1T with a new Centaur standard shroud (CSS)
- (4) Availability of launch vehicle engine forcing function data from previous flights of Titan and Centaur

DESCRIPTION

General

Figures 1 and 2 illustrate the Viking Orbiter System which is the responsibility of the Jet Propulsion Laboratory (JPL). The Viking Lander Capsule (VLC) built by the Martin Marietta Aerospace/Viking (MMA/V) combined with the VOS is the V-S/C that is attached to the Titan/Centaur launch vehicle. Figure 3 illustrates the Viking space vehicle and identifies the involved organizations. The total activity related to loads on the Viking space vehicle was coordinated by a Viking Load Working Subgroup chaired by Lewis Research Center. The items identified by an underline on Fig. 3 were designed and integrated as the VOS was developed.

The anticipated flight loads and environments for the structure are summarized in Fig. 4. Each environment was considered prior to the establishment of the appropriate design and qualification, loads, and tests.

The weights of the major substructure of the VOS are shown in Table 1, and the substructures are shown in Fig. 2.

* This paper presents the results of one phase of research carried out at the Jet Propulsion Laboratory, California Institute of Technology, under Contract No. NAS 7-100, sponsored by the National Aeronautics and Space Administration

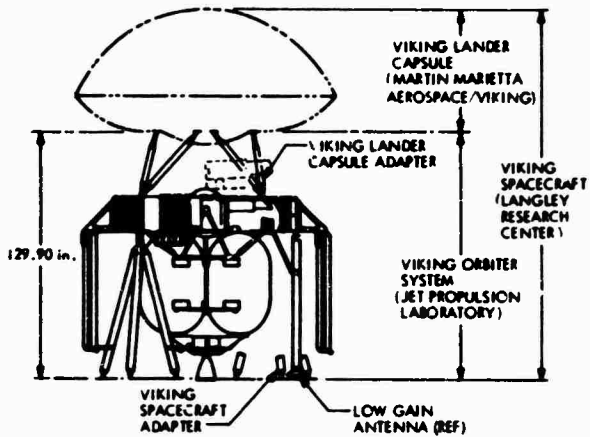


Fig. 1 - Viking spacecraft configuration

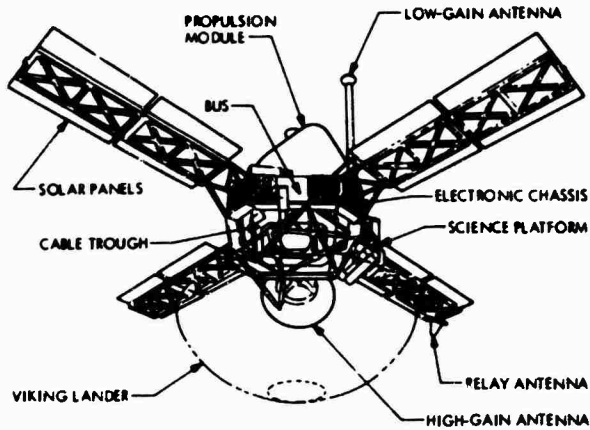


Fig. 2 - Viking Orbiter substructures

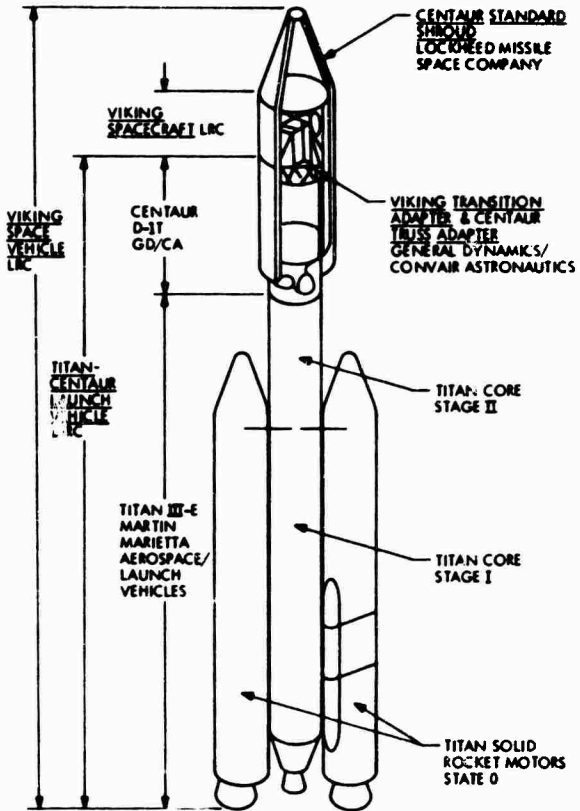


Fig. 3 - Viking space vehicle configuration

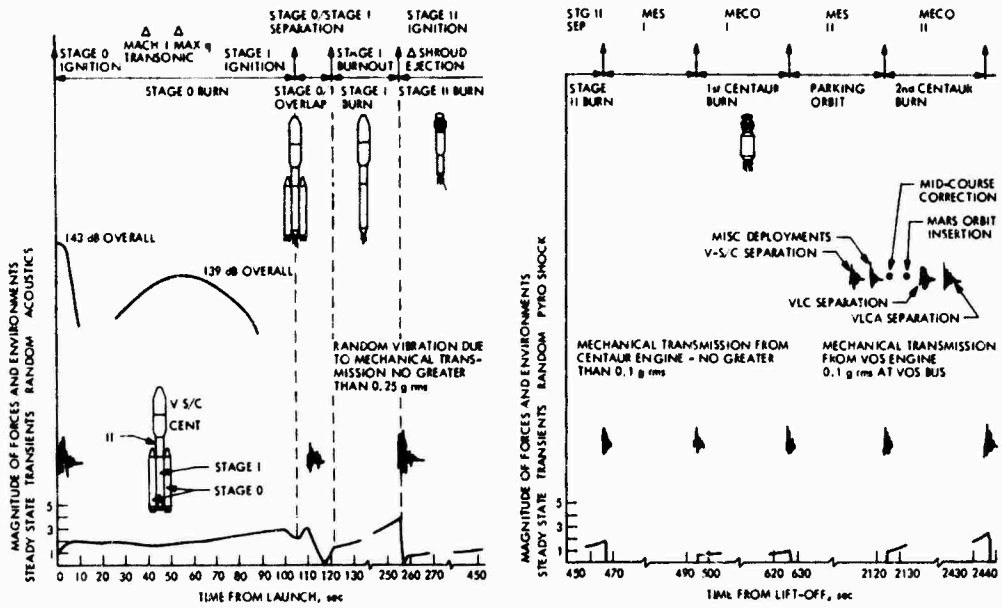


Fig. 4 - Flight loads and environments

TABLE 1
Viking Orbiter System Weight
Summary

Substructure	Weight (lb)
Bus	
Bus with low-gain antenna	948
VLCA	30
V-S/C-A	131
Scan platform	201
High-gain antenna	47
Solar panel with relay antenna	67
3 Solar panels	177
Cable trough	49
Propulsion module (Mission B)	3650
Estimated total	5300

Schedule

The overall schedule for events discussed in the paper is shown in Fig. 5.

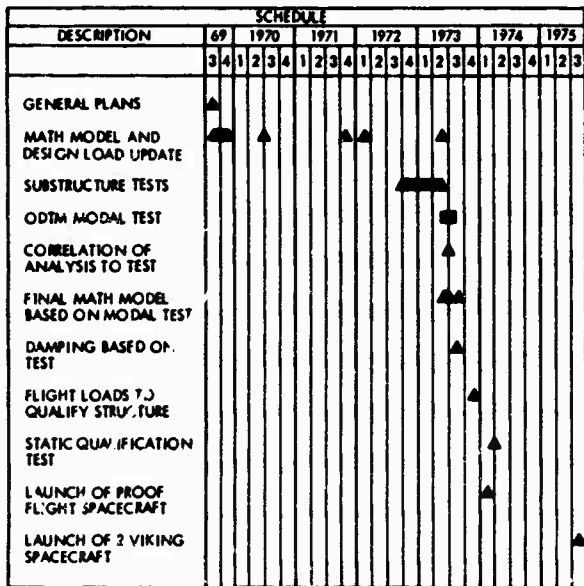


Fig. 5 - Schedule of structures and dynamic development program

Dynamics

The dynamic characteristic of the VOS was a consideration in the selected approach. The low resonant frequencies and the high density of low frequencies of the VOS and the V-S/C are summarized in Tables 2 and 3. The resonant frequencies are of the V-S/C combined with the Viking Truss Adapter (VTA) and Centaur Transition Adapter (CTA). The VTA and

CTA is a 54-in.-high truss-type adapter between the V-S/C and the Centaur. Figure 6 illustrates the damping of the VOS with a rigid mass simulation of the VLC based upon modal test data. The solid line is the original estimate of the damping at the initiation of the program. The designation and description of hardware is given in Table 4.

CLASSIFICATION OF LOADS AND TESTS

The source of the loads on the VOS and the related tests to qualify the structure were evaluated for the load profile as shown in Fig. 4. The loads and the associated qualification test programs were subdivided into three categories. The categories were defined by frequency ranges illustrated in Fig. 7. The associated test program is shown in Table 5.

LOW-FREQUENCY RANGE

Definition of Loads

1. Origin of Loads

The loads in the low-frequency range are a result of quasi-static loads superimposed with various transient loads anticipated during the launch phase of the VOS. In this frequency range, the forces in the structural members calculated by analysis is the basic parameter. The low-frequency range was defined to be between 0 Hz and a range between 20 and 40 Hz. The upper limit is directly dependent on the ability to accurately calculate VOS member forces. The upper-frequency limit will be selected after the VOS and Viking Lander Capsule (VLC) modal tests to establish the adequacy of the mathematical models. The analysis process to obtain member forces is referred to as load analysis.

2. Load Analysis

Load analysis is an analysis process used to define design loads and flight loads to qualify the structure. Design loads are obtained using mathematical models of the V-S/C not verified by test. Flight loads are obtained using mathematical models of the new hardware that are verified by a test program.

During the VOS program, five load analysis cycles are performed as shown in Table 6.

The load analysis effort for each load cycle varied and a few were not applicable to the evaluation of VOS loads. The objective was to minimize the quantity of analysis by the use of conservative bounds on the launch vehicle forcing functions considered to result in small VOS member forces. The conservatism was decreased for the more severe forcing functions by increasing the quantity of analyses.

The design and qualification member forces were obtained by statistically combining the N member forces resulting from N forcing

TABLE 2
Frequency of Viking Orbiter Spacecraft With Rigid Lander

Mode No.	Frequency (Hz)	Mode No.	Frequency (Hz)	Mode No.	Frequency (Hz)
1	4.42	12	17.67	50	56.76
2	4.44	14	20.53	55	59.12
3	7.52	16	23.08	60	65.01
4	7.95	18	23.69		
5	10.22	20	24.37		
6	11.93	25	27.88		
7	12.28	30	34.55		
8	13.19	35	35.82		
9	13.26	40	43.53		
10	14.96	45	52.29		

TABLE 3
Frequency of Viking Spacecraft

Mode No.	Frequency (Hz)	Mode No.	Frequency (Hz)	Mode No.	Frequency (Hz)
1	4.33	12	13.41	50	34.71
2	4.41	14	14.87	55	35.89
3	6.93	16	15.87	60	38.51
4	7.03	18	16.46	65	40.78
5	9.05	20	17.63	70	43.35
6	9.67	25	22.22	75	45.64
7	10.34	30	25.22	80	50.10
8	10.71	35	27.57	85	53.16
9	12.05	40	29.75	90	56.18
10	13.05	45	32.54	95	57.55

TABLE 4
Identification of Hardware

Hardware	Description
Orbiter Development Test Model (ODTM)	Flight-type primary structure that simulates the dynamic characteristics of the Flight Orbiter up to 50 Hz
Proof Test Orbiter (PTO)	Similar to the Flight Orbiter used for qualification testing
Flight Orbiter (FO)	The flight spacecraft that are subjected to a limited set of environments. The environmental levels are those anticipated in flight

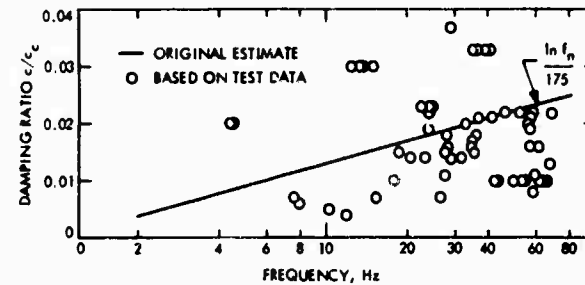


Fig. 6 - Damping of VOS with rigid VLC

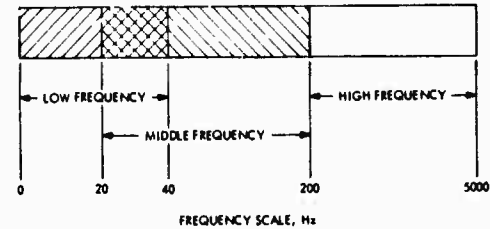


Fig. 7 - Frequency ranges by category

TABLE 5
Summary of Tests

Frequency Range (Hz)	Type Approval Tests Qualification or Margin Test		Test Margin Between Qualification and Acceptance Levels	Flight Acceptance Tests Acceptance Test	
	Type of Test	Hardware		Type of Test	Hardware
Low (0 - 20) (0 - 40)	Static	ODTM	1.25	Static	ODTM
Middle (20 - 200)	Sine test	PTO	1.50	Sine test	FO
High <td>Acoustic</td> <td>PTO</td> <td>6 dB (overall) level</td> <td>Acoustic</td> <td>FO</td>	Acoustic	PTO	6 dB (overall) level	Acoustic	FO
	Pyrotechnic firing	PTO	1.00 ^a	Pyrotechnic firing	FO

^aA statistical probability of a higher level of the PTO exists since the PTO is subjected to three firings and the FO to only one.

TABLE 6
Load Cycles Description

Load Cycle	Approximate Date of VOS Model Delivery	Description
1	6/69 to 11/69	Analysis with a preliminary VOS configuration to establish design loads
2	7/70	Analysis with a final VOS configuration to update design loads
3	11/71	Analysis with a VOS model based on a firm design prior to hardware fabrication to confirm design loads
4	7/73	Analysis of VOS model based on modal test data to establish flight loads for structural qualification tests
5	2/74	Analysis of Proof Flight Spacecraft to verify the load analysis process

functions obtained from past launch vehicle flights for a staging event. The summary of the analyses performed for various events are shown in Table 7.

The schedule required between the generation of a VOS mathematical model and the results of load analysis could not entirely support the VOS design process. Consequently, a method (internal to JPL) to obtain loads was initiated. The process is referred to as the internal loads analysis. The internal loads analysis assumes that the six acceleration-time histories at the base of Titan Stage II (See Fig. 3) are invariant to small changes in the V-S/C dynamic characteristics.

Thus JPL applied the six acceleration-time histories at the base of Titan Stage II as the VOS mathematical model was varied to obtain estimated design loads.

3. VOS Mathematical Model

A detailed finite element dynamic mathematical model is required to obtain the VOS member forces. The size of the mathematical model increased with the load cycle number of Table 6. The size of the VOS model itself required the use of modal coupling techniques to allow its solution with current computer programs. Additionally, modal coupling proved to be economical, since each substructure was

TABLE 7
Load Analysis of Various Events

Events	No. of Forcing Functions or Conditions
Ground conditions	6
Stage 0 ignition	21
Airloads	5
Stage 0 max. acceleration	1
Stage I ignition	12
SRM separation	1
Stage I burnout	29
Stage II ignition	3
Stage II burnout	19
Centaur main engine start I (MES I)	1
Centaur main engine cutoff I (MECO I)	1
Centaur main engine start II	1
Centaur main engine cutoff II (MECO II)	1

independently modeled, checked, and tested. The substructure selection was carefully selected, based upon availability of hardware, interfaces internal to JPL, and interfaces external to JPL. The substructure selected for the VOS and the size of the mathematical model are shown in Table 8.

The resonant frequencies of the VOS model with and without the flexible VLC are listed in Tables 2 and 3.

The size of the Viking space vehicle (VSV) mathematical model required each organization to send the modal characteristics rather than a finite element model. The VOS modal characteristics were sent to Martin Marietta Aerospace/Launch Vehicle who combined the modal characteristics of the models from five other organizations. The data flow is shown in Fig. 8. Careful modal truncation of each model was necessary to solve the VSV eigenvalue problem with the available computer program while retaining the accuracy of the model to its highest frequency.

4. Load Analysis Factor

To account for potential increases in member forces between load cycles (or as the VOS design progressed), a load analysis factor was defined. The load analysis factor (LAF) accounts for:

- (1) VLC mathematical model variation
- (2) VOS mathematical model variation
- (3) Launch Vehicle mathematical model variation
- (4) Centaur standard shroud mathematical model variation
- (5) Definition of the forcing functions
- (6) Load analysis process

TABLE 8
Size of VOS Mathematical Model

Structure	Elastic Degrees of Freedom	Dynamic Degrees of Freedom	Interface Degrees of Freedom	Normal Modes
Bus	1720	153	75	0
CTA/VTA	42	0	36	0
Bay super element	392	0	32	0
4 Solar panel	3444	452	28	20
Scan platform	580	84	14	3
Cable trough	192	153	20	0
Propulsion module	695	78	16	12
3-Hole Tab ^a	20000	0	192	0
Mickey Mouse Tab ^a	3400	0	24	0
Siamese Tab ^a	1760	0	22	0

^aPart of propulsion module

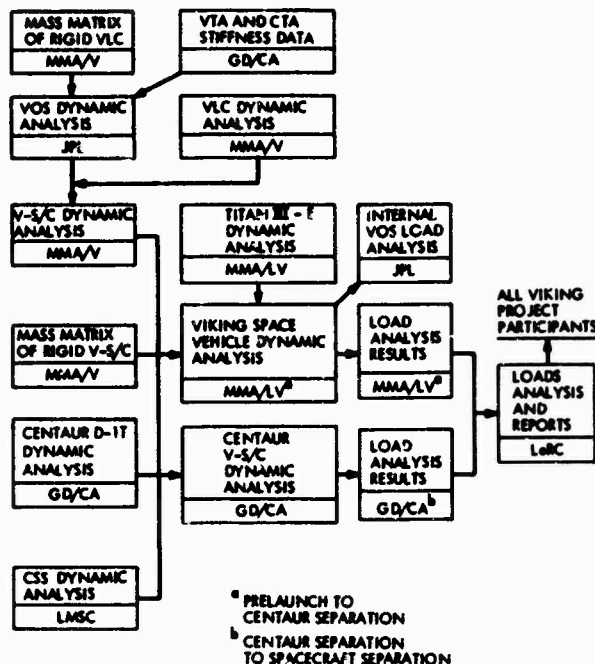


Fig. 8 - Data flow for loads analysis

The LAF was defined as follows.

$$\begin{aligned}
 & \text{(Design loads or flight loads)} = \\
 & \text{LAF} \cdot \text{(loads from load analysis)}
 \end{aligned}$$

The LAF is a number allowed to change during the VOS Program as more accurate information is acquired. The initial value for LAF was 1.30 and was reduced to 1.00 for load cycle 4.

5. Primary Structure vs Secondary Structure

Early in the program, specific hardware items were established to be designed by load analysis. The hardware items were selected using engineering judgement to select the hardware with design loads in the LF range. To be specific, the primary structure hardware is listed in Table 9. All the other structure is designed by the loads in the middle-frequency (MF) and high-frequency (HF) range and is referred to as secondary structure.

Development Test Program

1. General Plan

An objective of the development test program was to obtain early confidence in the hardware integrity. Another objective was to verify the resonant frequencies, mode shapes, modal damping, load transformation, displacement functions as well as other characteristics of the mathematical model. The static and dynamic tests were closely coordinated.

TABLE 9
Primary Structure Members

Viking Spacecraft adapter
Viking lander capsule adapter
Upper plane truss
Propulsion module structure
Scan platform outriggers
Top and bottom bus rings
Main longerons
Solar panel outriggers
Solar panel spars

2. Substructure Test Program

The various substructure test programs are summarized in Table 10. In many cases the strain gauges installed and calibrated on the substructures will be retained through the development and ultimate static test of the ODTM.

The substructure mathematical models were updated from the tests. As an example, the propulsion module modal test (Fig. 9) and propellant effective weight test (Fig. 10) are presented. Figure 11 illustrates the effective moment of inertia of the fuel from the propellant effective weight test, and Table 11 shows changes in the propulsion module dynamic model based upon both tests.

3. VOS Modal Test

Figure 12 shows the ODTM modal test configuration used to verify the VOS mathematical model. The correlation of the results of the ODTM modal test and the mathematical model was excellent. The frequency comparison is shown in Table 12 and the orthogonality of mode shapes is shown in Table 13. Other test data acquired and compared with analyses are:

- (1) Strain energy comparison
- (2) Modal force comparison
- (3) Effective weight comparison
- (4) Kinetic energy comparison
- (5) High-level damping data
- (6) Linearity check

The results of the test are in Ref. 3 and the analysis/test comparison are in Ref. 4.

TABLE 10
Substructure Tests

Parameters Verified	Tests
V-S/C Mission B mass matrix	All the modal tests and the propellant effective weight tests
Model of bus with CTA/VTA	Static test on ODTM bus and ODTM modal test. The CTA/VTA is only included in the ODTM modal test
Displacement functions of propulsion module	Modal and static test of propulsion module and ODTM modal test with referee fluid
Displacement functions of scan platform	Modal test of scan platform and ODTM modal test without joint slippage. The joint slippage was included for load analysis, since higher forces would result in joint slippage
Displacement functions of cable trough	Cable trough modal test and ODTM modal test
Displacement functions of solar panel with relay antenna	Modal and static tests of solar panel with a relay antenna
Displacement functions of solar panel	Based upon a mathematical model of the solar panel with a relay antenna. The relay antenna was removed from the mathematical model for this configuration
Damping matrix for V-S/C Mission B configuration	Data based upon modal tests were available. The damping matrix was diagonalized at each transformation. The kinetic energy evaluation of the modes was used as a guide to estimate damping. Solar panel viscous dampers were not included but estimated as a modal damping
Stiffness matrix for V-S/C Mission B configuration	ODTM substructure and system modal and static tests
Load transformations	ODTM substructure and system modal and static tests

Based upon the modal test data, a special committee established for the model review recommended a LAF = 1.0. The good correlation of the mathematical model is directly attributed to the substructure development tests.

4. Proof Launch Spacecraft

A good dynamic simulation of the V-S/C referred to as the Viking Dynamic Simulator will be launched in January 1974. A thorough modal survey of the proof launch spacecraft in addition to a good set of flight instrumentation should provide data to check the load analysis process. The flight instrumentation includes axial forces of the six VLCA members[†] and six accelerometers that will provide the six components of acceleration across an interface. A comparison of data from a load analysis using the actual proof flight forcing function and the flight data should provide a measure of conservatism.

Qualification Test Program

The VOS primary structure will be qualified by a static test on the ODTM. The objective is to apply a set of external loads to load each primary structure member type to its qualification force. The qualification force will include in addition to flight loads:

- (1) Thermal loads
- (2) Manufacturing loads

A development static test using loads from load cycle 3 demonstrated the feasibility of loading each primary structure type within 5% of the required load. The desired test applied member loads is multiplied by the test factor to account for the test tolerances.

The structure was originally designed to a 5% higher load. The development static test on the ODTM is shown in Fig. 13.

[†]The two Viking Flights will include the six VLCA members strain gauge output as part of the flight telemetry data.

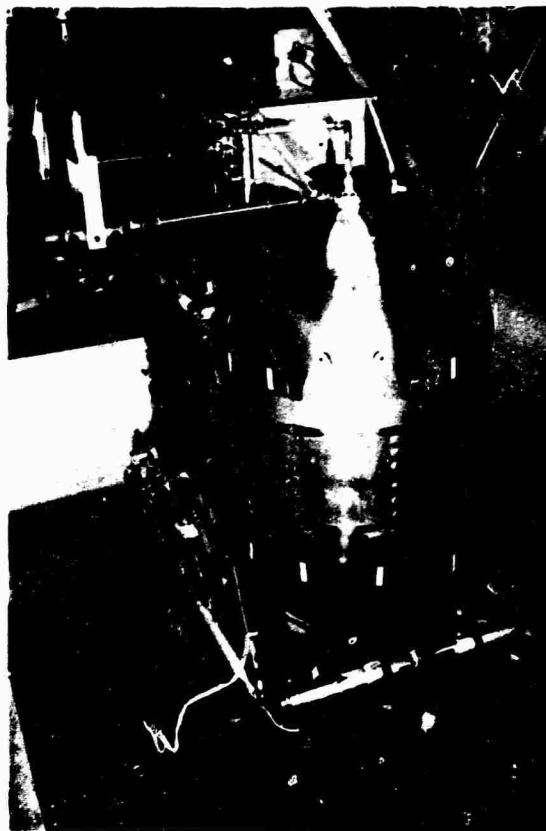


Fig. 9 - Propulsion module modal test

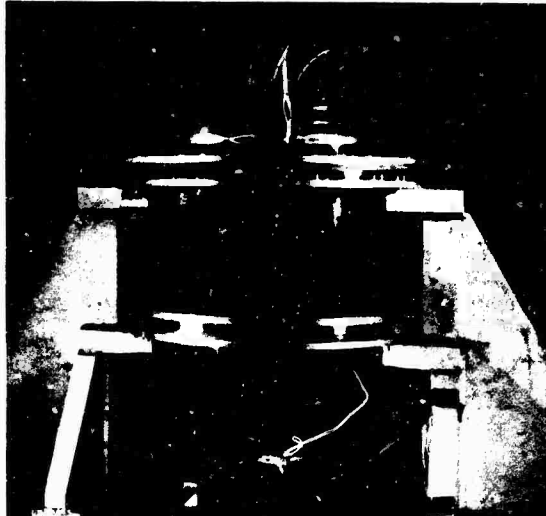


Fig. 10 - Propellant effective weight test

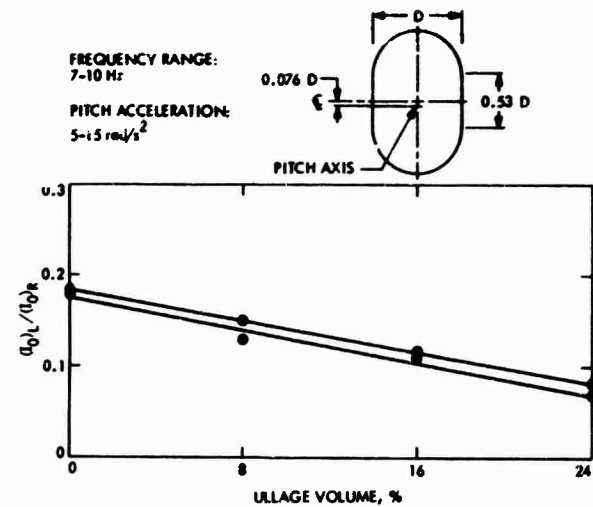


Fig. 11 - Effective moment-of-inertia ratio

TABLE 11
Propulsion Module Dynamic Model

Mode	Model Identification				
	E^a	F_b^a	F_c^a	Modal Test	VC3R ^b
Frequency (Hz)					
1	7.69	12.56	12.11	12.95	12.95
2	9.19	15.86	14.90	17.66	16.63
3	12.26	19.39	19.24	20.80	19.83
4	16.06	20.72	22.43		
5	19.90	26.83	25.76	28.97	26.70
6	27.70	27.99	27.50	28.33	28.30
7	29.81	44.79	35.57		
8	45.77	60.75	39.67	32.76	34.25
9				42.80	45.75
10	49.52	66.80	41.62	50.67	49.69
11	51.32	69.68	42.11	50.40	54.69

^aMathematical model before propulsion module modal test

^bMathematical model after propulsion module modal test

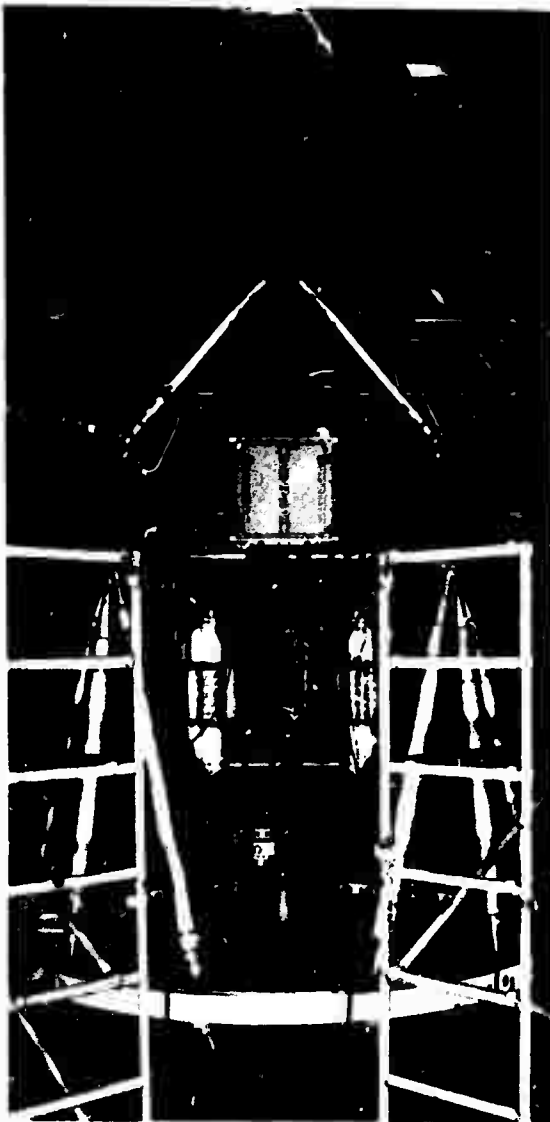


Fig. 12 - ODTM modal test configuration

MIDDLE FREQUENCY RANGE

Definition of Loads

1. Origin of Loads

Since the environment or loads in the middle frequency (MF) between a frequency range of 20 to 40 Hz and 200 Hz cannot be estimated by analysis, estimates of accelerations were made based on flights of other launch vehicles. Since the environment was an estimate, it was selected to be compatible with existing test equipment.

2. Primary Structure

Since the MF range overlaps with the LF range, the MF test is constrained to limit the

TABLE 12
Comparison of Modal Frequencies -
VOS Mathematical Model Versus
Modal Test Results

Mode	Frequency (Hz)		
	Analysis	Test	Error (%)
1	4.35	4.51	3.5
2	4.40	4.63	5.0
3	7.48	7.87	5.0
4	7.83	8.30	5.7
5	10.92	11.51	5.1
6	13.36	14.09	5.2
7	14.64	15.35	4.6
8	17.95	19.49	7.9
9	18.81	19.83	5.1
10	23.42	24.85	5.8
11	26.18	29.54	11.4
12	24.28	26.49	8.3

primary structure to loads established by load analysis.

3. Environment

The sine test level is defined in Fig. 14. The environment is defined at 12 locations on the VOS bus and not at the base of the VOS structure.

Development Test

4. Hardware

A development vibration test will be performed on the combined ODTM and Lander Dynamic Test Model (LDTM). Figure 15 illustrates the configuration of the Z-axis vibration test.

5. Axial Test

The sinusoidal vibration input into the V-S/C is provided by a 30,000-lb Ling shaker system. The electronic control system includes:

- (1) 36 control channels, including the 12 input control accelerometers. The other 24 are selected member forces and/or accelerations that will control the test.

TABLE 13
Orthogonality of VOS Modal Test Results

$$[\phi]^T [m][\phi]$$

Mode No.	1	2	3	4	5	6	7	8	9	10	11	12
1	100.0	6.2	-0.2	1.1	-0.3	1.1	-2.3	-0.6	-1.7	0.6	-2.4	0.0
2		100.0	0.1	-1.2	-4.1	-3.0	-0.9	-2.5	1.0	1.2	3.4	-1.5
3			100.0	0.4	0.8	1.6	-0.2	3.5	-1.5	-0.5	-0.7	0.4
4				100.0	1.0	1.3	1.2	-0.1	-1.8	1.2	1.1	-0.5
5					100.0	0.6	0.8	4.6	-1.0	0.2	1.7	-0.4
6						100.0	0.4	-0.5	1.3	4.4	-0.6	1.6
7							100.0	-0.2	-0.1	3.6	-0.1	-1.3
8								100.0	-1.1	-1.9	-0.2	-1.5
9									100.0	5.9	-2.9	2.7
10										100.0	1.0	-3.4
11											100.0	2.5
12												100.0

(2) 59 peak limit channels that will terminate the test if the preselected levels are exceeded.

6. Lateral Test

The lateral test configuration is similar to the modal test setup shown in Fig. 11 except that the VTA/CTA adapters are not included. The ODTM is mounted directly to the floor. Four 150-lb shakers will be pendulously supported and attached to the VOS bus. The sinusoidal vibration levels of Fig. 14 cannot be achieved by this test. The structure will be excited at its resonant frequencies and will establish the degree of dynamic interaction between the ODTM and the LDTM.

The ODTM/LDTM will be vibrated in two orthogonal directions. The test at the specification levels was not considered necessary, since high lateral motions are anticipated in the axial test.

The control system is identical to the axial test.

Qualification Test

The VOS with a rigid lander will be qualified in the MF range using the PTO. The current

plan includes tests similar to the development test. Figure 16 illustrates a rigid lander on the ODTM on the axial vibration system.

HIGH-FREQUENCY RANGE

Definition of Environments

The high-frequency environment (>200 Hz) is an estimate of the acoustic level based upon past programs and firing of flight-type pyrotechnic devices. The acoustic spectrum is shown in Table 14 and the anticipated pyrotechnic environment is shown in Fig. 17.

Qualification Test

The VOS will be qualified in the HF range using the PTO. The PTO will be acoustically tested and subjected to a limited number of flight-type pyrotechnic firings.

CONCLUSION

The VOS Program has identified the sources of loads and environments. The analysis, design, development test, qualification test and flight data measurements have been coordinated to assure achievement of the Viking Project structural objectives.

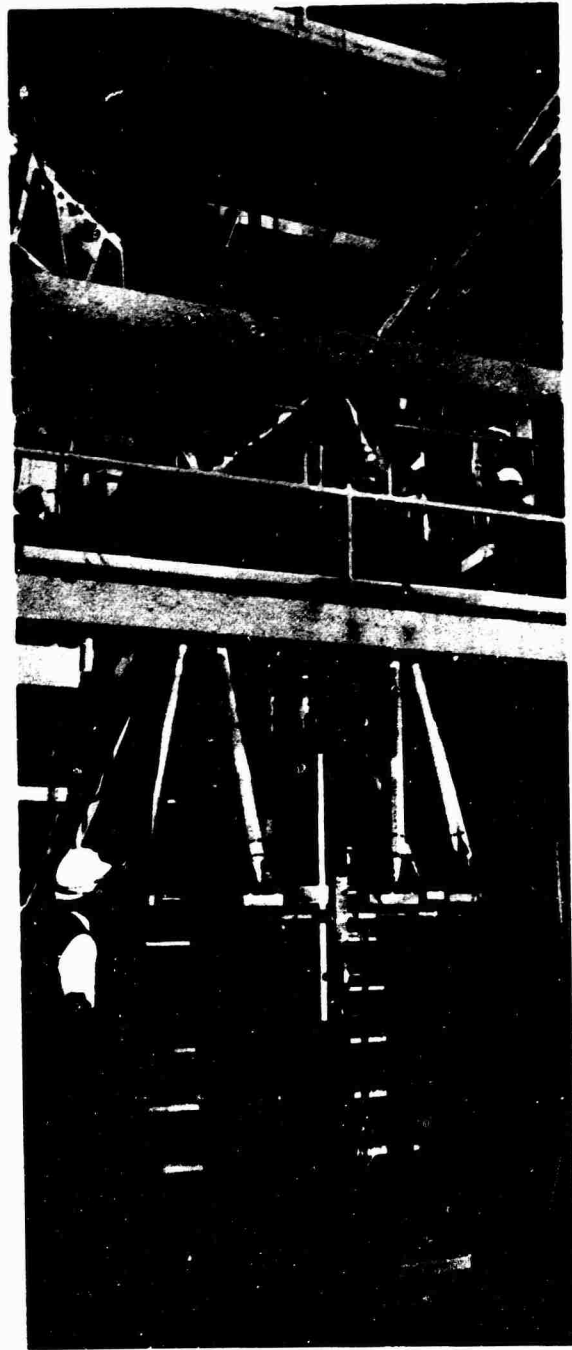


Fig. 13 - Development static test on ODTM

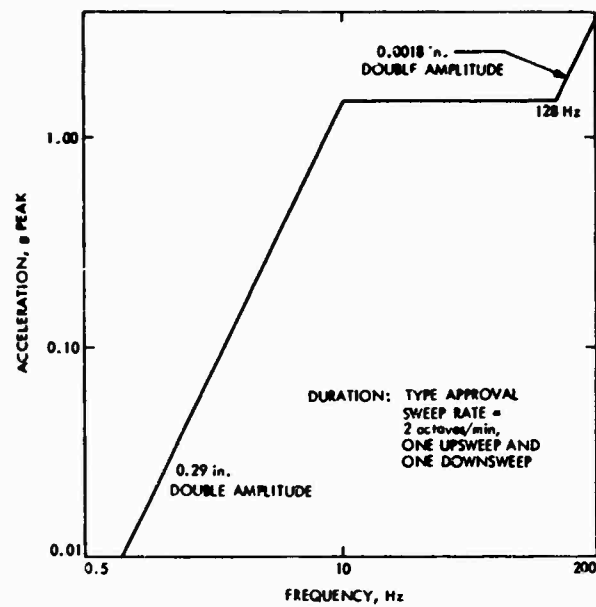


Fig. 14 - Sine test level (lateral and longitudinal)

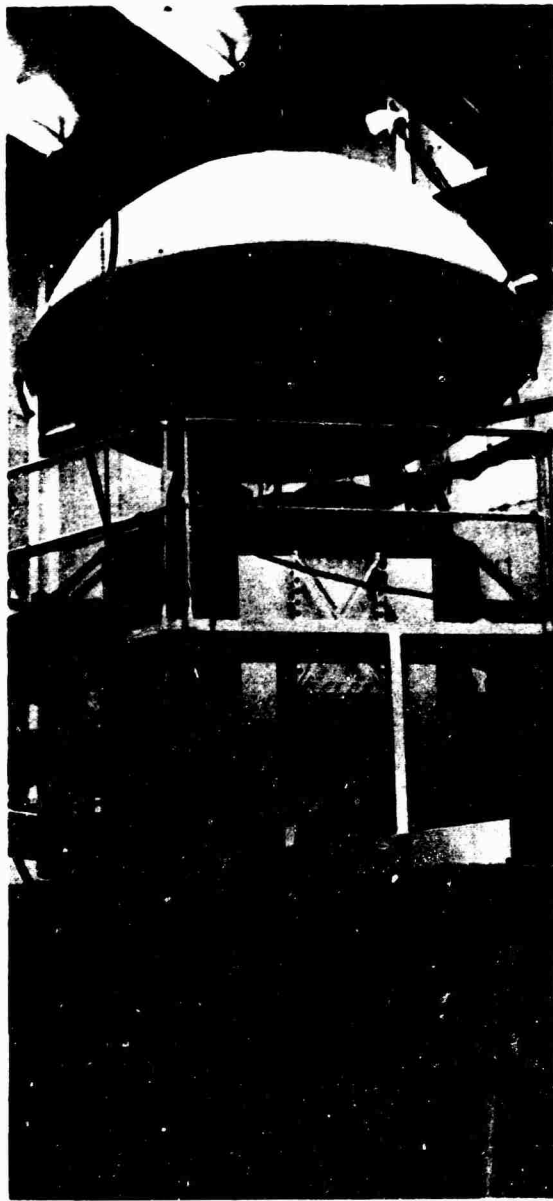


Fig. 15 - ODTM/LDTM Z-axis sine vibration test setup

TABLE 14
Qualification Acoustic Spectrum

1/3 Octave Band Center Frequency (Hz)	Sound Pressure Level in 1/3 Octave Bands (dB ref 2×10^{-4} dynes/cm 2)
50	133.5
63	134
80	134.5
100	135
125	137
160	139
200	140
250	140.5
315	140
400	138.5
500	137
630	136
800	135
1,000	134
1,250	133
1,600	132
2,000	131
2,500	130
3,150	129
4,000	128
5,000	127
6,300	126
8,000	125
10,000	124
Overall	149
Duration: 10 minutes	



Fig. 16 - ODTM rigid VLC Z-axis sine vibration test setup

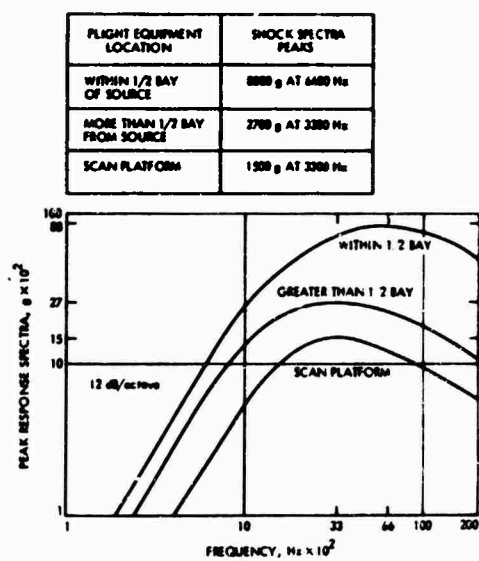


Fig. 17 - Separation device response shock spectra ($Q = 20$)

REFERENCES

1. Snyder, R. E., "Viking Spacecraft-Dynamic Overview," to be presented at the 44th Shock and Vibration Symposium, Houston, Texas, December 1973.
2. Pohlen, J., "Viking Capsule Lander-Dynamic Overview," to be presented at the 44th Shock and Vibration Symposium, Houston, Texas, December 1973.
3. Leppert, L., Miyakawa, R., and Wada, B., "Modal Test Results of the Viking Orbiter," to be presented at the 44th Shock and Vibration Symposium, Houston, Texas, December 1973.
4. Wada, B., Garba, J., and Chen, J., "Development and Correlation, Viking Orbiter Analytical Dynamic Model with Modal Test," to be presented at the 44th Shock and Vibration Symposium, Houston, Texas, December 1973.

VIKING LANDER DYNAMICS

J. C. Pohlen*
Martin Marietta Aerospace
Denver, Colorado

The Viking spacecraft will deliver a payload of scientific and communication equipment to Mars. During the mission the vehicle will be exposed to a variety of dynamic environments, five of which are of particular importance: acoustically-induced random vibration, rapidly-decaying (transient) vibration, pyrotechnic shock, parachute-mortar shock, and landing shock. In order to assure that the spacecraft will survive these environments in a satisfactory manner, the Viking Dynamics Group at Martin Marietta Aerospace, Denver, was required to define the environments and specify the dynamic tests necessary to qualify the vehicle and its components. The procedure being followed to achieve this goal, using an empirical approach for initial estimates followed by analyses performed on detailed math models and system-level, full-scale verification tests, is described herein.

INTRODUCTION

The Viking '75 Project objective is to deliver scientific and communication equipment to Mars orbit and the surface of the planet on two dual-system spacecraft. During the course of each of the two missions, these equipment

systems and their supporting structures and primary structures are subjected to various dynamic environments, such as those outlined in Table I. The primary function of the dynamics group on the Viking '75 Project was to define

TABLE I
Source of Dynamic Environments

	Acoustics	Random Vibration	Sine Vibration	Pyro Shock	Landing Shock	Steady State	Transients
Ground Test	X	X	X	P	P		
Launch (Powered Flight)	X	X		X		X	X
Cruise		O		X		O	O
Deorbit		O		X		O	O
Entry and Parachute	X	X		X		X	X
Terminal Descent	X	X		X		X	
Landing					X		X
Post Landed				X		X	

O - Negligible Load Environment
P - Not Done on Flight Articles

* Mr. Pohlen is Unit Head of the Space Dynamics Unit in the Structures and Materials department.
Work performed by Martin Marietta Aerospace under NASA Contract NAS1-9000.

and verify these environments, and to specify the necessary tests at the component and systems level, to qualify the vehicle for the flight.

The procedure for getting these environments was three phased:

1. The analytical/empirical phase - Completed without the benefit of system-level dynamic models (preliminary design);
2. The analytical phase - Completed with system-level, multi-degree-of-freedom dynamic models with no test verification (post design/pre-hardware);
3. The test phase - Experimental data was taken during system-level tests to corroborate predicted loads and/or component environments.

During the analytical/empirical phase of the program, test plans were devised for proving the various systems and subsystems, and the following models were defined:

1. The Thermal Effects Test Model (TETM) - To prove the thermal control system and analyses;
2. The Lander Structural Test Model (LSTM) - To apply calculated flight loads statically, to determine structural adequacy;
3. The Lander Dynamic Test Model (LDTM) - To apply dynamic environments and model surveys to verify component environments

and analytical models;

4. The Proof Test Capsule (PTC) - A flight article for environmentally testing to qualification levels to prove the system capability and margins.

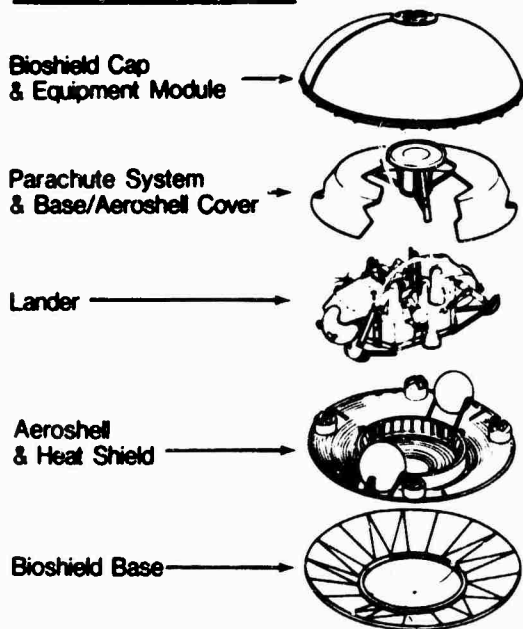
Many documents were written to control the design and the test program. The Master Integrated Test Plan is a collection of all the tests on the aforementioned test articles; Test Methods and Procedures dictates the system and subsystem test tools and tolerances for performing the tests; and Structural Design Criteria gives safety margins, ultimate-to-limit ratios, tank fracture mechanics criteria, and proof and burst test margins.

The LDTM was built from Viking Lander Capsule (VLC) flight article drawings for primary structure and bracketry. The VLC major structural parts and their weights and design load conditions are shown in Figure 1. The components were mass simulated if they weighed more than one pound.

There were three types of tests proposed on the LDTM:

1. Those which confirm the math model;
2. Those which load any or all of the flight structure;
3. Those which are precursors for either PTC or flight article tests.

SPACECRAFT ASSEMBLIES



DESIGN CONDITION	APPROX WEIGHTS
Hoisting	
Bioshield separation	100
Bioshield pressure	
Mortar fire	
Parachute opening	240
Pressure	
Entry	
Landing	1400
Leg deployment	
Entry (shell)	
Random (RCS eng brckts)	600
Boost (launch longerons)	
(RCS tank truss)	
Pressure (sep ring + struts)	150
Boost (struts)	
(base ring)	

Fig. 1 - Viking Lander Capsule Component Design Conditions and Weights

Some tests actually are more than of one type. The total objective is to qualify the structure by the loading event itself, by confirming the analysis and letting the analysis qualify the structure, or by using the confirmed analysis to calculate loads which will be applied to the LDTM and thereby effecting qualification.

During the second analytical phase of the program, multiple-degree-of-freedom computer models were generated. These models were used in combination with orbiter math models to calculate powered flight loads, to obtain package response to transient events in the mission, and to generate structural loads for applying to the LDTM.

During the third phase of the program, the LDTM was put through a twelve month test program (now complete). The types of tests applied consisted of modal tests, drop tests, acoustic tests, vibration tests, mortar firing tests, and pyrotechnic separation tests.

ENVIRONMENTS

Five major types of environments, which require further discussion, were covered specifically during extensive testing on the Viking project; they are: 1) the random levels seen by the components when the system level acoustic test is performed, 2) the component vibration levels and structural loads observed during the system level sine test, 3) the component shock levels during pyrotechnic actuated separations, 4) structural loads and component shock levels measured during parachute mortar firing, and 5) the total response of the vehicle to the landing resulting in structural and component loading. These five environments will now be individually discussed.

Random Environment

An acoustic test was performed on the launch configuration in a 14-ft diameter, 20-ft steel shroud. The sound pressure level (SPL), measured/specified is depicted in Figure 2. The 149-dB overall SPL specified contained a 6-dB qualification test margin. During the 300-sec exposure, SPL's and random power spectral densities (PSD) were measured as response.

Approximately 150 accelerometers were used to measure the PSD's, and Figure 3 depicts a typical response curve as compared to the pre-test predicted level.

Sine Environment

Early in the program a system level test was conceived to "fill in" the dynamic environment associated with launch transients in the frequency range between 30 and 200 Hz. The available analytical models are adequate to predict responses below 50 Hz and the

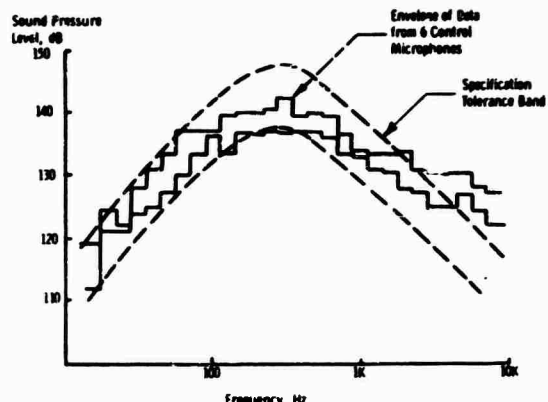


Fig. 2 - Launch Acoustics Spectra

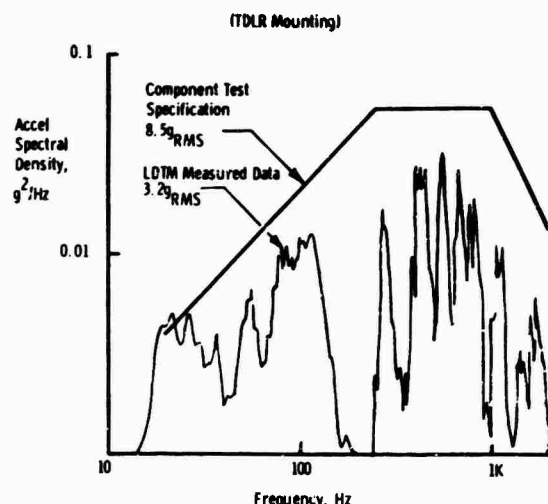


Fig. 3 - Component Specification vs Measured Acceleration Spectral Densities

environment is known to be mostly random (from acoustics) and pyro shock (from separations) in excess of 150 Hz. The levels for the system test and the component test specifications are shown in Figure 4.

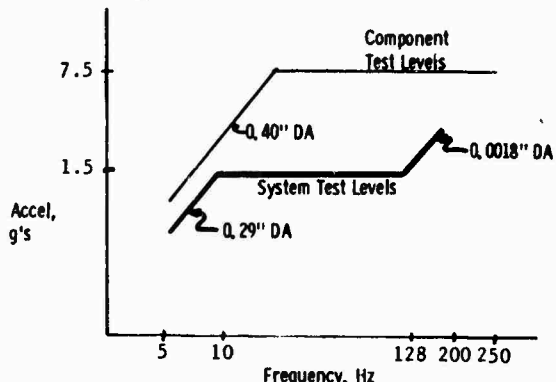


Fig. 4 - Sine Vibration Test Levels

The location for the system level test input was defined to be at the base of the truss which supports the Viking lander capsule (VLC) above the Viking orbiter in the launch configuration. The system level sine test was not allowed to be a design load condition for the primary structure of the vehicle. The test was controlled by limiting the loads in the primary structure to levels calculated during the launch-transient-loads analyses. This limiting only existed below 50 Hz.

Pyro Shock Environment

Sources of pyrotechnic shock (pin pullers, cable cutters, explosive nuts) are scattered throughout the VLC. Component test environments were defined on a spectral basis by using the reduction vs distance curves presented as Figures 5 and 6.

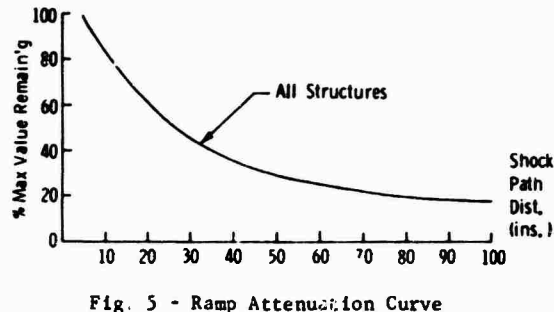


Fig. 5 - Ramp Attenuation Curve

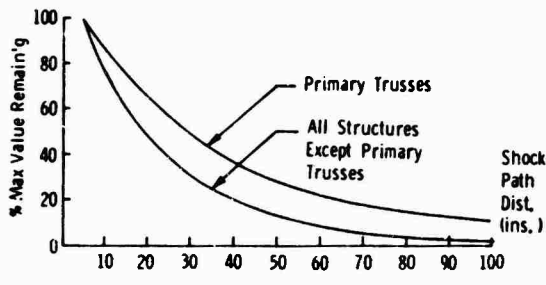


Fig. 6 - Peak Attenuation Curve

These two types of reductions, when applied to the spectral plot, are for: reducing the peak value (Figure 6), which is the high frequency reduction; and for reducing the 9 dB/octave roll-up-portion of the spectral plot and controlling the lower frequencies (Figure 5). A further 60% reduction factor is applied to the peak value for each of the first three mechanical joints between the component and the source.

The actual source and component levels of shock were measured during the separation testing on the LDTM. A typical spectral plot of the component test requirement and the environment seen on the LDTM is presented in Figure 7.

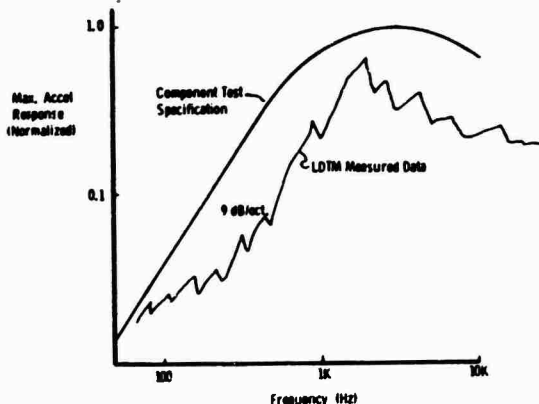


Fig. 7 - Component Pyro Shock Spectra

Mortar Shock Response

The parachute phase of the mission is started abruptly by mortaring approximately 100 pounds of canopy, risers, bridle, and attending hardware to a relative velocity of about 120 fps. This event not only has a pyrotechnic shock associated with it, but a significant velocity change similar to the landing event. Due to the fact that certain components are required to function after the mortar event, but not after landing, special precautions had to be taken to assure that proper low frequency, high acceleration tests were performed.

Landing Shock Environment

Although the landing environment is regarded as a shock, it is of a different nature than the pyrotechnic shock. Consequently, the component test to cover the event was specified in the form of the acceleration time curve specified in Figure 8.

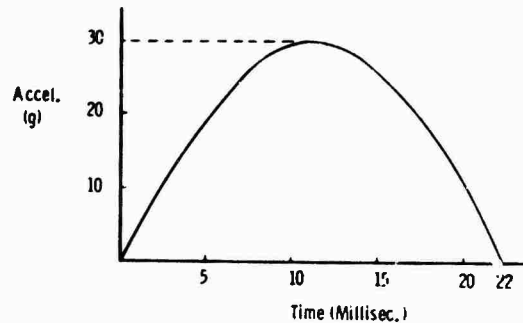


Fig. 8 - Component Landing Shock Test Specification

In order to prove that this stipulation was adequate for the myriad of possible landing conditions that could exist on Mars, a Monte Carlo approach to the problem was

undertaken. This consisted of developing an analytical model of the landing configuration of the vehicle, verifying by test that the analytical model was accurate (or at least conservative), and then determining the component landing environment based on 300 Monte Carlo selected landing events.

The dynamic model used to analyze the landing event contained 628 dynamic degrees-of-freedom. This model was forced with loads calculated through program which assumes a rigid center body with articulated tripodal legs. The landing conditions used in the rigid body program were: 1) the LDTM drop test conditions which were used to verify the adequacy of the model, and 2) the randomly chosen (Monte Carlo) landing conditions on Mars.

Two methods of prediction were used to get force vs time to drive the dynamic model for purposes of verifying its ability to predict the response of packages. The first was the analytically derived leg loads calculated by the rigid body computer program, and the second was the as-measured-with-strain-gages leg loads when the LDTM was dropped on the test surface. A typical accelerometer g-time history is presented for the two methods of prediction vs the "as tested" result (Figure 9).

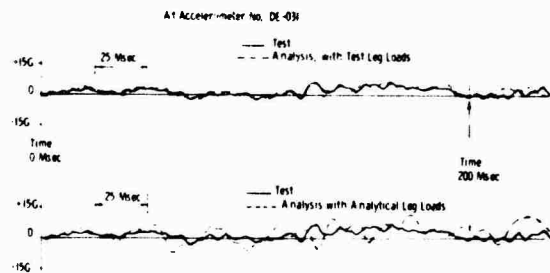


Fig. 9 - Typical Accelerometer Correlation - LDTM Drop No. 4

The degree of satisfaction or "goodness" of this type of comparison is relative and depends on the eyes and mind of the beholder. Peak g's predicted for the drop tests correlated quite well with those measured during the tests. Since there were really only two gates that needed to be closed with regard to whether the qualification test on a component is adequate, we concerned ourselves only with these parameters. They were: is the test done on the component (Figure 8) of sufficient magnitude-plus-margin to cover loads expected on Mars? and, does the frequency content of the pulse (Figure 8) cover the frequency content expected in the Mars landing?

The first gate was easily satisfied by searching through the 300 landings for the peak vector acceleration on each package, and comparing it to 30 g. No problem was uncovered.

The second gate, that of frequency content comparison, was checked by spectrally analyzing the data with an assumed dynamic amplification of 10. Figure 10 is a spectral representation of the same two acceleration time-histories comparisons depicted in Figure 9 which were time traces. As shown, the comparison using actually-tested forcing functions is quite good, whereas the comparison using analytically-determined forcing functions is not as good and is conservative.

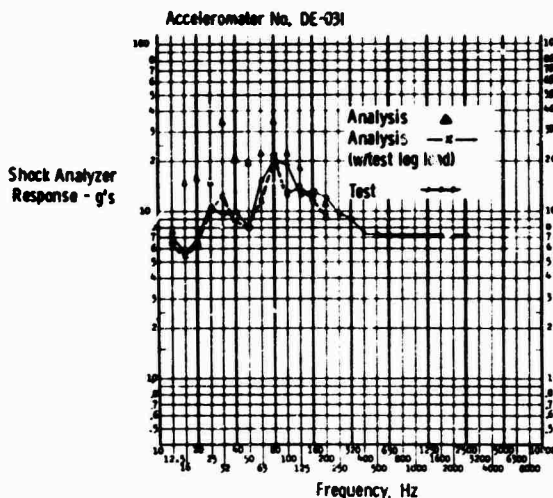


Fig. 10 - Typical Spectral Correlation - LDTM Drop No. 4

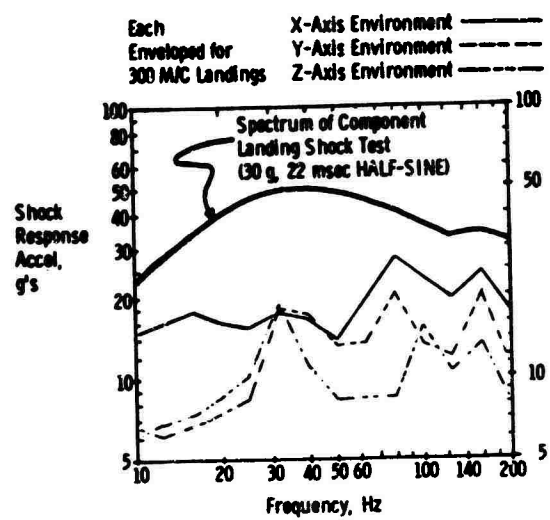
This methodology was then used to determine the landing shock environment for all components.

SUMMARY

In summary, the steps used are as follows:

1. Verify by test that the analysis can predict package response;
2. Do 300 analytical Mars landings, determine peak g's, and envelope the spectral response of each of the packages for all the landings;
3. Compare peak-g's-predicted to that of the component test pulse (Figure 8);
4. Compare the enveloped spectral plot of each package for all 300 landings to the spectrum of the component test pulse.

The spectral comparison for one of the components is presented in Figure 11 comparing each axis spectral plot to the test spectrum.



STRUCTURAL DYNAMICS

PERFORMANCE OF STATISTICAL ENERGY ANALYSIS

R. F. Davis and D. E. Hines
McDonnell Douglas Astronautics Company
Huntington Beach, California

High-frequency random vibration environments have become increasingly significant in the design of aerospace structures. Analytical prediction of these environments is beyond the current scope of classical modal techniques. Statistical energy analysis methods have been developed that circumvent the difficulties of high-frequency modal analysis. These statistical energy analysis methods are evaluated by comparing analytical predictions to test results. Simple test methods are developed for establishing statistical energy analysis parameter values. Techniques are presented, based on the comparison of the predictions with test values, for estimating statistical energy analysis accuracy as a function of frequency for a general structure.

INTRODUCTION

The increasing performance of aerospace vehicles has resulted in external acoustic fields and aerodynamic boundary layers that cause increasingly significant high-frequency random vibration environments. While classical modal analysis techniques for predicting dynamic response work well in the frequency range of the lower structural resonances, their application to these high-frequency regimes is limited by model complexity and required solution time.

Statistical energy analysis (SEA) techniques that can successfully circumvent the problems of classical determination of high-frequency response were introduced a decade ago, but have received minimal usage for flight hardware. Reference 1 contains an excellent bibliography of the development of SEA which has occurred.

The first SEA application to a complex vehicular structure was performed for the UpSTAGE program (see Reference 2). The SEA effort on UpSTAGE was directed to the scaling of data from an acoustic test specimen into design and component vibration test criteria for a flight design. Because of the specific interest in using SEA as a scaling technique, the approach was not evaluated in depth as a predictive technique. However, a considerable amount of vibration response test data was obtained with controlled acoustic inputs, which could provide a basis for a more comprehensive evaluation of SEA in application to a complex system.

This paper is devoted to the evaluation of SEA in application to a complex structure. This

evaluation incorporates a test program that successfully provided damping and coupling parameter values through the use of very simple test methods. A technique for introducing acoustic energy into the SEA model is presented which gives good results with reverberant acoustic fields. This statistical structural analysis, in conjunction with the simple test methods, resulted in high-frequency vibration response predictions with an accuracy of ± 3 dB in comparison with test measurements. Frequency scaling methods are presented that may be used to evaluate the frequency range in which this accuracy can be expected for general structures. The complex structure considered in this report is an elliptical cone excited with a range of acoustic configurations. In many respects, this represents a more complex analysis problem than that for typical vehicles. Considering the complexity of the structure examined in this study, together with the various types of acoustic input configurations, one can expect the results to be valid for a wide range of structural problems.

DEVELOPMENT OF STATISTICAL ENERGY ANALYSIS EQUATIONS AND SOLUTION FORMAT

Statistical energy methods have been developed to consider the distribution and transfer of energy among the modes of a vibrating system. These methods assume that the modes of a system being analyzed contain all the vibratory energy of that system. Therefore, for SEA to have valid application, all significant energy of a system must be resonant as opposed to nonresonant.

The SEA methods separate the frequency range of interest into frequency bands, which are analyzed independently. The methods assume that the energy in the modes of one frequency band is not transmitted (through coupling) to modes in other frequency bands either within an element or among the elements of a system.

These energy analysis techniques are denoted statistical because they involve averaging structural response over portions of the structure. This averaging is performed over time, space, and in frequency bands. The time averaging results in the use of root-mean-squared representation for quantities, such as acceleration, which vary with time. The space averaging assumes that the energy of a system element is evenly distributed throughout the element. The frequency band averaging consists of the assumption that the energy of an element in one frequency band is evenly distributed among the element modes occurring at frequencies within the band.

An important factor in validating the space and frequency averaging is the number of modes included in each frequency band. With many modes excited in one frequency band of an element, the vibratory energy may be expected to be well distributed throughout the element and among the various modes, and averaging will furnish a valid approximation to actual values. When frequency bands that are a constant percentage of the center frequency, such as third-octave bands, are utilized for analysis, the bands will contain progressively greater numbers of modes as the center frequency increases. Therefore, a closer approximation to the true response is obtained as frequency increases. The use of very wide frequency bands should permit SEA to have valid application at lower frequencies. However, problems with frequency resolution require a compromise. One-third-octave bandwidths were chosen for the analysis and tests that are reported here.

The assumptions upon which statistical energy analysis is based are:

- A. The modes of the elements of a system contain all the vibratory energy of the system.
- B. Only modes occurring within the same frequency band are coupled.
- C. The energy in one frequency band of a system element is equally distributed among the modes of that element occurring in the frequency band.
- D. For two coupled elements, all of the modes occurring in one of the elements in one frequency band are equally coupled to each mode occurring in the same frequency band in the other element.

ANALYTICAL MODEL OF UpSTAGE SPECIMEN

The UpSTAGE acoustic test specimen was a design configuration of the flight vehicles consisting of the load-carrying structure (i.e., external skin, field joints, and internal bulkheads) without internal components, except for a model of a laser gyro. The specimen, shown in Figure 1, is an elliptical cone which is separated into four sections by three field joints. Internally, the specimen has 12 bulkheads, the 3 field joints, and a closure plate at each end. The skin thicknesses of the sections vary, decreasing from the rear to the front.



Figure 1. UpSTAGE Acoustic Test Specimen

The mathematical model used initially for the present analysis is identical to the model used for the earlier UpSTAGE predictions (see Reference 2). This model separates the specimen lengthwise at the field joints into four basic elliptical sections. The aft section was further divided into four elliptical subsections to allow for localized acoustic inputs at locations that simulate the positions of the UpSTAGE aerodynamic control forces.

The external skin of each section was modeled with four elements, one for each quadrant, with junctions occurring at the points where the two radii of curvature coincide. Since there are seven sections and subsections, this modeling resulted in 28 skin elements as indicated with Arabic numerals in Figure 2. Each of the internal bulkheads, field-joint bulkheads, and closure plates was modeled as a single element. The complete mathematical model therefore consists of 45 elements. Table 1 presents the elements of the complete model. Because this 45-element model does not treat the aft section consistently with the other sections, an alternate model was also utilized. This alternate model was developed

from the original 45-element model by greatly increasing the coupling factor between the subsections within the aft section. This change caused the 4 subsections to respond as if they were only 1 section and resulted in a model with essentially 37 elements. This modeling is more consistent with that for the three forward sections. However, it does cause the local acoustic excitation to be effectively spread over a larger area although the total input acoustic power remains the same. The skin sections of this alternate model are indicated in Figure 2 with Roman numerals.

The matrix format for SEA systems is

$$([D] + [C])\{E\} = \{S\}$$

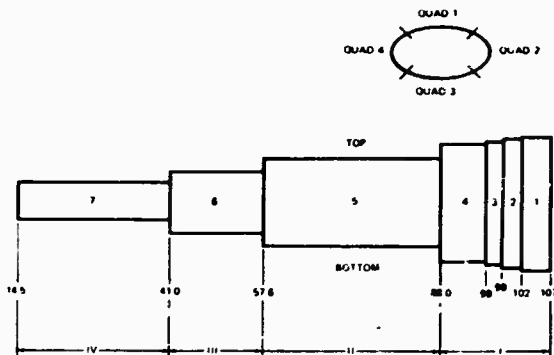


Figure 2. Skin Elements

Table 1

UpSTAGE MODEL ELEMENTS

Element No.	Description	Section or Subsection No.	Quad No.	Element No.	Description	Sta.	Section or Subsection No.
1	Skin	1	1	29	Aft Bulkhead (B.H.)	107.0	1
2	Skin	1	2	30	Forward B.H.	14.5	7
3	Skin	1	3	31	Field Joint B.H.	88.2	4-5
4	Skin	1	4	32	Field Joint B.H.	57.6	5-6
				33	Field Joint B.H.	41.0	6-7
5	Skin	2	1	34	Internal B.H.	97.0	3
6	Skin	2	2	35	Internal B.H.	92.0	4
7	Skin	2	3				
8	Skin	2	4	36	Internal B.H.	83.5	5
9	Skin	3	1	37	Internal B.H.	76.3	5
10	Skin	3	2	38	Internal B.H.	68.0	5
11	Skin	3	3				
12	Skin	3	4	39	Internal B.H.	51.2	6
				40	Internal B.H.	46.2	6
13	Skin	4	1				
14	Skin	4	2	41	Internal B.H.	36.7	7
15	Skin	4	3	42	Internal B.H.	31.9	7
16	Skin	4	4	43	Internal B.H.	28.0	7
				44	Internal B.H.	24.0	7
17	Skin	5	1	45	Internal B.H.	19.4	4
18	Skin	5	2				
19	Skin	5	3				
20	Skin	5	4				
21	Skin	6	1				
22	Skin	6	2				
23	Skin	6	3				
24	Skin	6	4				
25	Skin	7	1				
26	Skin	7	2				
27	Skin	7	3				
28	Skin	7	4				

where the elements of the damping matrix, [D], are $d_j = \omega n_j$

ω = Center frequency of analyzed frequency band in radians/sec

$n_j = 2 \times (\text{damping/critical damping})$ for the j^{th} element

[C] is the coupling matrix where

$$c_{j,k} = -\phi_{j,k} N_j \text{ for } j \neq k$$

$$c_{j,j} = - \sum_m c_{m,j} \text{ for } j \neq m$$

$\phi_{j,k}$ = average mode-to-mode coupling between j and k , and are zero for uncoupled elements.

N_j = Number of modes in element j .

It is assumed that the total energy of an element may be represented by

$$E_i = m_i \overline{v_i^2}$$

and that the bandwidths of analysis are sufficiently narrow so that

$$E_i = m_i \overline{v_i^2} = m_i \frac{\langle a^2 \rangle}{\omega^2}$$

is a valid expression for the vibrating system.

In matrix notation

$$\{E\} = \frac{1}{\omega^2} [M] \langle a^2 \rangle$$

The diagonal matrix [N] must be formed in order to obtain [C]. The number of modes in a given element is

$$N(\omega) = n(\omega) \cdot (\Delta\omega)$$

where $n(\omega)$ = modal density

The structure presently being analyzed is made up of flat plates (end plates and internal bulkheads) and curved plates (external skin). The modal density of a plate is given as

$$n_p = \frac{A_s}{4\pi \sqrt{\frac{D}{\rho h}}}$$

where

A_s = area

D = bending stiffness

* d_j was improperly defined as $2\omega n_j$ in Reference 2.

ρ = density in mass/volume

h = thickness

The modal density for a curved plate is

$$n_c = n_p \cdot (CF)$$

CF is a correction factor that accounts for the curvature effects of the panel. An approximate value used for CF is

$$CF = \left(\frac{\omega}{\omega_r} \right)^{2/3} \text{ for } \omega < \omega_r$$

$$= 1 \text{ for } \omega > \omega_r$$

where ω_r is the ring frequency of the system.

For the UpSTAGE specimen analysis, the damping factor and the base value for the coupling parameter were evaluated by a series of tests, which will be examined in the following section.

The relative values of coupling in the [C] matrix were assigned on the basis of engineering judgment and the accuracy of the predicted results (see Reference 3).

The base coupling value (from the test program) was considered to apply to the coupling across the field joints between the four sections. The other element coupling is between skin and internal bulkheads (and end-plates), and circumferentially around the skin. The initial coupling values relative to the field joints were selected as 1/3 for the bulkhead/skin coupling and 10 for the circumferential coupling.

The acoustic input term is developed by considering a separate acoustic field coupled to each excited model element. The power flow terms for the acoustic element are

$$\phi_{j,ac} N_j E_{ac} - \phi_{j,ac} N_{ac} E_j$$

The first of these terms represents the acoustic power input to the element. The second term is the power radiated from the element to the acoustic field and will be accounted for in the damping term for the element. However, this term can be used to evaluate the acoustic coupling element $\phi_{j,ac}$.

Reference 4 presents an expression for the acoustic power radiated in terms of the radiation efficiency. Equating the given value to the radiation term above gives

$$\phi_{j,ac} N_{ac} E_j = \sigma_j A_j \rho_o c_o \overline{v_j^2}$$

where

$$\sigma_j = \text{radiation efficiency}$$

Substituting for E_j and solving for the acoustic coupling factor

$$\phi_{j,ac} = \frac{\sigma_j A_1 \rho_0 c_0}{N_{ac} n_j}$$

This expression may now be substituted into the acoustic input term, giving

$$\phi_{j,ac} N_j E_{ac} = \frac{\sigma_j A_1 \rho_0 c_0}{N_{ac} n_j} N_j E_{ac}$$

Reference 5 provides useful expressions for the number of modes, N_{ac} , and total energy, E_{ac} , of a reverberant chamber:

$$N_{ac} = \frac{\omega_0^2 V (\Delta\omega)}{2\pi^2 c_0^3}$$

$$E_{ac} = \frac{\langle p^2 \rangle V}{\rho_0 c_0^2}$$

Consequently the acoustic input term will be expressed as

$$S_j = \phi_{j,ac} N_j E_{ac} = \frac{2\pi^2 c_0^2 A_1 \langle p^2 \rangle \sigma_j}{\omega_0^2 (\Delta\omega) n_j} N_j$$

or

$$\{S\} = \frac{2\pi^2 c_0^2}{\omega_0^2 \Delta\omega} \left[A \right] \left[\frac{1}{m} \right] \left[\frac{\sigma}{n} \right] \left[\frac{N}{V} \right] \left[\langle p^2 \rangle \right]$$

The values for radiation efficiency were obtained from data in Reference 4. These data were scaled on both the ring and the critical frequencies of the elements.

The properties relating to the acoustic medium that appear in this expression for the input are c_0 , $\langle p^2 \rangle$, and σ . The only one of these terms that is unique to the assumed reverberant field is σ . Therefore, this representation would seem to be valid for nonreverberant acoustic fields if a proper value for σ can be determined for the field.

The following section will consider the elements of the two matrices not yet defined, $[D]$ and $[C]$.

TEST PROGRAM

Tests were performed to (1) determine SEA parameter values for the damping and coupling for use in analyzing the UpSTAGE acoustic test specimen, (2) provide general insight into the characteristics of the SEA coupling parameter, and (3) establish a method of determining SEA damping and coupling parameters by performing tests on simplified structures.

The test program was carried out with three basic test specimens, each one consisting of two panels with connecting tee-joint fabricated to simulate the aft joint of the UpSTAGE acoustic specimen. Figure 3 shows the general specimen configuration.

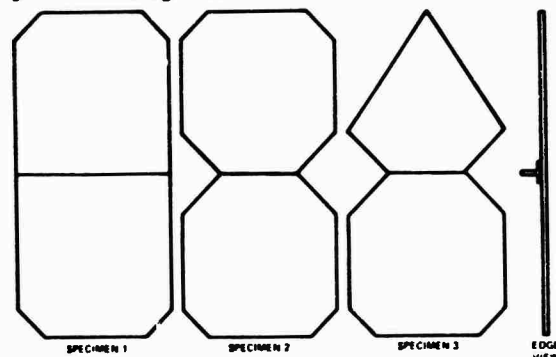


Figure 3. Panel Test Configurations

Specimens 1 and 2 were designed to furnish information on the effects of joint length on the coupling parameter, while Specimen 3 was designed to evaluate an unsymmetric configuration. The panels were made of aluminum with a basic size of 3 feet by 3 feet. Because the skin thickness is different on the two sides of the UpSTAGE joint being simulated, three panels were fabricated for Specimen 1, two with a thickness of 0.160-inch and one with a thickness of 0.125-inch so that a joint with the appropriate skin thickness variation could be examined, as well as a joint that was completely symmetric. Specimens 2 and 3 used only panel thicknesses of 0.160-inch. The connecting tee for the panels was 0.125 inch thick, with a 1.0 inch overlap on each panel. A cross-section of this joint is identical to a cross-section of the UpSTAGE aft joint.

The primary purpose of the tests was to evaluate the coupling parameter ϕ . This was done by exciting one panel, measuring the response in both panels, and solving for $\phi_{1,2}$ or ϕ^* in the expression

*The subscripts on ϕ will be dropped when only two-element systems are being considered.

$$\frac{E_1}{E_2} = \frac{E_1}{E_2} \cdot \frac{\eta_{1,2}}{\eta_{1,2} + \eta_1}$$

where

$$\eta_{1,2} = \frac{\phi E_2}{\omega}$$

The damping of the panels (η) must be evaluated before ϕ can be obtained. In addition, η is required in the analysis of the total system. This led to two types of testing, the first to determine damping, and the second to determine ϕ . All testing was accomplished with the test specimen suspended on elasticized cords (bungees).

Damping was determined by striking a panel with a steel hammer or wooden stake (bop testing) and recording a decay trace of the panel vibration response with an oscilloscope. The response signal from an accelerometer mounted on the panel was routed through an adjustable bandpass filter prior to being recorded with the oscilloscope. This filter permitted various bandwidths and center frequencies to be selected. The data obtained from the testing consisted of decay traces using both octave and third-octave bandwidths with center frequencies encompassing the range of 400 to 4,000 Hz. This method permitted the vibration response of the panels to be observed graphically as it decayed to about one-tenth of the initial level. This decay was plotted on semi-logarithmic paper and a straight line drawn to approximate the decay slope.

This approximate decay slope permitted the fraction of critical damping to be evaluated for an assumed exponential type of decay. The damping for each specimen was measured with both octave and third-octave bandwidths at two locations on the specimen.

Early in the test program it became evident that the damping of the system would have to be increased to obtain meaningful values of the coupling parameter (see below). This was accomplished by applying a single layer of Scotchfoam damping tape to the panels.

The damping values which will be presented are averaged values of all the data taken at each center frequency. Since two locations were used for each panel together with two analysis bandwidths, the averages are of four values at the octave center frequencies (400, 800, 1,600, 3,200 Hz) and two values for each of the other frequencies.

Figure 4 presents the damping data obtained for a damped 0.160-inch panel of each of the three configurations. The range of values for the damping parameter is from 0.005 to 0.015. Two phenomena are shown in the graph. First, close examination reveals a peaking effect which occurs for the Specimen 1 and

2 panels near 2,000 Hz, but not for the Specimen 3 panel. The effect is greater for the Specimen 1 panel. This seems to indicate a shape effect which diminishes as the panels become less square. The frequency of this peaking effect corresponds to a bending wave speed of about 3,000 ft/sec or 1.5 ft/cycle (half the width of the panel). The second phenomenon is evident when the 2,000 Hz peaking is removed from the data; namely, the reduction in damping as frequency increases.

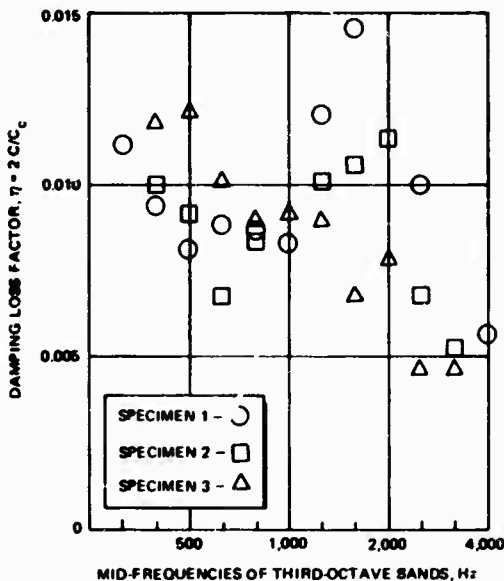


Figure 4. Damping Loss Factor for 0.160-inch Panels (with Damping Tape Applied)

Figure 5 presents a comparison of the damping data for the 0.125-inch and 0.160-inch panels of Specimen 1. These data illustrate the greater effect of the damping tape on the thinner panel. The same type of peaking and frequency rolloff is evident for the 0.125-inch panel as was found for the 0.160-inch panels.

Figure 6 presents the damping data for the undamped panels. It is noteworthy that these damping values agree with data published in Reference 6 (and summarized in Reference 7) for the 6061-T6 aluminum alloy panel material. The addition of the damping tape is noted to have increased the damping by a factor of 8.

The vibration portion of the testing was accomplished by exciting the panels with a 1-pound force Goodman shaker. The input spectrum for the testing was furnished by a random noise generator. The evaluation of joint coupling required only that the relative level of vibration on the two panels of a specimen be determined; consequently, no specific input was required. Input control was achieved by operating consistently at an overall level of 5 G rms.

The average mode-to-mode coupling parameter, ϕ , was evaluated with the equation for the relative energies of a two-element system.

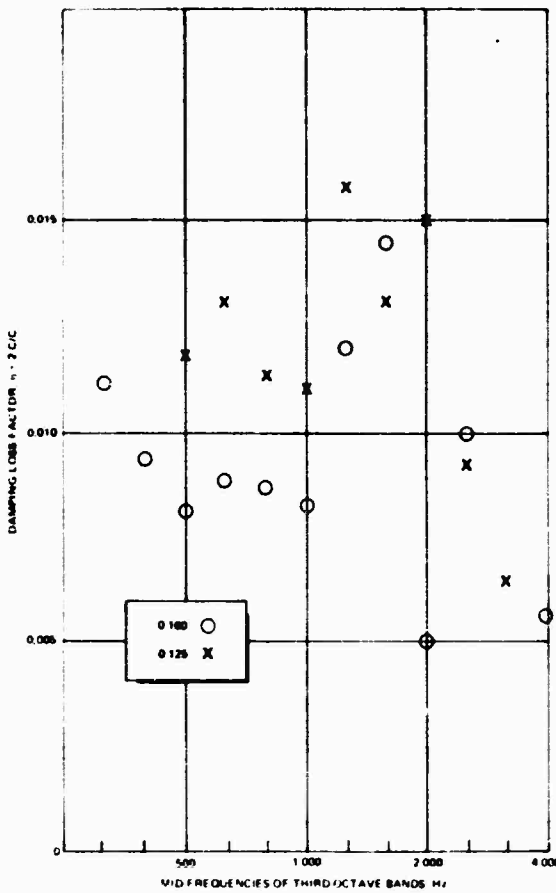


Figure 5. Damping Loss Factor for Two Configurations of Specimen 1 (with Damping Tape Applied)

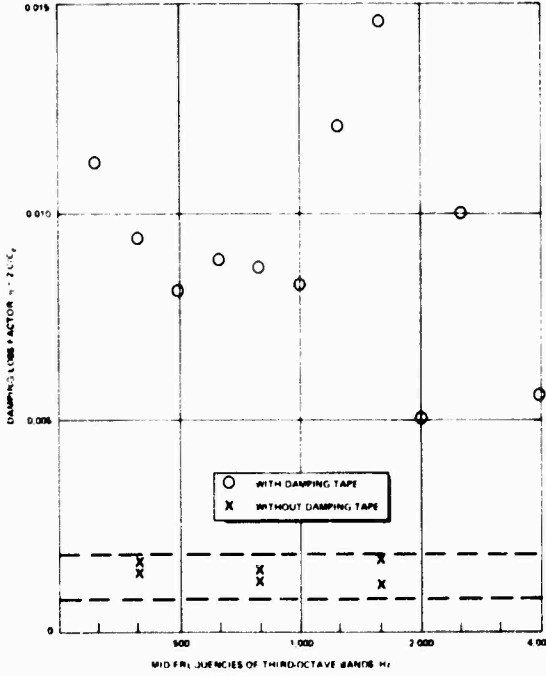


Figure 6. Damping Loss Factor for Specimen 1 Panels with and without Damping Tape

$$\frac{E_1}{E_2} = \frac{m_1}{m_2} \frac{\langle a_1^2 \rangle}{\langle a_2^2 \rangle} = \frac{m_1}{m_2} \frac{n_{1,2}}{n_{1,2} + n_1}$$

$$= \frac{\frac{\phi N_2}{\omega_0}}{\frac{m_1}{m_2} \frac{\phi N_2}{\omega_0} + n_1}$$

This equation indicates that for very small damping,

$$\frac{\phi N_1}{\omega_0} \gg n_1$$

the ratio E_1/E_2 will be very close to unity. This situation occurred when attempting to evaluate the coupling parameter before adding Scotchfoam to the panels. Measurement inaccuracy made it impossible to obtain reliable coupling values.

For the symmetric Specimens 1 and 2, the coupling relation reduced to

$$\frac{\frac{\langle a_1^2 \rangle}{\langle a_2^2 \rangle}}{\frac{\phi N_2}{\omega_0}} = \frac{\frac{\phi N_2}{\omega_0}}{\frac{\phi N_2}{\omega_0} + n_1}$$

while the element masses and modal density ratios were required for Specimen 3 (also for the 0.160/0.125 configuration of Specimen 1). The modal density was calculated with the relation presented previously for plates.

The optimum shaker location that could be determined resulted in an approximate average variation of 6 dB across a panel, with a maximum of about 10 dB within the frequency range of interest. In order to minimize the effects of this variation, acceleration was measured at a number of points on each panel for every test configuration and averaged to establish response values.

The damping values utilized in calculating the mode-to-mode coupling for each center frequency for each specimen were from the data points shown in Figures 4 and 5.

Figure 7 presents the values determined for the average mode-to-mode coupling of the 0.160-inch panel specimens. Specimen 3 exhibits the highest value at each frequency, while Specimen 2, except at one frequency, has always the lowest value. Comparing values for Specimens 1 and 2, the doubling of the joining length causes the coupling parameter value to increase by a factor ranging from two to five. The same type of comparison for Specimens 2 and 3 indicates that this type of nonsymmetry causes the

coupling parameters to increase by a factor of 5 to 20 over the symmetric configuration. The dashed line indicates the approximate values for coupling used during the analysis.

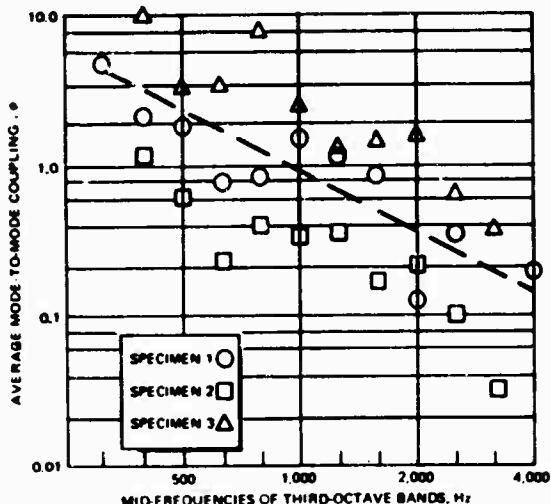


Figure 7. Mode-to-Mode Coupling of 0.160-inch Panel Specimens

Figure 8 presents comparisons of the mode-to-mode coupling for the two configurations of Specimen 1. The data for the 0.125/0.160 configuration demonstrate much less frequency dependence than is apparent for the other configurations. The data are, in fact, remarkably flat. Comparison of these data for those for Specimens 2 and 3 indicates that two different effects of nonsymmetry are present with the panels. The nonsymmetry effect of shape (Specimens 2 and 3 data) causes a shift in coupling, while no such shift is evident for nonsymmetry in modal density (data for the two configurations of Specimen 1).

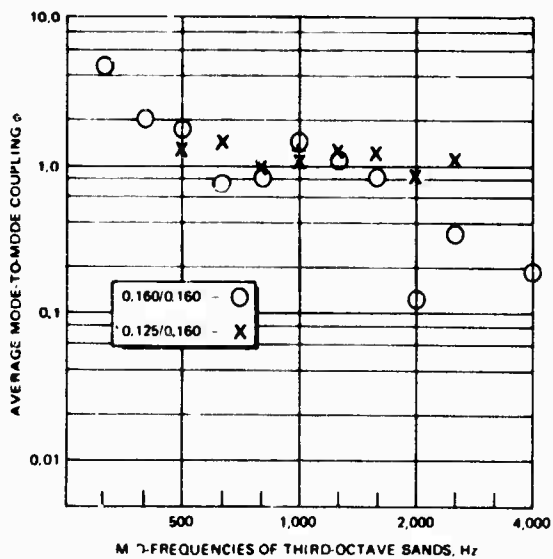


Figure 8. Mode-to-Mode Coupling of Two Specimen 1 Configurations

The data from the panel tests were examined statistically to evaluate accuracy. The fractional error, defined as the standard deviation divided by the average value of the quantity being evaluated (fractional error = σ/μ), was chosen as the measure of accuracy. For the damping measurements, the fractional error in the data is about 0.1. The value is approximately 0.35 for the panel vibration measurements, corresponding to a standard deviation of about 2 dB on the panels. These values result in a fractional error for the calculated coupling factors of 0.48. An initial series of tests was repeated and an attempt made to increase the accuracy of the vibration measurements without success.

The UpSTAGE acoustic test specimen was made available, so testing was performed to establish the damping of the specimen and also to attempt a direct evaluation of the joint coupling values. The UpSTAGE specimen was separated at the three joints into the four basic sections. Bop tests were performed with each individual section suspended on bungees. Decay data in octave and third-octave bandwidths were reduced for both an external skin and an internal bulkhead location on each of the sections. A graph of the average values obtained for Sections II, III, and IV is presented in Figure 9. Section I had been fitted with a wooden bulkhead for use as a wiring mockup and was therefore not considered a valid dynamic test specimen. The dashed lines indicate damping parameter values used during analysis.

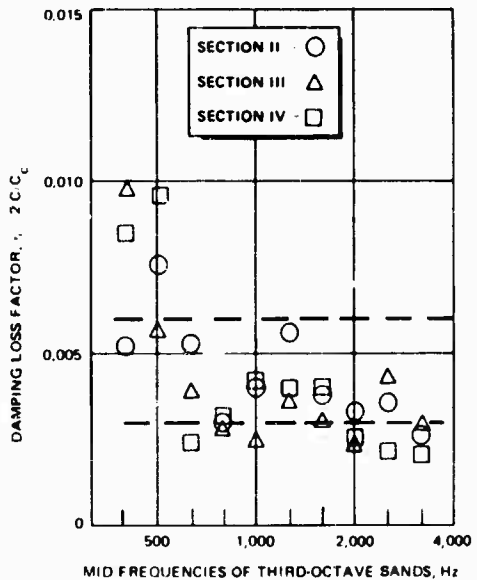


Figure 9. Damping Loss Factor for Sections of the UpSTAGE Acoustic Test Specimen

In order to evaluate the SEA coupling factors for this complex specimen, a very gross four-element SEA system was assumed with each of the four sections representing one element. The specimen was suspended on bungees and Section I excited by the 100-pound force CALIDYME shaker shown in Figure 10. Three configurations consisting of Sections I and II; I, II, and III; and I, II, III, and IV were tested. With the four element modeling, coupling values were obtained by using an average response determined from a survey of each element and assuming this average response to be valid for the total mass of the element. This method permits the coupling parameter values to be evaluated for the forwardmost joint of each configuration (for example, in the configuration with Sections I, II, and III, the parameter values for the joint between Sections II and III may be evaluated) with the simple relation:

$$\frac{\frac{m_1}{m_2} \frac{\langle a_1^2 \rangle}{\langle a_2^2 \rangle}}{1} = \frac{n_1}{n_2} \frac{n_{1,2}}{n_{1,2} + n_1}$$

since this model appears as a two-element system about the joint with an input to the system from an outside source. The modal densities were taken as calculated for the computer model of the specimen.



Figure 10. CALIDYME Shaker

The resulting values obtained for the average mode-to-mode coupling by this technique are shown in Figure 11 with a comparison of the values obtained with panel Specimen 1. This approximation technique resulted in a few negative values which are omitted from the graph.

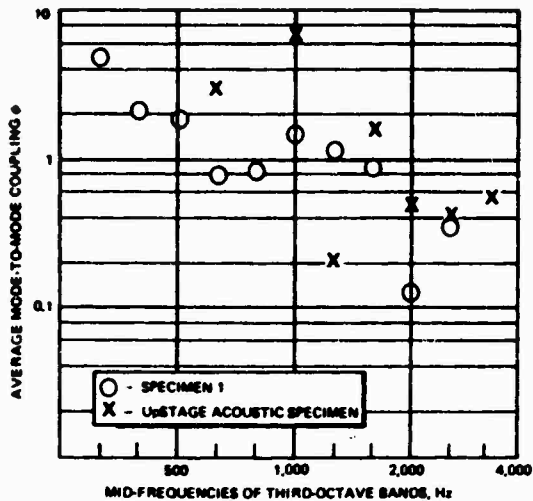


Figure 11. Approximate Mode-to-Mode Coupling Measured for UpSTAGE Acoustic Test Specimen

RESULTS OF COMPLEX ANALYSIS

The computer analysis of the UpSTAGE acoustic specimen provides comparisons between computed and measured values to indicate the accuracy of SEA in conjunction with simple test methods, in predicting vibration response.

Before making the comparison of test data with the analytical predictions, the test configurations will be discussed. Two basic test configurations were utilized. The first of these configurations simply mounted the test specimen on bungees in a reverberant chamber so that the entire exterior surface of the specimen was exposed to a uniform acoustic field. This configuration will be referred to as Reverberant.

The second configuration for testing was attained by mounting the specimen through the wall between the reverberation chamber and an adjoining anechoic chamber. The space between the specimen and the wall was sealed with a lead sheet and lightly packed with fiberglass, as shown in Figure 12. This test configuration achieved a reduction in sound pressure level across the wall of at least 24 dB throughout the frequency range of interest and furnished a convenient means of localizing the acoustic input.

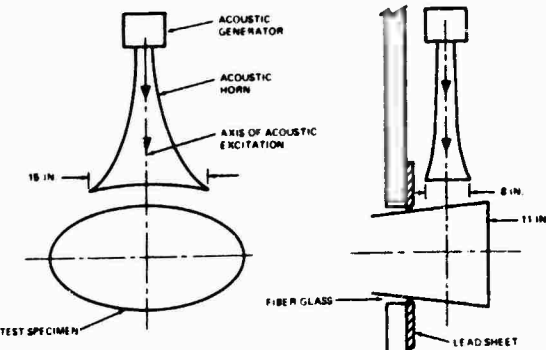


Figure 12. Configuration for Direct Impingement Acoustical Test

Two types of testing were accomplished with this second configuration. The first type was performed by mounting the specimen flush with the wall so that only the aft closure plate of the specimen was excited. A reverberant field was used for this testing and it will be referred to as Reverberant (aft plate only).

The second type of testing with this configuration was accomplished by positioning the specimen so that the aft 11 inches protruded into the reverberation chamber as shown in Figure 12. Acoustic input was accomplished with an acoustic horn directed at the aft section of the specimen. This setup permitted a localized nonsymmetric input to be attained for the specimen. The side of the specimen which was excited in this configuration will be referred to as the "top" and the opposite side as the "bottom." This test configuration will be referred to as "Direct Impingement." These tests and the specimen are discussed in detail in References 2 and 3.

The indicated nomenclature will be used to describe test configurations throughout the remainder of this paper.

The values used for the basic coupling parameter (ϕ_0) of the field joints of the model were taken from Figure 7 as was previously noted. Two basic sets of values were available for the damping parameter. One set of values was from the tests on bare (prior to applying Scotchfoam) aluminum panels, while the other set resulted from tests on the actual acoustic specimen. The predictions are parameterized on these two sets of values. Each set of data was enveloped with two values as indicated in Figures 6 and 9. These bounds are $\eta = 0.0005$ and 0.001 for the panel test data, and $\eta = 0.003$ and 0.006 for the acoustic specimen data. These bounds for the two sets of data differ by a factor of six.

In order to avoid cluttering the prediction comparisons with unnecessary information, predictions for each of the four damping values will not be shown for all comparisons. These values are omitted when a straightforward interpolation is indicated for the additional values.

The exterior skin levels are considered the more significant aspect of the comparison. The test program was designed to establish coupling parameter values between skin segments and the majority of the acoustic test measurements were made on the external skin. Internal transmission of vibration through bulkheads and substructures is directly analogous to the Reverberant (aft plate only) configuration, which will be examined.

Consequently, the apparent neglect of internal response in the present study (in order to concentrate the test effort) does not diminish the validity or usefulness of SEA throughout an aerospace vehicle.

The predictions for the completely reverberant excitation will be considered first. Because each of the exterior elements of the specimen is being directly excited in this configuration, the computed response should be most directly controlled by the damping values selected for the model elements and the acoustic-structure coupling factor (radiation efficiency) rather than the coupling values between the structural sections.

Figures 13 to 16 provide comparisons of the external skin response in each of the four major regions for this fully reverberant configuration. For this case, the damping based on the panel tests yields predicted responses that agree very well with test data at frequencies above 1,600 Hz, except for a single data point at 2,000 Hz in region IV. The damping obtained from the UpSTAGE specimen results in a computed response which is consistently lower in the high frequencies than the measured values.

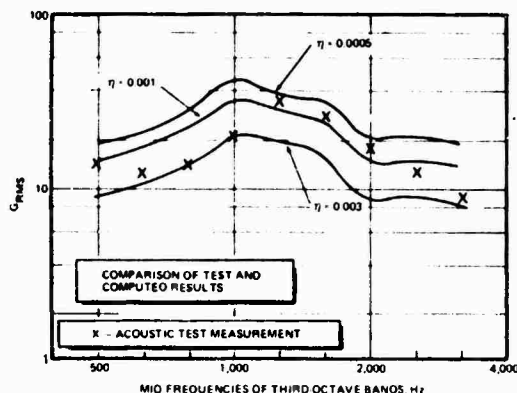


Figure 13. Reverberant - Section I

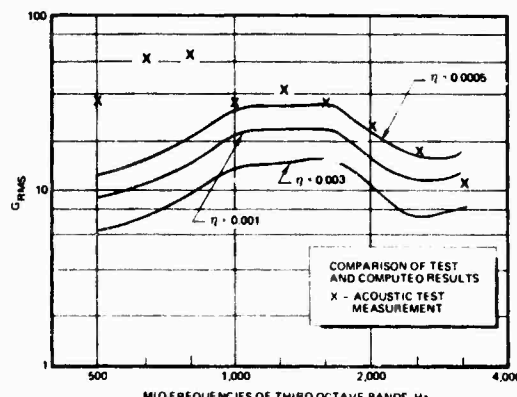


Figure 14. Reverberant - Section II

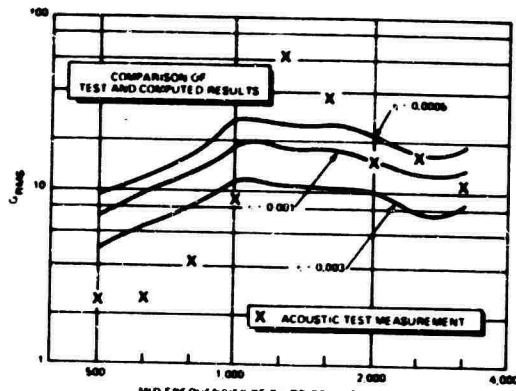


Figure 15. Reverberant - Section III

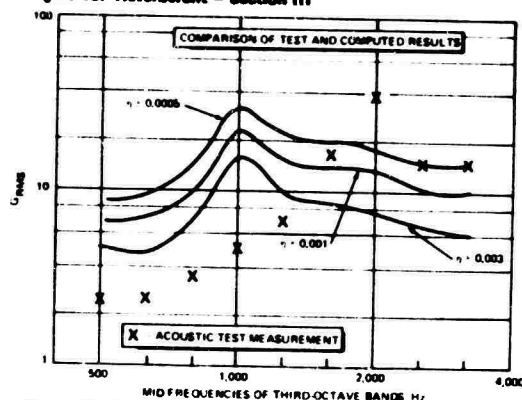


Figure 16. Reverberant - Section IV

The computed values are higher than measured values in the lower frequencies except in Region II. A peak is also indicated by the measurements at 1,250 Hz which does not show up in the computations. These values were obtained with the 45-element modeling of the specimen (this acoustic input configuration should be insensitive to aft section modeling).

The next configuration to be considered is Reverberant (aft plate only). Figures 17 to 20 present a comparison between computed and measured values for both 37- and 45-element models with only one value of damping. It was the very low predicted response for the 45-element model with this lowest value of damping which led to the development of the 37-element model. The constraint of energy flow toward the

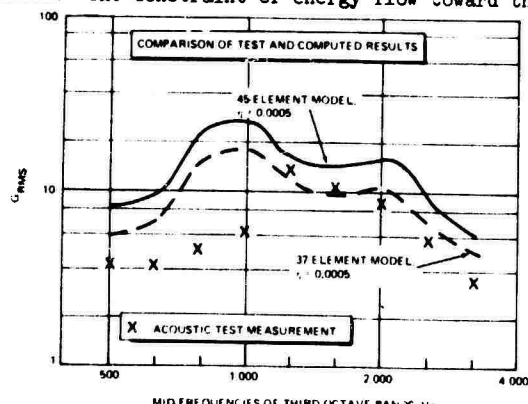


Figure 17. Reverberant - Aft Plate Only - Section I

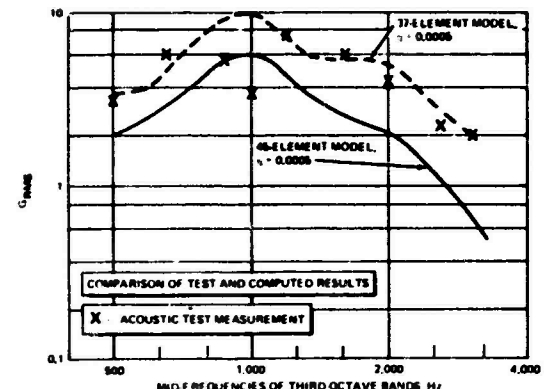


Figure 18. Reverberant - Aft Plate Only - Section II

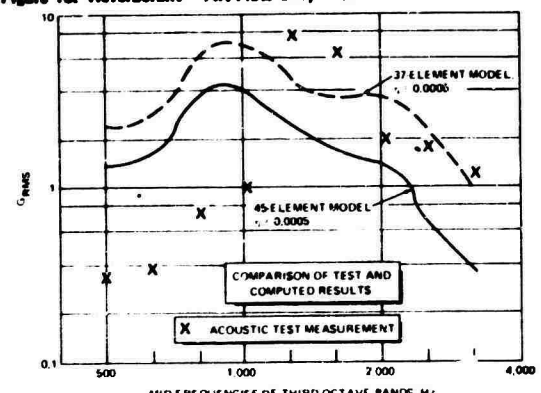


Figure 19. Reverberant - Aft Plate Only - Section III

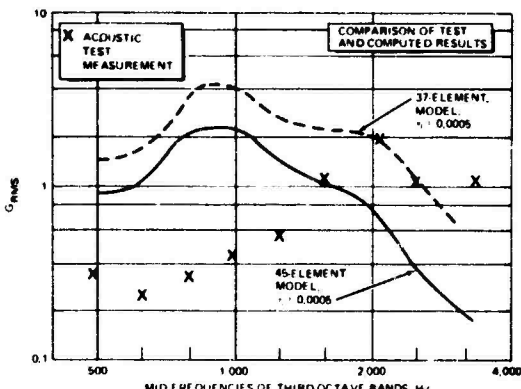


Figure 20. Reverberant - Aft Plate Only - Section IV

front of the model by the additional joints of the 45-element model is very obvious in these figures. Likewise, this configuration is the most dependent upon selection of suitable coupling values since energy must flow the entire length of the specimen to excite Section IV.

The remainder of the prediction comparisons are for the Direct Impingement configuration. Three cases were examined for this configuration. These cases correspond to tests performed with varying applications of Scotchfoam damping tape to the test specimen.

Figures 21 to 25 present the response comparison for this Direct Impingement configuration with no damping tape applied to the specimen. Test measurements were made on the top and bottom of the aft two sections and these are shown in the figures. These figures indicate that a corrected estimate of the circumferential coupling, ϕ_c , as 50 times the basic field joint coupling value yields acceptable relative levels between the top and bottom portions of the aft two sections.

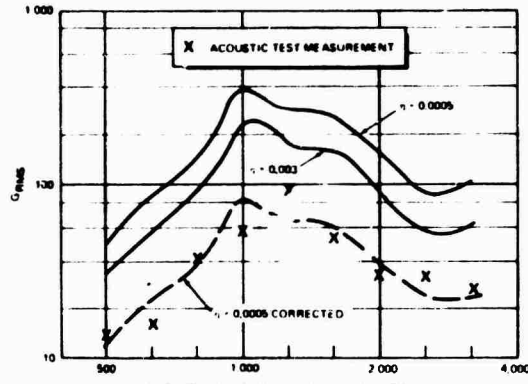


Figure 21. Direct Impingement - Section I - Top - 37-Element Model - $\phi_c = 50\phi_0$

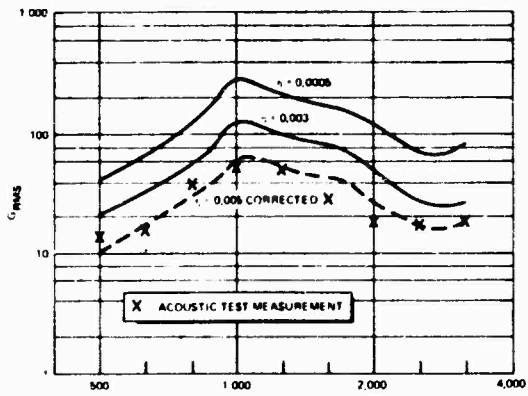


Figure 22. Direct Impingement - Section I - Bottom - $\phi_c = 50\phi_0$

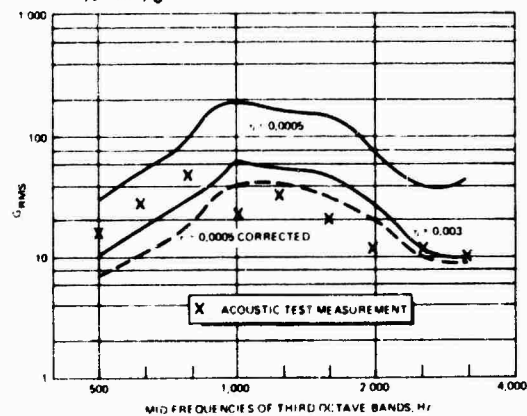


Figure 23. Direct Impingement - Section II - Top - $\phi_c = 50\phi_0$

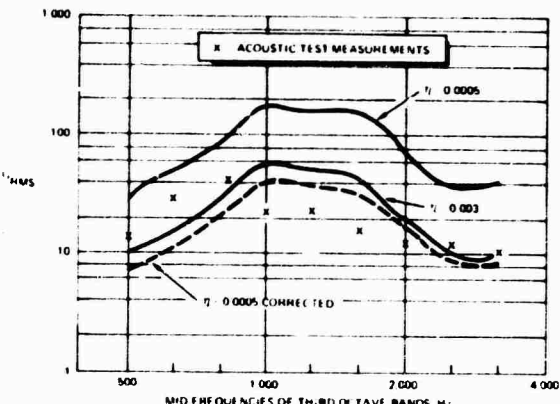


Figure 24. Direct Impingement - Section II - Bottom - $\phi_c = 50\phi_0$

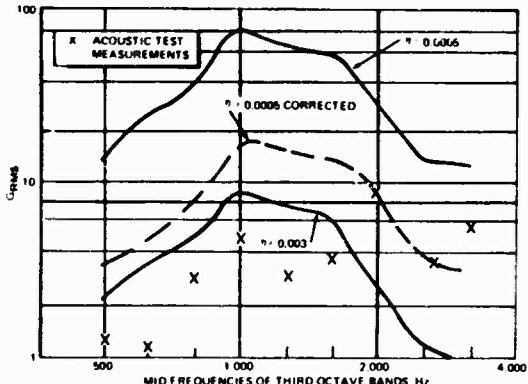


Figure 25. Direct Impingement - Section IV - Top - $\phi_c = 50\phi_0$

The curves on these figures represent the predicted values for $\eta = 0.0005$ and $\eta = 0.003$ as well as a curve labeled $\eta = 0.0005$ corrected. The corrected curve is discussed below.

This configuration is excited by nearly normally incident acoustic energy and the exciting field is not as well defined as it was in the original case. In addition, the analysis of the first two configurations confirmed the damping and axial structural coupling factors for the model. For these reasons it was assumed that the discrepancy resulted because of improper definition of the energy input. To test this assumption the predicted value for $\eta = 0.0005$ was reduced until acceptable agreement was achieved for both measurements in Section I. This reduction was applied to the $\eta = 0.0005$ predicted values for all of the sections. The general agreement between the measured and the corrected prediction values substantiates the assumption of the discrepancy being in the input.

Figures 26 to 30 present the same type of comparison for a case with damping tape applied to the aft three subsections of Section I. Based on experience with the panels, the addition of the damping tape was assumed to increase the damping by a factor of eight over bare structure. The two values of damping noted on the figures are for the bare structural areas and the damped areas of the specimen. The results for this case are essentially the same as for the bare specimen.

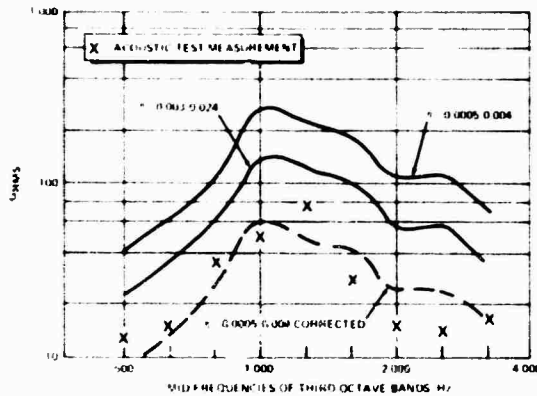


Figure 26. Direct Impingement - Section I - Top - $\phi_c = 50 \phi_0$ - Damping Tape Applied to Section I

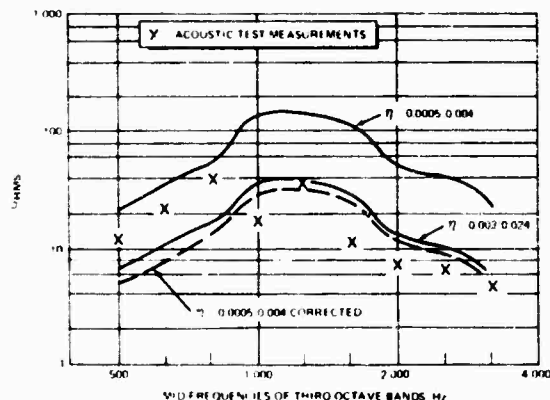


Figure 27. Direct Impingement - Section I - Bottom - $\phi_c = 50 \phi_0$ - Damping Tape Applied to Section I

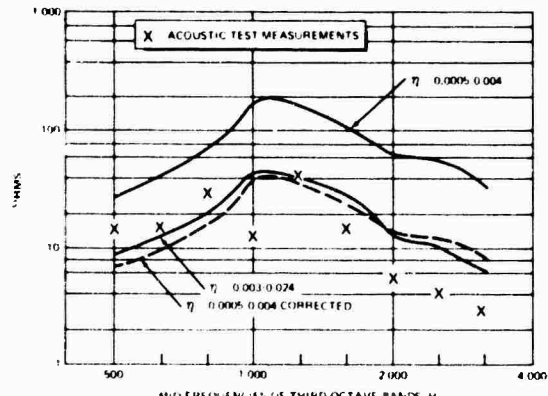


Figure 28. Direct Impingement - Section II - Top - $\phi_c = 50 \phi_0$ - Damping Tape Applied to Section I

The final case adds damping tape over a portion of Section II, which is assumed to increase the damping by a factor of three. The Section I damping is retained as in the preceding case, and circumferential coupling is likewise 50 times field joint coupling. The results are shown in Figures 31 to 33. From these figures it appears that the effectiveness of the damping tape was slightly underestimated in Section II.

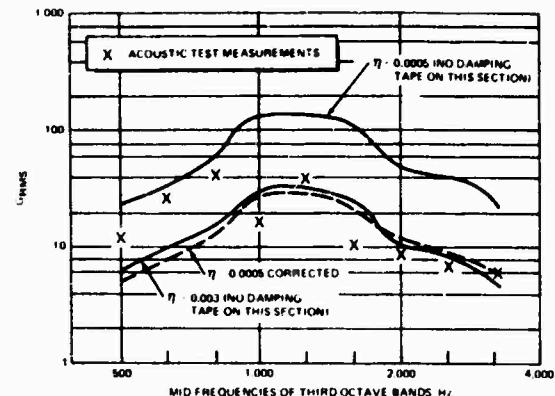


Figure 29. Direct Impingement - Section II - Bottom - $\phi_c = 50 \phi_0$ - Damping Tape Applied to Section I

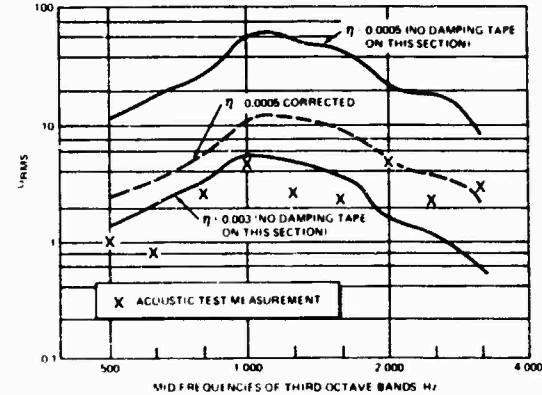


Figure 30. Direct Impingement - Section IV - Top - $\phi_c = 50 \phi_0$ - Damping Tape Applied to Section I

It should be noted that the acoustic input configurations which have been examined cover the entire realm of response problems:

A. Fully Reverberant - vehicle completely surrounded by a significant acoustic field.

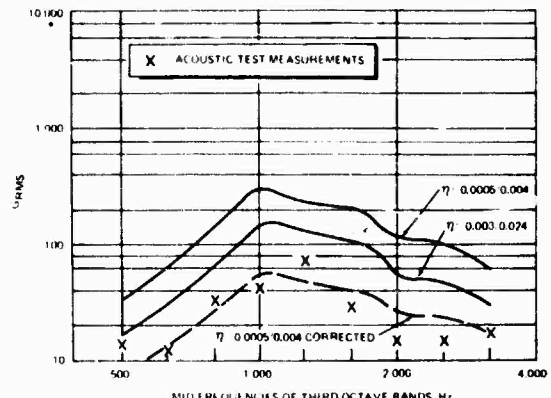


Figure 31. Direct Impingement - Section I - Top - $\phi_c = 50 \phi_0$ - Damping Tape Applied to Sections I and II

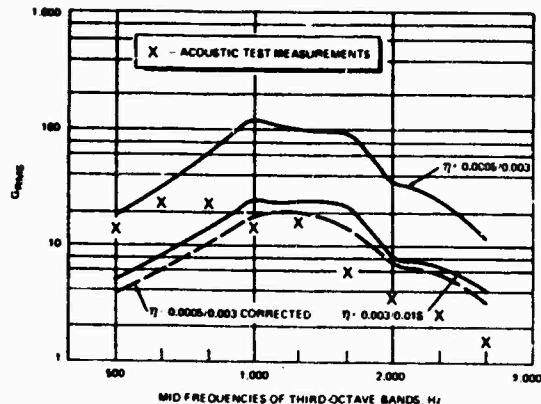


Figure 32. Direct Impingement - Section II Top - $\phi_c = 50\%$ - Damping Tape Applied to Sections I and II

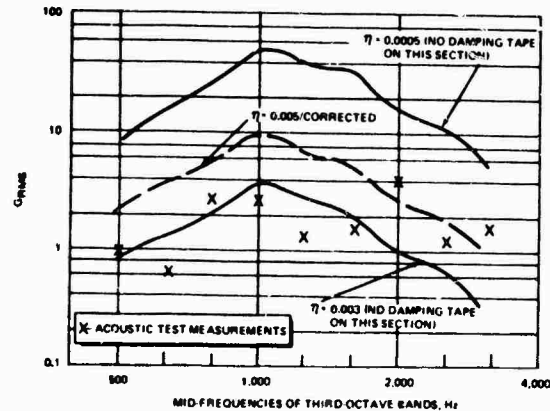


Figure 33. Comparison of Test and Computed Results - Direct Impingement - Section IV - Top - $\phi_c = 50\%$ - Damping Tape Applied to Sections I and II

- B. Reverberant (aft plate only) - identical to internal structure or substructure excited by a portion of the external skin.
- C. Direct Impingement - vehicle has localized hot spots on the skin.

Because SEA consists of linear techniques, the contribution to a system of each type of excitation may be determined and the squares of the responses summed, therefore providing the total response.

A scaling method must be developed in order to evaluate the significance of this study to general structural systems. A classical means of scaling frequency dependent data on cylindrical shells is to replace frequency with frequency times radius of curvature ($f \cdot r$). This scaling minimizes the effects of curvature on the values being evaluated.

Figure 34 compares the accuracy of the predictions, using predicted response for $\eta = 0.0005$ divided by measured response as the indicator of accuracy, as a function of such a scaled frequency for the fully-reverberant case.

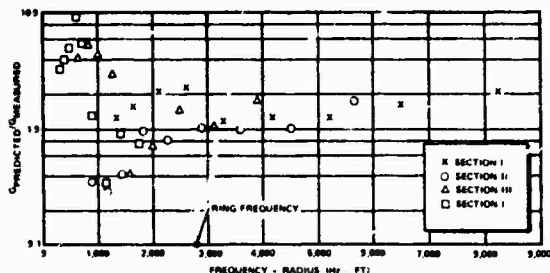


Figure 34. Prediction Accuracy of SEA as a Function of Adjusted Frequency - Reverberant

The first observation is that a damping value of $\eta = 0.001$ would yield better agreement (since η is inversely proportional to g^2) and that error in the prediction does not exceed ± 3 dB above $fr = 2,500$ Hz ft (except for one point). If the error band is increased to ± 6 dB, the value for the applicable range of fr can be reduced to approximately 1,500 Hz ft. These frequencies correspond to a little less than the ring frequency to one-half of the ring frequency. It should be noted that although it appears that damping was underestimated, the same results would be obtained by overestimating the acoustic input.

The same presentation for the aft plate excitation is presented in Figure 35. The predicted value is based on $\eta = 0.0005$. The error in the predicted value is less than 3 dB for values of fr greater than 2,500 Hz ft. This agreement does indicate that the discrepancy in Figure 34 is the result of underestimating the acoustic input or, at least, the damping value of 0.0005 is compatible with the coupling factor used.

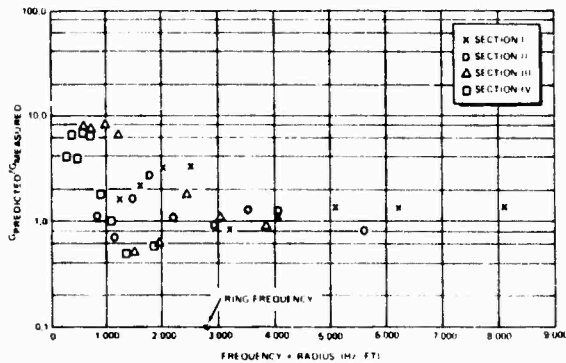


Figure 35. Prediction Accuracy of SEA as a Function of Adjusted Frequency - Reverberant (Aft Plate Only)

Figure 36, which presents the direct impingement data, shows that the proper correction to apply to the predicted values of $n = 0.0005$ would be 4 and that the scatter band does not exceed 3 dB above $fr = 3500$.

The main conclusions to be drawn from Figures 34 to 36 are that if the input energies were properly defined, the UpSTAGE analysis, using damping and coupling factors measured on simple systems, would yield results with ± 3 dB accuracy above the ring frequency of local structure and acceptable estimates of the levels to one-half of the ring frequency. These conclusions are based on curved panels that have about 20 percent of the area and modes of cylinders with corresponding curvature. Therefore, the conclusions drawn above may be conservative. Because of this conservatism, it is possible that the ± 3 -dB accuracy would extend to even lower corrected frequencies.

The classical scaling of frequency with radius which has been accomplished is very useful when cylindrical or curved structures are being considered. However, a scaling method which is valid for flat or curved structures would have even more general use. Since the lower limit of validity for SEA is considered to be a function of the number of element modes participating in the frequency bands, scaling by number of modes would seem to be indicated.

Figures 37 to 39 evaluate system accuracy based on the number of element modes present in each frequency band. The main change from the scaling on radius is that Section II replaces Section I as having the most significant (largest scaled frequencies) values. The fully reverberant and direct impingement cases exhibit slightly less accuracy than with radius scaling, while the aft plate excitation shows extremely good accuracy. Convergence to the limits of accuracy appears to occur at about 20 element modes per band.

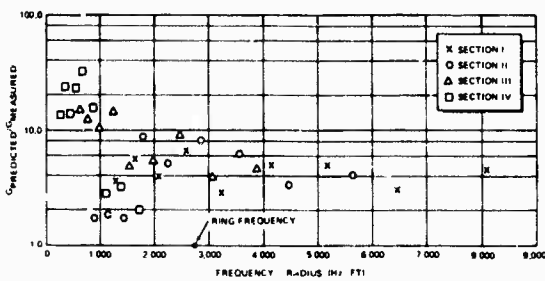


Figure 36. Prediction Accuracy of SEA as a Function of Adjusted Frequency - Direct Impingement

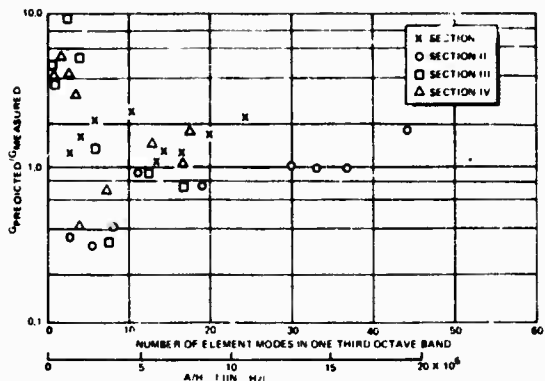


Figure 37. Prediction Accuracy of SEA as a Function of Number of Element Modes Participating - Reverberant

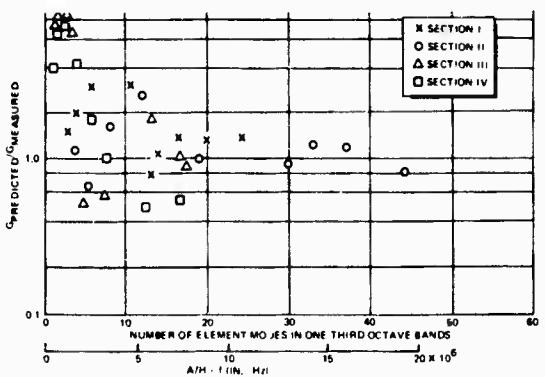


Figure 38. Prediction Accuracy of SEA as a Function of Number of Element Modes Participating - Reverberant (Aft Plate Only)

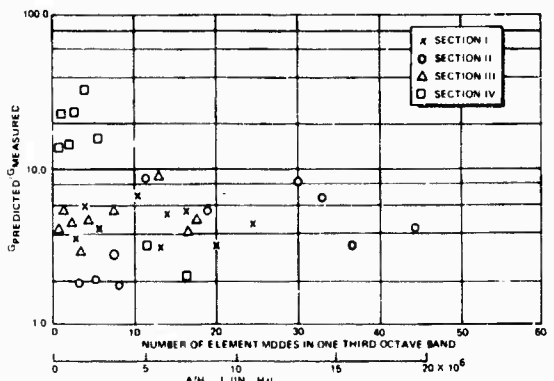


Figure 39. Prediction Accuracy of SEA as a Function of Number of Element Modes Participating - Direct Impingement

The number of modes per element when using constant percentage bandwidths for flat plates is strictly a function of $(A/h) \cdot f$. Figures 37 to 39 have their abscissas marked to show the corresponding value of this scaling parameter (valid for aluminum or steel) to aid in application of the graphs. The spacing of the points plotted on the graphs indicates the effects of curvature on distribution of modal density with frequency.

Due to the positioning of the acoustic input for the specimen, the frequency scaling on radius or size (number of modes) may be misleading with regard to the accuracy of SEA in this study. The scaling places major emphasis on predictions in Sections I and II. Because these sections are adjacent to the input, response is most directly affected by the input and by the damping, but not necessarily coupling. Consequently, Figures 40 to 42 are included to demonstrate accuracy without scaling of the frequency.

These figures still indicate a convergence of the predicted levels. Much of the spread in the high frequencies is due to Section IV, which has the lowest scaled frequencies.

These figures show that the accuracy in Sections I, II, and III converges very closely to the same value in the high frequencies for all three input configurations. This indicates the same parameter or parameters is causing the inaccuracy in all sections. This would indicate the coupling values are correct, since the coupling would affect Section III predictions relative to Section I. Consequently, the overemphasis on Sections I and II when using the scaling techniques should not be misleading as to the indicated accuracy of the SEA approach.

It should be pointed out that the general effect of varying the damping values used for the prediction comparisons would be to displace all points on a figure vertically by a similar distance. Consequently, the damping parameter controls the value of predicted response divided by measured response to which the figures converge, but does not significantly affect the variation about this value.

Combining the information provided by the three accuracy evaluation techniques, this study indicates that SEA is capable of prediction accuracies of ± 3 dB above the ring frequencies of curved structure or when the structural model has 20 or more modes per element participating in a one-third-octave frequency band. This accuracy was attained in conjunction with simple test methods used to evaluate the damping and coupling parameters for the structure. Consequently, the results verify the validity of the simple test methods as a means of evaluating these SEA parameters for complex structures.

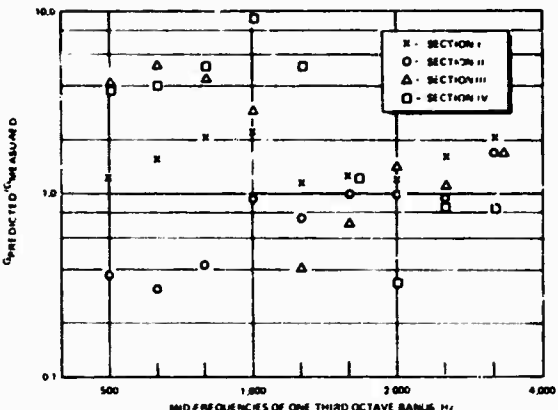


Figure 40. Prediction Accuracy of SEA as a Function of Frequency — Reverberant

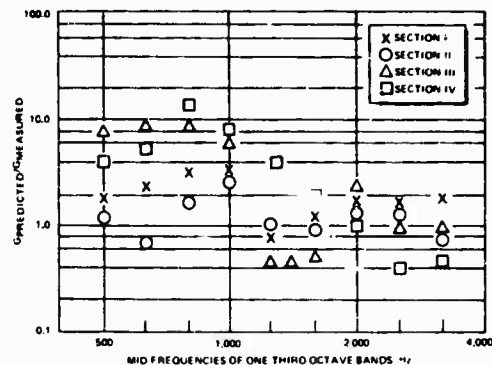


Figure 41. Prediction Accuracy of SEA as a Function of Frequency — Reverberant (Aft Plate Only)

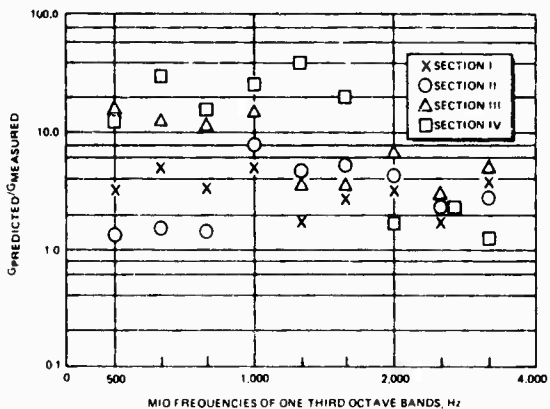


Figure 42. Prediction Accuracy of SEA as a Function of Frequency — Direct Impingement

CONCLUSIONS

The primary conclusions reached are:

- A. SEA has a demonstrated capability of structural response prediction accuracies of ± 3 dB above the ring frequency of cylindrical structure or when 20 or more modes per model element are participating in a one-third octave frequency band.
- B. The simple test methods and panel specimens presented are capable of defining the SEA damping and coupling parameters for complex structures. Of special interest is that the very low damping obtained during test did yield the proper results.
- C. Overmodeling of continuous structural elements can be an important obstacle to a successful SEA application.

ACKNOWLEDGMENTS

This study was funded by Marshall Space Flight Center through NASA Contract NAS8-28435. The complete study is reported in Reference 3.

REFERENCES

1. Jerome E. Manning and Paul J. Remington, "Statistical Energy Methods," Report 2064,

Bolt Beranek and Newman, March 26, 1971;
also NASA CR-118987, March 1971.

2. D. E. Hines, G. R. Parker and R. D. Hellweg, "Prediction of UpSTAGE Random Environments Using a Statistical Energy Approach," 41st Shock and Vibration Bulletin, 1970.
3. R. F. Davis and D. E. Hines, "Final Report - Performance of Statistical Energy Analysis," MDC-C4741, McDonnell Douglas Astronautics Company, June 1973, also NASA CR-124322, June 1973.
4. Richard H. Lyon and Gideon Maidanik, "Statistical Methods in Vibration Analysis," AIAA Journal, Vol. 2, No. 6, June 1964, pp. 1015-1024.
5. P. M. Morse, Vibration and Sound, Second Edition, McGraw-Hill Book Company, Inc., 1948.
6. L. T. Lee, "A Graphical Compilation of Damping Properties of Both Metallic and Non-Metallic Materials," Technical Report No. AFML-TR-66-169, Air Force Materials Laboratory, May 1966.
7. B. J. Lazan, Damping of Materials and Members in Structural Mechanics, Pergamon Press Inc., 1968.

DISCUSSION

Mr. Mains (Washington University): Do you intend to use this technique mostly for the higher frequencies and use some other technique for the lower frequency range?

Mr. Kalbfleisch: Yes we use classical finite element modelling in the lower frequency region and we augment it with statistical energy analysis in the higher frequency region.

Mr. Mains: At what frequency do you distinguish between the two?

Mr. Kalbfleisch: 500 cycles, 1000 cycles and up, depending upon the frequency region where the primary ring frequency lies.

Mr. Wassman (Naval Ordnance Laboratory): Do you think that the dependence in the accuracy on modal density implies that a constant percentage bandwidth analysis is contraindicated and that perhaps a constant bandwidth analysis of a relatively broad bandwidth at low frequencies would yield better results with the statistical energy method? I realize that the reason for doing that was probably for your experimental data.

Mr. Kalbfleisch: We used a constant percentage bandwidth; as you use wider bandwidths you can get more modes in per band, I think the bandwidth is really dictated by the number of modes. You will have better accuracy if you use more modes in a bandwidth.

PREDICTION OF SHOCK ENVIRONMENTS BY TRANSFER FUNCTION MEASUREMENT TECHNIQUES

G. C. Kao, J. M. Cantril, G. D. Shipway
Wyle Laboratories, Scientific Services and Systems Group

and

M. A. Boyd
U. S. Army, Corps of Engineers
Huntsville, Alabama

The vertical shock environments of electrical power equipment cabinets supported by a shock-isolated platform were estimated. The mechanical impedances of the isolator system, and the mobilities of the platform and equipment cabinets were measured and used to determine the transfer function of the whole system under five different preload conditions of the isolators. An input shock spectrum and the system transfer function were then used to determine the vertical shock environments for each preload condition. Appreciable attenuation of the input energy was observed from 5 Hz to 50 Hz and moderate attenuation above 50 Hz.

INTRODUCTION

The objective of this paper is to demonstrate the application of transfer function measurement techniques to estimate the vertical shock environments of electrical equipment cabinets supported by a shock isolated platform. Specific emphasis was placed on the high-frequency energy transmission characteristics of the isolator system, and evaluation of such effects on the responses of the equipment. The computation of the shock environments was limited to the frequency range between 5 Hz and 500 Hz.

The transfer function of the whole system was obtained by combining the appropriate transfer functions of identifiable subsystems. The response data of the subsystems were measured and digitally reduced to compute the digital transfer functions. The obvious advantage of this technique is that it allows the synthesis of transfer functions of large, complex structures from the transfer functions of subsystems which are amenable to measurement techniques.

The system studied is shown in Figure 1. Basically, the system consists of three electrical equipment cabinets, which are bolted to the steel platform. The platform, in turn, is connected to four mechanical spring shock isolators through the end posts located at the four corners of the platform. The upper ends of the isolators are attached to a buried, reinforced concrete structure. The input motion, which is defined in terms of a shock spectrum as shown in

Figure 2, is transmitted through the upper attachment points (UAP) of the isolators. The corresponding responses at the platform/equipment interface defined the shock environments of the equipment cabinets.

In order to provide realistic estimates on system shock environments, it is necessary that both the nonlinear characteristics of the isolators and system structural damping be modeled accurately in formulating analytical solutions. However, it is often difficult, if not impossible, to obtain exact response solutions for a complex structural system, such as the present system. This is particularly true in the case where high-frequency vibrations are of prime interest.

The computation of shock environments was based on the transfer function technique employing measured transfer function data of individual elements to synthesize the system transfer function. The transfer functions establish the input/output relationships between the upper attachment points of the isolators and the load transfer points at the equipment/platform interface. The measured transfer function data automatically contains the information on structural damping. Consequently, computed responses will be more consistent with the system dynamic amplification effects.

The transfer function technique is valid for linear systems. To justify the validity of the linear analysis, it is assumed that the shock isolation system is linear with the isolator springs in a deflected position as long as the induced vibrations with respect to the deflected shock isolation

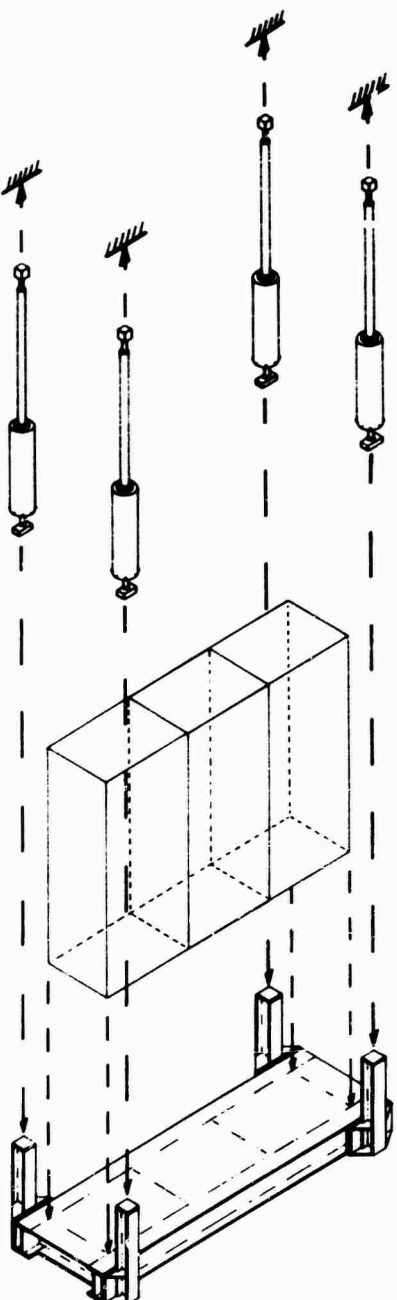


Figure 1. Exploded View of Shock Isolated Equipment Cabinets System

system position remain small. Toward this goal, the transfer functions of the isolators were measured under five different end constraints, representing the nominal, two intermediate and two extreme deflected conditions. The computed responses at the equipment/platform interface would thereby provide the response "trend" for the shock isolation system under the input shock motion.

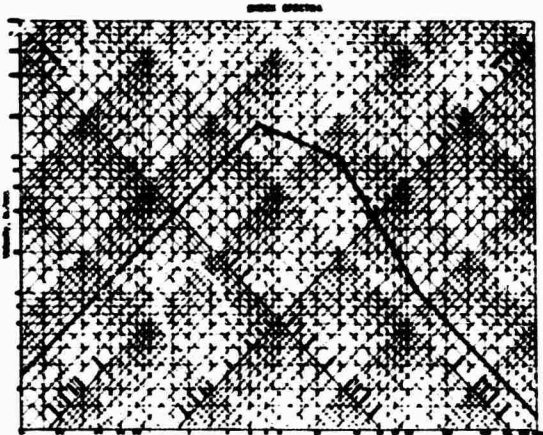


Figure 2. Undamped Vertical Input Shock Spectrum

DESCRIPTION OF THE SHOCK-ISOLATED SYSTEM

The shock-isolated system, as shown in Figure 1, employed four isolators having two different spring rates and designated as M-33 and M-34. The typical construction of an isolator is shown in Figure 3. The stationary part of these isolators consists of a cylindrical housing which contains the spring housing assembly and the pendant (3-1/2 in. O.D. steel tubing). The movable part consists of a coil spring, a one-inch diameter steel connecting rod and two circular retaining plates, which are used to precompress the spring to a predetermined length to fit within the spring housing. The upper retaining plate is fastened to the connecting rod. The lower retaining plate is fastened to the housing by a total of eight 3/8-inch cap screws. Therefore, the isolator spring is always in compression. One swivel joint is provided at each end of the isolator assembly to allow lateral movements of the system. The upper attachment point (UAP) and the lower attachment point (LAP) of the isolator are installed respectively to the ceiling structure of a building and the supporting platform. The approximate physical dimensions, weights and spring stiffnesses of the isolators are tabulated in Table I. The M-33 isolators are attached to the front end of the platform, and the M-34 isolators are attached to the rear end of the platform.

The overall dimensions of the supporting platform are 4 ft x 8 ft. The structural frame was fabricated from 12 in. wide flange (WF 27) beams; and a 3/8-inch steel plate was welded at the top. A total of eighteen 5/8-inch diameter holes were provided on the platform for anchoring the equipment cabinets.

The physical dimensions of each of the three equipment cabinets are 40 in. (wide) x 30 in. (deep) x 90 in. (high). Each side cabinet was connected to the center cabinet with a total of twenty bolts through the side panels. The total weight of the three cabinets is 6,779 pounds. The

front and rear views of the cabinets are shown in Figure 4, in which the cabinets are supported on the air springs in the process of testing.

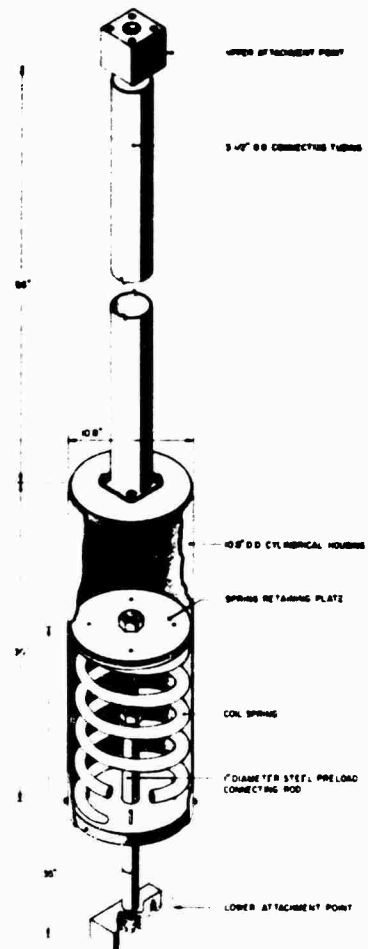
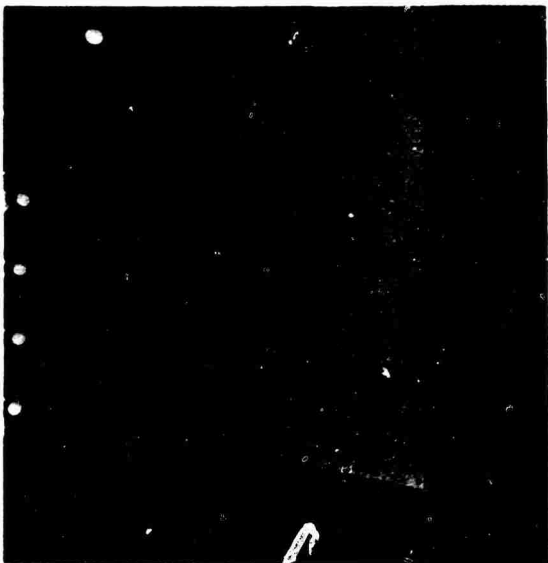


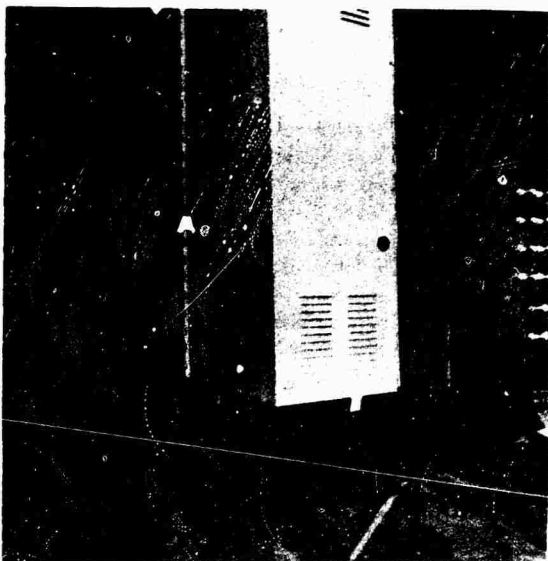
Figure 3. Typical Construction of a Shock Isolator

TABLE I
WEIGHTS AND STIFFNESSES OF ISOLATORS

Isolator Type	Weight (Lb)		Measured Static Stiffness* (lb/in.)
	Stationary Parts	Movable Parts	
M-33	133	56.0	355
M-34	133	36.5	275



(a) Front View of Cabinets



(b) Rear View of Cabinets

Figure 4. Front and Rear View of the Equipment Cabinets

SYNTHESIS OF SYSTEM TRANSFER FUNCTION

In formulating the transfer function model for the system under consideration, a set of load transferring points was assumed at the interface of adjacent subsystems to define the load paths of the entire system. Each subsystem consisted of a set of input points which received the incoming motion and a corresponding set of output points which transmitted the outgoing motion to its adjacent subsystem. The load transferring points of the isolator-platform-equipment are defined in Figures 5 through 7.

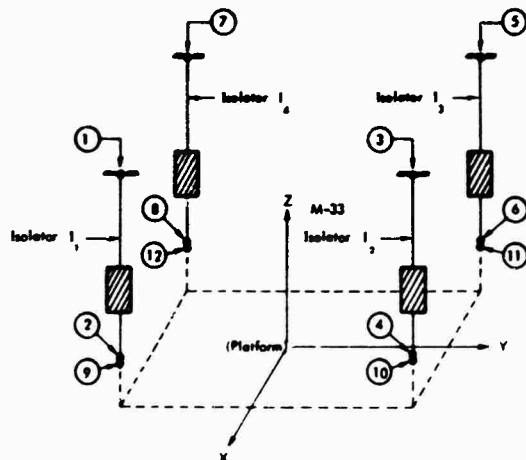


Figure 5. Isolator Load-Transferring Points

The load transferring points of the isolator are defined by the UAP's and LAP's of the individual units. Therefore, the four isolators have a total of eight load transferring points as shown in Table II. The locations and numbering of the platform load transferring points are shown in Figure 6 and summarized in Table III. Points 9, 10, 11 and 12 are located at the end posts and defined as the input points of the platform. These points receive the output motion from the lower attachment points of the isolators. The output points of the platform are transmitted through a total of ten load transferring points at the platform. These points are denoted as Points 13 through 22. The corresponding load transferring points of the equipment cabinets are designated as Points 23 through 32, as shown in Figure 7 and summarized in Table IV. These points received the output motion from the platform.

TABLE II
LOAD TRANSFERRING POINTS OF ISOLATOR

Isolator Type	Designation	UAP	LAP
M-33	1 1	1	2
	1 2	3	4
M-34	1 3	5	6
	1 4	7	8

Based on the load transferring points as defined above, the transfer function model of the shock-isolated system could be represented as shown in Figure 8.

The input and output motions of the individual systems are defined as follows:

TABLE III
DEFINITION OF FORCING FUNCTIONS AND
RESPONSES FOR PLATFORM MOBILITY MATRIX
(Reference: Figure 6)

Type of Excitation	Force Reference Axis	Load Application Points	Corresponding Response Measurement Points	Symbol for Forcing Function	Symbol for Response
Discrete Vertical Force	Z - Axis	9	9	F_9	V_9
		10	10	F_{10}	V_{10}
		11	11	F_{11}	V_{11}
		12	12	F_{12}	V_{12}
In-Phase Vertical Forces	Z - Axis	13, 20	13, 20	F_{13}	V_{13}
		14, 21	14, 21	F_{14}	V_{14}
		15, 22	15, 22	F_{15}	V_{15}
In-Phase Lateral Forces	X - Axis Y - Axis	20, 22	20, 22	F_{20}	V_{16}
		15, 22	15, 22	F_{15}	V_{17}
Moments Parallel to Y - Axis	Z - Axis	13, 20	13, 20	F_{13}	V_{18}
		14, 21	14, 21	F_{14}	V_{19}
		15, 22	15, 22	F_{15}	V_{20}
Moments Parallel to X - Axis	Z - Axis	16, 17	16, 17	F_{21}	V_{21}
		17, 18	17, 18	F_{22}	V_{22}
		18, 19	18, 19	F_{23}	V_{23}
Torque about Z - Axis	X - Axis	20, 22	20, 22	F_{20}	V_{24}

TABLE IV
DEFINITION OF FORCING FUNCTIONS AND
RESPONSES FOR EQUIPMENT MOBILITY MATRIX
(Reference: Figure 7)

Type of Excitation	Force Reference Axis	Load Application Points	Corresponding Response Measurement Points	Symbol for Forcing Function	Symbol for Response
In-Phase Vertical Forces	Z - Axis	23, 30	23, 30	F_{25}	V_{25}
		24, 31	24, 31	F_{26}	V_{26}
		25, 32	25, 32	F_{27}	V_{27}
In-Phase Lateral Forces	X - Axis Y - Axis	30, 32	30, 32	F_{28}	V_{28}
		25, 32	25, 32	F_{29}	V_{29}
Moments Parallel to Y - Axis	Z - Axis	23, 30	23, 30	F_{30}	V_{30}
		24, 31	24, 31	F_{31}	V_{31}
		25, 32	25, 32	F_{32}	V_{32}
Moments Parallel to X - Axis	Z - Axis	26, 27	26, 27	F_{33}	V_{33}
		27, 28	27, 28	F_{34}	V_{34}
		28, 29	28, 29	F_{35}	V_{35}
Torque about Z - Axis	X - Axis	30, 32	30, 32	F_{36}	V_{36}

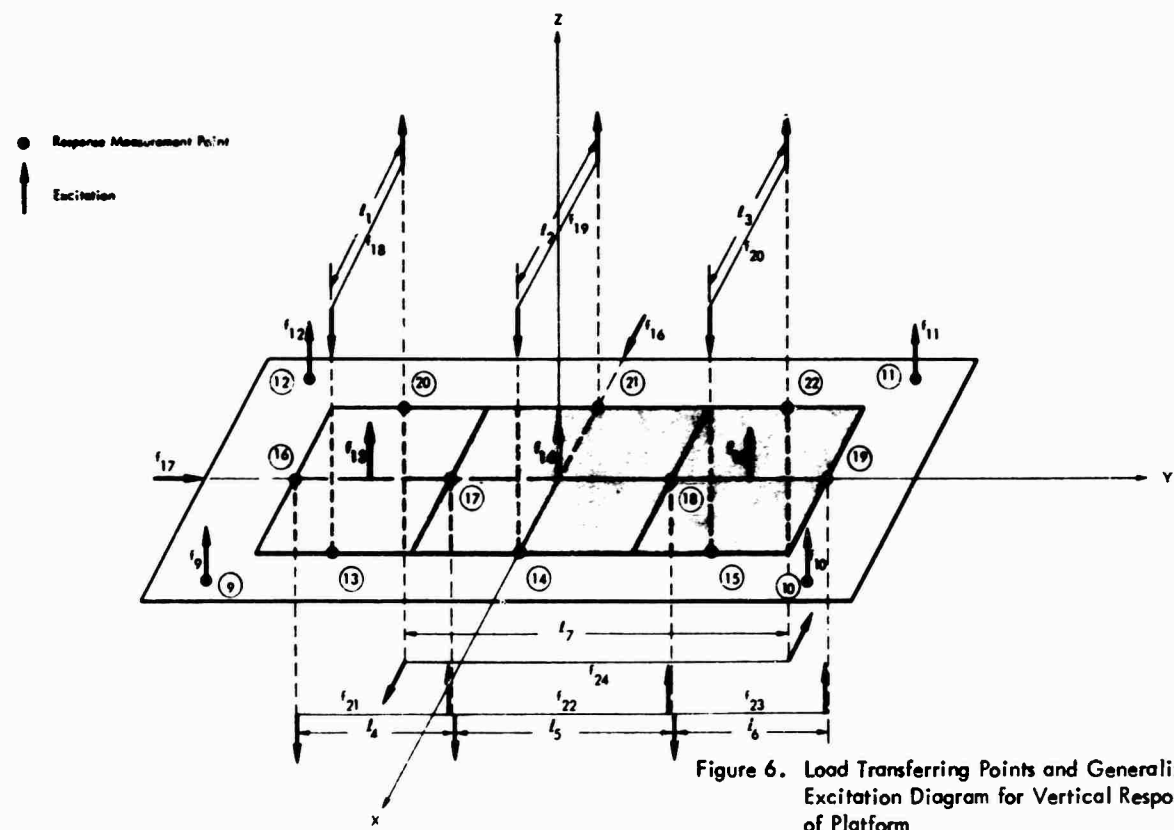


Figure 6. Load Transferring Points and Generalized Excitation Diagram for Vertical Response of Platform

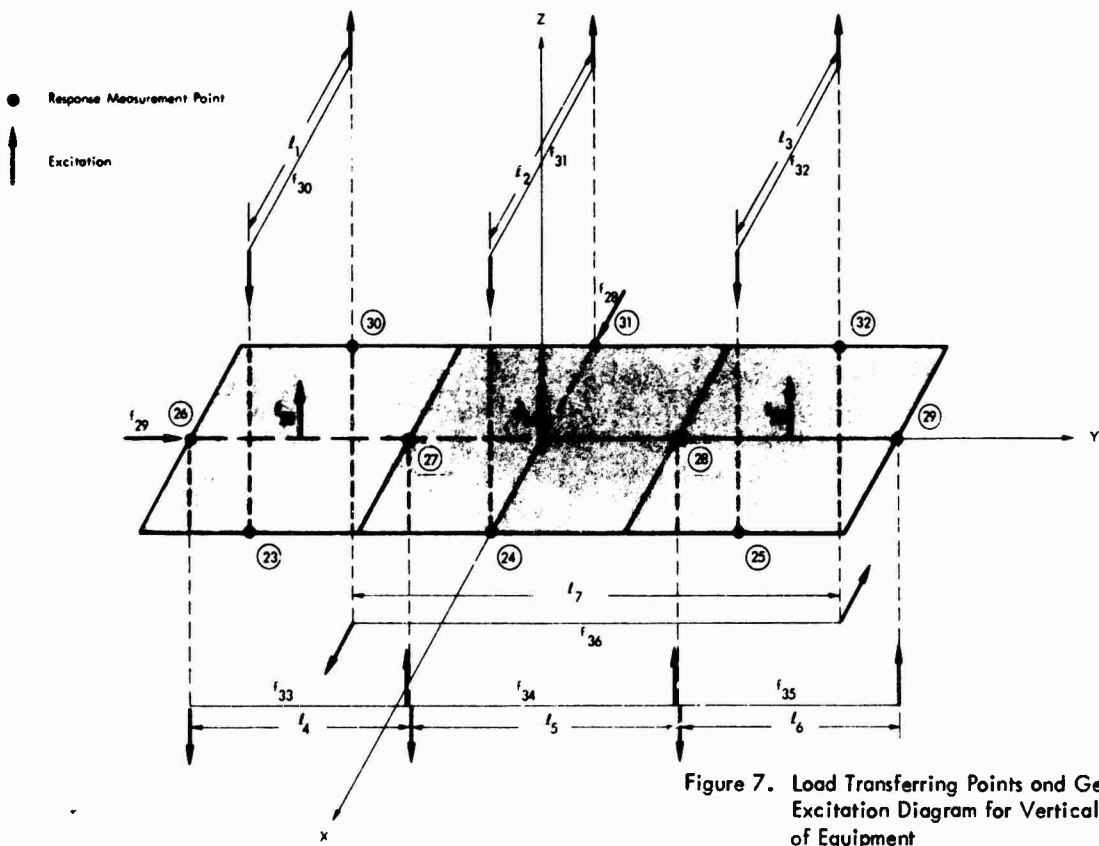


Figure 7. Load Transferring Points and Generalized Excitation Diagram for Vertical Response of Equipment

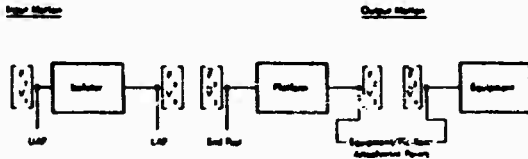


Figure 8. Transfer Function Models for the Isolator-Platform-Equipment System

Isolators F_1 = Input forces at the upper attachment points
 V_1 = Input motions at the upper attachment points
 F_2 = Output forces at the lower attachment points
 V_2 = Output motions at the lower attachment points

Platform \tilde{F}_2 = Input forces at the end posts
 \tilde{V}_2 = Input motions at the end posts
 F_3 = Output forces at the equipment/platform interface
 V_3 = Output motions at the equipment/platform interface

Equipment \tilde{F}_3 = Input forces at the equipment/platform interface
 \tilde{V}_3 = Input motions at the equipment/platform interface

Since measurements are generally made with accelerometers, the gravitational unit, g ($1 g = 386 \text{ in./sec}^2$), was adopted to specify motions at all load transferring points. The input or output points corresponding to a forcing function was referred to by a "station" number to identify forcing or response locations.

The transfer function of the isolators is defined by Equation (1) in terms of an impedance matrix:

$$\begin{bmatrix} f_1 \\ f_2 \\ f_3 \\ f_4 \\ f_5 \\ f_6 \\ f_7 \\ f_8 \end{bmatrix} = \begin{bmatrix} z_{11} & 0 & 0 & 0 & z_{12} & 0 & 0 & 0 \\ 0 & z_{22} & 0 & 0 & 0 & z_{34} & 0 & 0 \\ 0 & 0 & z_{33} & 0 & 0 & 0 & z_{36} & 0 \\ 0 & 0 & 0 & z_{77} & 0 & 0 & 0 & z_{78} \\ z_{21} & 0 & 0 & 0 & z_{22} & 0 & 0 & 0 \\ 0 & z_{43} & 0 & 0 & 0 & z_{44} & 0 & 0 \\ 0 & 0 & z_{45} & 0 & 0 & 0 & z_{66} & 0 \\ 0 & 0 & 0 & z_{87} & 0 & 0 & 0 & z_{88} \end{bmatrix} \begin{bmatrix} v_1 \\ v_2 \\ v_3 \\ v_4 \\ v_5 \\ v_6 \\ v_7 \\ v_8 \end{bmatrix} \quad (1)$$

The above input/output relationship of the isolator system is now written in simplified form as:

$$\begin{bmatrix} F_1 \\ F_2 \end{bmatrix} = \begin{bmatrix} z_{11} & z_{12} \\ z_{21} & z_{22} \end{bmatrix} \begin{bmatrix} V_1 \\ V_2 \end{bmatrix} \quad (2)$$

where the submatrices indicated by the dashed line in Equation (2) are equated to the correspondingly indicated submatrices of Equation (1).

The platform transfer function is defined in terms of a mobility matrix which is generated by four types of forcing functions defined as follows:

- Discrete vertical force
- Pair of equal-magnitude, in-phase, vertical forces
- Pair of equal-magnitude, in-phase, lateral forces
- Moment generated by a pair of equal-magnitude, vertical forces with 180° phase shift
- Moment generated by a pair of equal-magnitude, lateral forces with 180° phase shift

The forcing matrix consists of a total of sixteen input forcing functions. The definition of these forces and the corresponding responses are presented in Table III, and an illustration of each forcing function is presented in Figure 6. The relationship between the input forces and output responses of the platform is defined as follows:

$$\begin{bmatrix} \tilde{V}_2 \\ \tilde{V}_3 \\ \vdots \\ \tilde{V}_{24} \end{bmatrix} = \begin{bmatrix} m_{11,1} & \cdots & m_{11,12} & \cdots & m_{11,24} \\ m_{12,1} & \cdots & m_{12,12} & \cdots & m_{12,24} \\ \vdots & \vdots & \vdots & \vdots & \vdots \\ m_{13,1} & \cdots & m_{13,12} & \cdots & m_{13,24} \\ m_{14,1} & \cdots & m_{14,12} & \cdots & m_{14,24} \\ \vdots & \vdots & \vdots & \vdots & \vdots \\ m_{24,1} & \cdots & m_{24,12} & \cdots & m_{24,24} \end{bmatrix} \begin{bmatrix} \tilde{F}_2 \\ \tilde{F}_3 \\ \vdots \\ \tilde{F}_{24} \end{bmatrix} \quad (3)$$

Equation (3) is now also written in simplified form as:

$$\begin{bmatrix} \tilde{V}_2 \\ \tilde{V}_3 \\ \vdots \\ \tilde{V}_{24} \end{bmatrix} = \begin{bmatrix} \tilde{M}_{22} & \tilde{M}_{23} \\ \tilde{M}_{32} & \tilde{M}_{33} \end{bmatrix} \begin{bmatrix} \tilde{F}_2 \\ \tilde{F}_3 \\ \vdots \\ \tilde{F}_{24} \end{bmatrix} \quad (4)$$

where again the submatrices indicated by the dashed lines in Equation (4) are identified with the correspondingly indicated submatrices in Equation (3).

The equipment transfer function is also defined in terms of a mobility matrix. Since the platform shares the same load transferring points with the equipment at the interface, the forcing functions of the equipment are defined in a similar manner as those of the platform. These forcing functions and responses of the equipment are defined in Table IV and illustrated in Figure 7. The equipment mobility matrix is expressed as follows:

$$\begin{bmatrix} v_{25} \\ \vdots \\ v_{36} \end{bmatrix} = \begin{bmatrix} m_{25,25} & \cdots & m_{25,36} \\ \vdots & \ddots & \vdots \\ m_{36,25} & \cdots & m_{36,36} \end{bmatrix} \begin{bmatrix} f_{25} \\ \vdots \\ f_{36} \end{bmatrix} \quad (5)$$

and is rewritten as:

$$\begin{bmatrix} \tilde{v}_3 \end{bmatrix} = \begin{bmatrix} \tilde{M}_{33} \end{bmatrix} \begin{bmatrix} \tilde{f}_3 \end{bmatrix} \quad (6)$$

In the notation as used in Equations (2), (4) and (6), the relationship between the forcing function and the three subsystems can be rewritten in algebraic forms as follows:

Isolators:

$$F_1 = \mathcal{Z}_{11} V_1 + \mathcal{Z}_{12} V_2 \quad (7)$$

$$F_2 = \mathcal{Z}_{21} V_1 + \mathcal{Z}_{22} V_2 \quad (8)$$

Platform:

$$\tilde{V}_2 = \tilde{M}_{22} \tilde{F}_2 + M_{23} F_3 \quad (9)$$

$$V_3 = M_{32} \tilde{F}_2 + M_{33} F_3 \quad (10)$$

Equipment:

$$\tilde{V}_3 = \tilde{M}_{33} \tilde{F}_3 \quad (11)$$

where \mathcal{Z}_{ij} 's and M_{ij} 's are the impedances and mobilities of the systems under consideration.

The equilibrium and the compatibility equations at the attachment points are defined as follows:

$$F_2 = -\tilde{F}_2 \quad (12)$$

$$F_3 = -\tilde{F}_3 \quad (13)$$

$$V_2 = \tilde{V}_2 \quad (14)$$

$$V_3 = \tilde{V}_3 \quad (15)$$

From Equations (7) through (15), the relationship between V_1 and V_3 can now be established as:

$$V_3 = -\tilde{M}_{33} \cdot R_{32} \cdot (1 - \mathcal{Z}_{22} \cdot M_{22})^{-1} \cdot \mathcal{Z}_{21} \cdot V_1 \quad (16)$$

The transfer function between the upper attachment points of the isolator system and the equipment/platform interface is defined by Equation (17) as shown below:

$$T_{13} = -\tilde{M}_{33} \cdot R_{32} \cdot (1 - \mathcal{Z}_{22} \cdot M_{22})^{-1} \cdot \mathcal{Z}_{21} \quad (17)$$

$$\text{where } R_{32} = [M_{33} + \tilde{M}_{33}]^{-1} \cdot M_{32}$$

MEASUREMENT OF TRANSFER FUNCTIONS

The input forcing functions were generated by a pair of 25 force-lb electro-dynamic shakers (MB Model PM25). These shakers provided sinesweep input forces at the designated forcing input points on the test structures. All measurements were made over the frequency range of 5 Hz to 500 Hz with a sweep rate of one octave per minute.

The responses at the load transfer points of the test structures were acquired through piezo accelerometers. The instrumentation block diagram is shown in Figure 9.

The impedance elements associated with each isolator were measured under two restraining conditions. In the first case, the UAP of an isolator was fixed to a reaction mass so that the velocity at the fixed end was zero and the input force to the isolator was applied to the LAP. In the second case, the end restraining condition and the forcing input position were reversed. The measured force and response signals provided the data used to compute individual impedance elements. Using Isolator 1₁ as an example, the

measured impedances are defined by the following equations:

$$Z_{11} = \frac{f}{v_1} \Bigg|_{v_2=0} \quad (18)$$

$$Z_{22} = \frac{f}{v_2} \Big|_{v_1=0} \quad (19)$$

$$Z_{12} = Z_{21} = \frac{f}{v_2} \Big|_{v_1=0} = \frac{f}{v_1} \Big|_{v_2=0} \quad (20)$$

Figures 10(a) and 10(b) show the typical set-ups for measuring isolator impedances in the UAP-Fixed and LAP-Fixed conditions, respectively. At the driving end, the Endevco Impedance Head was used as the force transducer and an additional (2106E) piezo accelerometer was used to acquire the driving end response data. At the fixed end, the force signal was acquired through an Endevco Impedance Head. Each isolator was tested under five different preload conditions. The preloads were applied to the isolators by adjusting the length of the test fixture with a pair of spacers at the bottom. This allows the isolator under testing to be

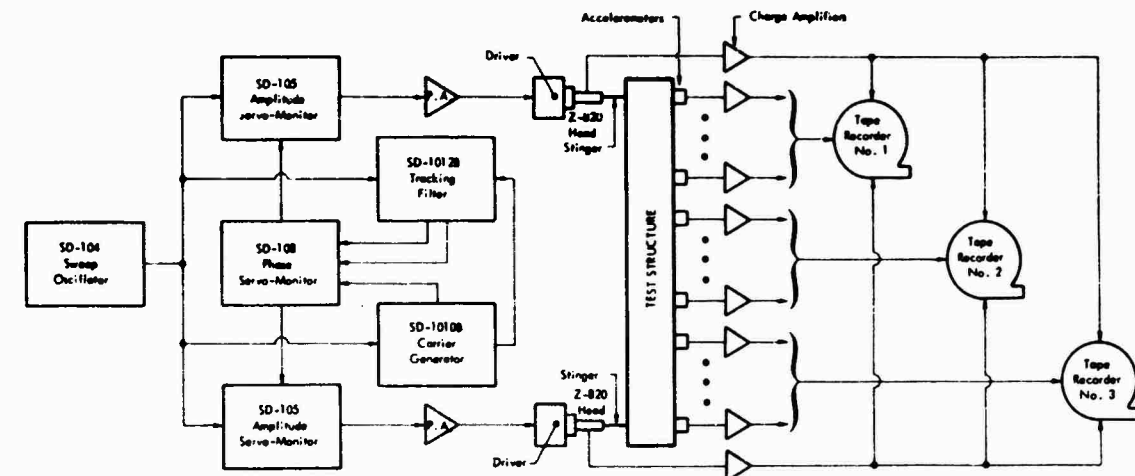
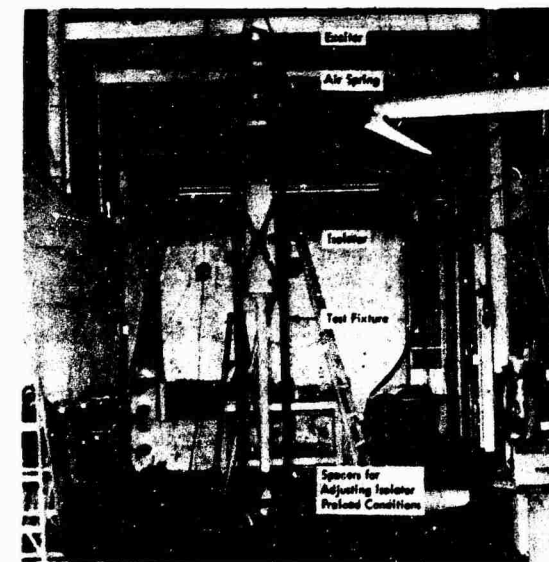
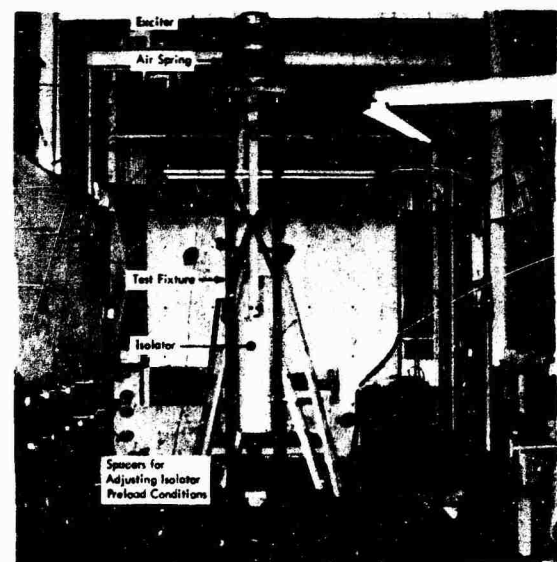


Figure 9. Typical Instrumentation Block Diagram for Response Measurements



(a) UAP-Fixed Condition



(b) LAP-Fixed Condition

Figure 10. Typical Test Set-ups for Isolator Impedance Measurements

either stretched or compressed. A total of five preload conditions as shown in Figure 11 was used in the measurements. Details of these conditions are described as:

- **Nominal Extension** — The isolator was stretched to a predetermined length which corresponds to the static deflection due to the combined weights of the equipment and the supporting platform. The stretched length was approximately 9 ~ 9.5 inches.
- **+8-Inch Extension** — The isolator was compressed to a position which was 8 inches above the nominal condition.
- **-8-Inch Extension** — The isolator was extended to a position which was 8 inches below the nominal condition.
- **Non-Extended** — The isolator was slightly stretched to provide just enough preload to perform the measurements.
- **Fully-Extended** — The isolator was stretched approximately 21 inches to create a fully compressed condition for the spring.

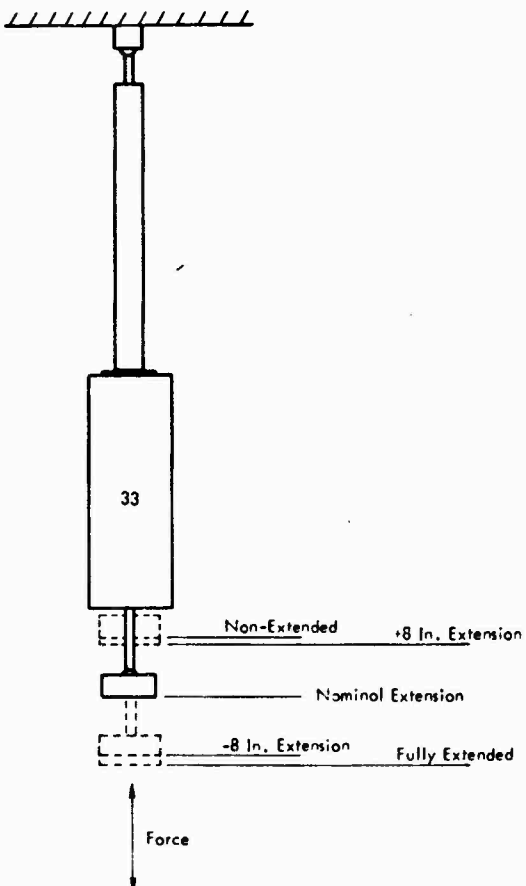
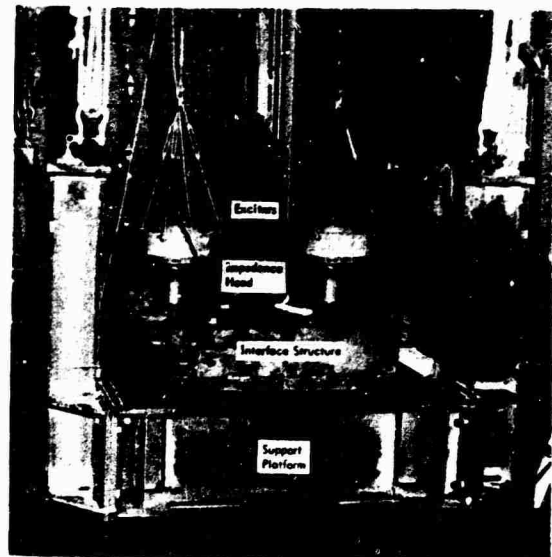
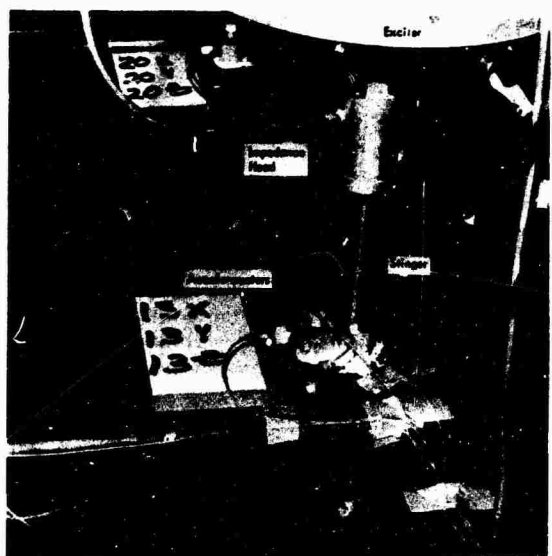


Figure 11. Isolator Preload Conditions

The platform mobility measurements were made based on the forcing functions, as defined in Table III employing two different kinds of supporting conditions. When discrete input forces were applied at the end posts, the platform was suspended by four air springs at its four corners. The exciter was suspended by three coil springs



(a) Test Set-up for Platform Measurement



(b) Close-up View of Exciter and Transducer Locations at the Platform

Figure 12. Typical Test Set-up for Measuring Platform Mobilities — Vertical Force Input of the Platform

which in turn were attached to a temporary fixture for support of the exciter. When two exciters were used to generate input motions, the platform was suspended by bungee cords at its four corners as shown in Figure 12(a). Notice that an interface structure used to simulate the dynamics of the base structure of the cabinet was welded to the platform. The addition of the interface structure was necessary in order to simulate the dynamic properties of the base structure of the cabinet. The weight of the platform was approximately 1800 pounds. The measurement errors attributed to the interface structure were considered as not significant enough to affect the final predicted responses. A close-up view of the exciter and transducers used in generating the vertical inputs in pairs is shown in Figure 12(b). The same bungee-cord supporting condition was used in measuring mobilities due to lateral forces applied along the X-X and Y-Y directions.

The measurements of equipment mobilities due to vertical input forces were made with the air springs supporting the system as shown in Figure 13(a). Lateral stability of the cabinets was provided by connecting the upper four corners of the cabinets with bungee cords to four anchoring points located inside the test facility, as shown in Figure 13(a). Figure 13(b) shows the configuration of a single exciter assembly.

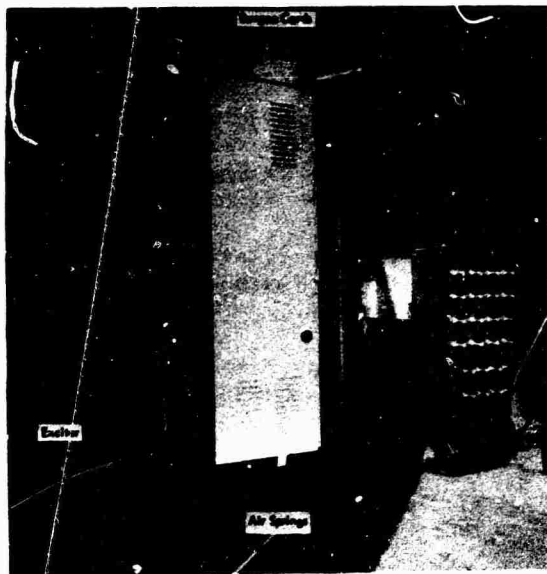
The measurement of equipment mobilities for input forces applied along the X-X and Y-Y directions were made by suspending the cabinets at their four upper corners on steel cables.

DATA REDUCTION

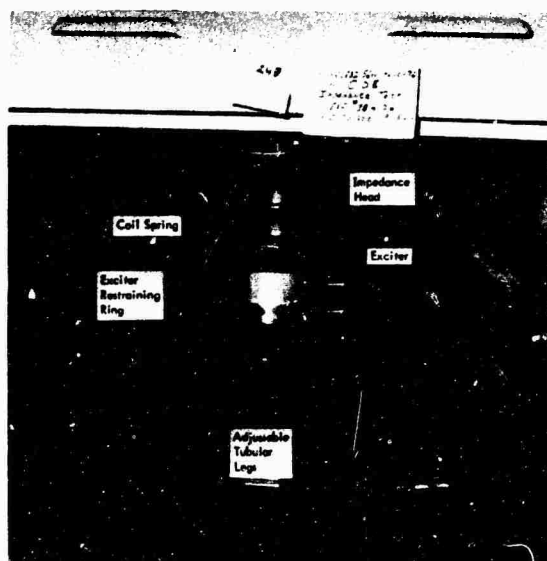
The data reduction effort consists of digitizing the recorded analog signals and analyzing the data to obtain impedance and mobility elements by a sinesweep analysis computer program. The analog to digital (A/D) data conversion was carried out by the data acquisition system described in Figure 14.

During the course of the data reduction process, it was discovered that the phase-shift errors between the odd and the even channels of the analog tape recorders used in measurement (recording and analysis playback) could not be adjusted mechanically to be within the specified tolerance limits. This problem was resolved by recording a 5 to 500 Hz constant amplitude sinesweep signal on all channels and obtaining numerically as a function of frequency the phase difference between each individual data channel and the frequency reference channel. A cubic polynomial for each data channel was obtained by a least squares fit to the phase differences and the polynomial used to correct the data at analysis time.

The most critical aspect of sinesweep data collection is controlling the data sampling rate. Sampling rate must be high enough to adequately define each cycle, but low enough to cover several cycles so that a statistical average over several cycles is available from the analysis. The method of controlling sampling rate in the present case is to divide the frequency range into a series of octaves (based on frequencies at integral powers of 2) and maintain a constant sampling rate in each octave; the sampling rate



(a) Test Set-up for Equipment Measurement



(b) Supporting Fixture for the Exciter

Figure 13. Typical Exciter Set-up for Measuring Equipment Mobilities — Vertical Force Input

in each octave is chosen to give at least 20 samples per cycle at the beginning of each octave and 10 samples per cycle at the end.

The frequency sweep rate during test is set on a logarithmic scale (base 2) such that a fixed number of octaves are covered per unit time. A set of digital data is taken at constant time intervals after the start of the sweep from the

recorded analog force and acceleration responses of the specimen and the frequency reference channel, and is stored on digital magnetic tape by means of the computer driven analog/digital conversion system. The data sets are comprised of 200 15-bit samples from each of the recording analog channels with the data from the force and acceleration channels taken in alternating sequence so that a known time relationship is maintained between samples from which the phase relationship between force and acceleration may be obtained. Ideally the samples should be taken simultaneously from each channel but the multiplexing A/D channels through one sample and hold amplifier in the configuration of Figure 14 prevents this. The significance of the constant time interval between sets of sampled data is that the intervals in frequency increase logarithmically, thus giving a typical resolution of better than 2 Hz at 50 Hz and a resolution of about 12 Hz at 500 Hz.

The acquisition of the raw digital sinesweep data was accomplished in four major steps. The first step was an amplitude calibration run to insure proper transmission of the analog signal to the Sigma 5 computer and proper identification of data channels. The second step was the acquisition of a 5 Hz to 500 Hz sinesweep signal to determine the phase relations among the data channels. The third step consisted of calibration runs to obtain sensitivities for the later analysis. The final step was the acquisition of the raw test data.

Analysis of the sinesweep data consists of determining the frequency, the amplitude, and the phases of the force and acceleration responses for each set of data recorded during the test. The frequency is determined from the frequency reference channel by calculating the auto-correlation function of this channel at enough positive lag points to cover just over one cycle. A quadratic interpolation procedure is used to find the time lag of the second

maximum in the auto-correlation function and this time is the period of the signal.

The force and acceleration amplitudes and phase are determined from the cross-correlation of the force and acceleration channels and the auto-correlation of the force channel. Again, quadratic interpolation is used to find values of maxima and minima and the times at which they occur. The auto-correlation of the force channel is used to give the force amplitude and the cross-correlation of the two channels yields the amplitude of the acceleration and the phase between the two channels. It should be noted that it is not adequate in calculating amplitudes simply to take mean square values (i.e., auto-correlation at zero lag) since the data does not, in general, have zero mean. Amplitudes are determined by taking the difference between a maximum and minimum on the auto-correlation and cross-correlation curves. Phase is determined from the lagged time at which the first positive maximum occurs, this is converted to a ratio by dividing by the overall period for this data set and the resulting fraction is multiplied by 2 to produce the phase angle, adjusted for quadrant according to the acceleration leading or lagging the force. A fixed phase shift between force and acceleration is introduced by the sampling process and must be corrected during the analysis. The phase shift is the equivalent of a half sample interval shift in time between the two channels. A further noteworthy point is the effect of the cross-correlation calculation between force and acceleration; this has the effect of suppressing the uncorrelated noise in the two transducers and also serves to suppress higher harmonics which may be excited in the structure.

Impedance or mobility magnitude is then obtained by taking the appropriate ratio of force and acceleration amplitudes.

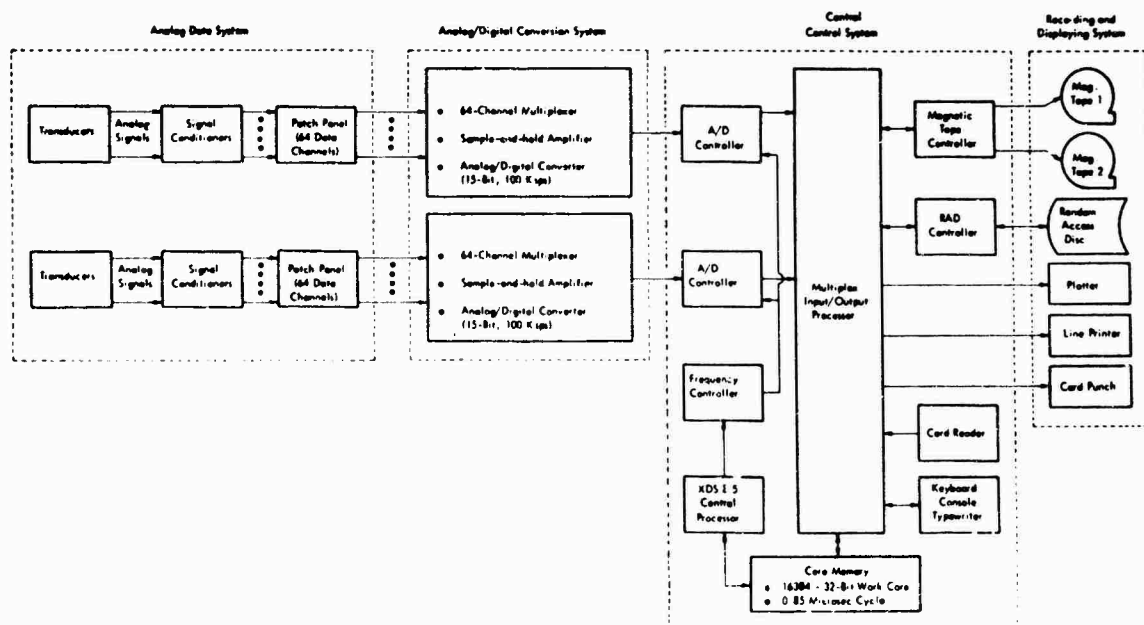


Figure 14. Block Diagram of the Analog/Digital Data Acquisition System

COMPUTATION OF SHOCK ENVIRONMENTS

The original impedance and mobility elements were defined by approximately 500 frequency intervals over the frequency range between 5 Hz to 500 Hz. Since the exact starting and terminating frequencies used in measurements varied between test runs, the frequency intervals obtained from different sinesweep runs were not the same. Therefore, a set of standard frequency intervals was needed for performing response computations. The standard frequency intervals were defined on a 3% constant percentage bandwidth, and a total of 180 frequency intervals were used to convert analyzed impedance and mobility elements by interpolation techniques.

The magnitudes of input impedance and mobility data were checked against the analog input impedance plots, and the phases of these quantities were checked by the known phase information of a single-degree-of-freedom system. Necessary corrections were made on detected deviations for each element prior to the computation of shock environments.

The computation of shock environments at the platform/equipment interface was based on Equation (17).

A total of twenty isolator impedance measurements were made according to the test requirements as outlined previously. The analog velocity input impedance plots of M-33 and M-34 isolators is presented in Figures 15 and 16, respectively.

Generally speaking, the majority of the measured data appear to be valid for frequencies above 40 Hz. Signals below 15 Hz were dominated by the electronic noise of the measurement system and no information in this frequency range was obtained. The measured dynamic stiffnesses of the isolators vary from a minimum of 10,000 lb/in. to a maximum of 200,000 lb/in. These values do not represent the actual stiffnesses of the isolators, rather, they represent the longitudinal stiffnesses of the isolator assemblies with the coil spring firmly pressed against the wall of the circular cylindrical housing. The high stiffnesses were caused by the buckling of the coil springs inside the housing. The resulting frictional forces between the springs and the walls were of such high magnitudes as to prevent any movements of the springs under the low amplitude excitations of the electro-dynamic exciters.

The longitudinal stiffness of each isolator assembly may be estimated to be the sum of the stiffness of the upper tubing, the cylinder and the rod. The approximate stiffness of individual elements was computed to be 141,300 lb/in.

This value approximates the maximum measured data, i.e., 200,000 lb/in.; and the slippage between the spring and the housing might account for the reduction of dynamic stiffness as measured during testing, as shown in the +8 in. case of Figure 16.

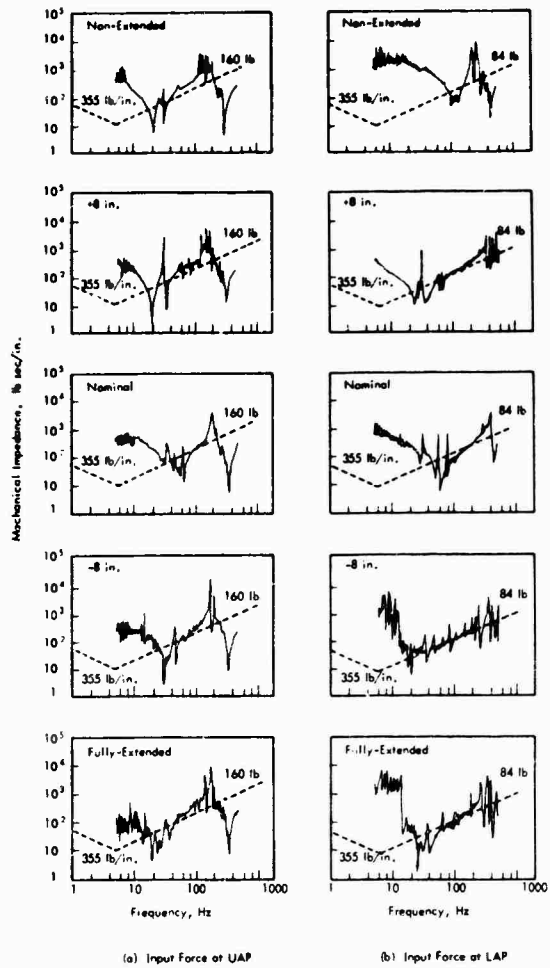


Figure 15. Comparison of Input Velocity Impedances of Isolator M-33

In order to correct the low frequency isolator data, a single-degree-of-freedom system was used to generate impedances between 5 Hz to 60 Hz. The upper frequency of 60 Hz was chosen on the basis that the majority of the impedance curves approach their respective mass lines at approximately 60 Hz. Therefore, the computed mass lines represent valid data for the measured system.

The equations used to compute the input and transfer impedances are expressed by Equations (21) and (22), respectively, as follows:

$$Z_i = C + j \left(m\omega - \frac{k}{\omega} \right) \quad (21)$$

$$Z_t = C - \frac{jk}{\omega} \quad (22)$$

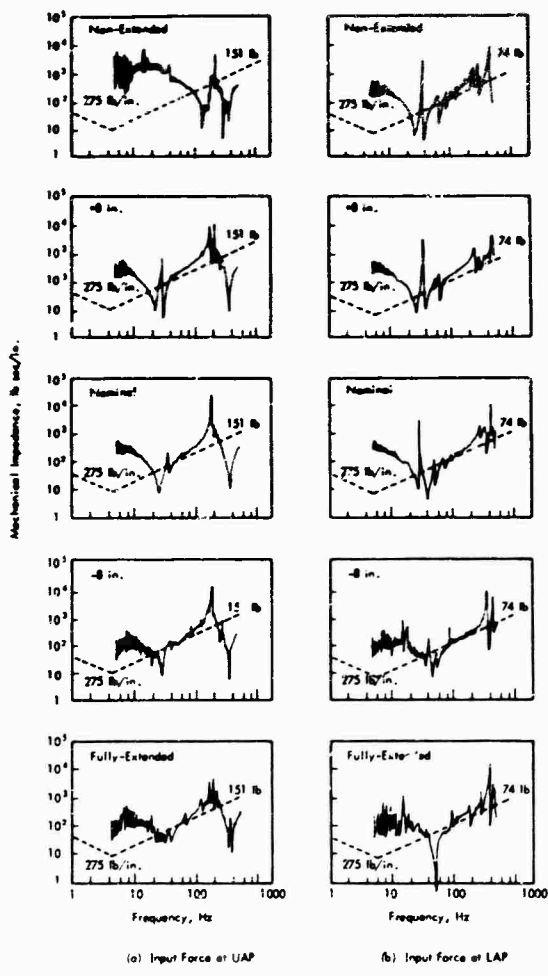


Figure 16. Comparison of Input Velocity Impedances of Isolator M-34

The values assigned to the mathematical models of the M-33 and M-34 isolators are tabulated in Table V.

TABLE V
ISOLATOR MODEL PARAMETER VALUES

Isolator Type	Force Input	k (lb/in.)	C (lb-sec/in.)	ζ (..)
M-33	UAP	355	9.95	160
	LAP	355	9.95	84
M-34	UAP	275	6.2	151
	LAP	275	6.2	74

In general, results on the input mobility data of the platform and the equipment are considered excellent; but, significant electronic noise levels are observed in transfer mobility data. This problem is attributed to the low-level force inputs and can be corrected with more powerful excitors.

The fundamental frequency of the platform is 27 Hz. Major resonances also occur between the frequency range of 80 Hz and 500 Hz. These frequencies can be identified from the input mobility plots such as shown in Figure 17.

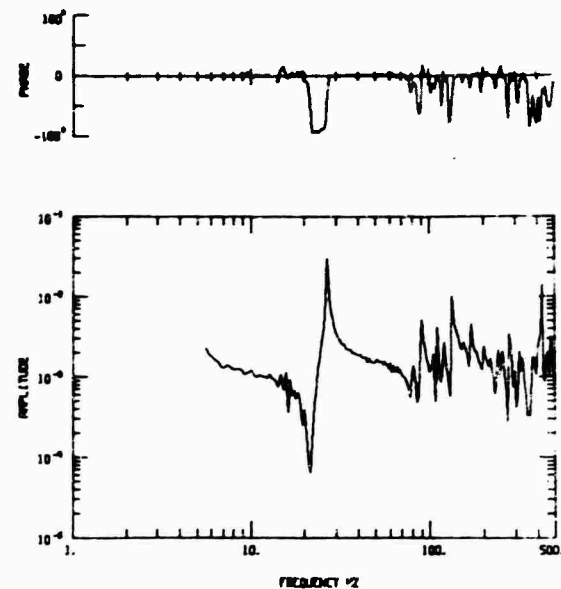


Figure 17. Acceleration Input Mobility of Load Transfer Point

The major resonant frequencies of the cabinets occur between 120 Hz and 400 Hz. These frequencies can be observed from the input mobility plots such as shown in Figure 18.

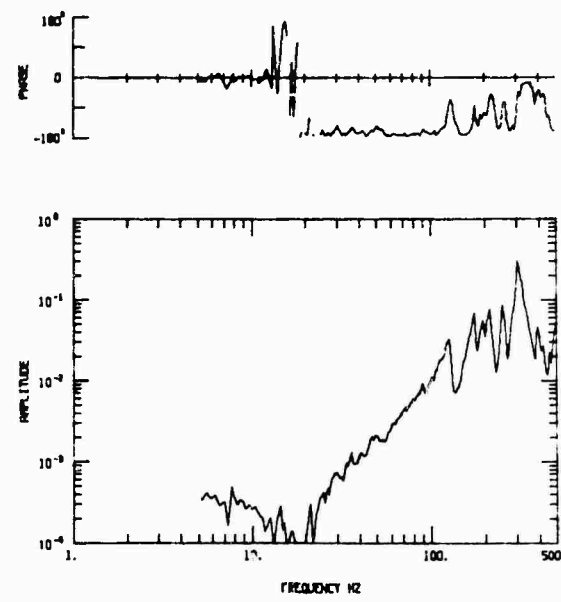


Figure 18. Acceleration Input Mobility of Load Transfer Point

The computation of shock spectra at Load Transfer Points 13, 14 and 15 was based on the input motion as defined by Figure 19. The corresponding time-history of the shock spectrum was obtained through the waveform synthesization program (NWAWSYN, Reference 1). This time-history was further transformed into the frequency domain by a Fast Fourier Transformation (FFT) computer program. The Fourier Spectrum plot of the input motion is shown in Figure 20. The responses at Load Transfer Points 13, 14 and 15 were computed by Equation (23) as follows:

$$G_3(\omega) = T_{13}(\omega) G_1(\omega) \quad (23)$$

where G_3 = Acceleration Frequency Response of Equipment Cabinet

G_1 = Input Acceleration at the Isolator UAP as shown in Figure 19

T_{13} = Acceleration Transfer Function as defined in Equation (17)

The measured impedance and mobility matrices are not symmetrical. The computations of the system transfer function, T_{13} , for each of the isolator preload conditions were based on the modified symmetrical matrices derived from their original ones by replacing each element in the upper off-diagonal part of the matrix with that of the corresponding element in the lower off-diagonal part of the matrix.

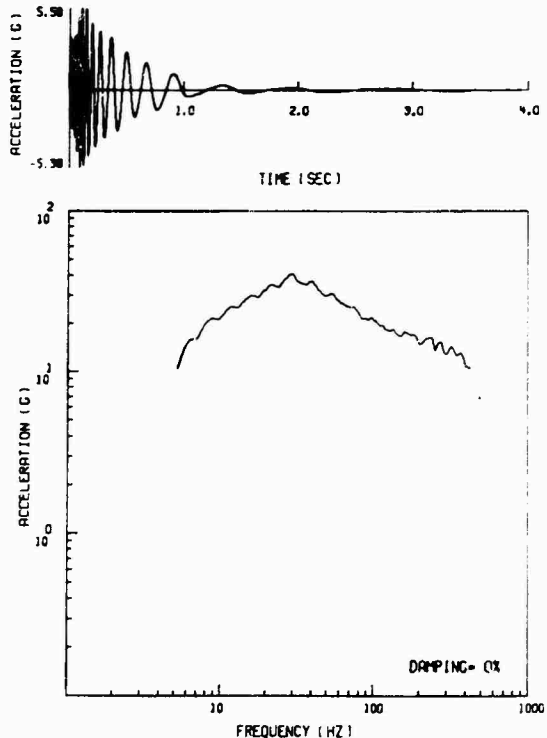


Figure 19. Time-History and Shock Spectrum of the Input Floor Motion

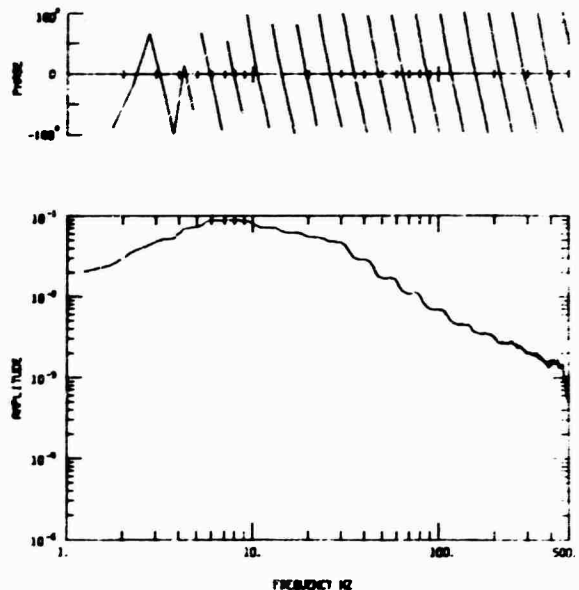


Figure 20. Fourier Spectrum of the Input Motion

The time-motion history corresponding to each element in the G_3 matrix was obtained by inverse transforming the frequency spectrum by the following equation:

$$G_3(t) = \int_{-\infty}^{\infty} G_3(\omega) e^{-i 2\pi \omega t} d\omega \quad (24)$$

The output shock spectrum with a zero initial displacement condition is computed based on Equation (25) as follows (Reference 2):

$$Y_3(t) = 2\zeta \omega_n \int_0^t G_3(\tau) e^{-\zeta \omega_n (t-\tau)} \cos \omega_d (t-\tau) d\tau \quad (25)$$

where $\omega_n = 2\pi f_n$ = Natural frequency

$\omega_d = 2\pi f_d$ = Damped natural frequency

ζ = Damping factor

The shock spectra at Stations 13, 14 and 15 under the five preload conditions of the isolators are shown in Figures 21 through 25.

The computed shock spectra at Stations 13, 14 and 15 are summarized and results are presented in Figure 26, which was obtained by overlaying individual spectrum plots. In addition, the shock spectra, representing respectively the input motion from the ceiling and the mean shock spectrum of the nominal case are also presented.

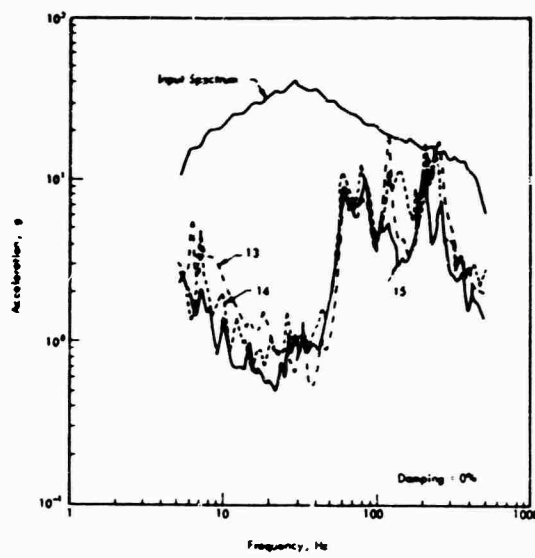


Figure 21. Vertical Shock Spectra —
Non-Extended Case

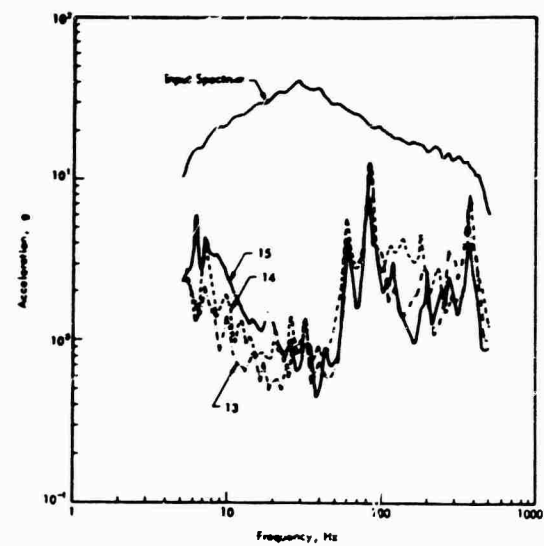


Figure 23. Vertical Shock Spectra —
Nominal Case

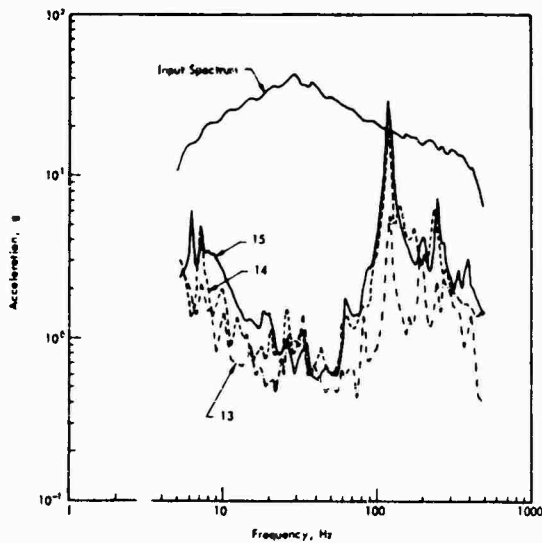


Figure 22. Vertical Shock Spectra — (+8 in.)

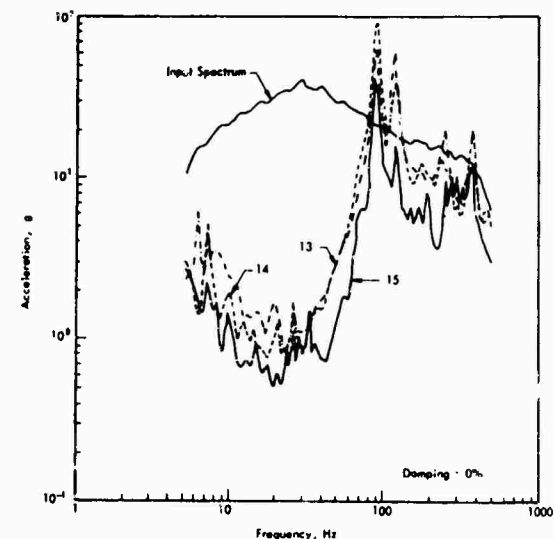


Figure 24. Vertical Shock Spectra — (-8 in.)

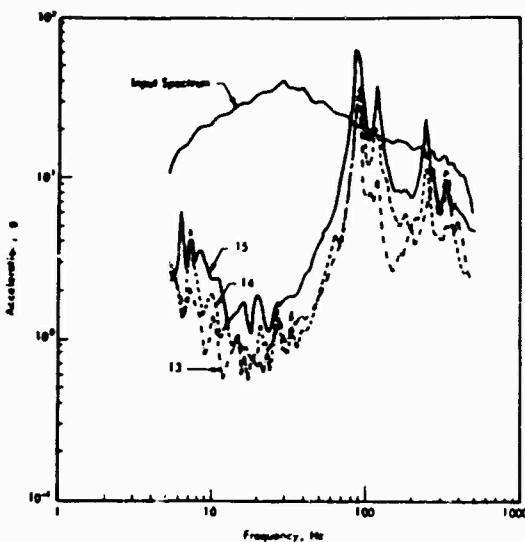


Figure 25. Vertical Shock Spectra — Fully Extended Case

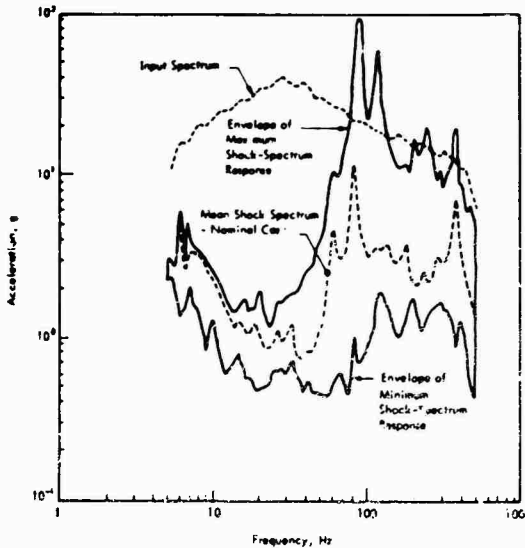


Figure 26. Summary of Shock Environments at Stations 13, 14 and 15

It can be observed that the shock isolating system is quite effective in attenuating input energy for frequencies below 50 Hz. But the results also show moderate attenuation in input energy for frequencies above 50 Hz. The high-frequency amplification effects are more pronounced for the "minus 8 inch" and the "fully extended" conditions, as shown in Figures 24 and 25, respectively. Such phenomena are attributed to the excessive buckling of the coil spring inside the canisters and the secondary high-frequency input due to subsequent "rubbing" effects between the coils and the walls of the canisters. The amplified responses at 90 Hz, 110 Hz, 270 Hz and 400 Hz, as shown in Figure 26, indicate that such pronounced "rubbing" problems might prevail under actual conditions. The amplified portions are limited to the -8" and the full-extended cases.

Finally, the mean nominal spectrum is approximately equal to the arithmetic mean between the two extremes of the spectrum envelopes for the portion below the input spectrum. Therefore, the spectrum representing the nominal condition could be used to estimate mean shock environments for systems with similar arrangements.

CONCLUSIONS

The conclusions drawn from the results of this program are summarized as follows:

- The feasibility of applying digital transfer function measurement techniques to predict responses of complex structural systems has been demonstrated. The approach is particularly well adapted for the prediction of high frequency responses. Its limitations are confined to the capability of the exciter system to provide adequate low frequency (1Hz - 20 Hz) excitations and the capability of the data acquisition system to provide adequate signal-to-noise ratios during analog recording and during the subsequent playback to the computer. Low frequency excitations could be improved by employing electrohydraulic excitors or eccentric mechanical excitors rather than electrodynamic excitors.
- The isolators are effective in attenuating input motion for frequencies below 50 Hz; moderate attenuation of high-frequency input motion is also observed.
- Under fully-extended conditions, the spring is at its solid height. The isolators would generate secondary high-frequency inputs to the equipment due to the "rubbing" phenomena between the coil springs and the canister walls.
- The worst shock environments occur at the extremes of isolator motion (i.e., the -8" and the fully-extended conditions). Should the isolators ever reach these extremes, all the available rattle space would be used. Such a condition would be beyond the scope for which the isolators are intended.

ACKNOWLEDGMENTS

The work reported herein was supported by the Corps of Engineers, Huntsville Division, under Contract No. DACA-87-72-C-0040. The authors are indebted to Professor R. Plunkett of the University of Minnesota for his technical advice in formulating this problem, to Mr. C. Huang of Corps of Engineers, Huntsville, Alabama, for his support and comments during this program, and to Mr. A. Jolly for his assistance in computer programming.

REFERENCES

1. U.S. Army Engineer Division, Huntsville, Alabama, "Safeguard BMD System, Modification of the WAVESYN Computer Program," Document No. SAF-82, 30 April 1971.
2. Kelly, R.D. and Richman, G., "Principles and Techniques of Shock Data Analysis," The Shock and Vibration Monograph Series, SVM-5, SVIC, 1969.

DISCUSSION

Mr. DeCapua (Bell Telephone Laboratories): It appears that you have a pendulum configuration with your equipment in isolators. Have you considered the problem of the large laterally induced displacements in the low frequency operating environments?

Mr. Kao: Yes. We proposed a prediction of both the vertical and the lateral environments, however because of funding we were unable to complete the lateral phase of the program. It can be done, we have prepared all the test programs and the analytical methods.

Mr. DeCapua: It seems that the main problem would be the large excursions and the possible collisions with adjacent equipment and walls.

Mr. Kao: It is the rattle space that is of concern.

Mr. Davis (Hughes Aircraft Co.): Would you comment on the effect of the stiffness of the cabinets at the higher frequencies?

Mr. Kao: I think it is a very difficult problem to describe because at high frequencies the mobility plot doesn't appear to strictly follow the stiffness line, it more or less follows a mass line. We suspend the cabinets by air bags so any stiffness has to be evaluated based on the peaks and notches in a mobility plot, and we have that data available.

Mr. Fritz (General Electric Co.): If I understand you correctly, you took the spectrum and transformed it to a time history and then did your solution with the time history, and this circumvents problems of phasing between modes. But since the spectrum did not have phasing information how do you anticipate getting correct phasing between modes when the phasing information is not present in the first place?

Mr. Kao: Converting the shock spectrum into a corresponding time history is a very crude method because once we derive the shock spectrum the phase information is lost. The method that we used to crank out the time history seems to be the only one available; in the future if

there is a better method we might use it, but for the present we have to stick with the non unique type of transformation.

Mr. Fritz: Have you tried to steer your time history to recover some of that uncertainty?

Mr. Kao: No.

Dr. Mains: There is a publication of the ASME on mechanical impedance methods applied to shock and vibration where there is a fairly complete disclosure of how to do this with complex transfer functions, and account for phase.

Mr. Kao: If you measure the mechanical impedance there is no problem of keeping track of phase. The question was how do we convert the time history from the shock spectrum and there the phase information is totally lost.

Mr. Sepcenko (The Boeing Company): It is not possible to convert a shock spectrum into a pulse, however certain approximations exist whereby one can fit a shock spectrum with a few pulses and it is a trial and error procedure.

Mr. Kao: It is. The basic mathematics involved in converting a shock spectrum into an equivalent time history is a trial and error process. The Wavesyn method that we used is one approach, I think Sandia also has another approach that uses damped sine waves, and there is another one developed by Bechtel using so called spectrum modification techniques. So in all there must be four or five techniques that have been developed to solve a problem of this kind, but as we realize they do not have a unique one to one type of correspondence. You could pin it down a little more precisely but you might have to describe the peak G value that you are looking for together with the time duration that is required. That would bring about more stringent requirements on certain time history motions.

Dr. Mains: I would like to call your attention, in the sake and interest of purity, to the fact that he was measuring mobility not impedance.

DETERMINATION OF GUIDEWAY ROUGHNESS FROM CONSTRUCTION TOLERANCES

B. J. Brock
Vought Systems Division
ETV Aerospace Corporation
Dallas, Texas

This paper describes a technique whereby the roughness PSD of a guideway can be estimated from the construction tolerances. A sample calculation is included and the significance of various types of irregularities is discussed.

INTRODUCTION

Ride quality has been identified as a prime factor in the passenger acceptability of future mass transportation systems. Many of these systems are envisioned as high-speed vehicles operating on dedicated guideways. There are two main areas that impact the ride quality of such vehicles: the vehicle suspension system and the guideway roughness (or, if you prefer, smoothness). Total systems costs must be minimized if these new transportation systems are to be economically feasible, thus vehicle suspension system sophistication (and cost) must be traded off against guideway cost. Generally, the guideway construction and maintenance costs will increase with increased demands for accuracy, and a few dollars extra cost per mile of guideway adds up in a hurry. Therefore, construction and maintenance requirements must be established in a form compatible with surveying and construction practice so that guideway costs can be accurately estimated and traded off against vehicle suspension sophistication.

The problem of maintaining satisfactory ride comfort becomes ever more difficult as vehicle speed increases. Richardson, et al [1] have shown that the general form of a roughness PSD can be approximated by

$$S(\Omega) = \frac{A}{\Omega^2} \frac{\text{ft}^2}{\text{rad}/\text{ft}} \quad (1)$$

Where $S(\Omega)$ is the roughness PSD, Ω is the spatial frequency in rad/ft , and A is the guideway roughness parameter in feet. The temporal frequency corresponding to Ω for a vehicle moving over the guideway at a velocity V is

$$\omega = V \cdot \Omega \quad \text{or,} \quad \Omega = \omega/V \quad (2)$$

The expression for the guideway power spectrum now becomes

$$S(\omega) = \frac{\sqrt{2}A}{\omega^2} \frac{\text{ft}^2}{\text{rad}/\text{ft}} \quad (3)$$

If we further convert the units to $\text{ft}^2/(\text{rad}/\text{sec})$ by noting that $\text{rad}/\text{sec} = V \times \text{rad}/\text{ft}$ we obtain

$$S(\omega) = \frac{\sqrt{VA}}{\omega^2} \frac{\text{ft}^2}{\text{rad}/\text{sec}} \quad (4)$$

The PSD of the vehicle response is determined by the product of the vehicle transfer function and the guideway roughness PSD, and the rms of the response is the square root of the integral of the vehicle response PSD. Therefore, the vehicle response rms increases as the square root of the forward velocity. Target speeds for ground transportation vehicles are currently in the 300 mph range and undoubtedly will be even higher in the future so that the problem of guideway roughness/smoothness will become ever more acute.

Now, it is relatively easy to determine a maximum allowable guideway roughness PSD for operation of a given vehicle over a certain speed range. Unfortunately, surveyors and construction contractors are not accustomed to building to tolerances expressed in the form of allowable PSD of roughness. A method is described in this paper by which allowable roughness PSD can be translated into the form of usual construction tolerances.

TECHNICAL APPROACH

The current trend is to use power-spectral-density (PSD) techniques to evaluate ride quality of transportation vehicles. This is a logical step because guideway roughness is basically random in nature although there may also be discrete frequency components in the irregularities associated with joint spacings and the like.

A straightforward approach capable of step-by-step intuitive checking was adopted for this first cut analysis. Briefly, samples of random guideway were generated by mathematical simulation and the resultant samples were analyzed as though they were digitized, measured data.

CALCULATION OF POWER SPECTRAL DENSITY

The basic definition of a power spectral density is given by the relation

$$S(\Omega) = \lim_{N \rightarrow \infty} \frac{1}{N} \int_0^N e^{-i\Omega x} f(x) dx / 2 \quad (5)$$

However, this definition does not lend itself to convenient analysis of digitized data, so one of two alternate definitions is usually used. One is to take the Fourier transform of the autocorrelation function and the other is given by

$$S(\Omega) = \lim_{B \rightarrow 0} \lim_{N \rightarrow \infty} \frac{1}{BN} \int_0^N f^2(x, \Omega, B) dx \quad (6)$$

where B is the bandwidth of a "perfect" filter with a center frequency Ω , and $f(x, \Omega, B)$ is $f(x)$ "filtered" through the

bandwidth B . This relation is often approximated by dropping the limits so that an estimate of the power spectrum is obtained from

$$S(\Omega) = \frac{1}{BN} \int_0^N f^2(x, \Omega, B) dx \quad (7)$$

The reader is directed to one of the excellent references (e.g. [2]) available for further discussions of power-spectra and their properties. Also, the philosophical questions surrounding the replacement of a function defined over an infinite time with one defined over a finite time will not be addressed here. Suffice to say, all three definitions of PSD mentioned above were evaluated and the last one (equation 7) seemed to converge most rapidly and to be the most stable. For this reason it was chosen for the studies to be described in this paper. It has the further advantage that it is the most intuitive of all the definitions and thereby readily lends itself to intuitive checking and insight.

Numerical Filtering

The implementation of a numerical technique to evaluate the integral of equation 7 required the use of a frequency filter. A digital band-pass filter was formulated based on the Nyquist-Kotelnikov-Shannon sampling theorem as described in [3]. The form of the filter is shown below.

$$f(x, \Omega, B) = \sum_{j=-\infty}^{\infty} \frac{f(x_j)}{\pi x_j} \left\{ \sin\left[\left(\Omega + \frac{B}{2}\right)x_j\right] - \sin\left[\left(\Omega - \frac{B}{2}\right)x_j\right] \right\} \quad (8)$$

Here again we are faced with the problem of infinite limits. This problem was investigated empirically by checking the

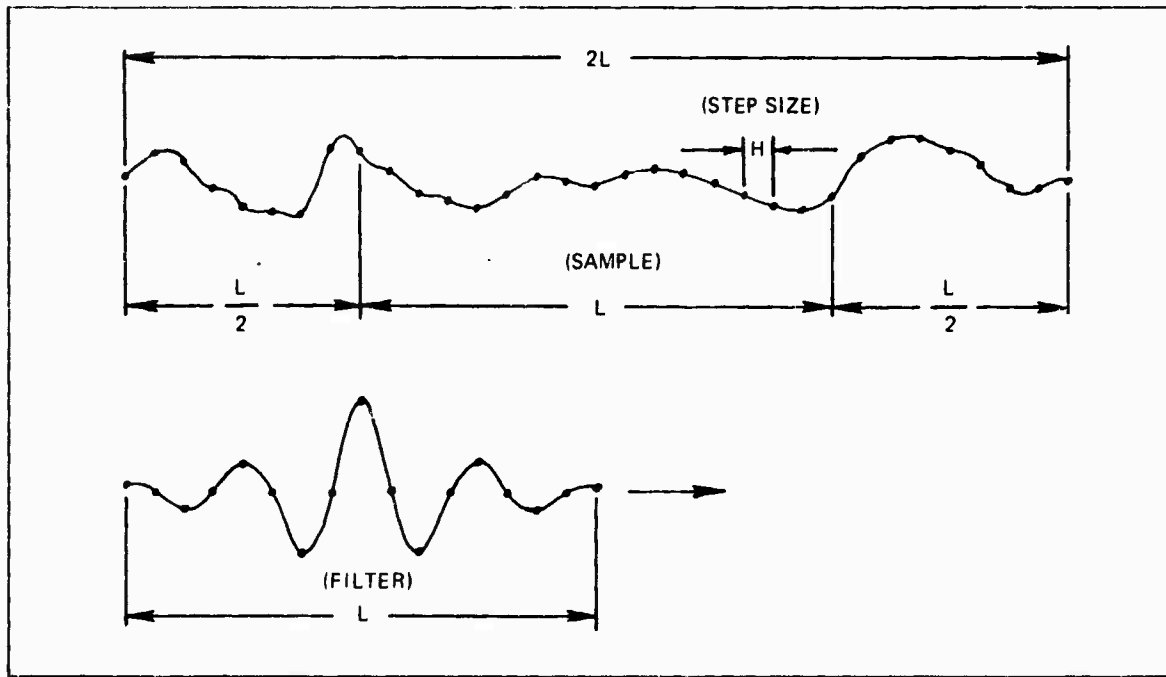


Figure 1. Numerical Filtering

sharpness of the cut-off of a sine function as the nondimensional sample length (normalized on the period of the sine function) was increased. It was concluded that a sample length of ten times the longest wave-length of interest was sufficient to achieve adequate filtering. A sample length twice the length of the sample to be analyzed was generated and the "inner" half was analyzed. This process is illustrated in Figure 1. The filtering action is achieved by (1) multiplying the filtering function and the sample to be filtered together term by term, (2) summing the result, (3) shifting the filter function "over" one step, and repeating (1) and (2) at each point for the entire sample. The resultant function is squared at each point, integrated numerically, and divided by the product of the bandwidth and the sample length to obtain a point on the PSD curve.

CHOICE OF WAVE LENGTH LIMITS

The wave length range chosen was based on an apparent frequency range of 0.5 Hz to 40 Hz for a vehicle operating over the hypothetical guideway at 300 mph. This covers the range from just above the kinetosis (motion sickness) range at one end of the scale to the acoustic range on the other. The wave length and frequency are related by $\lambda = V/f$ which results in a wave length range from 880 feet to 11 feet. These were rounded off to 900 feet and 10 feet for convenience. The cut-off frequency for digital signals is determined by the step size (h), specifically, $f_{\text{cut off}} = V/2h$. Therefore, a step size of 5 feet was chosen to achieve a cut-off frequency of approximately 40 Hz.

MATHEMATICAL MODELING OF GUIDEWAY ROUGHNESS

The guideway irregularities were broken down into various types of construction inaccuracies. The types of inaccuracies considered and the magnitudes of the deviations were chosen based on (1) the AASHO* Standard Construction tolerances, (2) various highway construction specifications and civil engineering tabs, and finally (3) consultation with members of the academic community and representatives of construction firms. The amplitudes of the various types of inaccuracies were obtained by generating random numbers with prescribed statistical properties. The random numbers were generated with routines from the IMSL† package [4]. (A note of caution to those who are inclined to pursue analyses of this nature. The family of random numbers generated must be random in their sequence (noncorrelated) as well as random in their amplitude distribution.)

Information about the distribution of amplitudes of deviations within construction tolerances is very slender indeed and, for this reason, both normal (Gaussian) probability density distributions with the standard deviation set equal to one-third of the construction tolerance and uniform

probability density distributions with the limits of plus and minus the construction tolerances were evaluated. The "DC" component was eliminated by correcting the amplitudes to a least squares straight line of zero. That is, a least squares line for the generated guideway sample was calculated and subtracted out to eliminate any residual zero frequency component.

It was assumed that the various components of the guideway roughness were independent (the cross power spectra are zero) so that each component could be considered separately and a composite spectra obtained by adding contributions of each component together.

GUIDEWAY CONSTRUCTION INACCURACIES

The various types of construction inaccuracies used in the analysis of this paper are described below. The objective was to identify and define a specific type of inaccuracy that would result from a given process, surveying, setting of piers, screeding, or the like.

Guideway Misalignment with Random Walk

Guideway misalignment with a random walk deviation is the type of irregularity resulting from a surveying inaccuracy that would result from each reference point being set relative to the preceding point. A variation (not evaluated) would be to set two or more points from a single level set point. The resultant irregularity is illustrated in Figure 2. The δ 's are the point-to-point deviations from the ideal. This is considered to form the baseline curve, and all of the other irregularities are superimposed on it.

Guideway Simple Misalignment

Guideway simple misalignment is defined as inaccuracies in setting the level of the guideway from the surveyed level. The resultant irregularity is illustrated in Figure 3. The δ 's are deviations from an ideal straight line.

Joint Misalignment

Joint misalignment is defined as mismatches between adjacent guideway sections. This irregularity is illustrated in Figure 4. The δ 's are the heights of joint discontinuities measured from an ideal straight line.

Guideway Waviness

The guideway waviness is defined as the "dips" and "humps" resulting from guideway pouring and finishing inaccuracies. This irregularity was represented by half-wave-length sine curves with random amplitudes. Three different wave length waviness irregularities were considered; that is, wave lengths of twice, equal, and one-half the length of a guideway section. These irregularities are illustrated in Figure 5. These were designated first, second, and third order waviness respectively.

* Association of American Highway Officials

† International Mathematical and Statistical Libraries

(These types of irregularities represent a preliminary choice and should not be considered the only ones possible.)

The reader is encouraged to improve on them or develop others if he engages in this sort of analysis.)

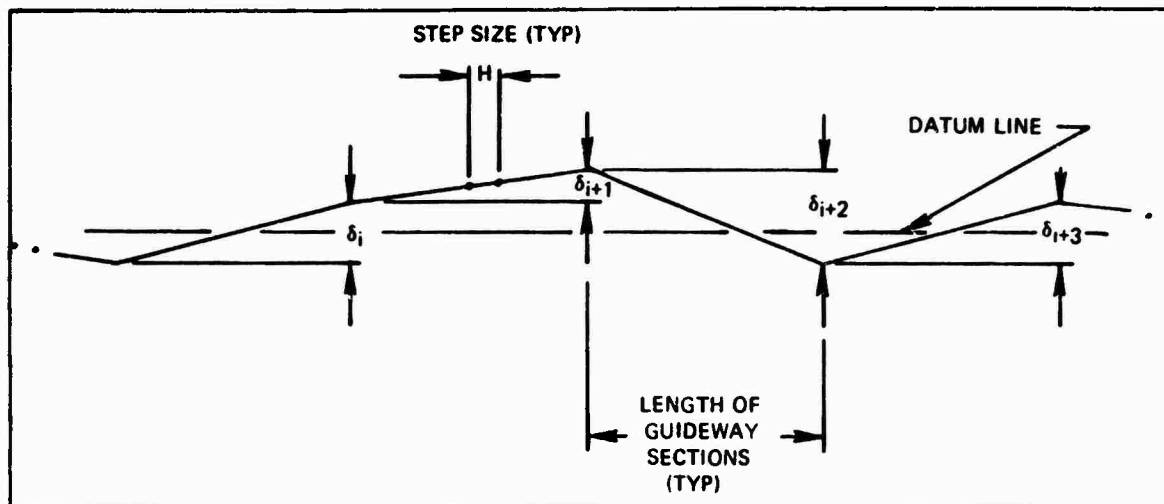


Figure 2 Guideway with Random Walk Irregularity

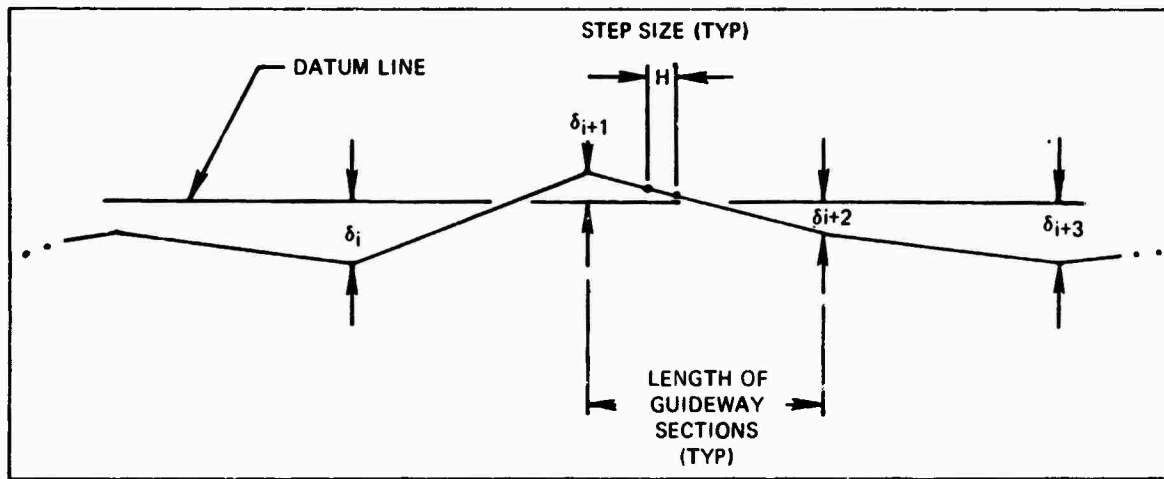


Figure 3 Guideway with Simple Misalignment Irregularity

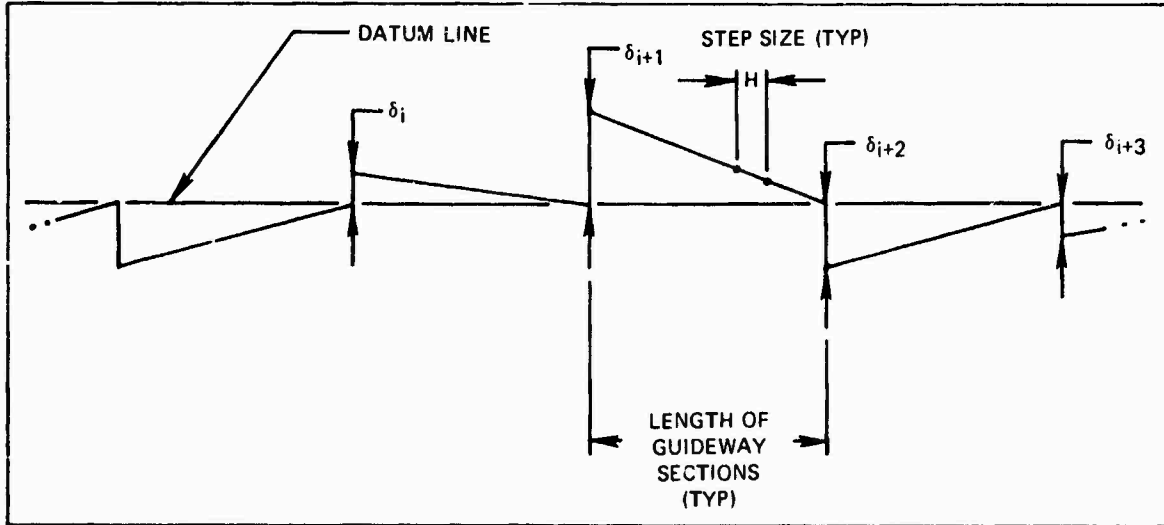


Figure 4 Guideway with Joint Misalignment Irregularity

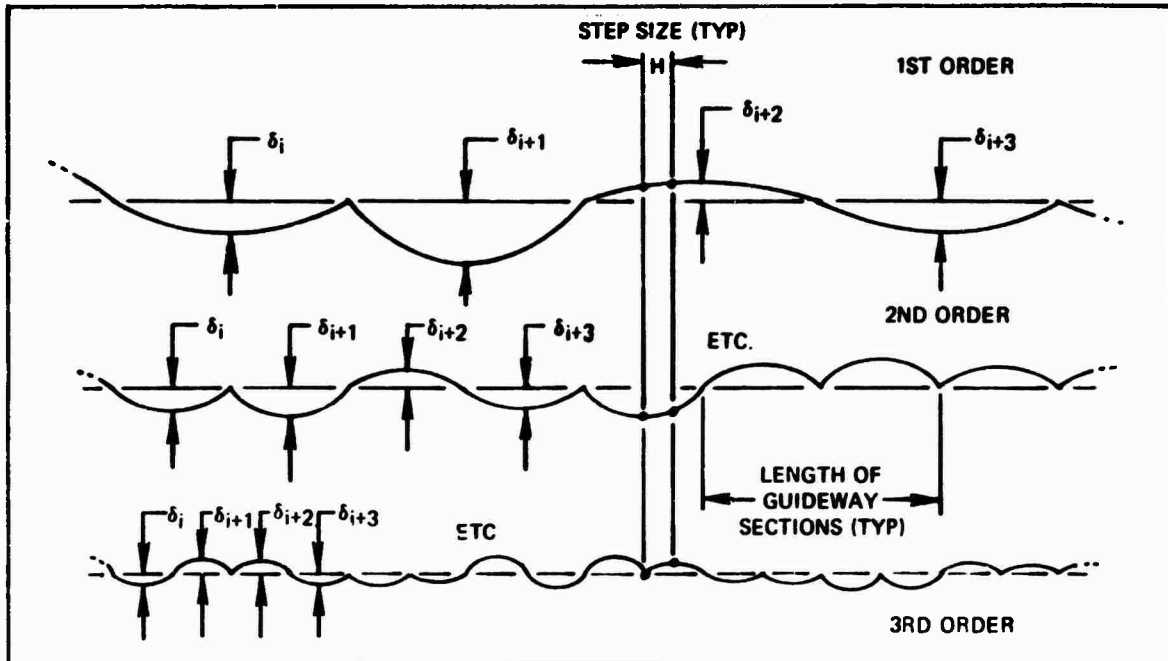


Figure 5 Guideway with Waviness Irregularities

GUIDEWAY ROUGHNESS PSD'S

PSD's of guideway roughness for the various components contributing to the overall roughness described above were calculated for a unit amplitude of a one-foot tolerance. The PSD for any other tolerance amplitude can then be obtained by multiplying the "unit amplitude" PSD by the square of the tolerance in feet. The guideway section length was chosen as 100 feet and the total sample length was set at 9000 feet (which means the total sample length generated was 18,000 feet so that the inner half could be analyzed).

UNIT AMPLITUDE PSD'S

The influence of the probability density distribution (normal versus uniform) on the roughness PSD is illustrated on Figure 6. It was found that characteristics were very similar except that the PSD's for the uniform probability distribution was roughly a factor of three (plus or minus ten percent point-to-point) greater than the corresponding PSD's for the normal probability distribution. The normal distribution seems more intuitively attractive, so the remainder of the PSD curves presented on Figures 7 through 12 are those based on normal probability distributions.

The purpose of this paper is to describe the approach to this problem; the solutions presented here are for illustration only. The guideway misalignment with random walk tolerance appears to be the single most important parameter in determining the guideway roughness, especially in the low frequency range. The other irregularities have various characteristics, with the joint discontinuity and higher order waviness irregularities tending to fill in the higher frequency ranges.

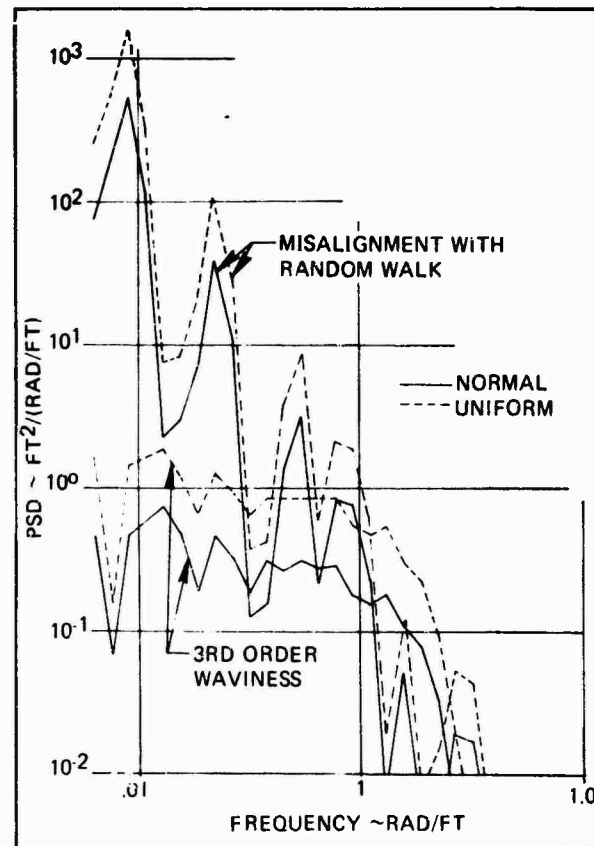


Figure 6. Comparison of PSD's Obtained Using Normal and Uniform Probability Density Distributions for Construction Tolerances

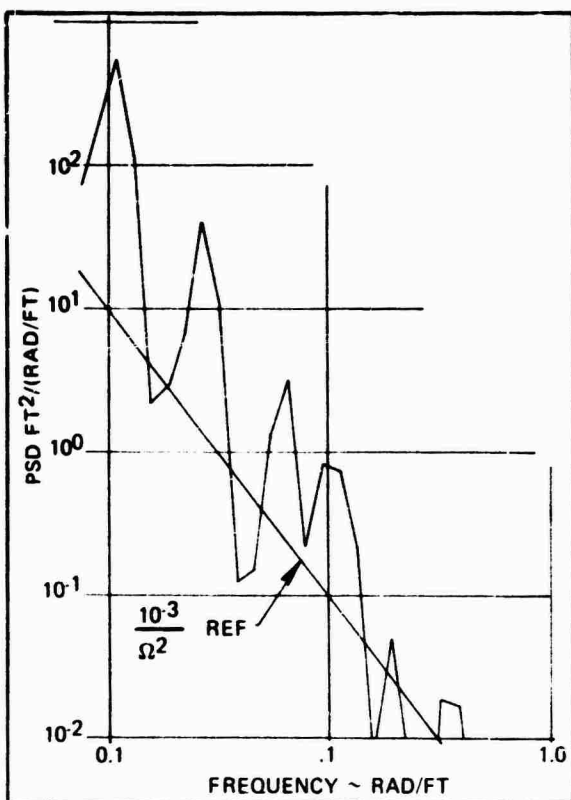


Figure 7 PSD of Guideway with Random Walk Misalignment

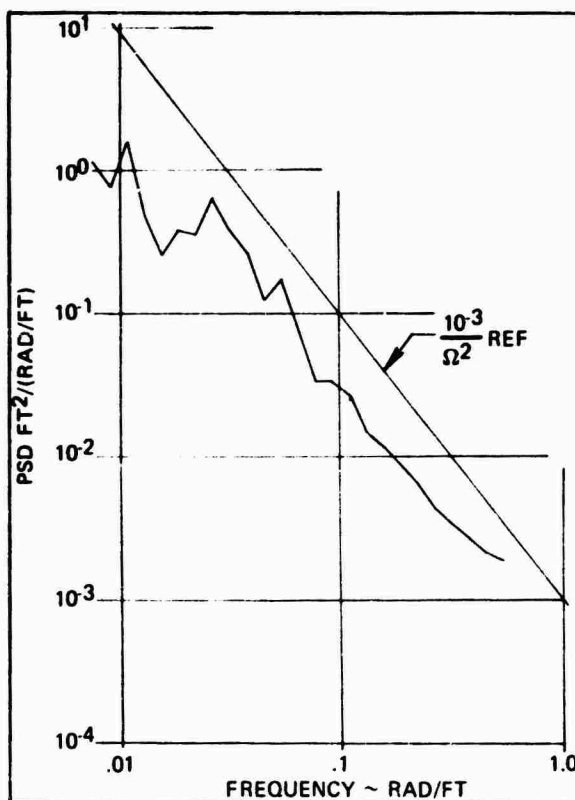


Figure 9 PSD of Guideway with Joint Discontinuities

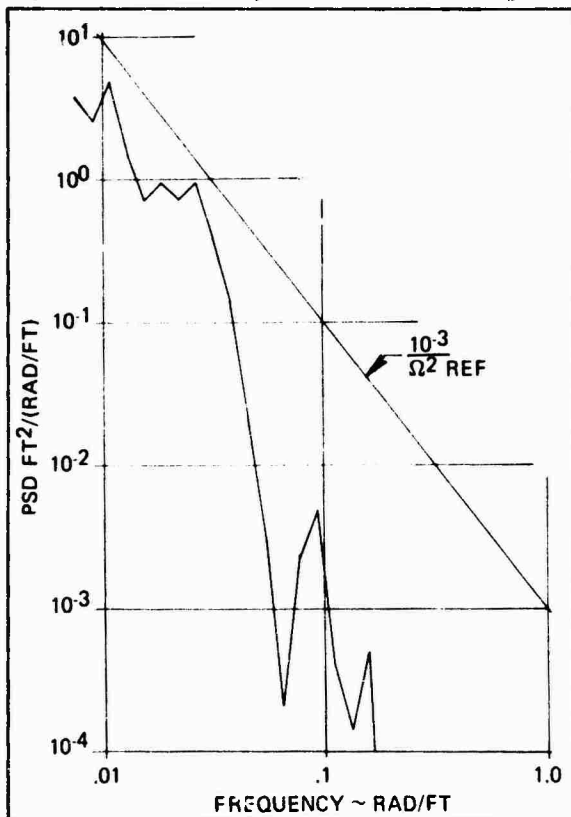


Figure 8. PSD of Guideway With Simple Misalignment

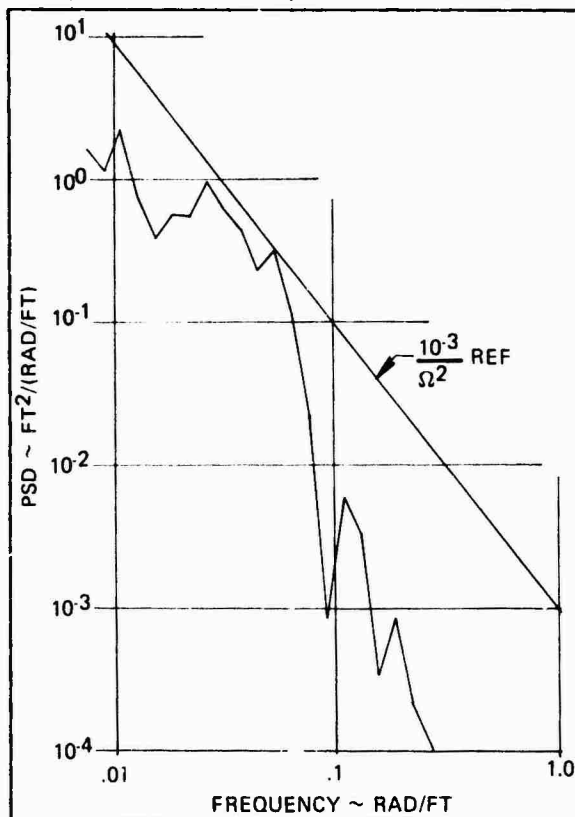


Figure 10 PSD of Guideway with 1st Order Waviness

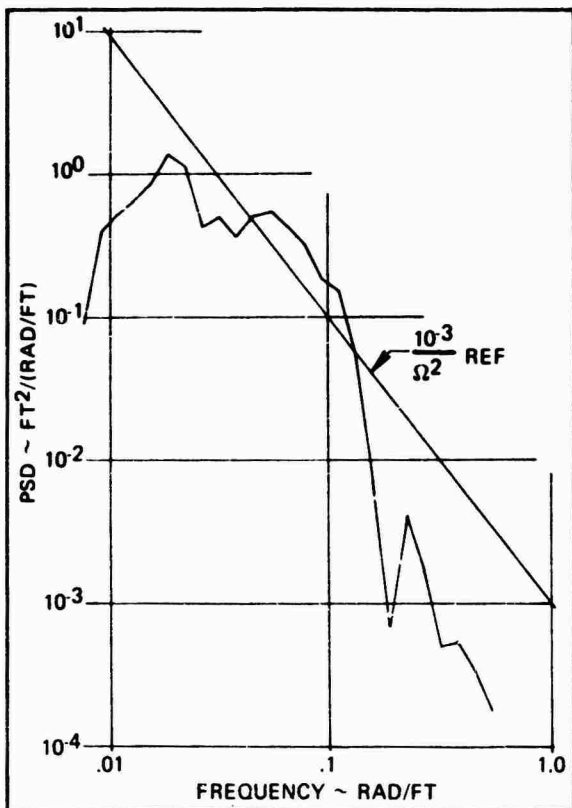


Figure 11 PSD of Guideway with 2nd Order Waviness

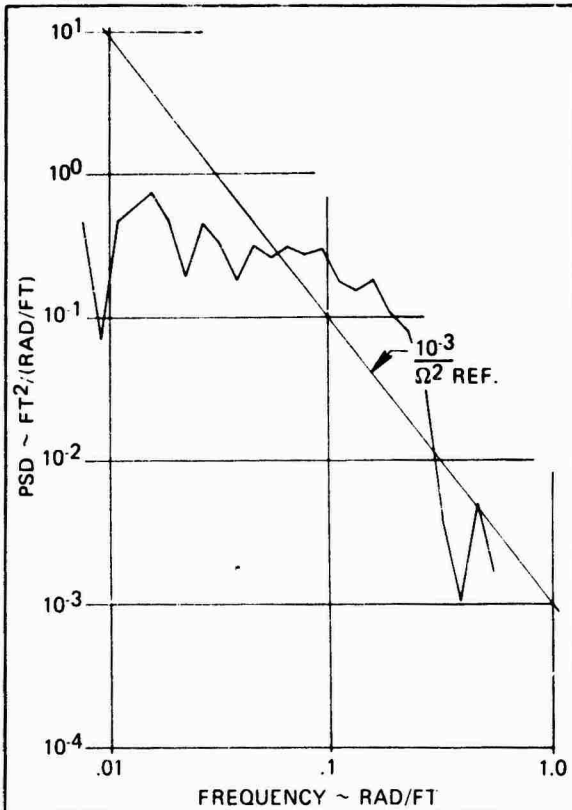


Figure 12 PSD of Guideway with 3rd Order Waviness

COMPOSITE ROUGHNESS PSD

A composite PSD of the overall guideway roughness was obtained by multiplying each PSD by the square of the tolerance in feet of each corresponding irregularity. It was found that actual tolerances of highway construction and how they are applied in the field are difficult to pin down. The tolerances presented here were estimated from information gleamed from several sources, and it is unclear whether they are the best achievable or what the general practice actually is. Another problem is that of soil instability which varies widely from location to location. Therefore, the tolerances shown below should be regarded as only indicative of the order of magnitude of these tolerances.

Type of Irregularity	Tolerance (feet)
Random Walk	0.01
Simple	0.01
Joint	0.01
1st Order Wave	0.075
2nd Order Wave	0.0375
3rd Order Wave	0.01875

The resultant composite PSD of roughness obtained is shown on Figure 13. The somewhat uneven nature of the individual PSD's tend to smooth out when they are combined. A couple of roughness PSD's obtained from [1] are shown on the same plot for comparison. One of these is for

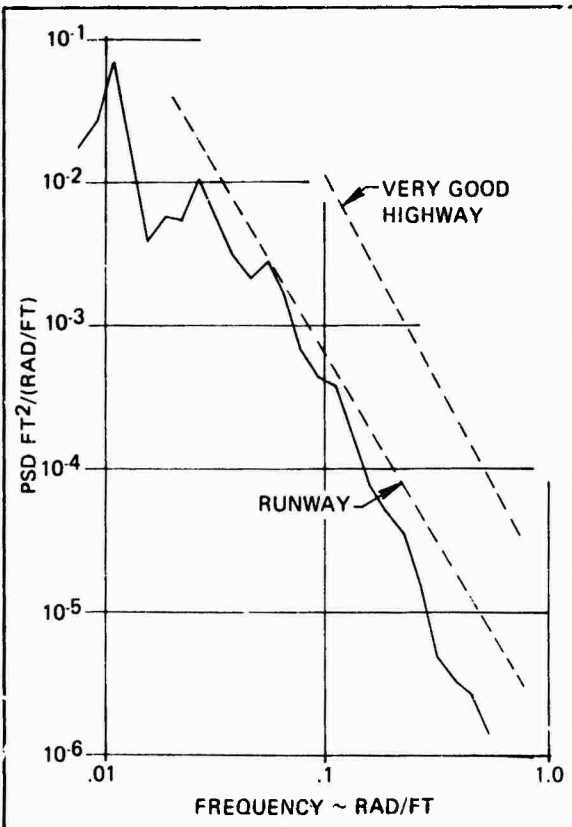


Figure 13 Composite PSD of Guideway Roughness

what is called "very good highway" and the other is for a "runway" (the smoothest shown in [1]). The calculated curve is lower than either, although it is in fair agreement with the "runway" curve. There are several possible explanations, e.g. (1) the actual tolerances are somewhat greater than those used here, (2) the soil has shifted under the samples before their roughness was measured, (3) terrain roughness overshadows construction inaccuracies, or (4) the probability density of amplitudes is more nearly uniform. Nevertheless, the general agreement obtained is considered to be indicative of the validity of the approach.

CONCLUSIONS

A method of estimating roughness power-spectral-densities (PSD's) of guideways from construction tolerances has been presented. Although the technique described was applied to guideways, it could be used in any situation where tolerances could be placed on certain types of irregularities.

The PSD calculated for the mathematically simulated roughness is in reasonable agreement with PSD's determined for measured guideway roughness, especially the trend with frequency, but it tends to the low side. It is probable that this is due to a combination of optimism in the level of construction tolerances achievable in the field and soil shifting after the guideway is constructed.

REFERENCES

- (1) H. H. Richardson, K. M. Captain, and W. A. Ribich, "Dynamics of Simple Air Supported Vehicles Operating Over Irregular Guideways", DOT Report DSR 76110, 4 June 1967.
- (2) Julius S. Bendat, Principles and Applications of Random Noise Theory, John Wiley & Sons, Inc., New York 1958.
- (3) Granino A. Korn and Theresa M. Korn, Mathematical Handbook for Scientists and Engineers, McGraw - Hill Book Company, New York, 1968.
- (4) "The IMSL Library, Vol. 1", IMSL LIB3-0002, International Mathematical & Statistical Libraries, Inc., Houston, Texas, 1972.

DISCUSSION

Mr. O'Hearne (Martin-Marietta Corp.): Have you investigated the tolerances used on rocket sled tracks?

Mr. Brock: They are very tight and actually I haven't investigated those. I have run across some data for welded steel rails that are considerably smoother than any of my data.

Dr. Mains: One of the problems associated with this roadway-guideway problem is that eventually it all has to be supported on the soil, the ground. If you could design a set of foundations, or a subgrade, and guarantee that you would have no more than 3/4 of an inch differential settlement from support to support, or along a hundred foot length of slab on grade, you would be doing very well. Guaranteeing this would be sticking your neck way out. Another factor to be considered is that the slabs tend to curl as a result of thermal expansion and contraction over a period of time, and that is why the slabs become dished up so that the ends stick out relative to the middle over a period of time.

SELECTED SYSTEM MODES USING THE DYNAMIC* TRANSFORMATION WITH MODAL SYNTHESIS

E. J. Kuhar, Jr.
General Electric Company
Valley Forge, Pa.

This paper presents a dynamic transformation method which provides an accurate definition of modes in a selected frequency range. The transformation is derived from the partitioned equations of motion at a selected system frequency and is used to reduce the generalized mass and stiffness matrix obtained with existing modal synthesis methods. Eigenvalue solutions are obtained from the reduced matrices and the results are used to revise, and assess the accuracy of, the solution. Three examples using the dynamic transformation with two different methods of modal synthesis demonstrate the method for selected system modes.

NOMENCLATURE

$[K]$	= generalized stiffness matrix for total structure in $\{q\}$ modal coordinates
$[k_{CPL}]$	= stiffness matrix in physical coordinate for coupling substructures
$[M]$	= generalized mass matrix for total structure in $\{q\}$ modal coordinates
n	= number of degrees of freedom
p	= reduction circular frequency
$\{q\}$	= generalized modal coordinates
$[R]$	= transformation matrix relation $\{q^R\}$ to $\{q^K\}$
$[T]$	= dynamic transformation matrix
$[\gamma]$	= eigenvector matrix for $[M]$, $[K]$
λ	= system eigenvalue
Ω	= system circular frequency

ω	= substructure circular frequency
$[\phi]$	= substructure physical eigenvectors
$\Delta\lambda$	= percent eigenvalue error
$\Delta\phi$	= eigenvector deviation
$\Delta\lambda_s$	= eigenvalue shift after back substitution

SUBSCRIPTS

1	= substructure 1
2	= substructure 2
i	= refers to the i th subset or term
I	= inertial coupling
S	= stiffness coupling

SUPERScripts

A	= attachment coordinates
B	= boundary coordinates
I	= interior coordinates not on boundary
K	= kept coordinates
R	= reduced coordinates
$-$	= revised value
00	= second time derivative

*This research was performed for the NASA-Marshall Space Flight Center

1. INTRODUCTION

The dynamic characteristics of complex structures are accurately described using discrete parameter models. When large systems are to be investigated, the vibration analysis may require at least 500 to 1000 degrees of freedom (DOF) to accurately describe the dynamic behavior of the structure in a particular frequency range. Models of this size far exceed the core capacity of the computer and require intricate computer programs to obtain an eigenvalue solution. Considerable computer run time can be expended to obtain the desired results. Some of the current approaches used to reduce the run time include iterative techniques which use the complete mode¹ for a partial eigensolution, condensation methods which reduce the order of the eigenvalue problem and modal synthesis. Modal synthesis, or a combination of modal synthesis with a condensation method, appears particularly attractive for reducing computer run time and obtaining accurate results.

The low frequency modes of a complex structure are easily obtained using current modal synthesis methods.^(1, 2) These methods synthesize the vibration modes of the complete structure from substructure analyses. The size of the eigenvalue problem is reduced by selecting only a portion of the low frequency vibration modes from each substructure to participate in the solution. Although excellent results can be obtained for the low frequency system modes, all of these methods are approximate in that the effects of the truncated high frequency component modes are not included in the solution. Due to truncation, the modes highest in frequency from the reduced eigenvalue problem will be inaccurate. If these modes occur in a desired frequency range, the accuracy of the solution can be improved by either increasing the size of the eigenvalue problem through the inclusion of more substructure modes or by employing some iterative technique based upon successive eigenvalue solutions.

Although existing modal synthesis methods vary in formulation and in the type of component modes used to represent the substructures, most of the methods can be classified into two general types based upon the method of substructuring. Those substructures obtained by defining attachment coordinate degrees of freedom at a common boundary between substructures describe the first category of substructuring. In the methods of Hurty, Craig and Bampton, and Bajan and Feng, the substructure natural modes obtained from constraining the attachment points are used in conjunction with rigid body and/or constraint modes.^(3, 4, 5) In the methods of Goldman and Hou, the use of free-free component modes eliminates the need for constraint modes.^(6, 7) All of the aforementioned methods assemble the structure by imposing

⁽¹⁾ See the References Section

compatibility conditions on attachment coordinates at a common boundary between substructures. Because the modal coupling occurs at a common mass point, this type of modal synthesis will be referred to as "inertial coupling."

The second category for most modal synthesis methods will be referred to as "stiffness coupling". Substructures belonging to this category have no common boundary degrees of freedom. At the General Electric Space Division, a stiffness coupling method that eliminates the need to retain a large number of attachment coordinates has been extensively used.^(1, 8, 9) This method uses free-free substructure vibration modes. The assembly of the structure parallels that of the displacement method of structural analysis since the substructures' attachment coordinates are connected by flexible links which can be represented by a finite element stiffness matrix.

The approach taken in this paper is to use a dynamic transformation method to obtain system solutions for modes in a selected frequency range. From the complete equations of motion, a frequency dependent transformation is obtained which includes the effects of modes not retained explicitly in the eigenvalue solution. This transformation is then used to reduce the generalized mass and stiffness matrices which describe the dynamic behavior of the coupled system. After solving the reduced eigenvalue problem, selected modes are revised using new transformations at the calculated frequencies. Comparisons of the revised and initial solutions are used to assess the accuracy of the modes. If all of the modes of interest have not been obtained, the procedure is repeated using the results to select a new set of retained modes and reduction frequency. Since the transformation is derived from the coupled equations of motion, the method can be used with any of the basic modal synthesis methods.

Both an inertial and stiffness coupling method of modal synthesis were chosen in order to demonstrate the general applicability of the dynamic transformation. The remainder of the paper consists of three sections; the analytical development of the dynamic transformation method; the derivation of the transformation for stiffness and inertial coupling; and the numerical results for three sample problems. A more detailed development for the equations presented in this paper may be found in Reference 1.

2. DYNAMIC TRANSFORMATION METHOD

The dynamic characteristics of structures are readily described by finite element models consisting of a mass matrix and a stiffness matrix. For large models with several degrees of freedom, an eigenvalue solution using the total mass and stiffness matrices may become impractical. Current modal synthesis methods provide an approach to solving the large eigenvalue problem by dividing a large structure into several

smaller substructures easily manipulated by the computer. By imposing equations of equilibrium and compatibility between adjacent substructure interfaces and using substructure vibration analysis data, some general transformation can be defined which modally couples the substructures together. The coupled equation of motion representing the total structure can be written in terms of a generalized mass matrix, $[M]$, and generalized stiffness matrix, $[K]$, as

$$[M] \{q\} + [K] \{q\} = 0 \quad (1)$$

where the $\{q\}$ coordinates correspond to some transformed set of physical or modal substructure coordinates. In its present form, the equation of motion has no fewer degrees of freedom than that of the total structure when described by the mass and stiffness matrices in physical coordinates. Low mode solutions are generally obtained by partitioning the $\{q\}$ coordinates into two groups: kept, $\{q^K\}$, and truncated, $\{q^R\}$. The truncated coordinates correspond to the higher frequency substructure modes and are completely omitted from the equation of motion. Those degrees of freedom remaining, $\{q^K\}$, determine the final reduced size of the eigenvalue problem. Let n^K represent the number of $\{q^K\}$ coordinates, n^R the number of $\{q^R\}$ coordinates, and n the number of degrees of freedom of the total structure, then $n = n^K + n^R$, and the reduced sizes of the generalized mass and stiffness matrices will be $n^K \times n^K$.

Let us now define a dynamic transformation. If Ω_i^2 corresponds to an exact eigenvalue of Eq. (1), the relationship between the eigenvalue and its eigenvector may be expressed in terms of the partitioned $\{q^K\}$ and $\{q^R\}$ coordinates as:

$$\Omega_i^2 \begin{bmatrix} -M_{KK} & M_{KR} \\ M_{RK} & M_{RR} \end{bmatrix} \begin{bmatrix} q^K \\ q^R \end{bmatrix} = \begin{bmatrix} K_{KK} & K_{KR} \\ K_{RK} & K_{RR} \end{bmatrix} \begin{bmatrix} q^K \\ q^R \end{bmatrix} \quad (2)$$

Expanding Eq. (2) into two equations for some general frequency, $p^2 = \Omega_i^2$, and solving the second equation for $\{q^R\}$ in terms of $\{q^K\}$ gives

$$\begin{bmatrix} q^R \\ n^R x 1 \end{bmatrix} = [R] \begin{bmatrix} q^K \\ n^K x 1 \end{bmatrix} \quad (3)$$

where

$$[R] = - \begin{bmatrix} K_{RR} - p^2 M_{RR} \\ K_{RK} - p^2 M_{RK} \end{bmatrix}^{-1} \begin{bmatrix} K_{RK} - p^2 M_{RK} \\ K_{RR} - p^2 M_{RR} \end{bmatrix} \quad (4)$$

Using Eq. (3) for some reduction frequency, p , we can write

$$\begin{bmatrix} q \\ n \\ x \\ 1 \end{bmatrix} = \begin{bmatrix} q^K \\ q^R \\ Rq^K \\ Rq^R \end{bmatrix} = \begin{bmatrix} I \\ R \\ R \\ R \end{bmatrix} \begin{bmatrix} q^K \\ q^R \end{bmatrix} \quad (5)$$

and the dynamic transformation, $[T]$, is then defined as:

$$[T] = \begin{bmatrix} I \\ R \\ R \\ R \end{bmatrix} \quad (6)$$

The reduced equation of motion is obtained by substituting the coordinate transformation defined by Eq. (5) into Eq. (1). Pre-multiplying by the transpose of $[T]$ preserves the symmetry of the generalized mass and stiffness matrices and reduces their size to $n^K \times n^K$.

Conventional methods of determining eigenvalues may be applied to the reduced equation of motion to obtain a set of frequencies, Ω^K , and mass normalized eigenvectors, $\{y^K\}$. Using the coordinate transformation defined in Eq. (3), the eigenvectors, $\{y^R\}$, corresponding to the $\{q^R\}$ coordinates are given as

$$\begin{bmatrix} y^R \\ n^K x 1 \end{bmatrix} = [R] \begin{bmatrix} y^K \\ n^K x 1 \end{bmatrix} \quad (7)$$

and the complete set of eigenvectors can be written as

$$\begin{bmatrix} y^{KR} \\ n^K x 1 \end{bmatrix} = \begin{bmatrix} y^K \\ y^R \end{bmatrix} \quad (8)$$

Having defined a frequency dependent transformation for some general reduction frequency, p , the method is not restricted to low mode solutions. Since all of the modes can be included through the transformation, those modes corresponding to some set of $\{q^R\}$ coordinates will be referred to as the "reduced" modes. The selected set of substructure modes corresponding to the $\{q^K\}$ coordinates will be referred to as the "kept" modes. Because most modal synthesis methods use similarity transformations to obtain the generalized mass and stiffness matrices, the eigenvalues, λ^K , will be the eigenvalues of the total structure. However, the eigenvectors, $\{y\}$, describe the modal coordinates, $\{q\}$. The general coordinate transformation used to modally couple the substructures together must be used in order to obtain the eigenvectors representing the physical structure.

If the $\{q\}$ coordinates corresponding to substructure normal modes are arranged in ascending order

according to the substructures' natural frequencies, the $[\gamma]$ will exhibit banded characteristics. The $[\gamma]$ set can be thought of as a measure of the modal participation from each substructure and will be referred to as participation factors. For a correct selection of kept modes, the $[\gamma^K]$ will contain the maximum valued component mode coefficients. Large coefficient values in the $[\gamma^R]$ set would indicate which modes should have been selected as kept modes. Significant improvement can be obtained in the modes and frequencies by using a Rayleigh-Ritz approach in conjunction with the dynamic transformation for individual modes. For each Ω_i^K to be considered, a revised mode shape can be determined by substituting $p = \Omega_i^K$ in $[K]$ and mass normalizing the mode shape. A new estimate of the frequency will then be given by

$$\Omega_i^2 = \left[\begin{bmatrix} \gamma KR \end{bmatrix}^T \right]_i [K] \left[\begin{bmatrix} \gamma KR \end{bmatrix} \right]_i \quad (9)$$

This part of the dynamic transformation will be referred to as back-substitution. Note that back-substitution as defined with the dynamic transformation may not be used repetitively for convergence to a particular mode. The method only alters the relationship between the kept and reduced modes by obtaining a new γ_i^R for each Ω_i^K using Eq. (7). A new γ^K set of participation factors can be obtained by selecting a new set of $\{q\}^K$ and/or a new reduction frequency, p , and repeating the reduction process.

If certain modes have been selected for back-substitution, two indicators as to the accuracy of the solution are provided by the method: the normalization factor and a frequency shift. The normalization factor is that scalar quantity used to mass normalize the back-substituted γ_i^{KR} . For an exact solution, the value would be unity. The frequency shift is measured by

comparing $\Omega_i^{K^2}$ from Eq. (9) to the $\Omega_i^{K^2}$ obtained before back-substitution. A zero frequency shift and a normalization factor of unity would indicate an exact solution. Both of these factors may be used in conjunction with the participation factors to aid in determining the exactness of the solution. The solution will always be exact for any Ω_i^K which is the same as the reduction frequency, p , regardless of choice in partitioning the q^K , q^R coordinates.

3. DYNAMIC TRANSFORMATION WITH STIFFNESS AND INERTIAL COUPLING

The stiffness coupling method of modal synthesis selected for solution with the dynamic transformation is that of one used at the General Electric Space Division (1, 8). The method resembles the displacement method for structural analysis in that stiffness matrices are used for coupling substructures together. Each substructure is analyzed with free attachment coordinates to determine the component vibration

modes. The total structure is represented by connecting the substructures through flexible links as indicated by the models shown in Fig. 1. The flexible links are defined by some finite-element stiffness matrix relating the interface forces from one set of substructure attachment coordinates to another. Using the mass-normalized substructure eigenvectors to define a coordinate transformation, the coupled, generalized mass and stiffness matrices can be formed in terms of the $\{q\}$ modal coordinates. For simplicity, the generalized mass and stiffness matrices will be presented by considering only two substructures.

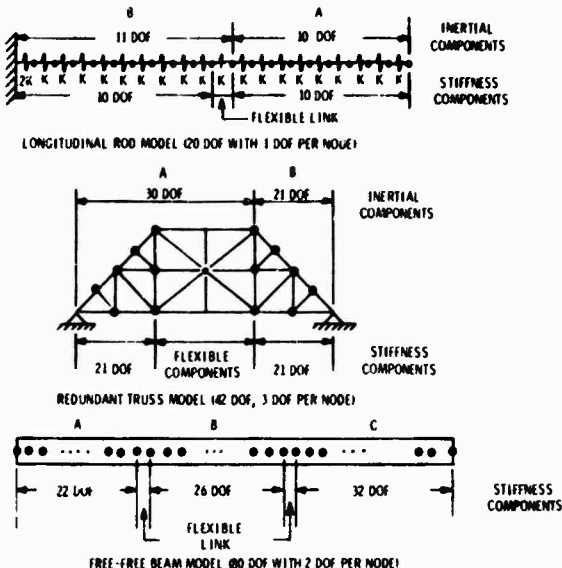


Fig. 1. Models and Substructures Used for Analysis

For each substructure with n_i degrees of freedom, a set of eigenvalues, ω_i^2 , and a set of mass normalized eigenvectors, $[\phi_i]$, can be obtained. Let $[k_{CPL}]$ represent the stiffness matrix used to relate the interface forces between the connecting n^A attachment coordinates. Assuming there is no inertial coupling between the connecting degrees of freedom, the mass properties of the flexible link are included in each of the substructures. The generalized mass and stiffness matrices after one coordinate transformation may simply be expressed as:

$$[M_s] = [I]$$

$$[K_s] = \begin{bmatrix} 2 & 1 & 0 \\ \omega_1 & - & - \\ 0 & 2 & - \\ - & - & 2 \end{bmatrix}_{nxn} + [\phi^A]^T [k_{CPL}] [\phi^A]_{n^A \times n^A} \quad (10)$$

where

$$[\phi^A] = \begin{bmatrix} \phi_1^A & 1 & 0 \\ - & - & - \\ 0 & 1 & \phi_2^A \end{bmatrix}_{n^A \times n^A} \quad (11)$$

and $n = n_1 + n_2$. Note that the rows of ϕ_1^A contain only those coordinates from ϕ_1 which correspond to the attachment degrees of freedom. The resulting matrices need only to be assembled in terms of the $\{q^K\}$ and $\{q^R\}$ coordinates before applying the dynamic transformation.

Due to the form of $[M_s]$ and $[K_s]$, $[T]$ reduces to a simplified form where

$$[R_s] = - \begin{bmatrix} K_s^{RR} - p^2 I \\ n \times n \end{bmatrix}^{-1} \begin{bmatrix} K_s^{RK} \\ n \times n \end{bmatrix} \quad (12)$$

and the reduced generalized mass and stiffness matrices can be written in partitioned form as:

$$\begin{aligned} [M_s^K] &= [I] + [R_s]^T [R_s] \\ [K_s^K] &= [K_s^{KK}] + 2 [K_s^{KR}] [R_s] \\ &+ [R_s]^T [K_s^{RR}] [R_s] \end{aligned} \quad (13)$$

The inertial coupling method of modal synthesis selected solution with the dynamic transformation is that of Craig and Bampton (4). This method uses two types of component modes to represent the substructure: constraint and normal. The constraint modes are defined by separately deflecting each boundary coordinate a unit displacement with all other boundary points fixed. The normal vibration modes are determined by solving the eigenvalue problem with all of the boundary points fixed. These modes are then used to define a coordinate transformation at the substructure level. The total structure is represented by connecting the transformed substructure models at their common boundary points as shown in Fig. 1. Compatibility conditions are imposed by the coordinate transformation used to couple the substructures together.

For each substructure with n_1^B "boundary" degrees of freedom and n_1^I "internal" degrees of freedom, the size of the substructure will be given by $n_1 = n_1^I + n_1^B$. If n^B represents the total number of boundary coordinates in the coupled structure (N.B., $n^B \neq \sum n_1^B$), then the generalized mass and stiffness matrices after two coordinate transformations will be given by:

$$[M_I] = \begin{bmatrix} M^{BB} & M_1^{BI} & M_2^{BI} \\ M_1^{IB} & I & 0 \\ M_2^{IB} & 0 & I \end{bmatrix} n^B \quad n \times n$$

$$[K_I] = \begin{bmatrix} K^{BB} & 0 & 0 \\ 0 & \omega_1 & 0 \\ 0 & 0 & \omega_2 \end{bmatrix} n^I \quad n \times n \quad (14)$$

and $n = n_1^I + n_2^I$. Due to the introduction of constraint modes for inertial coupling, the $\{q\}$ will consist of a mixed set of generalized coordinates. If the substructures mass and stiffness matrices are defined in the coupled structure's coordinate system, the physical deflections at the boundary will be the q deflections corresponding the n^B degrees of freedom. Only the n^I degrees of freedom correspond to a generalized modal coordinate. The coordinate transformation used to obtain the generalized mass and stiffness matrices must be used to obtain the physical deflections. To use the dynamic transformation, the $[M_I]$ and $[K_I]$ need only to be partitioned into some $\{q^K\}$, $\{q^R\}$ set.

The resulting form of $[R]$ for the dynamic transformation reduces to a simplified form different than that for stiffness coupling where

$$[R_I] = p^2 [K_I^{RR} - p^2 I]^{-1} [M_I^{RK}] \quad (15)$$

and the reduced mass and stiffness matrices will be given by

$$\begin{aligned} [M_I^K] &= [M_I^{KK}] + 2 [M_I^{KR}] [R_I] + [R_I]^T [R_I] \\ [K_I^K] &= [K_I^{KK}] + [R_I]^T [K_I^{RR}] [R_I] \end{aligned} \quad (16)$$

where $[K^{RR}]$ may be completely diagonal or contain a portion of the coupled boundary coordinates. If all of the boundary degrees of freedom are contained in $\{q^K\}$ the calculation of $[R]$ is greatly simplified due to the diagonal form of $[K^{RR}]$. Unlike stiffness coupling, only those q 's corresponding to some n_1^I degree of freedom can be used as a measure of modal participation.

4. NUMERICAL RESULTS

The dynamic transformation with stiffness and/or inertial coupling was used to solve the three structural models shown in Fig. 1. The 20 DOF uniform longitudinal rod (1 DOF per node) and the 42 DOF planar truss (3 DOF per node) were analyzed as two substructures. The 80 DOF uniform beam (2 DOF per node) was represented by three substructures of varying sizes. Due to the two methods of modal synthesis

used, slight differences exist in the substructures used to describe the same model. For inertial coupling, the substructure boundaries for the rod and truss occur at the center of a boundary degree of freedom with half the mass and stiffness contained in each substructure model. Since the normal vibration modes are determined with fixed attachment coordinates, there are no rigid body normal modes for the substructure models defined with inertial coupling. The rigid body motion of the substructure models is contained in the constraint modes. For stiffness coupling, there are no common boundary degrees of freedom between the substructure models. Each substructure model includes the total boundary mass but not the stiffness of the flexible links coupling the substructures together. Note that substructure A for the rod has one rigid body mode, each substructure for the truss has one rotational rigid body mode, and each substructure for the beam has two rigid body modes. Complete solutions for each model were obtained for partial solution comparisons. The Jacobi threshold method was used for the eigenvalue solutions, and an overall check was made on the implementation of the methods using the closed form solution for the longitudinal rod model.

Three parameters were varied in the analyses: (1) the set of kept coordinates for the eigenvalue problem; (2) the reduction frequency, p ; (3) the size of the kept and/or reduced coordinate set. The q^K were selected as a sequential group from the frequency ordered component modes and/or the constraint modes depending on the method of modal synthesis used and the frequency range of interest. The remaining degrees of freedom were used as the q^R set. Several values of the reduction frequency were chosen for each set of selected q^K to show general trends. Since one solution would be exact for some reduction frequency equal to one of the system frequencies regardless of the modes included in q^K , the reduction frequency was selected between system modes; i.e., $p^2 = .5(\lambda_n + \lambda_{n+1})$. The size of the kept coordinate set, n^K , was incremented in steps of approximately $.2n$ with major emphasis placed on the $0.2n$, $0.4n$ solutions.

The results of the analyses used eigenvalue and eigenvector errors to evaluate the accuracy of the results. Eigenvalue errors, $\Delta\lambda$, were obtained by comparing the reduced solution eigenvalues to the corresponding system eigenvalues obtained from a complete solution of the problem. All eigenvalue errors will be expressed in terms of percent deviation where the $\Delta\lambda_i$ for any i th mode is defined as $\Delta\lambda_i = 100(\lambda_i -$

$\lambda_{i\text{exact}})/(\lambda_{i\text{exact}})$. The eigenvector errors, $\Delta\phi$, were obtained for the corresponding eigenvalues by using the standard error of estimate given by $\Delta\phi_i = [\sum(x_j -$

$x_{j\text{exact}})^2/n]^{1/2}$ where the x_j corresponds to the

j th physical deflection for same mode. Because of large variations in the magnitude of the x_j mass normalized elements for different models and frequencies, the $\Delta\phi$ errors were calculated using re-normalized vectors of unit length.

Some of the specific analyses performed for the rod and truss are shown schematically in Figs. 2 and 3. Each of the figures show the substructure modes used in the analysis for q^K and q^R ; the values of several reduction frequencies, p , used for a particular set of q^K solutions; and the results of the analyses for both inertial and stiffness coupling using $\Delta\lambda$ and $\Delta\phi$ as error criteria. The kept modes, q^K , are indicated by a solid arrow spanning the frequency ordered substructure modes and the reduced modes, q^R , are shown with a dashed line. The values of the reduction frequency, p , are indicated by the horizontal lines between the system eigenvalues and, as indicated before, were obtained from the numerical average of the two adjacent system eigenvalues. Each horizontal line represents one eigenvalue solution for the n^K modes shown by the solid arrow. The method of modal synthesis used to which the dynamic transformation was applied is indicated by the run number. STC designates solutions using stiffness coupling and MPC solution using inertial (Mass point) coupling.

The results of the analyses are shown using the $\Delta\lambda$ and $\Delta\phi$ errors as acceptance criteria. The "o" marks shown in Figs. 2 and 3 indicate system modes obtained from a solution for a value of $\Delta\lambda_i \leq 1$. The "x" marks are used in combination with the "o" to indicate those system modes obtained for a value of $\Delta\phi_i \leq 0.01$. Associated with the "o" and "x" designated modes is a horizontal arrow that indicates the value of the reduction frequency that provided the maximum number of modes satisfying both the $\Delta\lambda$ and $\Delta\phi$ criteria. Multiple horizontal arrows were drawn when several values of p yielded identical results for any one run. No attempt was made to select an optimum set of q^K coordinates.

The results shown in Fig. 2 for the longitudinal rod are for a constant value of $n^K = 0.4n$. Considering only the λ errors, 62% to 100% of the available modes were accepted as solutions in all cases for both methods of modal synthesis. For stiffness coupling using both the $\Delta\lambda$ and $\Delta\phi$ criteria, 50% to 87% of the available modes were accepted. For inertial coupling it was necessary to investigate the influence of the boundary degrees of freedom when used in the q^K set for middle and high mode solutions.

The best results were obtained when the system degree of freedom corresponding to the substructures' boundary point was included in the q^R set of coordinates. For these cases (Fig. 2), 62% to 75% of the available modes were accepted using both the $\Delta\lambda$ and $\Delta\phi$ error criteria. However, increased vector errors were observed for middle/high mode solutions containing the boundary coordinates as, for example, in Run No. MPC018 where no solutions satisfy the $\Delta\phi$ criterion.

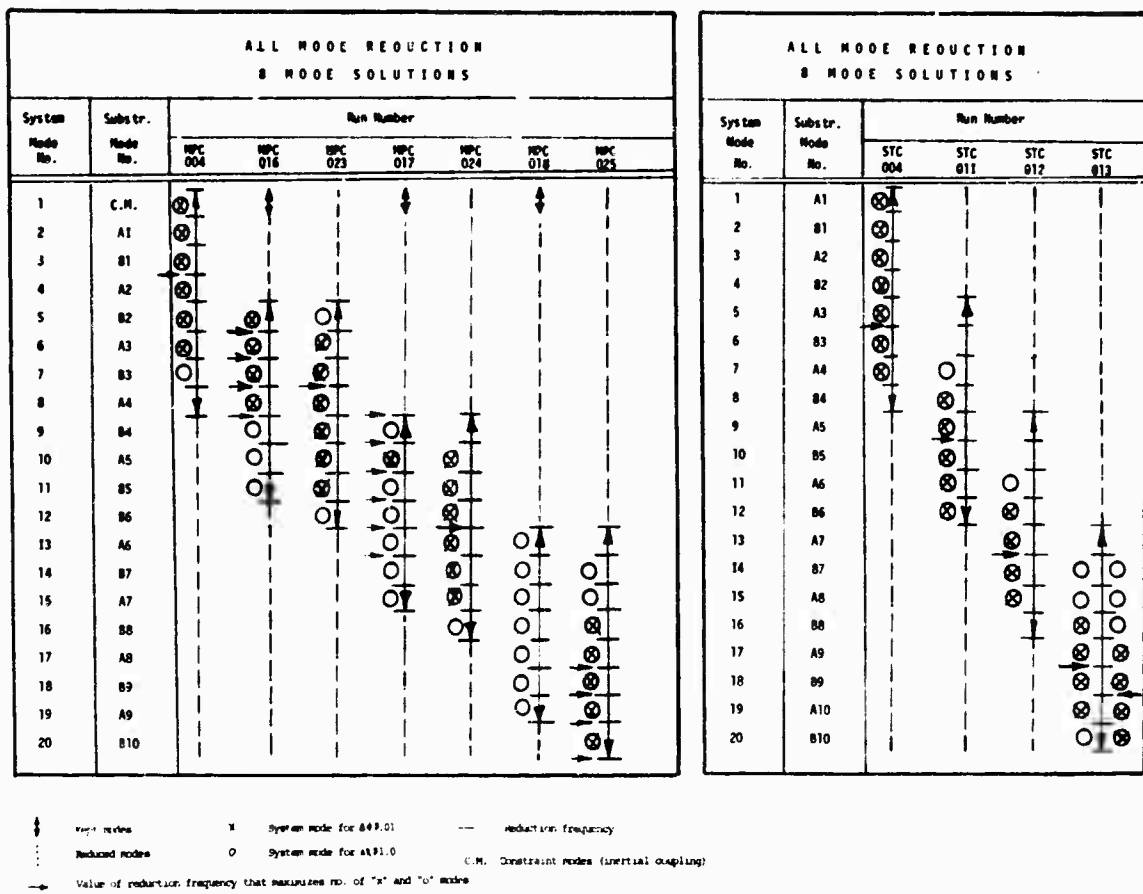


Fig. 2. Longitudinal Rod Analyses

The results shown in Fig. 3 are for the planar truss with a constant value of $n^K \approx 0.4n$. The number of acceptable modes for stiffness coupling using both error criteria ranged from 75% to 100% for most cases. Of particular interest is Run No. STC510 where 100% of the modes were acceptable for seven different values of the reduction frequency, p . The uncoupling of the high frequency modes from all the others was reflected in the banded participation factors. For inertial coupling the selection of q^K coordinates was complicated due to the introduction of nine boundary degrees of freedom. As in the case of the rod, increased vector errors were observed for the high mode solutions with the boundary coordinates included in the q^K set. Although solutions were obtained for the middle modes both with and without the boundary degrees of freedom, the poor selection of kept coordinates is indicated by some acceptable modes appearing beyond, or close to, those degrees of freedom defined by the solid arrows. No attempt was made to select the correct q^K set for an optimum system solution. For the rod and truss models, the results indicated that the vector deviation, $\Delta\phi$, was the controlling factor in accepting modes using both methods of modal synthesis.

Typical results indicating the effect of the reduction frequency, p , on $\Delta\lambda$ are shown in Fig. 4. The curves are for an eight mode stiffness coupling solution (Fig. 2, STC001) and show the actual $\Delta\lambda$ values of modes 5 through 12 for four values of p . The reduction frequencies were chosen at average eigenvalue points so that the curves do not show a sharp error reduction near the system modes. In general, those modes closest to the reduction frequency will have the least eigenvalue error. For increasing mode numbers away from p , one can expect progressively greater eigenvalue errors with the maximum errors occurring at those modes farthest from p . The corresponding eigenvector errors, $\Delta\phi$, are shown in Fig. 5, and exhibit the same characteristics as the $\Delta\lambda$. Because unit length vectors are used for the calculation, the range of values for $\Delta\phi$ will not vary as greatly as those of $\Delta\lambda$. For all cases considered, no value of $\Delta\phi$ exceeded 1.0.

The corresponding normalization factors (n. f.) and eigenvalue shifts ($\Delta\lambda_{Si}$) for Run No. ST011 are shown in Figs. 6 and 7. In order to make similar comparisons, the n. f. and $\Delta\lambda_{Si}$ were plotted as percents where $N. F. i = 100 (n. f. i - 1)$ and $\Delta\lambda_{Si} = 100 (\lambda_i - \lambda_{i-1})$. The

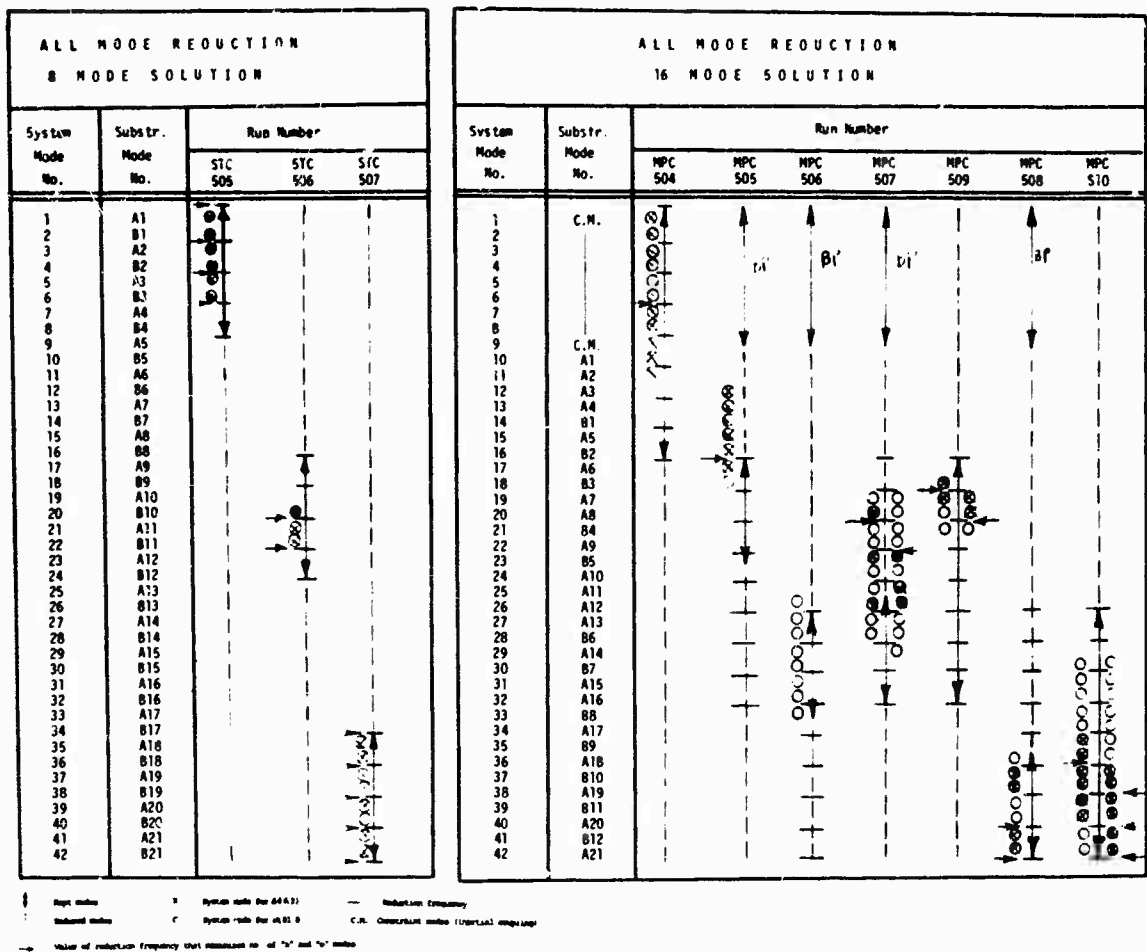


Fig. 3. Redundant Truss Analyses

results show that N. F. and $\Delta\lambda_s$ exhibit the same pattern as the eigenvalue and eigenvector errors for modes around the reduction frequency. However, those modes farthest away from the reduction frequency do not show any general pattern. In particular, both N. F. (Fig. 6) and $\Delta\lambda_s$ (Fig. 7) show smaller errors for Mode 5 than for Mode 6. The p_1 curve (Fig. 6) for Mode 12 has the smallest N. F.; yet that mode has the largest eigenvalue error as shown in Fig. 4 for $\Delta\lambda$. If the normalization factors and eigenvalue shifts are to be used as error indicators, the location of the modes relative to the reduction frequency must also be considered.

The effects of back-substitution on the eigenvalue and eigenvector errors are illustrated in Figs. 8 and 9 where the solid line indicates back-substitution values. Although the results have been shown only for one optimum case (Fig. 2, STC011), they are representative of the improvements obtained from the middle/high mode solutions for both stiffness and inertial coupling. In order to show the range of values for $\Delta\lambda$ and $\Delta\phi$ more clearly, the errors are plotted in the form of a distribution function where the percent of

acceptable modes have a value less than or equal to the value shown on the horizontal axis. For the eigenvalue errors, Fig. 8 shows that 62% to 75% of the modes obtained were acceptable based on a $\Delta\lambda \leq 1.0$ with and without back-substitution. The major improvement occurs in the range for $\Delta\lambda \leq 0.2$. Results from the analyses showed that $\Delta\phi$ errors in the range given by $0.1 \leq \Delta\phi \leq 1.0$ definitely reflected unacceptable modes in all cases. The arbitrary selection for $\Delta\phi \leq 0.01$ appeared to yield satisfactory mode shapes for most cases. Fig. 9 shows that back-substitution more than doubles the number of acceptable modes for this eigenvector criteria. Results for individual modes showed that back-substitution for modes near a reduction frequency, p , reduced the $\Delta\lambda$, $\Delta\phi$ errors several orders of magnitude.

Although back-substitution usually improved both eigenvalues and eigenvectors for those modes closest to p , inertial coupling results with the dynamic transformation showed exceptions to this general trend. This may be best illustrated by considering Run No. MPC018 and MPC025 from Fig. 2 for the longitudinal rod. The solution for MPC018 contains the boundary

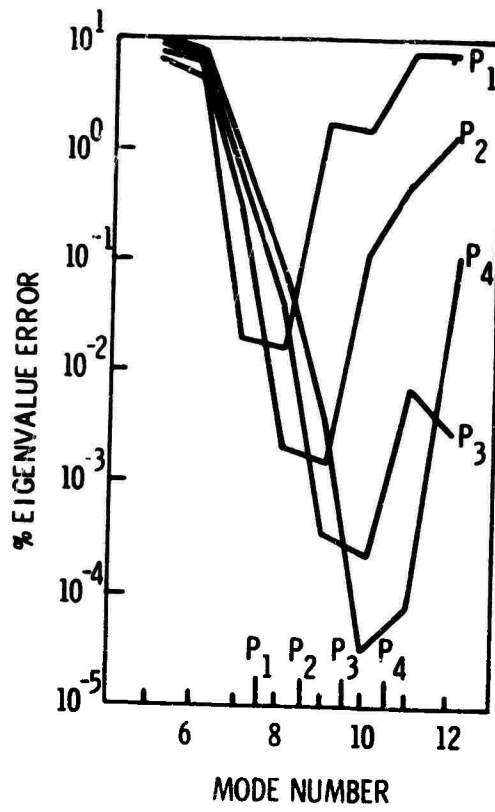


Fig. 4. Eigenvalue Errors

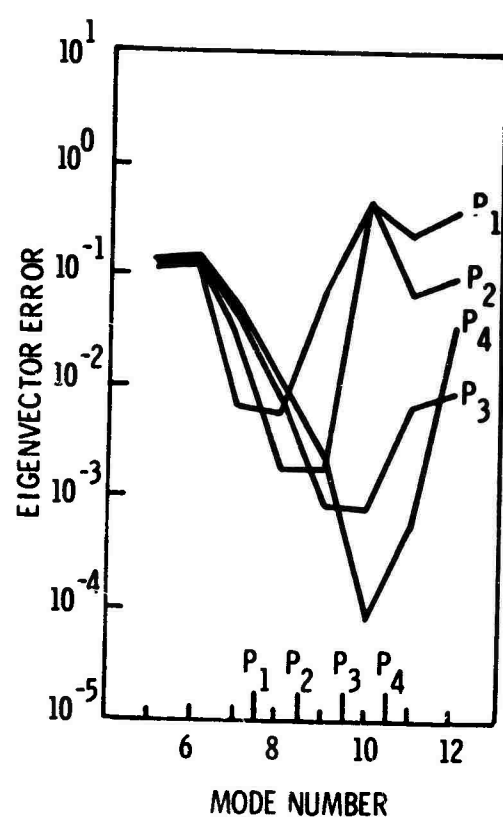


Fig. 5. Eigenvector Errors

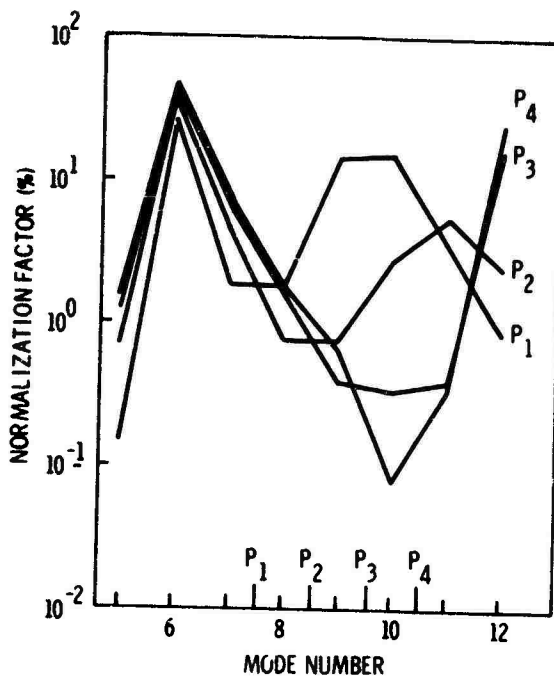


Fig. 6. Normalization Factors

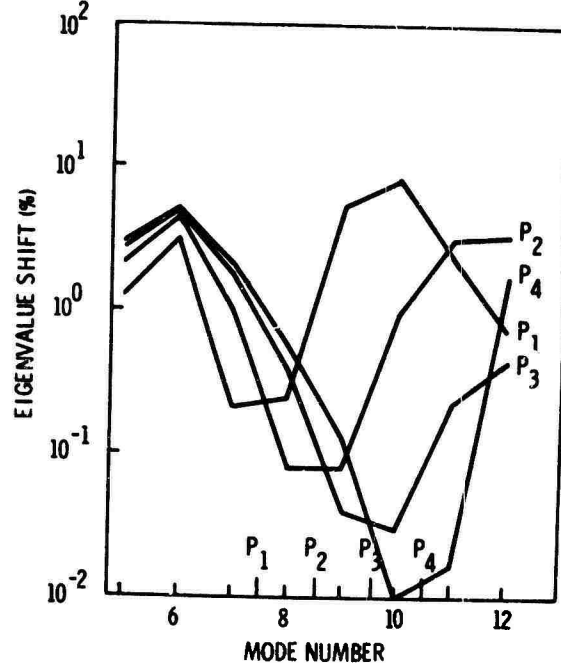


Fig. 7. Frequency Changes

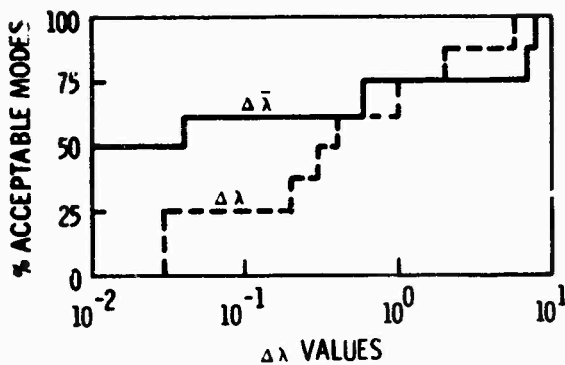


Fig. 8. Backsubstitution Effects On $\Delta\lambda$

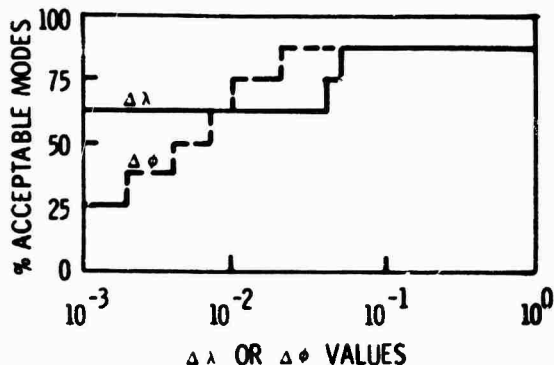


Fig. 11. Rod Errors Without Boundary Point

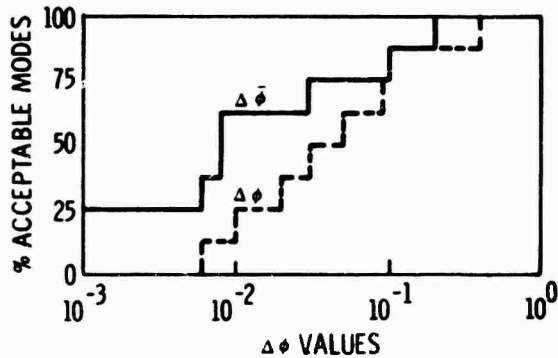


Fig. 9. Backsubstitution Effects on $\Delta\phi$

coordinate in the q^K set while the solution for MPC025 does not. Both $\Delta\lambda$ and $\Delta\phi$ are shown in Fig. 10 plotted in distribution function form for MPC025. Even when the eigenvalue errors were on the order of 2×10^{-5} , there were no modes satisfying $\Delta\phi \leq .01$. On the other hand, Fig. 11 (MPC025) shows 62% of the modes satisfying the $\Delta\phi$ criterion and 87% of the modes satisfying $\Delta\lambda \leq 1.0$. The results indicated that acceptable solutions for inertial coupling are extremely sensitive to coordinate selection if both error criterion are to be satisfied.

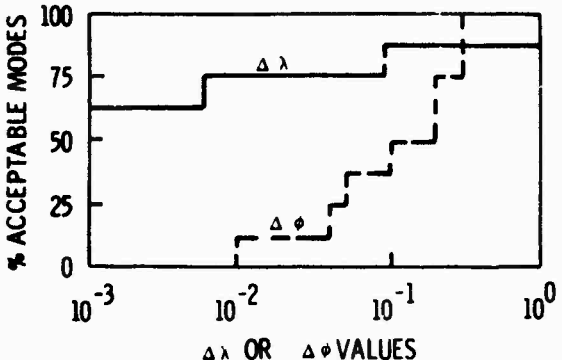


Fig. 10. Rod Errors With Boundary Point

Some insight into the effect of kept coordinate selection can be obtained from examination of the results for middle mode solutions for the free-free beam with stiffness coupling. The system eigenvalue errors for the 16 system modes obtained from the solutions using three different reduction frequencies are given in Table 1. Heavy horizontal lines between $\Delta\lambda$ are used to indicate the reduction frequency. The percent of modes kept was based upon the total number of substructure modes having participation factors ≥ 0.1 . The percentage obtained reflects the portion of those modes included in the q^K set. The number of modes satisfying $\Delta\lambda \leq 1.0$ is 15 for the first solution, 13 for the second, and 8 for the third. The first two reduction frequencies are in the range of solutions that contain the substructure modes having major participation in the system modes. The third solution tries to force the system modes to correspond to the reduction frequency and provides a good solution for the modes adjacent to the reduction frequency even though a large percentage of the substructure modes were omitted from the kept set. Of particular interest is Mode 42 from the second solution. One would expect the eigenvalue error for this mode to be approximately that of Mode 39. Inspection of the modal participation factors shows a small percentage of those contributing substructure modes were included in the kept set. These results indicate that a match with regard to kept substructure modes and reduction frequency is needed to maximize the number of accurate system modes obtained from any one solution. The use of predicted participation factors to improve subsequent solutions for unacceptable system modes was not investigated in this study. Table 2 presents the frequency errors ($\Delta\Omega$) obtained from four rod solutions using stiffness coupling and indicates a possible approach to determining the system modes. Each solution is for $nK = 0.4n$ with a maximum frequency error in any one mode of approximately 0.04%. Sufficient overlap exists to assure the analyst that all the modes are obtained. If a sequential solutions is used, results from the first solution can be used to

Table 1. Eigenvalue Errors of Beam Middle Mode Solutions

System Mode No.	Percent Modes Kept*	$P^2 = .5 (\lambda_{33} + \lambda_{34})$	$P^2 = .5 (\lambda_{40} + \lambda_{41})$	$P^2 = .5 (\lambda_{47} + \lambda_{48})$
		% λ Error	% λ Error	% λ Error
31	55.6	.61	1.05	
32	71.5	.04	.31	
33	53.8	<u>.0007</u>	.13	1.0
34	83.3	.002	.10	1.8
35	100.0	.07	.009	3.3
36	75.0	.08	.009	.10
37	100.0	.09	.0001	1.1
38	100.0	.68	.003	.96
39	100.0	.13	.0001	.95
40	87.5	.97	<u>.0001</u>	.34
41	77.8	.97	.0001	.46
42	33.3	1.9	1.1	64
43	45.5	.94	.12	62
44	83.3	.98	.26	.88
45	62.5	.47	.77	1.4
46	40.0	.12	1.1	2.7
47	28.6			<u>.15</u>
48	50.0			.06

*Based on substructure modes having participation factors ≤ 0.1

Table 2. Percent Frequency Error in Sequential Solutions of Rod Dynamic Transformation

Mode No.	1	2	3	4	5	6	7	8	9	10	11	12	13	14	15	16	17	18	19	20
1	7×10^{-5}	4×10^{-5}	1×10^{-5}	2×10^{-5}	2×10^{-4}	3×10^{-3}	4×10^{-2}	3×10^0												
2					4×10^0	4×10^0		3×10^{-1}	2×10^{-2}	2×10^{-4}	1×10^{-4}	4×10^{-3}	1×10^{-3}							
3								3×10^0	1×10^0	2×10^{-1}	2×10^{-2}	3×10^{-4}	2×10^{-5}	2×10^{-5}	4×10^{-5}	4×10^{-4}	8×10^{-4}	7×10^{-3}	2×10^{-2}	
4										2×10^{-1}	2×10^{-2}	2×10^{-3}	2×10^{-4}	2×10^{-5}	4×10^{-5}	4×10^{-4}	8×10^{-4}	7×10^{-3}	2×10^{-2}	

select kept substructure modes and a reduction frequency for the second solution. The results, as presented, show the feasibility of using small sequential solutions to obtain the system modes.

Due to the complexity in determining acceptable modes

based upon eigenvalue and eigenvector errors, a frequency error of 0.1% or less ($\Delta\lambda \leq 0.2$) was selected to summarize the results of all the analyses. For most cases, this error tended to correspond to a maximum modal deflection error of 5%. Table 3 summarizes the results for low, middle, and high mode solutions using

Table 3. Portion of Calculated Modes with Frequency Error Less Than 0.1%, All Mode Solutions

Model	Method	Solutions for $n^K \approx 0.2$ N					Solutions for $n^K \approx 0.4$ N				
		Truncation	Dynamic Transformation				Truncation	Dynamic Transformation			
			Low Modes	Middle Modes	High Modes	Low Modes	Middle Modes	High Modes			
Longitudinal Rod	Stiffness	0	1.00	0.50/0.75	1.00		0	0.87	0.62/0.75	0.75	
	Inertial, constraint modes kept	0.25	0.75	0.75/1.00	0.75	0.37	0.75	0.87	0.87	0.87	
	Inertial, no constraint modes kept	-	-	0.75	1.00	-	-	-	0.75/0.87	0.87	
Redundant Truss	Stiffness	0	0.75	0.37	1.00	0.06	0.87	0.75	1.00		
	Inertial, constraint modes kept	-	-	-	-	0.56	0.69	0.38/0.69	0.50		
	Inertial, no constraint modes kept	-	-	-	-	-	-	-	0.25	0.62	
Free Free Beam	Stiffness	0	0.79*	0.62	0.75	0.10*	0.83*	-	-	-	

*Elastic DOF

0.2n and 0.4n for the eigenvalue problem size. In most analyses, over half the solution modes have frequency errors of less than 0.1%.

5. CONCLUDING REMARKS

A method of vibration analysis which allows selected system modes to be obtained by solving an eigenvalue problem much smaller in size than that of the structural model has been described and numerical results presented. The method can be applied with any basic modal synthesis technique. For large problems, modes can not only be reduced through the dynamic transformation, but those modes least affecting the solution can be truncated. Modal participation factors can be used to indicate the major contributing substructure modes. As presented, the dynamic transformation method uses back-substitution to increase the accuracy of the modes. The resulting normalization factors and eigenvalue shifts provide error indicators to aid in assessing the accuracy of the modes. It is felt that further experience in the application of the method may indicate that back-substitution should be used selectively.

REFERENCES

1. Kuhar, E.J., and Stahle, C.V., "A Dynamic Transformation Method for Modal Synthesis", AIAA/ASME/SAE 14th Structures, Structural Dynamics, and Materials Conference, Williamsburg, Va., March 20-22, 1973.
2. Hart, G.C., Hurty, W.C., and Collins, J.D., "A Survey of Modal Synthesis Methods." Proc National Aeronautic and Space Engineering and Manufacturing Meeting, Los Angeles, California, September 28-30, 1971.
3. Hurty, W.C., "Dynamic Analysis of Structural Systems Using Component Modes." AIAA J, Vol 3, No. 4, April 1965.
4. Craig, R.R., and Bampton, M.C.C., "Coupling of Substructures for Dynamic Analysis." AIAA J, Vol 6, No. 7, July 1968.
5. Bajan, R.L. and Feng, C.C., "Free Vibration Analysis by the Modal Substitution Method." AAS Paper 68-8-1, July 1968.
6. Goldman, R.L., "Vibration Analysis by Dynamic Partitioning." AIAA J, Vol 7, No. 6, June 1969.
7. Hou, S.N., "Review of Modal Synthesis Techniques and a New Approach." The Shock and Vibration Bulletin, No. 40, Naval Research Laboratory, Washington, D.C., December 1969.
8. Roach, R.E., Jr., "Joining Subsystems Together in Modal Coordinates," General Electric Company, Missile and Spacecraft Department, PIR 4T45-17, August 1966.
9. Cokonis, T.J., and Sardella, G., "Vibration Analysis and Test of the Earth Resources Technology Satellite," The Shock and Vibration Bulletin No. 42, Part 2, January 1972.

DISCUSSION

Mr. Haskell (Ballistics Research Laboratory): What added effort has to be put into your method compared to current methods? What extra time do you need to get it working?

Mr. Kuhar: Do you mean the additional effort that is required? Just the derivation of the "R" matrix for the transformation and going to the triple product for the reduction.

STRUCTURAL DYNAMICS COMPUTATIONS
USING AN APPROXIMATE TRANSFORMATION

Clifford S. O'Hearne and John W. Shipley

Martin Marietta Aerospace
Orlando, Florida

Engineering structural analyses are often performed in closely-overlapping, small subspaces of a linear vector space of high finite order. The different subspaces correspond to differences in mass or stiffness distribution. In these cases an approximate transformation from one subspace to the other is very useful. Such circumstances are described, and illustrated by computations of air blast loads on the SAM-D launcher. The transformation is the pseudoinverse of the matrix of basis vectors of the first subspace postmultiplied by the matrix of basis vectors of the second.

INTRODUCTION

Structural analysis problems nowadays often lead to force and motion relations expressed as transformations on linear vector spaces of large finite dimension. The largeness is usually the consequence of the natural decomposition of an engineering structure into strength-of-materials type elements at a high degree of fineness, and there is otherwise no need for such refinement. In fact, for practical reasons, it is necessary to have a method of coarsening. Resort to a two-stage reduction of order is often used. First a Rayleigh-Ritz type reduction is applied (the simplest is the Guyan), then eigenanalysis is used for both further reduction and decoupling of the equations. The spatial and temporal distributions of applied forces are taken into account in selecting the reductions. The structural equations are thus ultimately expressed in a displacement subspace of small dimension. A basis of this subspace is the columns of the product of the reduction transformations. When changes are made in the structural mass or stiffness distributions or the boundary conditions, but the global coordinates are retained, the analysis subspace will change. Often the new subspace largely overlaps the old. The approximate transformation of the title is one which carries one basis as closely as possible into another, or projects a vector in one space into its representation in the other according to a minimum error criterion. Some examples of the use of such a transformation are:

1) The normal-mode motion solution of an artillery rocket launcher in ripple fire (rapid sequential fire). Say the launcher has zero-length rails, then, at the instant of each launch the normal modes and static equilibrium of the launcher change. If the elastic deformation motion of the launcher, which affects

the rockets' trajectories, is to be solved through several bounds, the approximate transformation carries the terminal conditions in the old normal coordinates into the initial conditions in the new.

2) The bending motion solution of a rocket at stage separation. Again for normal mode solutions, the transformation carries the terminal conditions in the lower stage coordinates into initial conditions in the upper stage coordinates.

The computation described herein is another instance, but the motivation and application are not so quickly described. To state precisely the definition and use of the subject transformation in a large-order, linear system analysis, the general system equations and conventional reduction transformations are first presented. The application of the reduction transformations as shown does not represent the ordinary sequence of computations in a particular structural analysis program, rather the form of presentation is intended to make definitions clear and establish notation. The transformation which is the subject of this paper is then introduced with the motivation for its use. Its derivation is presented in an appendix.

The approximate transformation is then applied in an engineering computation. The structure is a launcher design for the SAM-D air defense missile. The response of the launcher to air blast in two weight conditions is calculated. Descriptions of the structure, of the application of the blast force, and of the structural loads solutions to be used for comparison are given. The results of conventional and approximate solutions are then compared. The paper concludes with a discussion of particularities and generalities.

GENERAL SYSTEM EQUATIONS AND ORDER REDUCTIONS

The equations of motion of a large-order, linearly elastic, mechanical system with time-dependent forcing may be represented as follows:

$$\ddot{\mathbf{M}}\mathbf{x} + \mathbf{K}\mathbf{x} = \mathbf{f}, \quad (1)$$

where \mathbf{M} is the $(m \times m)$ mass matrix, \mathbf{K} the $(m \times m)$ stiffness matrix, \mathbf{x} the displacement m -vector, $\ddot{\mathbf{x}}$, the second derivative of \mathbf{x} with respect to time, and \mathbf{f} is the forcing function m -vector. The components of the vector \mathbf{x} are the physical displacements of the nodes of the structure moving in rigid body motion and elastic deformation. Damping is usually not introduced until the equations are reduced to a lower order. At this stage, the order of the equations is too large for practical integration or eigenanalysis.

The equations may now have their order reduced (condensed). To begin, the forcing function usually is identically zero in many degrees of freedom,

$$\mathbf{f} = \mathbf{Bb}, \quad (2)$$

where \mathbf{B} is $(m \times k)$, $m > k$. \mathbf{B} contains a $(k \times k)$ identity submatrix and a $(j \times k)$, $j = m - k$, zero matrix, and \mathbf{b} is a k -vector. Now the Guyar transformation, Reference 1 (or equivalently, the Kaufman-Hall transformation, Reference 2) is used to select a subvector, \mathbf{x}_R , of vector \mathbf{x} .

$$\mathbf{x} = \mathbf{Gx}_R, \quad (3)$$

where \mathbf{G} is of order $(m \times n)$, $m > n$, and contains the $(n \times n)$ identity matrix as a submatrix. \mathbf{G} is such that,

$$\mathbf{K}_R = \mathbf{G}^T \mathbf{K} \mathbf{G}, \quad (4)$$

is precisely the stiffness matrix for the selected degrees of freedom. It is generally preferable, for convergence, to select all degrees of freedom in which \mathbf{f} -elements are not identically zero and all degrees of freedom in which large inertial loads are expected. The n -th order equations of motion are:

$$\mathbf{M}_R \ddot{\mathbf{x}}_R + \mathbf{K}_R \mathbf{x}_R = \mathbf{G}^T \mathbf{Bb}, \quad (5)$$

$$\text{where } \mathbf{M}_R = \mathbf{G}^T \mathbf{M} \mathbf{G}. \quad (6)$$

The equations are again reduced by selection of particular natural modes of motion (eigenvectors) of the reduced system. Generally these will correspond to lower frequency modes, but the spatial and temporal distribution of \mathbf{f} should be taken in account in making the selection.

If \mathbf{H} is the $(n \times p)$, $n > p$, matrix containing, as columns, the selected eigenvectors, and they are normalized such that,

$$\mathbf{H}^T \mathbf{M}_R \mathbf{H} = \mathbf{I}, \quad (7)$$

where \mathbf{I} is the $(p \times p)$ identity matrix, the equations of motion are:

$$\ddot{\xi} + 2\Omega\gamma\xi + \Omega^2\xi = \mathbf{H}^T \mathbf{G}^T \mathbf{Bb}, \quad (8)$$

where

$$\mathbf{x}_R = \mathbf{H}\xi, \quad (9)$$

and

$$\Omega^2 = \mathbf{H}^T \mathbf{K}_R \mathbf{H}, \quad (10)$$

is the diagonal matrix of squared-circular eigenfrequencies. A damping term has been introduced with uniform (scalar) damping ratio, γ .

The load or stress in elements of interest depends on the deformation:

$$\sigma = \mathbf{Ax} = \mathbf{AGH}\xi = \mathbf{D}\xi, \quad (11)$$

(mode displacement summation, Ch. 10, Ref. 3)

or

$$\sigma = \mathbf{AGH}\Omega^{-2} (\mathbf{H}^T \mathbf{G}^T \mathbf{Bb} - \xi) = \mathbf{D}\Omega^{-2} (\mathbf{Rb} - \xi), \quad (12)$$

(mode acceleration summation, Ch. 10, Ref. 3).

An element of σ may be a stress component, a finite element load or a reaction at a node. The load, or stress, vector σ is of dimension q , and \mathbf{A} , $(q \times m)$, is contained explicitly or implicitly in the structural analysis program. \mathbf{A} depends only on elastostatic properties of the system. The value of q may be less than one hundred while the value of m may be several thousands.

The subject transformation may now be introduced. It can be seen in the above equations that for each eigenanalysis, the transformations $\mathbf{D} = \mathbf{AGH}$ and $\mathbf{R} = \mathbf{H}^T \mathbf{G}^T \mathbf{B}$ must be computed for each weight distribution being analyzed. Let:

$$\mathbf{L} = \left(\frac{d^2}{dt^2} + 2\Omega\gamma\frac{d}{dt} + \Omega^2 \right). \quad (13)$$

Then the complete mode displacement solution may be written:

$$\sigma = \mathbf{AGH}^{-1} \mathbf{H}^T \mathbf{G}^T \mathbf{Bb} = \mathbf{DL}^{-1} \mathbf{Rb}. \quad (14)$$

Notice that L also contains G and H transformations implicitly. Let subscripts 1 and 2 distinguish eigenanalyses for two different weight conditions,

$$\begin{aligned}\sigma_1 &= D_1 L_1^{-1} R_1 b, \\ \sigma_2 &= D_2 L_2^{-1} R_2 b,\end{aligned}\quad (15)$$

then the subject approximation is:

$$\sigma_2 = D_1 T_{12} L_2^{-1} T_{12}^T R_1 b, \quad (16)$$

where

$$T_{12} = \begin{pmatrix} H_1 & H_2 \end{pmatrix}^{-1} H_1^T H_2. \quad (17)$$

The derivation of T_{12} is shown in the appendix. The motivation for substitution was the loss of the A matrix resulting from de-

gradation of a magnetic tape. It would have been very costly to reproduce the matrix. The structural model was in a stage of significant change at the time; so the recomputation was unjustified. The present computations are simply a computer experiment, a retrospective check of the accuracy of the earlier computation using the transformation as in equation (16).

SAM-D LAUNCHER

The Launcher Group/Missile Round unit of the SAM-D Air Defense System consists of a launcher mobilized on a semi-trailer vehicle, Figure 1. The launcher carries four missiles in canisters. The canisters serve as environmental and shipping containers and as launch cells. Each missile-canister unit is called a Missile Round. The missile rounds are attached to the erecting platform, Figure 1, and to one another by various connecting devices

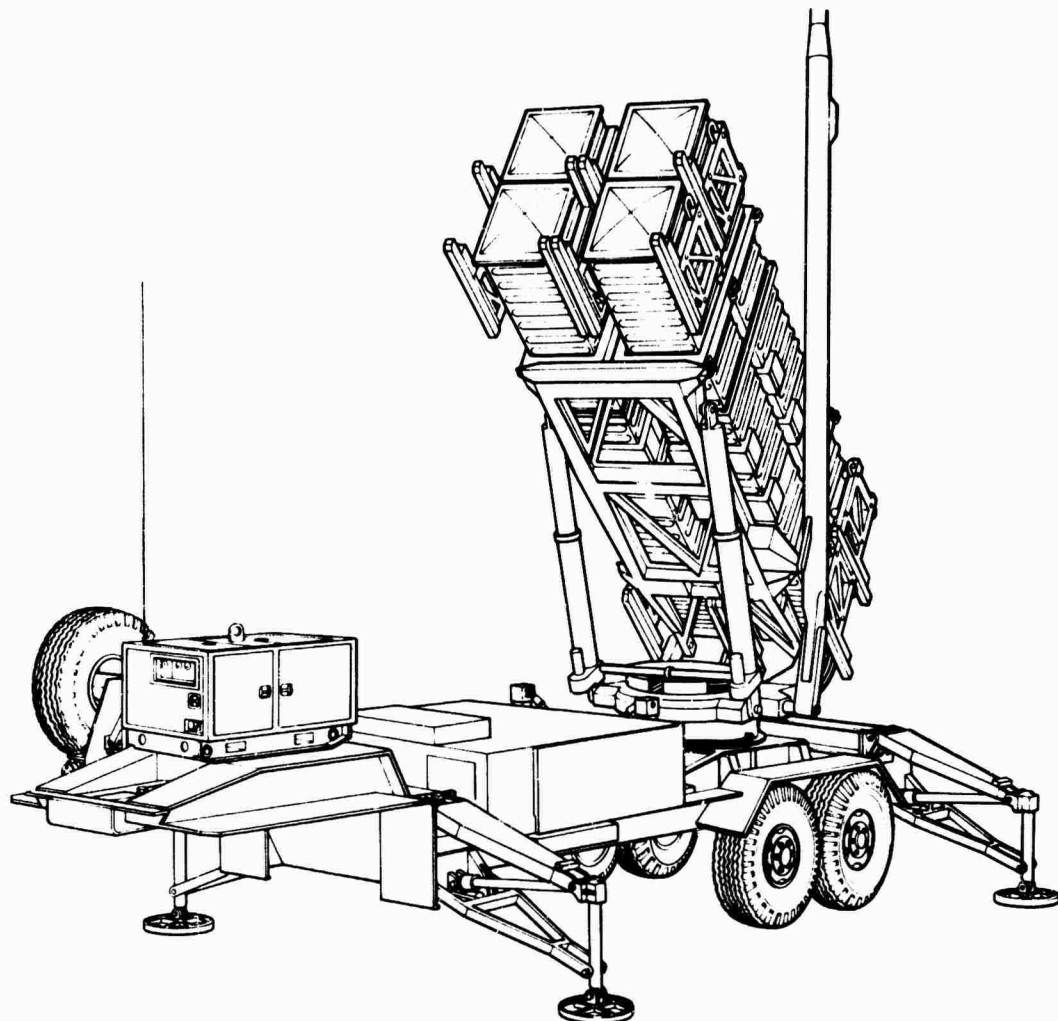


Figure 1. SAM-D Launcher Group Missile Round

on the two main frames of the canisters. There are two pads on the top and bottom of each main frame with either index holes or index pins at their centers. Tie rods complete the vertical and lateral joining of missile-round four pack and launcher platform. The launcher platform is elevated by two jacks. It is mounted on a turntable for training in azimuth. The launcher and other components are mounted on an XM860 trailer. When emplaced, the trailer bed is stabilized and leveled on outrigger jacks.

ANALYSIS OF LAUNCHER RESPONSE TO AIR BLAST

Substructural components of the Launcher Group with launcher platform erected were statically coupled to form a structural model with 1372 degrees of freedom. (The level of static analysis was actually finer, if all element degrees of freedom were retained, there would be over 6000.) The 1372 dof's were reduced to 168 by Guyan reduction and then to twelve by use of the lower frequency eigenvectors. The major part of the structural analysis and the eigenanalysis were performed using MAGIC, References 4 through 9. All computations after the static coupling were performed in single precision on the IBM 370. For the comparison, the zero azimuth configuration was analyzed with two weight conditions:

A. Four missiles aboard,

B. One missile on board, in upper left canister.

In condition A bilateral symmetry prevailed in both mass and stiffness distributions, and the lower four modes divided into symmetric and antisymmetric cases with closely spaced natural frequencies in pairs. This symmetric/antisymmetric characterization broke down at the fifth mode because of the essentially three-dimensional nature of the structure. In condition B, the dynamic coupling destroyed the symmetry, so there were distinct differences in the two eigenvector bases. The effect of the weight change may be judged by comparison of the frequency spectra for the two conditions:

Mode	Freq. A		Freq. B	
	Hz	Hz	Hz	Hz
1	2.4003		2.9518	
2	2.6407		3.2530	
3	4.1607		5.1584	
4	4.1544		5.3137	
5	5.3106		6.4975	
6	11.0343		13.1867	
7	11.5189		14.0462	
8	13.4243		16.3718	
9	16.1172		18.0412	
10	18.0924		21.7832	
11	19.7636		23.2010	
12	21.3796		24.7719	

For the comparison, the response of the structure was analyzed for the blast approaching from the side, front and rear with the launcher at zero azimuth. The loads examined were the platform reactions at the erector jacks and turntable trunnion, Figure 2. The comparative results are shown in Tables I, II and III. A full comparison of platform loads was made for all cases, but the results are partially reproduced here. Very similar results were obtained in the other computations. All the loads are expressed in relation to the same base value. The time-of-occurrence parameter, placed in parentheses beneath each load, is normalized by the fundamental period in each case. The values in the columns labeled "conventional" and "approximate" are to be compared: There is no significant difference in the conventional and the approximate results.

Table I
Comparison of Conventional and
Approximate Load Computations
Side-On Impingement, Four Missiles

Reaction	σ _{AA}		σ _{AB}	
	Conventional	Approximate	Conventional	Approximate
Figure 2	Pos.	Neg.	Pos.	Neg.
1	0.00 (0.00)	4.70 (0.38)	0.00 (0.00)	4.67 (0.38)
2	0.00 (0.00)	2.44 (0.26)	0.00 (0.00)	2.37 (0.27)
3	0.23 (0.14)	0.91 (0.44)	0.23 (0.14)	0.91 (0.44)
4	4.57 (0.37)	0.00 (0.00)	4.53 (0.37)	0.00 (0.00)
5	0.00 (0.00)	2.43 (0.26)	0.00 (0.00)	2.35 (0.27)
6	0.95 (0.44)	0.25 (0.13)	0.94 (0.44)	0.26 (0.38)
7	4.70 (0.29)	0.00 (0.00)	4.70 (0.28)	0.00 (0.00)
8	0.00 (0.00)	2.77 (0.29)	0.00 (0.00)	2.77 (0.28)
9	0.00 (0.00)	4.67 (0.28)	0.00 (0.00)	4.67 (0.28)
10	2.76 (0.28)	0.00 (0.00)	2.75 (0.29)	0.00 (0.00)

$$\sigma_{AA} = D_{AA}^{-1} R_{AA} b$$

$$\sigma_{AB} = D_{AB}^{-1} T_{AB} R_{AB} b$$

$$\sigma_{AA, pos} = \max_t \left[\sigma_{AA} \cdot U \left(\frac{t}{\tau_{AA}} \right) \right]$$

$$\sigma_{AA, neg} = \max_t \left[-\sigma_{AA} \cdot U \left(\frac{-t}{\tau_{AA}} \right) \right]$$

U: Unit step function

max: max value in integration interval
t

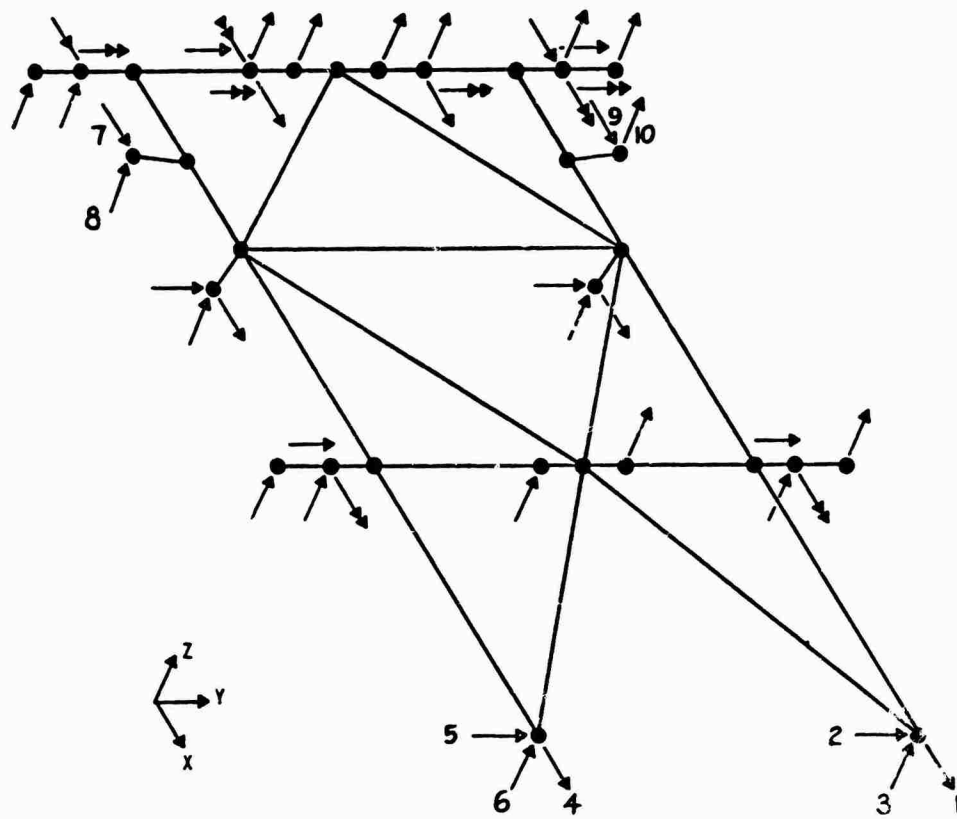


Figure 2. Platform Reactions, Trunnion: 1 thru 6, Erector Jacks: 7 thru 10.

Table II
Comparison of Conventional and Approximate Load Computations Side-On Impingement, One Missile

Reaction	σ_{BB}		σ_{BA}	
	Conventional	Approximate	Conventional	Approximate
Figure 2	Pos.	Neg.	Pos.	Neg.
1	0.00 (0.00)	5.37 (0.38)	0.00 (0.00)	5.40 (0.38)
2	0.00 (0.00)	2.63 (0.24)	0.00 (0.00)	2.70 (0.24)
3	0.49 (0.13)	1.25 (0.42)	0.49 (0.13)	1.25 (0.42)
4	5.07 (0.38)	0.00 (0.00)	5.10 (0.38)	0.00 (0.00)
5	0.00 (0.00)	2.62 (0.24)	0.00 (0.00)	2.68 (0.24)
6	1.12 (0.41)	0.44 (0.15)	1.12 (0.41)	0.44 (0.15)
7	5.30 (0.28)	0.00 (0.00)	5.33 (0.29)	0.00 (0.00)
8	0.00 (0.00)	3.13 (0.28)	0.00 (0.00)	3.14 (0.29)
9	0.00 (0.00)	5.17 (0.23)	0.00 (0.00)	5.13 (0.23)
10	3.03 (0.23)	0.00 (0.00)	3.03 (0.23)	0.00 (0.00)

$$\sigma_{BB} = D_B^{-1} L_B R_B b_s$$

$$\sigma_{BA} = D_A^{-1} T_{AB} L_B^{-1} T_{AB}^T R_A b_s$$

Table III
Comparison of Conventional and Approximate Load Computations Front-On Impingement, One Missile

Reaction	σ_{BB}		σ_{BA}	
	Conventional	Approximate	Conventional	Approximate
Figure 2	Pos.	Neg.	Pos.	Neg.
1	2.07 (0.88)	9.67 (0.32)	2.08 (0.88)	9.87 (0.32)
2	0.25 (0.73)	0.57 (0.44)	0.27 (0.73)	0.57 (0.45)
3	2.43 (0.39)	1.03 (0.08)	2.41 (0.39)	1.00 (0.08)
4	1.86 (0.88)	10.57 (0.38)	1.84 (0.88)	10.73 (0.37)
5	0.33 (0.72)	0.39 (0.44)	0.36 (0.72)	0.38 (0.44)
6	1.54 (0.40)	0.56 (0.08)	1.46 (0.41)	0.58 (0.08)
7	7.73 (0.40)	1.53 (0.88)	7.50 (0.40)	1.50 (0.88)
8	0.86 (0.88)	4.23 (0.40)	0.84 (0.88)	4.17 (0.40)
9	6.33 (0.31)	1.24 (0.88)	6.20 (0.31)	1.25 (0.88)
10	0.65 (0.88)	3.43 (0.42)	0.68 (0.88)	3.47 (0.44)

$$\sigma_{BB} = D_B^{-1} L_B R_B b_F$$

$$\sigma_{BA} = D_A^{-1} T_{AB} L_B^{-1} T_{AB}^T R_A b_F$$

PARTICULARITIES AND GENERALITIES

Obtaining and applying the transformation T requires a significant amount of computation. However, as compared to computing D and R this computation is generally of low order and can be performed in relatively small amount of computer core with no use of peripheral storage. Because the eigenvectors are linearly independent, $H^T H$ is positive definite; so the matrix inverse needed is the inverse of a positive definite symmetric matrix, which can be computed much more efficiently than the inverse of a general matrix, Reference 10.

There are a number of circumstances, other than the one elaborated in the paper, in which the subject transformation is useful. Some are mentioned above. If such use is planned, having the column order of the basic eigenvector set larger than the column order needed in the sets in which the approximation is to be used will improve accuracy. Reference 11 contains a useful algorithm to compute the overlap of two subspaces.

Another use of the transformation is the comparison of experimental and computed modal vectors. The transformation may indicate that measured modes are linear combinations of computed modes. Some of the differences in the two sets may be attributed to the difficulty of exciting pure modes when there is close frequency spacing, damping coupling, or poor shaker location. The eigenvectors should be normalized so the columns of T have unit length for this comparison.

In conclusion, it has been shown that the space spanned by the lower mode eigenvectors did not change markedly for a strong change in mass distribution in the case analyzed. This overlap will probably be found in most structural analyses, and as a consequence projections from the one subspace to the other may be used with accuracy when it is convenient.

REFERENCES

1. Guyan, R. J., Reduction of Stiffness and Mass Matrices, AIAA J., 3(2), February 1965, p. 380.
2. Kaufman, S. and Hall, D. B., Reduction of Mass and Loading Matrices, AIAA J., 6(3), March 1966, p. 550.
3. Bisplinghoff, R. L., Ashley, H. and Halfman, R. L., Aeroelasticity, Addison-Wesley, Reading, Massachusetts, 1955, Ch. 10.
4. Mallett, R. H. and Jordan, S., MAGIC: An Automated General Purpose System for Structural Analysis: Volume I. Engineer's Manual, AFFDL-TR-68-56, Volume I, Air Force Flight Dynamics Laboratory, Wright-Patterson AFB, Ohio, January 1969.

5. Jordan, S., Mallett, R. H. and Maddux, G. E., MAGIC: An Automated General Purpose System for Structural Analysis: Volume II. User's Manual, AFFDL-TR-68-56, Volume II, Air Force Flight Dynamics Laboratory, Wright-Patterson AFB, Ohio, July 1969.
6. DeSantis, D., MAGIC: An Automated General Purpose System for Structural Analysis: Volume III. Programmer's Manual, AFFDL-TR-68-56, Volume III, Air Force Flight Dynamics Laboratory, Wright-Patterson AFB, Ohio, January, 1969.
7. Jordan, S., MAGIC II: An Automated General Purpose System for Structural Analysis: Volume I, Engineer's Manual (Addendum), AFFDL-TR-71-1, Volume I, Air Force Flight Dynamics Laboratory, Wright-Patterson AFB, Ohio, May 1971.
8. Jordan, S. MAGIC II: An Automated General Purpose System for Structural Analysis, Volume II, User's Manual, AFFDL TR-71-1, Volume II, Air Force Flight Dynamics Laboratory, Wright-Patterson AFB, Ohio, January, 1971.
9. Gallo, A. M., MAGIC II: An Automated General Purpose System for Structural Analysis, Volume III, Programmer's Manual, AFFDL-TR-71-1, Volume III, Air Force Flight Dynamics Laboratory, Wright-Patterson AFB, Ohio, January, 1971.
10. Rubinstein, M. F., Structural Systems, Dynamics and Stability, Prentice-Hall, Englewood Cliffs, New Jersey, 1970, Ch. 4.
11. Bjorck, A., and Golub, G. H. Numerical Methods for Computing Angles Between Linear Subspaces, Mathematics of Computation, 27(123), July 1973.

APPENDIX: DERIVATION OF THE APPROXIMATE TRANSFORMATION

The subject transformation can be found in many places; e.g., the references at the end of this appendix. This derivation is appended in part for convenience of the reader and in part because it takes a geometric rather than an algebraic viewpoint. The former is believed to be more intuitively satisfying for structural engineers although the algebraic derivation is more concise.

$$T = \begin{bmatrix} H_1^T \\ H_2^T \end{bmatrix}^{-1} H_1^T H_2^T. \quad (A0)$$

The transformation is obtained by minimizing the magnitudes of the columns of E .

$$E = H_2 - H_1 T. \quad (A1)$$

The derivation follows. To simplify reading the notations let $H = H_2$ and $G = H_1$. Then let \underline{v} be expressed by components h in basis H and v by components g in basis G .

$$v = Hh, \underline{v} = Gg, \quad (A2)$$

and let,

$$g = Th. \quad (A3)$$

To make \underline{v} a minimum distance approximation of v , calculate T such that $\|v - \underline{v}\|^2$ is minimized. Using equation (A3),

$$\begin{aligned} \|v - \underline{v}\|^2 &= \|Hh - GTh\|^2 \\ &= h^T E^T Eh. \end{aligned} \quad (A4)$$

Because $E^T E$ is positive definite symmetric, the transformation T is exact only if $E^T E$ is the zero matrix. Since the off diagonals are bounded by the Schwarz inequality, minimizing the diagonal elements of $E^T E$ uniquely determines T . Let,

$$\begin{aligned} F(i, j, T) &= e_{pi} e_{pj} \\ &= h_{pi} h_{pj} - h_{pi} g_{pq} t_{qj} - t_{qi} g_{pq} h_{pj} \\ &\quad + t_{qi} g_{pq} g_{pr} t_{rj} \end{aligned} \quad (A5)$$

where $E = [e_{ij}]$, $H = [h_{ij}]$, etc.; and repeated indices p, q, r imply summation over the appropriate ranges. Then,

$$\begin{aligned} \frac{\partial F}{\partial t_{mn}}(i, j, T) &= \delta_{jn} \left(t_{qi} g_{pq} g_{pm} - h_{pi} g_{pm} \right) \\ &\quad + \delta_{in} \left(g_{pm} g_{pq} t_{qj} - g_{pm} h_{pj} \right) \end{aligned} \quad (A6)$$

where δ is the delta function.

The values of t_{ij} for which the derivatives of equation (10) are zero are solutions of,

$$G^T GT - G^T H = 0, \quad (A7)$$

from which equation (A0) follows.

The expression,

$$\left(H_1^T H_1 \right)^{-1} H_1^T, \quad (A8)$$

is the pseudoinverse of H_1 when $H_1^T H_1$ is non-singular, as it is for eigenvectors.

REFERENCES

- A1. Boullion, T. L. and Odell, P. L., *Generalized Inverse Matrices*, Wiley-Interscience, NY, 1971.
- A2. Rao, C. R., and Mitra, S. K., *Generalized Inverse of Matrices and Its Applications*, Wiley, NY, 1971.
- A3. Brock, J. E., *Optimum Matrices Describing Linear Systems*, AlAA J., Vol 6(7), July 1968.

LINEAR LUMPED-MASS MODELING TECHNIQUES FOR BLAST LOADED STRUCTURES

W. J. Liss, Jr., and N. J. DeCapua

Bell Laboratories
Whippany, New Jersey

The determination of building motions in a nuclear blast environment is essential in assessing the shock-mounting requirements for communications equipment in hardened installations. This paper presents linear lumped-mass modeling techniques employed in this determination. These techniques are applied to a rigid body soil-structure interaction case and to the flexural response of a buried building. Predicted responses are compared with measured accelerations obtained from full-scale TNT tests.

1. INTRODUCTION

To determine the expected motions of equipment in hardened buildings, the dynamic response of the building in a blast and the accompanying ground motion environment must be known. The first detailed model for predicting dynamic environments in Bell System hardened buildings was done by J. V. Poppitz [1], who developed a five-degree-of-freedom vertical model of the interior of a shallow buried building. In the Poppitz technique, slabs were modeled as single degree-of-freedom systems, and consequently, higher flexural modes were not included.

Subsequently a series of experiments was conducted by S. Wisnewski [2] at the Waterways Experimental Station (WES), Vicksburg, Mississippi, to either corroborate the Poppitz model or lead to a refinement of it. The steel structure employed in the WES tests was 6 ft by 6 ft in plan by 15 in. high, and it represented a two-story, 6-by-6 bay building buried in clay. The general conclusions reached by Wisnewski were that:

- The Poppitz five-mass model satisfactorily predicted displacement and velocity, and
- The accelerations predicted by the five-mass model were significantly less (1.3 to 6.7 times less) than the measured accelerations.

The results of the WES test and the conclusions drawn from them generally agreed with a theoretical study by L. W. Fagel [3] who analyzed the acceleration response of a plate subjected to blast loadings. He compared the

exact solution to solutions employing finite mode approximations and concluded that for systems with at least 1 percent of critical damping, nine modes were adequate to represent the plate's true response, and four modes may be non-conservative by up to 40 percent.

Further study of the WES data by Fagel [4] resulted in the following conclusions which differ somewhat from Wisnewski's initial observations:

- Acceleration response of small structures covered with soil can be appropriately calculated from a one-mode model for floor panels. The soil cover serves to damp the higher modes but does not add to the structure's mass.
- If no soil cover is provided or if some of the structure is above grade, floor panels should include higher modes.

Thus it seems that the Poppitz model is, in fact, a good technique for predicting vertical response of shallow buried buildings.

This paper uses the results of Poppitz and Fagel along with comparisons of data from full-scale blast loaded structures to develop a simple linear model for blast loaded above and below ground buildings. Coupled horizontal and vertical motions are included. The emphasis in the predictions is on the initial portion of the acceleration response since the peak acceleration usually occurs immediately after blast arrival. Moreover, a linear model can be expected to accurately predict only the initial response since longer term motions include the nonlinear behavior of the soil-structure interaction.

2. SOIL-STRUCTURE INTERACTION

2.1 Model of Rigid Body in Soil

The total response of a structure can be divided into two parts: (1) the rigid-body soil interaction and (2) the flexural response of the building members. The nature and magnitude of the first of these, rigid-body soil interaction, was documented [5] following a test performed during Operation Snow Ball on July 17, 1964. In the remainder of this section, simple linear modeling techniques are employed to predict these measured accelerations. Included in the Snow Ball test were two 5-ft-by-5-ft-by-6-ft solid concrete blocks which were buried in the ground and struck with a blast wave produced by a 500-ton TNT detonation. The first block was buried with its top flush with the ground while the second had a steel "sail" protruding 2 ft above grade. Load cells and accelerometers measured the magnitudes of the blast and the block response respectively. It remains to be seen how presently used soil-structure relationships can predict the actual response of the block.

Past models of soil-structure interaction have used the following stiffness relations for a rigid footing on an elastic half space [6].

$$\text{Vertical: } k_z = \frac{G}{1 - \nu} \beta_z \sqrt{4cd}, \quad (1a)$$

$$\text{Sliding: } k_x = 4(1 + \nu)G\beta_x \sqrt{cd}, \quad (1b)$$

$$\text{Rocking: } k_\theta = \frac{G}{1 - \nu} \beta_\theta 8cd^2, \quad (1c)$$

where G = shear modulus of soil,
 ν = Poisson's ratio of soil,
 c = half length along axis of rotation,
 d = half width perpendicular to axis of rotation, and
 $\beta_z, \beta_x, \beta_\theta$ = constants.

However, if the foundation is buried in the soil as in the case here, additional soil springs must be added to account for soil interaction with the vertical walls. The increased factor for vertical motion has been calculated [6], but at the time of this work there was no proven way to predict its effect on the horizontal and rocking stiffnesses.

To estimate this added stiffness, the vertical stiffness formula for a rigid plate on an elastic half space was used, i.e.,

$$K_{H \text{ walls}} = \frac{G'}{1 - \nu} \beta_z \sqrt{4cd}, \quad (2)$$

with the effective shear modulus, G' , in this direction to be much less than the actual modulus, G , to account for poorly compacted backfill at the site and the fact that it is not truly a half space in this direction. The various soil springs were then added to the block (Fig. 1) in a manner ensuring correct rotational stiffness.

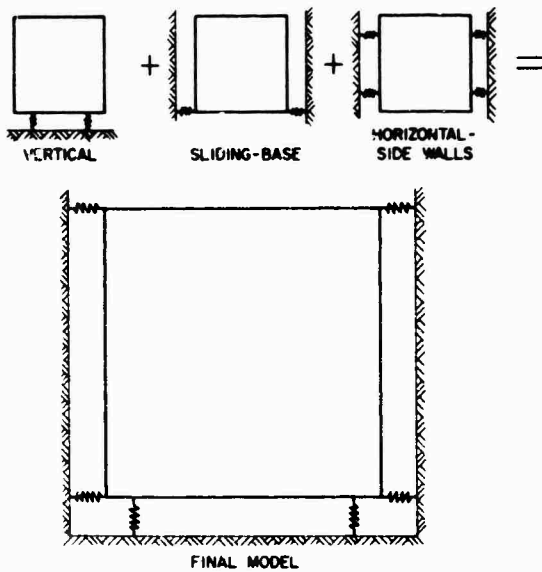


Fig. 1 - Soil springs for block

As shown in Fig. 1, four lumped masses were sized and located to preserve horizontal, vertical, and rotational inertia. A mathematical model of this arrangement was constructed to use in the Stiffness Matrix Structural Analysis Program [7] which determines the system's eigenvalues and eigenvectors. The three principle modes of vibration for one of the cases considered ($G = 4,000$ psi and $G' = 500$ psi) are shown in Fig. 2. The first is a coupled horizontal and rocking mode; the second is a pure vertical mode; and the third is nearly a pure rocking mode.

The response of the blocks under two combined dynamic inputs (ground motion and blast) can now be calculated using a modal analysis (see Appendix A). A computer program based on the modal analysis equations uses the eigenvalues, eigenvectors, modal damping, and appropriate forcing functions as input. Both the blast and ground motion were experimentally measured on site. The concept of modal analysis requires that the damping be small so that the eigenvalues and eigenvectors that are determined for an undamped system are good estimates of the actual eigenvalues and eigenvectors. If high damping is encountered for any particular mode during the analysis, it will result in some error whose

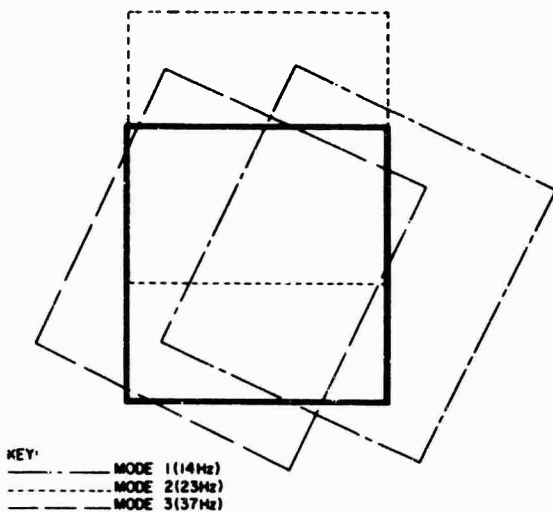


Fig. 2 - Mode shapes for block

magnitude depends on the degree of participation of that mode.

The loadings for a typical case are shown in Fig. 3. It is assumed that the loading on the top of the block is equal to the free field and can be approximated by a triangular pulse. The loading on the vertical buried surfaces is known to be equal to some fraction of the free field loading. This value may vary from 1/4 to 1 depending on the cohesiveness and moisture content of the soil [8]. For this case, best results were derived using a loading equal to 1/4 of the free-field value. The waveform of the free-field blast reflecting from the sail has been calculated [9] and approximated quite well by a single triangular pulse. The damping for the various modes of vibration has been well documented [6], and is given by

Vertical Damping Ratio:

$$D_z = \frac{0.425}{\sqrt{\beta_z}}, \quad \beta_z = \frac{(1 - \nu)m}{4\rho r_0^3}, \quad (3a)$$

Sliding Damping Ratio:

$$D_x = \frac{0.288}{\sqrt{\beta_x}}, \quad \beta_x = \frac{(7 - 8\nu)m}{32(1 - \nu)\rho r_0^3}, \quad (3b)$$

Rocking Damping Ratio:

$$D_\theta = \frac{0.15}{(1 + \beta_\theta)\sqrt{\beta_\theta}}, \quad \beta_\theta = \frac{3(1 - \nu)}{8} \frac{I_\theta}{\rho r_0^3}, \quad (3c)$$

where m = mass of foundation,

ν = Poisson's ratio of soil,

ρ = density of soil,

r_0 = equivalent circular radius of foundation, and

I_θ = moment of inertia of foundation.

Again, since at the time of the study there was no documentation available on the effect of side-wall soil on the horizontal and rocking damping, it was decided to use the corresponding formulae for unburied foundations on an elastic half space. This assumption will give conservative results, but it is felt to be reasonable since initial peak accelerations are generally not sensitive to this rigid body damping.

2.2 Response of Rigid Body to Blast and Ground Motion

Before the block response could be determined, a realistic estimate of the shear modulus, G , had to be made. Unpublished on-site static soil tests by G. Weissmann during full-scale TNT tests [5] indicate a value for the shear modulus, G , of 4,000 psi, except in the horizontal direction where some reduced value had to be used.

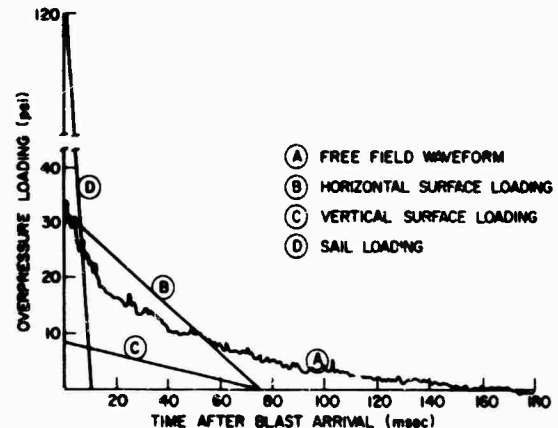
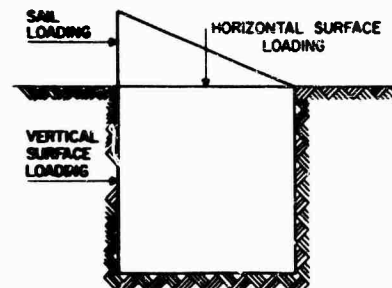
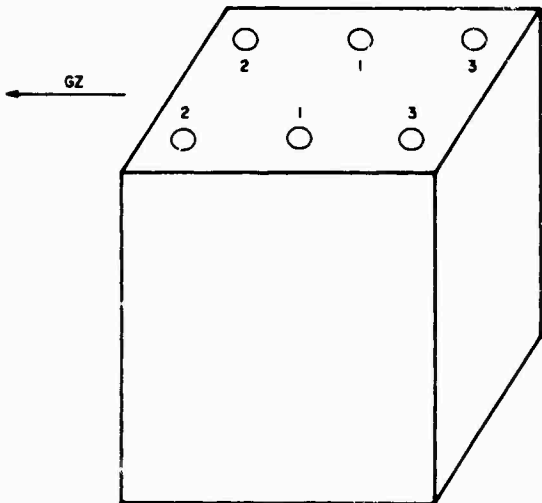


Fig. 3 - Overpressure loading of block with sail

The acceleration response of three points on the block (Fig. 4) were recorded at the test. The comparison of these peak responses to those calculated by the dynamic response program with various values of the horizontal soil shear modulus, G' , is shown in Table 1. The actual accelerometer records for the block with sail can be compared directly with the block response as predicted by the dynamic program (Fig. 5) for the case of $G = 4,000$ and $G' = 500$ psi. All of the predicted first peaks after blast arrival (50 msec) were within 9 percent or better of the actual response. However, the response prediction before and after the first peak did not meet with great success. The extremely high frequency response of the block immediately after the arrival of the blast is attributed to "ringing" of the sail structure which was not duplicated by the model. The response predictions for the block without the sail were quite good for two of the three points of interest. Both vertical peak responses were predicted to within 12 percent or better. However, the peak horizontal prediction was overestimated by nearly 40 percent.

This lumped-mass model has also been used to predict rotational displacements of the concrete blocks [10]. It was not expected that this model could accurately predict rotations since rotation response is of long duration and therefore involves the nonlinear behavior of the soil which can not be predicted with the simple linear approximations used here.



ACCELEROMETER NUMBER

1
2
3

DIRECTION
HORIZONTAL
VERTICAL
VERTICAL

Fig. 4 - Accelerometer locations on block

TABLE 1

Acceleration Response

Case	Gage 1 Horizontal (g's)	Gage 2 Vertical (g's)	Gage 3 Vertical (g's)
Buried Block With Sail			
1. $G = 4,000$ $G' = 2,000$	20.0	7.5	9.2
2. $G = 4,000$ $G' = 500$	18.7	6.4	10.0
3. Actual Response	17.2	6.7	10.2
Buried Block Without Sail			
1. $G = 4,000$ $G' = 2,000$	4.8	4.8	6.2
2. $G = 4,000$ $G' = 500$	3.2	5.3	5.6
3. Actual Response	2.3	6.0	5.2

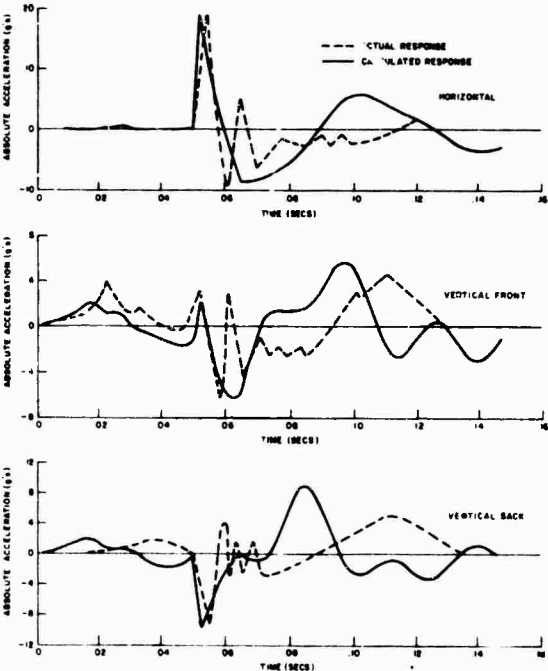


Fig. 5 - Measured and predicted response of block with sail

However, a complex soil-foundation model, including nonlinear effects, has been developed

by G. Weissmann [11], whose results show that the linear model predicts the actual rotations reasonably well for this case. Two accelerometers were used to measure peak block rotations of 6.5 and 10 milliradians — the difference in values probably caused by instrumentation inaccuracy. The lumped-mass model predicted a peak rotation of 8.25 milliradians.

The overall results of this test indicate that the actual peak acceleration responses of both blocks can be calculated very well using a linear dynamic motion program and a value for the horizontal shear modulus for the poorly compacted backfill of $G' = 500$ psi — much less than the actual measured shear modulus G .

3. RESPONSE OF AN UNDERGROUND BUILDING TO BLAST

3.1 General

Section 2 discussed the motion of a rigid foundation in a blast and the accompanying ground motion environment and recommended shear moduli. This information can now be used to develop a model of an underground structure that includes both rigid-body and flexural modes.

The modeled structure is an underground precast manhole, 26 ft by 13 ft with an 8-foot ceiling, as shown in Fig. 6. This particular structure was chosen to develop the model

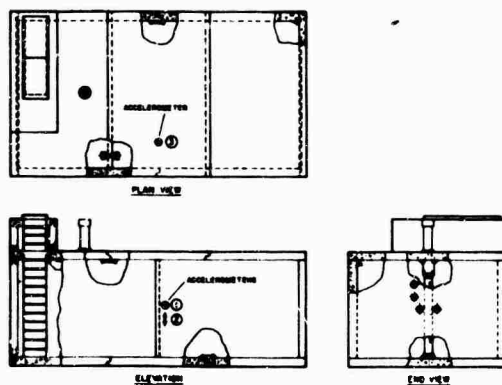


Fig. 6 - Manhole and accelerometer locations

because it was instrumented in a full-scale TNT blast environment [12]. Thus the monitored accelerations can be compared with predicted values, and the validity of the modeling techniques can be judged. The techniques employed are all linear and result in a lumped-mass, two-dimensional (vertical and horizontal) frame model of the actual structure.

3.2 Stiffness Model

The manhole is modeled as a two-dimensional frame as shown in Fig. 7. Soil-spring stiffnesses are determined as in Section 2 where it is shown that the effective horizontal shear modulus is approximately an order of magnitude less than the vertical or measured shear modulus. Since the compacting and settlement time for the block and manhole are very similar, the shear moduli to be employed are $G = 4,000$ psi and $G' = 500$ psi. The vertical value was obtained from data taken during Operation Snowball (1964) [5] for a location very close to the manhole location used in Event Dial Pack [12].

Because the precast slabs under consideration act as one-way slabs, the stiffness properties of the roof, base slab, and walls are the actual stiffnesses [13]; i.e., $I_{\text{wall}} = 2770 \text{ in.}^4$, $I_{\text{roof}} = 2235 \text{ in.}^4$, and $I_{\text{base}} = 2175 \text{ in.}^4$, for a 9-ft width. The stiffness of the interior support, which is primarily a compression member, results from a framework running down the center of the manhole as shown in Fig. 6. Also, since the precast slabs are keyed to each other, the joints are such that they are not moment carrying. These locations are indicated by circles in Fig. 7.

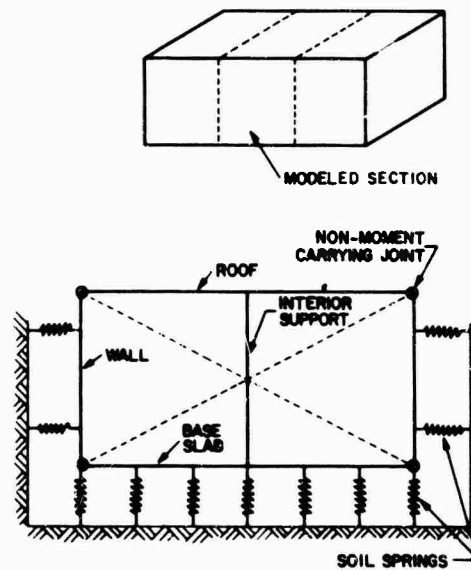


Fig. 7 - Stiffness model of manhole

Shear wall resistance is artificially achieved by two diagonal members as shown in Fig. 7. The members are sized to give the same lateral stiffness as that of the building acting as a shear beam.

3.3 Mass Model

A mass model of the system is necessary to determine eigenvalues and eigenvectors. Since the useful eigenvalue programs for structures are based on a mass model having lumped masses, it is necessary to model the continuous structure with an equivalent lumped-mass model. In some previous investigations, each element (such as a beam or slab) was modeled with one lumped mass. As mentioned previously [13], this type of assumption (especially for above-ground buildings) could lead to accelerations of significantly less g's than those predicted by a continuous mass model.

The technique [14] for modeling a continuous element by a single lumped mass is based on equating equivalent and actual kinetic energies, while equivalent loadings on these masses are determined by equating potential energies. This generally gives a good one-mode approximation. As an extension of this one-mass (one-mode) model, a three-mass model is proposed and used here. The objective of this approach is to include several higher modes of the element that could have a significant effect on predicted accelerations. The technique for determining the mass factors for converting from a continuous beam or one-way slab to a three-mass beam is presented in Appendix B. To verify the improvement over the one-mass assumption, Appendix C compares the acceleration responses of a blast-loaded, simply supported beam when modeled as a continuous beam, a one-mass beam, and a three-mass beam. The comparison shows that the addition of a second and third mode leads to a closer estimate of the acceleration response, as indicated in Fagel's study [3].

If the structure had included plate elements instead of beams or one-way slabs, the lumped-mass modeling would have been more complicated since the stiffness, as well as the mass and loading, would have had to have been modified. Also, many of the complex modes of a continuous plate would have been lost in modeling it as a beam. The factors necessary in modeling a plate as a lumped mass beam are indicated in Appendix D which shows that to obtain a reasonable comparison with continuous solutions, the plate must be modeled as a seven-mass beam instead of the three masses used for the one-way slab.

From Appendix B the three-mass model of the simply supported-clamped (SS-C) beam shown in Fig. 8 is related to the continuous mass beam as follows:

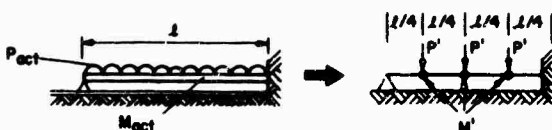


Fig. 8 - Continuous beam modeled as a three-mass beam

$$M' = 0.232 M_{act},$$

and

$$P' = 0.25 P_{act}. \quad (4)$$

Similarly, for a Simply Supported-Simply Supported (SS-SS) beam the relations are

$$M' = 0.247 M_{act},$$

and

$$P' = 0.263 P_{act}. \quad (5)$$

These mass factors can now be used to develop a mass model of the manhole as indicated in Fig. 9. As shown, masses M' are the three-mass equivalents determined by Eqs. (4) where the actual mass M_{act} is the slab mass

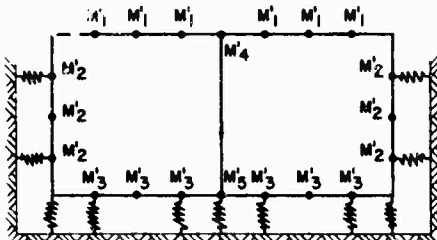


Fig. 9. - Mass model with soil springs

only and does not include any additional soil mass. This assumption is consistent with Fagel's findings [4] which are summarized in the introduction of this paper. The masses M'_2 and M'_3 , are the three-mass equivalents indicated by Eq. (5). Masses M_4 and M_5 are the lumped mass approximations of the interior support.

3.4 Frequencies and Mode Shapes

Figs. 7 and 9, the stiffness and mass models of the manhole, respectively, can now

be used (employing the JPL program [7]) to determine the system's frequencies and mode shapes (eigenvalues and eigenvectors).

Fig. 10a shows the first three modes, which are primarily rigid body, and Fig. 10b shows the second three modes, which are mainly flexural. Higher modes, although included in the results, are not shown in these figures.

3.5 Modal Damping

Before the dynamic response of the structure can be determined, the proper damping must be assigned to each mode. To facilitate this it is necessary to separate the rigid body and flexural modes. Rigid body modal damping is determined by the techniques discussed in Section 2. All flexural modes are assigned a damping value of 20 percent of critical. This is considered high for flexural damping of concrete structures, however Fagel [4] has indicated that the soil does damp the higher modes significantly. Thus the 20 percent value is considered reasonable.

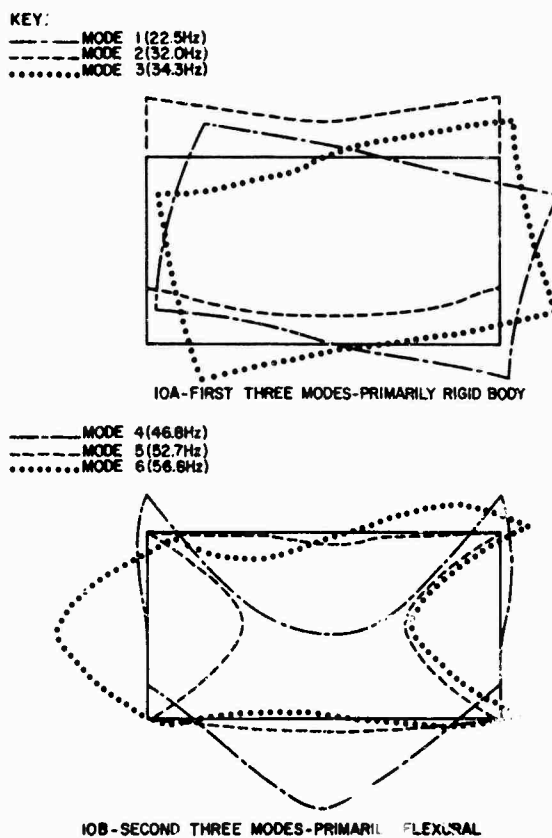


Fig. 10 - Mode shapes for manhole

3.6 Structural Response

The blast induced response of the structure can now be predicted by employing the modal analysis program (see Appendix A for a discussion of the program equations). Previously determined eigenvalues, eigenvectors, modal damping, and blast loading on the structure are the necessary input.

Unfortunately, the manhole was located at an anomalous overpressure location, since the two surface pressure gages on the same radius from ground zero and at about 5 ft from each wall of the structure indicated different free-field overpressures. These overpressures are shown in Fig. 11. Thus it was necessary to

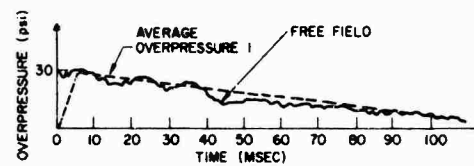
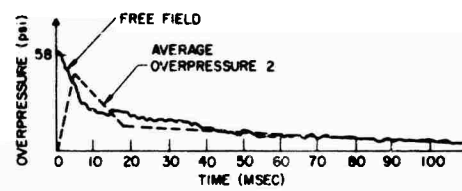


Fig. 11 - Overpressure loading for manhole

use two loading configurations in an attempt to get predictions that at least bound the measured values. The average free-field overpressure used to generate the loadings employed in the modal analysis program were determined by standard techniques [9] and are designated overpressures 1 and 2 in Fig. 11.

Loads on roof elements were determined from the full, average free-field overpressure by employing the load factor given in Eq. (4). The horizontal loadings on the wall elements were determined from an overpressure loading which is 1/4 of the average free-field overpressure and the load factors of Eq. (5). This 1/4 loading is consistent with the generally lower shear modulus on the side walls as indicated in Section 2 and the standard procedures of blast loadings on below-ground structures [8].

Three manhole acceleration histories were recorded in Event Dial Pack [12], specifically, the vertical response of the roof and the vertical and horizontal responses of a point on the manhole wall. The locations and directions of these three accelerometers are shown in Fig. 6.

Fig. 12 compares the measured manhole accelerations with the predicted responses resulting from overpressures 1 and 2. The peak accelerations for these cases are listed in Table 2.

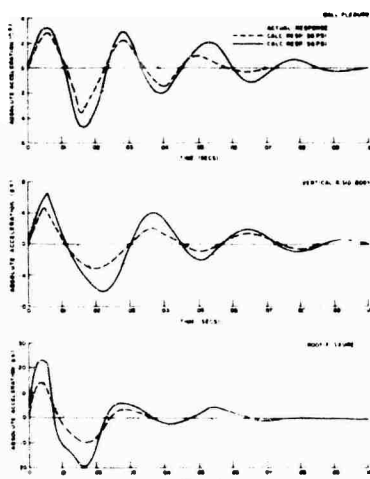


Fig. 12 - Measured and predicted response of manhole

TABLE 2
Peak Accelerations

	Roof Vertical	Wall Horizontal	Wall Vertical
Measured	16.0	5.4	9.0
Predicted			
Overpressure 1	14.0	3.5	4.5
Overpressure 2	22.5	4.7	6.5

As can be seen, the predicted peak-vertical roof acceleration for the two overpressure loadings bound the measured peak acceleration. Also, the measured time response is very similar to the predicted roof response (see Fig. 12a). The peak horizontal acceleration is underestimated by 13 percent using overpressure 2 and by 35 percent using overpressure 1. This indicates that the assumption of a horizontal load equal to 1/4 of the vertical load is slightly unconservative for the soil conditions existing at

the manhole. Also, Fig. 12b shows that the predicted and measured horizontal-acceleration-vs-time responses of the wall compare favorably for the first 30 msec, which is the important part of the response. Fig. 12c shows that predictions of the peak vertical-wall acceleration resulting from overpressure 1 is well below the measured value, while the peak value predicted from overpressure 2 is somewhat closer to the measured value. This may be due to a superimposed ground motion not considered in these calculations or to the technique of modeling a continuous element with a lumped-mass element. In the modeling indicated in Appendix B, it was not possible to preserve vertical reactions; and since the reactions of the roof elements are the vertical loadings on the wall elements, inaccuracies are inherent. Also, calculations have indicated that the reactions resulting on equivalent lumped-mass elements are always lower than the true reactions. This seems to be consistent with the results just discussed.

4. SUMMARY

The main points discovered or verified by this study may be summarized as follows:

1. The equivalent mass of the soil is a quantity postulated by past models that had to be added to the mass of the structure. This quantity was not used and apparently not needed in predicting the response of small shallow buried structures.
2. At the time of this work, there was no known method for determining the amount of horizontal soil stiffness of a buried structure. This value has been estimated in this paper through the use of a formula for soil stiffness in the vertical direction with an effective shear modulus, G' , which is less than the actual shear modulus, G . The specific value of G' does not have a large effect on the flexural response and the following guideline is considered reasonable:

G'/G	Site Condition
1/8	New site
1/2	Old site with well settled backfill

Since the completion of this study, M. Novak [15] has published a paper on embedded foundations which presents relationships that are probably more accurate than the procedure given here for rigid body stiffness and damping in the horizontal direction.

3. Past estimates of the horizontal blast loading on a shallow buried building range from 1/4 to 1 times the vertical free-field loading. Results of the present analysis show the factor of 1/4 to be slightly unconservative for this particular soil and weapon yield condition. It is

recommended that a factor of 1/2 to 1 be used for conservative predictions of building response to large-yield nuclear blast environments.

4. Because of the high soil damping and its effect on the higher modes, the one-mode (one-mass) approximation, although not documented in this study, and the three-mode (three-mass) approximation of the building response prove to be almost indistinguishable — each gives peak responses to within accuracies recorded in Section 3.6. Thus it is recommended that belowground structural elements need only be modeled as one-mass beams.
5. To obtain accurate results, building elements with only structural damping (5 percent to 10 percent) present (aboveground buildings and interior elements of belowground buildings) require a higher number

of lumped masses than those with high soil damping. Table 3 indicates the accuracy of lumped-mass systems with no damping as compared with continuous systems. Thus to predict responses within 20 percent accuracy, beams and one-way slabs require a three-mass model, while plates and two-way slabs require a seven-mass model.

6. In the element modeling technique described, continuous slabs and plates are converted to lumped-mass beams. Comparison of predicted and measured accelerations seems to indicate that the modeling technique is satisfactory for predicting vertical response of roof elements and horizontal response of wall elements, but is lacking in that element reactions are not preserved. These reactions are underestimated when employing the techniques described here.

TABLE 3
Accuracy of Lumped-Mass Systems

	Number of Masses In Beam Model	Peak Lumped Mass Response Peak Continuous Response
Beams or One-Way Slabs	1	0.69
	3	0.81
Plates or Two Way Slabs	1	0.43
	3	0.47
	7	0.83

APPENDIX A MODAL ANALYSIS PROGRAM

The modal analysis technique is based on decoupling the following equations of motion:

$$[m]\{\ddot{u}\} + [c]\{\dot{u}\} + [k]\{u\} = \{F(t)\} - [m]\{\ddot{s}\} = \{Q(t)\}, \quad (A1)$$

where $[m]$ = square mass matrix,

$[c]$ = square damping coefficient matrix,

$[k]$ = square stiffness matrix,

$\{F(t)\}$ = forces applied to each mass,

$\{\ddot{s}\}$ = column matrix of input accelerations, and

$\{u\}$ = column matrix of relative displacements.

The transformation which achieves this decoupling is

$$\{u\} = [\phi]\{\xi\}, \quad (A2)$$

where $[\phi]$ = square matrix of eigenvectors (mode shapes),

$\{\xi\}$ = column matrix of generalized coordinates,

and the decoupled equations are

$$\begin{aligned} \{\ddot{\xi}\} + 2[\beta]_D \{\dot{\xi}\} + [\lambda]_D \{\xi\} \\ = [M_G]_D^{-1} [\phi]^T \{Q(t)\}, \end{aligned} \quad (A3)$$

where $[\beta]_D$ = diagonal matrix of modal damping,

$[\lambda]_D$ = diagonal matrix of eigenvalues (frequencies), and

$$[M_B]D = \text{diagonal matrix of generalized masses.}$$

This is a system of n uncoupled equations. The solution of each equation that describes a structure with excitation $Q(t)$ is obtained by choosing a small integration interval Δt and representing the input $Q(t)$ by a linear function in this interval. Analytic solutions exist for these second-order linear differential equations with linear forcing functions. Thus each uncoupled equation can be solved by using the responses at the end of the previous interval

as the initial conditions for the subsequent interval.

The total solution for each u , \dot{u} , and \ddot{u} is obtained by transforming back from ξ to u through Eqs. (A2). A computer program was developed to accept the frequencies and mode shapes as well as modal damping, lumped masses, and digitized input, and to employ the modal analysis technique, as described above, to determine the response of each mass point in the system. Time-history plots of displacement and acceleration are routinely generated.

APPENDIX B EQUIVALENT THREE-MASS MODEL OF A CONTINUOUS BEAM

The blast response of the midpoint of a continuous beam can be equated to that of a three-lumped-mass model if the correct load and mass conversion factors can be determined. The easiest way to accomplish this is to first equate both the continuous and three-lumped-mass beam to a one-lumped-mass model. The conversion between a continuous beam and a one-lumped-mass beam is known [14] to be

$$M = 0.45 M_{act},$$

and

$$P = 0.58 P_{act}, \quad (B1)$$

where P_{act} and M_{act} are the continuous (or actual) load and mass, and P and M are the equivalent load and mass for a single lumped mass as shown in Fig. B1.

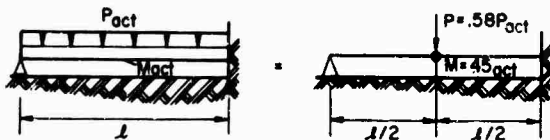


Fig. B1 - One-mass model of continuous beam

It remains therefore, to find the correct conversion between the three- and the one-lumped-mass models indicated in Fig. B2. To determine the mass factor, K_M , the kinetic energies of the two beams must be equated, i.e.,

$$\frac{1}{2} \sum_{n=1}^3 M_n V_n^2 = \frac{1}{2} M V^2, \quad (B2)$$

where $M_n = n^{\text{th}}$ mass, and

$$V_n = \text{velocity of } n^{\text{th}} \text{ mass.}$$

It is assumed that the velocity distribution is in the same form as the static deflection curve for the same beam, so

$$V = 4V_c \left[\frac{x}{l} - 3\left(\frac{x}{l}\right)^3 + 2\left(\frac{x}{l}\right)^4 \right], \quad (B3)$$

where V_c is velocity of center of beam. Equating the kinetic energies results in

$$M = 1.935 M'. \quad (B4)$$

This mass must equal the one-lumped-mass equivalent of the continuous beam. Thus

$$M = 1.935 M' = 0.45 M_{act}, \quad (B5)$$

or

$$M' = 0.232 M_{act}. \quad (B6)$$

The load factor, K_L , is determined by equating the strain energies of the beams, i.e.,

$$\sum_{n=1}^3 \frac{P_n y_n}{2} = \frac{1}{2} P y, \quad (B7)$$

where P_n = load on n^{th} mass and

$$y_n = \text{deflection of } n^{\text{th}} \text{ mass.}$$



Fig. B2 - One-mass model of three-mass beam

The deflection curve for this beam is

$$y = 4y_c \left[\frac{x}{l} - 3 \left(\frac{x}{l} \right)^3 + 2 \left(\frac{x}{l} \right)^4 \right], \quad (B8)$$

where y_c is center deflection.

This reduces to

$$P = 2.32 P'. \quad (B9)$$

This load must equal the load of the one-lumped-mass equivalent of the continuous beam. Thus

$$P = 2.32 P' = 0.58 P_{act}, \quad (B10)$$

or

$$P' = 0.25 P_{act}. \quad (B11)$$

It should be emphasized that this three-lumped-mass model is based solely on a first-mode static deflection shape [Eqs. (B3) and (B4)], and it remains to be shown whether this leads to an accurate prediction of the exact second and third frequencies. This question is discussed in Appendix C.

APPENDIX C

COMPARISON OF BLAST RESPONSE OF 3-MASS BEAM TO CONTINUOUS SOLUTION

The improvement in predicted blast induced accelerations of the three-mass model over the one-mass model for beams or one-way slabs can be indicated by direct comparison with a continuous solution. Consider a simply supported beam with the triangular blast loading as indicated in Fig. C1.

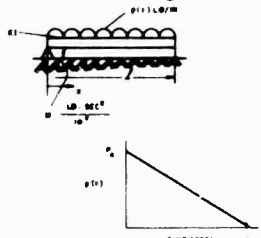


Fig. C1 - Beam loading

The exact solution to this problem, including all higher modes, for the location $x = l/2$ is known [16] to be

$$\tilde{y}\left(\frac{l}{2}, t\right) = \frac{4p_0}{m\pi} \sum_{n=1,3,5,\dots} \left[\frac{1}{n} \cos\left(\omega_n t - \frac{1}{\omega_n t_d} \sin \omega_n t\right) \sin \frac{n\pi}{2} \right], \quad (C1)$$

where

$$\omega_n = \frac{n^2 \pi^2}{l^2} \sqrt{\frac{EI}{m}}. \quad (C2)$$

The technique discussed in Appendix B can now be used to develop an equivalent three-mass model of the continuous beam. This is shown in Fig. C2 with the equivalent one-mass model.

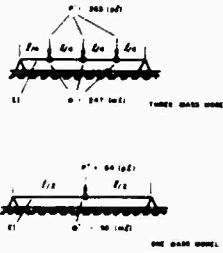


Fig. C2 - Beam modeling

For the specific case when $E = 4 \times 10^6$ psi, $I = 2235 \text{ in.}^4$, $l = 75 \text{ in.}$, $m = 0.2065 (\text{lb sec}^2)/(\text{in.}^2)$, $p_0 = 2880 \text{ lb/in.}$, and $t_d = 0.120 \text{ sec}$, which is similar to the slabs in the precast manhole with a corresponding loading, the following characteristic frequencies result:

TABLE C1

Frequency Comparison

Mode	Continuous Solution (Hz)	3-mass Model (Hz) [7]	One-mass Model (Hz)
1	58.0	58.4	58.4
2	232.0	231.9	-
3	522.0	492.5	-
4	930.0	-	-
5	1450.0	-	-
	⋮	-	-

As seen in Table C1, the one-mass model matches the first frequency accurately. However, the three-mass model yields three modes,

with the first and second frequencies comparing very closely with the continuous solution while the third mode is only 5 or 6 percent below the continuous frequency. Thus the three-mass model does include accurate second and third frequencies and should yield a better acceleration prediction in a blast environment than the one-mass model.

Fig. C3 shows the zero damping acceleration time response beam center as determined from (1) the continuous solution, Eq. (C1), (2) the three-mass model employing a modal analysis, and (3) the one-mass solution [17]. The one-mass solution is of course a single-frequency response and shows a peak acceleration of 47 g's; the three-mass model responds in two frequencies (the first and third) and its peak acceleration is 55 g's. These compare to the continuous solution peak of 68 g's. Thus,

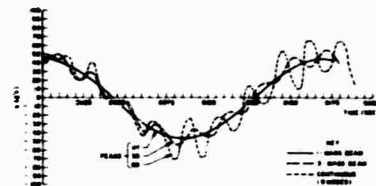


Fig. C3 - Beam modeling comparisons

for the zero damping case, the one-mass model gives a peak acceleration 31 percent below the continuous solution and the three-mass model gives a peak acceleration 19 percent below the continuous solution -- a significant improvement. These percentage differences would of course be reduced significantly when damping is included.

APPENDIX D

MODELING A CONTINUOUS PLATE AS A LUMPED-MASS BEAM

The modeling of the response of the center of a continuous plate by a lumped-mass beam can be achieved by employing the same techniques as employed for the modeling of a continuous beam by a lumped-mass beam as shown in Appendices B and C.

Consider the uniformly loaded, simply supported square plate shown in Fig. D1 and the equivalent three-mass beam whose center response will hopefully model the center response of the continuous plate. As before, the equivalence between the three-mass and one-mass models is first established. Then, because the equivalence between the simply supported plate and the one-mass model is known [18], it is

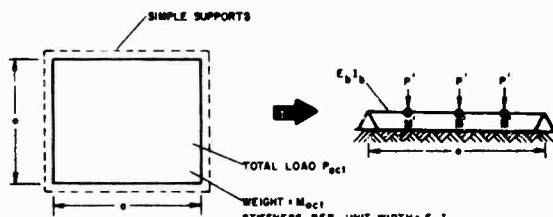


Fig. D1 - Three-mass beam model of plate

possible to find the three-mass beam which is the equivalent of the continuous plate. This results in the following relationships:

$$M' = 0.152 M_{act},$$

$$P' = 0.185 P_{act}, \quad (D1)$$

$$\text{and} \quad I_b E_b = 2.31 E_s I_s. \quad (D1)$$

Note that in this modeling the stiffness of the three-mass beam must also be changed to achieve equivalence, whereas this was not necessary in modeling either the continuous beam or the one-way slab as lumped-mass beams. The uncertainties involved in this modeling are greater than those in the modeling indicated in Appendices B and C since many of the complex plate modes are lost in modeling it as a lumped-mass beam. Also, the equivalence is once again based on a first-mode deflection shape. Thus a comparison with the continuous solution is necessary to corroborate the validity and possible advantages of this modeling.

The zero-damping acceleration response at the center point of the continuous plate from a step load is given by [3]

$$\ddot{y}(t) = \frac{P_o a^2}{M_{act}} \frac{16}{\pi^2} \sum_{i=1,3,5,\dots} \sum_{j=1,3,5,\dots} \frac{\sin(i\pi/2)}{i} \frac{\sin(j\pi/2)}{j} \cos \omega_{ij} t, \quad (D2)$$

where P_o is overpressure in psi, M_{act} is total weight, and

$$\omega_{ij} = \frac{\pi^2}{a^2} (i^2 + j^2) \sqrt{\frac{D}{\rho}}, \quad (D3)$$

where

$$D = \frac{Eh^3}{12(1-\nu^2)}.$$

Consider the specific case of $M_{act} = 200,000$ lb, $a = 222$ in., $E_s = 4 \times 10^6$ psi, $I_s = 130$ in.⁴/in., $P_0 = 50$ psi, $\rho = 150$ lb/in.³, and

$\nu = 1/3$. A plot of the response for this case, including the first nine modes (which Fagel [3] indicates is a good approximation of the exact response) is shown in Fig. D2. Also shown are the response of the center point of the equivalent three-mass beam obtained from employing the JPL program [7] to obtain eigenvalues and eigenvectors, a modal analysis (Appendix A), and the response of the one-mass model [19].

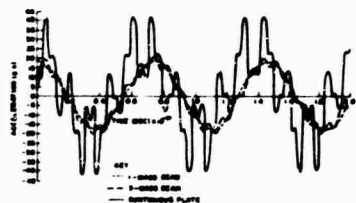


Fig. D2 - One- and three-mass beams vs continuous plate

The peak acceleration obtained from the continuous plate solution is 41 g's. This compares with 18 g's for the one-mass beam and 20 g's for the three-mass beam. Thus, it is obvious that the three-mass model, which includes three frequencies, is only slightly better than the one-mass model and about a factor of two less than the response of the continuous plate.

To obtain a better estimate of the acceleration response of the plate, it is necessary to develop a model that includes more than three frequencies. A seven-mass model would yield seven modes and would almost certainly give more accurate results. This model is shown in Fig. D3. Employing previous techniques results in the following equivalent mass, load, and stiffness for the seven-mass beam:

$$M' = 0.077 M_{act},$$

$$P' = 0.1265 P_{act},$$

and

$$L_b E_b = 2.31 a E_s I_s. \quad (D4)$$

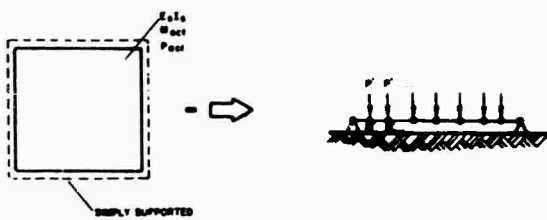


Fig. D3 - Seven-mass beam model of plate

The response of this seven-mass beam is shown in Fig. D4 and is compared with the continuous-plate solution. The peak acceleration for the seven-mass model is 35 g's, which is a good estimate of the 41-g continuous-plate peak acceleration and is far better than the three-mass peak of only 20 g's. Thus it is clear that

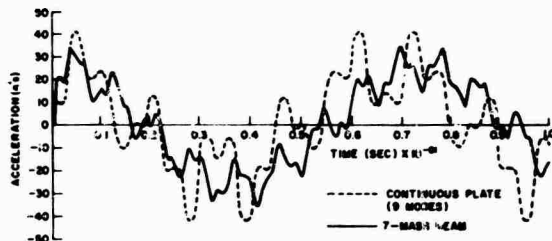


Fig. D4 - Seven-mass beam vs continuous plate

when modeling a continuous plate element with a lumped-mass beam, seven masses are necessary to obtain reasonable estimates of the peak accelerations. It should also be noted that these are all zero damping results, and when some amount of damping is included, the differences between the one-, three- and seven-mass peak accelerations and the continuous-plate accelerations are smaller.

REFERENCES

1. J. V. Poppitz, "Simplified Method for Determining the Dynamic Response of a Typical Hardened Buried Building," The Shock and Vibration Bulletin, 1968.
2. S. E. Wisnewski, unpublished work.
3. L. W. Fagel, "Acceleration Response of a Blast-Loaded Plate," The Shock and Vibration Bulletin, Jan. 1972.
4. L. W. Fagel, unpublished work.
5. Symposium Proceedings: Operation Snow Ball, Vol 1, Defense Atomic Support Agency, p. 144, Aug. 1965.
6. F. E. Richart, Jr., et al, "Vibrations of Soils and Foundations," p. 350, Prentice-Hall, 1970.
7. "Stiffness Matrix Structural Analysis Program," Jet Propulsion Laboratory, JPL-A Tech. Report No. 32-774, 1965.
8. "Principles and Practices for Design of Hardened Structures," Air Force Design Manual, Tech. Doc. No. AFSWC-TDR-62-138, Dec. 1962.
9. S. Glasstone, "The Effects of Nuclear Weapons," U. S. Atomic Energy Commission, Apr. 1962.
10. E. F. Witt, et al, 'Blast Induced Foundation Motion and Loading," DASA, to be published.
11. G. Weissmann, "A Mathematical Model of a Vibrating Soil-Foundation System," Bell System Technical Journal, Vol 45, pp. 177-228, Jan. 1966.
12. Event Dial Pack - Preliminary Report, Vol 1, Part 2, Defense Atomic Support Agency, pp. 497-512, May 1971.
13. "Design of Structures to Resist Nuclear Weapons Effects," ASCE Manual No. 42, p. 95, 1964.
14. J. M. Biggs, Introduction to Structural Dynamics, pp. 199-244, McGraw-Hill, 1964.
15. M. Novak, "Vibrations of Embedded Footings and Structures," ASCE Structural Engineering Meeting, April 9-13, 1973.
16. Biggs, p. 164.
17. Biggs, p. 43.
18. Biggs, p. 213.
19. Biggs, p. 38.

DISCUSSION

Mr. Garcia (General Electric Co.): Did you have to modify the soil interaction damping used in your computations to get your results to agree as well as they did?

Mr. Liss: No, we used the exact equations for damping of footings on soil. The only thing that was in question was the structural damping in contact with soil, which we increased to 20% rather than the normal 5 to 10%, and that parameter didn't seem to make too much difference especially in our initial peaks.

Mr. Garcia: Were the soil damping equations that you used developed by Richard and Whitman?

Mr. Liss: Yes, they are the ones for certain aspects of it; there are other equations that take into account the buried foundation and the side wall interactions with the soil.

DEVELOPMENT AND CORRELATION: VIKING ORBITER ANALYTICAL DYNAMIC MODEL WITH MODAL TEST*

B. K. Wada, J. A. Garba, and J. C. Chen
Jet Propulsion Laboratory
Pasadena, California

The Jet Propulsion Laboratory is responsible for the Viking Orbiter System, which is part of the overall Viking Project managed by the Viking Project Office at Langley Research Center for NASA.

The development of a mathematical dynamic model and its verification by a modal test is a significant milestone for many Projects including Viking Orbiter (VO). Difficulties encountered include performing a modal test, establishing a criteria for correlation of analysis with test, and modifying a large finite element mathematical model to match test data if required. Often the modal test is performed near the end of the Project development schedule; consequently, the time allotted to obtain a verified mathematical model is minimal.

The paper describes the VO experience in the achievement of a good mathematical model. Success can be attributed to the coordination of analysis and tests using substructure modal coupling techniques. The experience would benefit the overall planning of any project, such as Shuttle, especially if substructure modal coupling techniques are contemplated.

INTRODUCTION

The Jet Propulsion Laboratory (JPL) is responsible for the Viking Orbiter System, which is part of the overall Viking Project managed by the Viking Project Office at Langley Research Center (LRC) for NASA. The Spacecraft will be launched on a Titan III/Centaur Launch Vehicle in August 1975.

The total launch vehicle system consists of numerous subsystems that are developed by various aerospace organizations. The creation of a launch vehicle system model requires the transfer of each organization's mathematical models. One organization eventually creates the total model required for analyses. The complexity and size of the problem required the use of substructure modal coupling concepts.

To minimize schedule and cost, the goal was to limit the responsibilities of each organization to their own mathematical models and verification test program. A strong emphasis on technical accuracy existed.

The development of a test-verified mathematical dynamic model is a significant milestone for many projects including Viking Orbiter (VO). Difficulties encountered include performing a modal test, establishing a criterion for correlation of analyses with the test, and modifying a large finite element mathematical model to match test data if required. Since the modal test was performed near the end of the Project development schedule, the time available to obtain a test-verified mathematical dynamic model was minimal. This paper describes the VO plans and experience to

*This paper presents the results of one phase of spacecraft development carried out at the Jet Propulsion Laboratory, California Institute of Technology, under Contract No. NAS 7-100, sponsored by the National Aeronautics and Space Administration.

obtain a good model. Emphasis was placed on the early development of good mathematical models, performance of the modal test, and methods to correlate the analysis with test data.

A valid mathematical model for VO was required because the design and flight loads for the primary structure were established by load analysis. Load analysis is a procedure for obtaining VO member forces from the dynamic response of a complex finite element model of the complete Launch Vehicle System (including the VO) subjected to launch vehicle engine transients. Load analysis requires substructure modal coupling (Ref. 1) of the various structural subsystems of the Launch Vehicle System to allow a solution within present computer capabilities. In addition to the usual objectives of modal tests, determination of individual member forces is emphasized throughout the program.

A good mathematical model was generated by establishing an overall plan integrating subsystem analysis and test with the substructure modal coupling approach. Thus the model was continually updated during the program.

Emphasis was also placed on the modal test and the establishment of a measure of correlation of the analysis with the test. The measure of correlation is required to establish a factor directly related to the confidence placed in the member forces resulting from load analysis.

This paper describes three general activities that resulted in the VO analytical dynamic model, and that were updated and verified by test data during the Project.

- (1) The generation of the overall plan for load analysis, an analytical dynamic model, and development tests.
- (2) The performance of VO subsystem static and modal tests.
- (3) The correlation of the VO System modal analysis and test.

The details of the modal test are not included (Ref. 2). However, actual results are used to show the degree of success attained on a large complex structure. The substructure, tests, and update of substructure mathematical models occurred between July 1, 1972 and May 15, 1973, and the VO System modal test between June 1, 1973 and July 30, 1973. The

correlation of modal test results with analysis occurred between July 1, 1973 and July 30, 1973. The final mathematical model was completed on schedule by July 30, 1973.

DESCRIPTION OF HARDWARE

Figure 1 identifies parts of the Viking spacecraft (V-S/C), Viking transition adapter (VTA), and Centaur truss adapter (CTA) pertinent to this discussion.

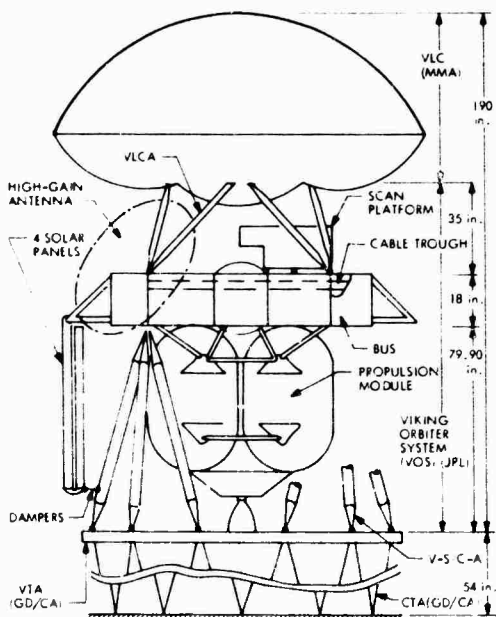


Fig. 1 - Viking spacecraft

The Viking Orbiter System was complicated because it is situated between the Viking lander capsule (VLC) on top and the Centaur adapter (VTA/CTA) on the bottom. The VLC and the VTA/CTA are the responsibility of Martin Marietta Aerospace (MMA) and General Dynamics/Convair Astronautics (GD/CA) respectively.

The weight of the hardware is summarized in Table 1.

Figure 2 is a description of the VO/VTA/CTA configuration for the modal test performed at JPL.

Figure 3 is a photograph of the test of the orbiter development test model (ODTM). The rationale of the configuration will be discussed. The major differences between the test and

TABLE 1
Approximate Weights*

Hardware	Weight (lb)	Responsible Organization
VLC	2567	MMA
VOS		JPL
Bus and adapters	1109	
High-gain antenna with support	47	
Scan platform with support	201	
Four solar panels	244	
Cable trough	49	
Propulsion module hardware	512	
Propellants*†	3138	
VTA	‡	GD/CA
CTA	‡	GD/CA
Total weight	7867	LRC

*The weights are the values used for analysis on 7/1/73.
†See Table 2.
‡Included in the Centaur Model.

TABLE 2
Approximate Propellant Weight and Ullage Summary

Configuration	Oxidizer				Fuel			
	Fluid	Rigid Weight (lb)	Slosh Weight (lb)	Ullage (%)	Fluid	Rigid Weight (lb)	Slosh Weight (lb)	Ullage (%)
Viking Mission A1	N ₂ O ₄	1379	431	20.9	MMH*	968	235	13.3
Viking Mission A2	N ₂ O ₄	1318	428	23.7	MMH	911	249	16.36
Viking Mission B	N ₂ O ₄	1470	415	17.62	MMH	1049	204	9.68
Modal test	Freon- TF	1735	371	17.62	Alcohol	902	227	9.68

*Monomethyl hydrazine.

NUMBERS IN PARENTHESES ARE NODE NUMBERS

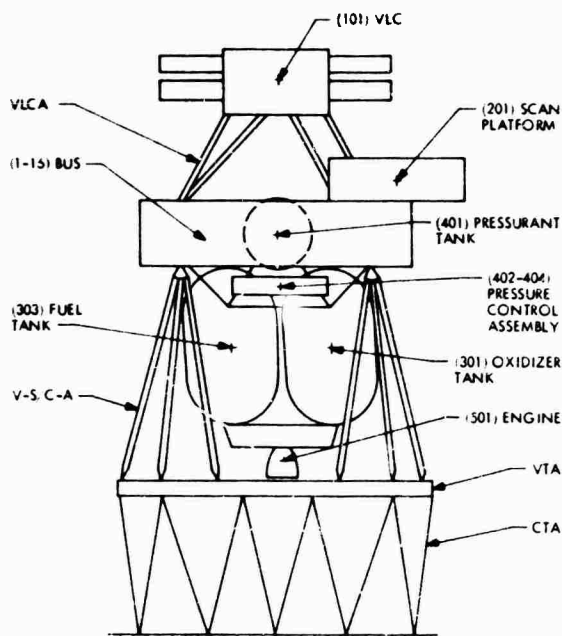


Fig. 2 - Test configuration and node identification

flight configurations are that the test configuration has:

- (1) Rigid VLC with inertia property simulation.
- (2) No solar panels and solar panel dampers.
- (3) No high gain antenna.
- (4) Propulsion propellant mass loading as shown in Table 2.
- (5) Mass and stiffness to represent dynamic characteristics up to 60 Hz.
- (6) No slippage of the scan platform joint along the serrations.

The propellant loading for different configurations is summarized in Table 2. The information will be of value for future discussion.

GENERAL APPROACH

The analysis plan and modal test approach were closely integrated with VO Project plans

and requirements (Ref. 3). Our belief is that a successful development of a mathematical model correlated by test is directly related to the overall analysis, hardware, and test plan.

A. Load Analysis and Its Impact

The design and flight loads for the primary structural members were established by load analysis. The load analysis is a dynamic analysis procedure to obtain VO member forces. The complete Launch Vehicle System including the VO is subjected to launch vehicle engine transients measured from past flights.

The use of load analysis for design and flight loads necessitated a continual reiteration of the VO mathematical model to update the design loads as the design evolved. A VO model of the final configuration verified by a



Fig. 3 - ODTM modal test

system test was required. The flight loads were used to establish forces for which the structure was qualified.

The establishment of flight loads and the structural qualification test program were near the end of the development schedule. Since the modal test was also near the end of the development schedule, confidence had to exist in the mathematical model when the modal test was performed.

Correlation of the modal test results to analysis was necessary to help establish a measure of uncertainty, which was required to establish the accuracy of flight loads. The measure of uncertainty is defined as the load analysis factor (LAF). The flight loads are the calculated loads times the LAF.

B. Member Loads

The significant parameter in load analysis is the member forces. The goal was to obtain accurate dynamic member forces, not accelerations. The modal test included the measurement of modal force coefficients.

C. Substructure Modal Coupling

The modal coupling of the VO with the VLC and VTA/CTA required consideration of:

- (1) Accurate selection of displacement functions.
- (2) Simplification of interfaces between organizations.
- (3) Provision for each organization to perform analyses and tests independent of the others.
- (4) Ability to verify the model by modal test.
- (5) Availability of test hardware.

The structure below the CTA was modeled as a planar structure (plane before deformation remains a plane after deformation) and the structure above the VTA was a three-dimensional model. The requirement to modally couple the V-S/C to the Centaur resulted in the decision to include the VTA/CTA with the VO. Otherwise, the number of compatibility relationships would have increased along with the possibility of erroneous data caused by round-off errors. Consequently, the CTA/VTA was included as a part of the VO

modal test. Another goal was to simulate the interfaces since truss joints were of concern.

The substructure modal coupling analysis techniques were also used on VO to:

- (1) Provide a cost effective solution.
- (2) Allow use of substructure test data as available.
- (3) Decrease the effort to update the mathematical model based on the test data.
- (4) Increase confidence in the final model.

A substructure was defined as being compatible with:

- (1) Deliverable hardware used to obtain test data incorporable into the models.
- (2) Ease of interface definition and analysis.
- (3) Area of engineering responsibility.

Substructure tests were used to verify and adjust the mathematical models. Errors were minimized since the responsible engineer of a substructure used engineering judgement to verify his mathematical model.

D. Rigid VLC

Various methods of modal coupling of the VO to the VLC were possible. The inclusion of the rigid VLC is mathematically equivalent to mass loading (Ref. 4) the VO interface with the VLC. The disadvantage of including VLC data into the VO analysis and test were offset by:

- (1) The capability to modify the rigid VLC inertia properties after the VO model was delivered to MMA.
- (2) The similarity of the VO displacement functions to V-S/C functions, thus fewer modes were required.
- (3) The capability to use the resulting representative configuration for the sine vibration tests.

ANALYSIS

The equations are developed to briefly illustrate the methodology in the creation of the

VO mathematical model. Also they are used as a basis to definitize the objectives of the tests and to define the data used to correlate the analyses with test data.

A. Substructures

The two general equations for the sub-structure are:

$$\begin{bmatrix} k_{II} & k_{IO} \\ k_{OI} & k_{OO} \end{bmatrix} \begin{Bmatrix} u_I \\ u_O \end{Bmatrix} = \begin{Bmatrix} f_I \\ f_O \end{Bmatrix} \text{ or } [k]\{u\} = \{f\} \quad (1)$$

$$[m]\{\ddot{u}\} + [c]\{\dot{u}\} + [k]\{u\} = \{0\} \quad (2)$$

$$\{P\} = [S]\{u\} \quad (3)$$

where

$[k]$ = stiffness matrix

$[c]$ = damping matrix

$[m]$ = mass matrix

$[f]$ = force matrix

$\{P\}$ = member forces

$[S]$ = force coefficient matrix

$\{u\}$ = displacement

I = subscript representing interface degree of freedom

O = subscript representing degree of freedom other than the interface

Equation (2) can be derived from the Lagrangian equation:

$$\frac{d}{dt} \left(\frac{\partial L}{\partial \dot{u}_j} \right) - \frac{\partial L}{\partial u_j} + \frac{\partial D}{\partial \dot{u}_j} = F_j \quad (4)$$

where

$$L = T - U$$

$$T = \frac{1}{2} \{u\}^T [m] \{u\} = \frac{1}{2} \sum_{j=1}^N \{\dot{u}_j\}^T [m]_j \{\dot{u}_j\}$$

$$U = \frac{1}{2} \{u\}^T [k] \{u\} = \frac{1}{2} \sum_{j=1}^N \{\dot{u}_j\}^T [k]_j \{\dot{u}_j\}$$

$$D = \frac{1}{2} \{u\}^T [c] \{u\} = \frac{1}{2} \sum_{j=1}^N \{\dot{u}_j\}^T [c]_j \{\dot{u}_j\} \quad (5)$$

F_j = force

N = number of finite elements

$\{u\}_j, \{\dot{u}\}_j, [m]_j, [k]_j$ = parameters associated with the j th finite element.

Other parameters for correlation of the analysis and test data are the kinetic energy T and the potential energy U. The dissipation function D cannot be used for correlation since the test data are used in the analysis. Equation (1) can be written as:

$$[u_O] = [k_{OO}]^{-1} ([f_O] - [k_{OI}] [u_I]) \quad (6)$$

and Eq. (2) as:

$$[m]\{\ddot{u}\} + [k]\{u\} = \{0\} \quad (7)$$

where experimental modal damping values are used. The $[c]$ is assumed to be of a form where the transformation formed by the eigenvectors of Eq. (7) uncouples Eq. (2).

B. Displacement Functions of Substructures

Often the dynamic characteristics of substructures are represented by a finite number of displacement functions to reduce the number of independent variables. The various forms of identification of displacement functions will be discussed.

C. Rigid Body Modes

Rigid body modes represent the motions $[\phi_R]$ of the substructure when a degree-of-freedom $[u_I]$ is displaced an arbitrary value without force. The $[\phi_R]$ is a solution to Eq. (6), where $[f_O] = 0$, $[u_I]$ is a unit matrix in the degrees of freedom associated with the

rigid body modes. The displacements of the substructure due to rigid body modes are

$$\{u_R\} = [\phi_R] \{q_R\} \quad (8)$$

The number of rigid body motions may range from 1 to ∞ . Rigid body motions in excess of 6 are related to linkages within the substructure.

If the displacement at the substructure interface gridpoints can be represented by a linear combination of rigid body modes, the interface is defined as statically determinant.

D. Constraint Modes (Ref. 1)

Constraint modes represent the motions $[\phi_C]$ of the substructure when the displacement of an interface degree of freedom (DOF) requires force as the other interface degrees of freedom are restrained. Constraint modes are used to define displacement functions corresponding to interface distortions. The constraint modes $[\phi_C]$ are the solution to Eq. (6), where $[f_O] = 0$, $[u_I]$ is a unit matrix in the degrees of freedom associated with constraint modes. A force matrix $[f_C]$ associated with constraint modes exists. Note that a distinction between rigid body modes and constraint modes is not required. The displacements of the substructure due to constraint modes are

$$\{u_C\} = [\phi_C] \{q_C\} \quad (9)$$

They are defined only if the interfaces are statically indeterminant. (Interface cannot be defined as a linear combination of rigid body modes.)

Features of constraint modes include orthogonal to normal modes evaluated with all interface degrees of freedom constrained.

E. Attachment Modes (Ref. 5)

The number of displacement functions necessary to represent the dynamic characteristics of the system may be minimized by the selection of substructure modes that closely represent system modes. In a combined structural system, a gridpoint of a substructure at which another substructure is attached is subjected to concentrated attachment forces. These forces result in a displacement function that may have to be represented by many normal modes.

Attachment modes are displacements $[\phi_A]$ of the substructure corresponding to concentrated loads $[f_A]$ on the substructure. Displacement $[\phi_A]$ are the solution to Eq. (6), where $[f_O] = [f_A]$ and $[u_I] = 0$. The displacements due to attachment modes are

$$\{u_A\} = [\phi_A] \{q_A\} \quad (10)$$

A disadvantage of attachment modes is nonorthogonality to the normal modes or to each other. Thus, unless extreme care is exercised, attachment modes that are nearly linear combinations of normal modes or other attachment modes may inadvertently be selected. If the system equations comprising substructure modes are not independent, the equations cannot be solved.

F. Normal Modes

The normal modes of the substructure are evaluated from Eq. (7). The displacements due to normal modes are

$$\{u_N\} = [\phi_N] \{q_N\} \quad (11)$$

G. Total Displacement Function

The displacement of the substructure can be any combination of displacement functions selected above.

$$\{u\} = \left[[\phi_R] [\phi_C] [\phi_A] [\phi_N] \right] \begin{Bmatrix} q_R \\ q_C \\ q_A \\ q_N \end{Bmatrix} = [\phi] \{q\} \quad (12)$$

H. Generalized Coordinates

Substitution of Eq. (12) into Eq. (7) and premultiplication by $[\phi]^T$ result in

$$[\phi]^T [m] [\phi] \{q\} + [\phi]^T [k] [\phi] \{q\} = \{0\}$$

or

$$\begin{bmatrix} m \\ q \end{bmatrix} \{q\} + \begin{bmatrix} k \\ q \end{bmatrix} \{q\} = \{0\} \quad (13)$$

$$[S] [\phi] \{q\} = \{P\}$$

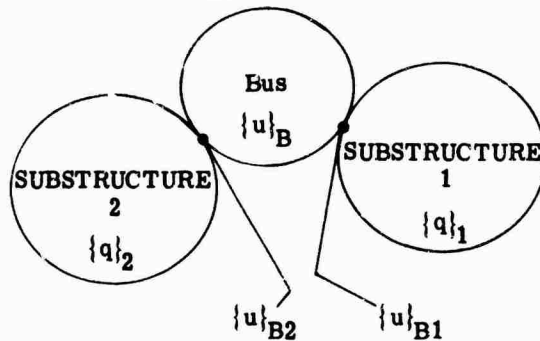
Damping corresponding to the displacement functions is introduced into Eq. (2) if desired.

$$[m_q] \{ \ddot{q} \} + [c_q] \{ \dot{q} \} + [k_q] \{ q \} = \{ 0 \} \quad (14)$$

I. Mixed Coordinates

Equation (14) represents the equation of motion of any substructure in terms of its generalized coordinates. The VO analysis approach uses hybrid coordinates where the real displacements of the bus are retained and the generalized coordinates of the substructure attached to the bus are used.

Mixed coordinates were used because of the order of the system equations of motion. Originally generalized coordinates for all subsystems were retained as described in Ref. 6. This approach resulted in numerical difficulties due to limitations of single precision arithmetic in the Structural Analysis and Matrix Interpretive System (SAMIS) on the Univac 1108 computer. The use of real coordinates for all subsystems was rejected because of size limitations in the eigenvalue routine. The symbols used are shown below.



The terms are defined. Subscripts differentiating substructures are introduced at this time.

$\{q\}_i$ = generalized coordinates of i^{th} substructure

$\{u\}_B$ = real displacement of the VO bus

$\{u\}_{Bi}$ = subset of $\{u\}_B$ defining compatibility of the i^{th} substructure to the bus. Often the displacements are in local coordinates.

The Eq. (14) for the i^{th} substructure with the interface degrees of freedom is

$$[m_q]_i \{ \ddot{q}_i \} + [c_q]_i \{ \dot{q}_i \} + [k_q]_i \{ q_i \} + [k_q]_i \{ u_{Bi} \} = \{ 0 \} \quad (15)$$

Two classes of interfaces are distinguished. Statically determinant and statically indeterminant interfaces result in different forms of the coefficient matrices $[m_q]_i$, $[c_q]_i$, and $[k_q]_i$.

A statically determinant interface exists when the interface coordinates $\{u\}_{Bi}$ represent linear combination of rigid body displacements. Although it can be greater than six, six is the maximum number for VO. The matrices are of the form

$$\begin{bmatrix} m_{qi}^{RR} & m_{qi}^{RE} \\ m_{qi}^{ER} & m_{qi}^{EE} \end{bmatrix}, \begin{bmatrix} 0 & 0 \\ 0 & c_{qi}^{EE} \end{bmatrix}, \text{ and } \begin{bmatrix} 0 & 0 \\ 0 & k_{qi}^{EE} \end{bmatrix} \quad (16)$$

where superscripts

R = rigid body motion

E = elastic motion

Statically indeterminant interface coordinates $\{u\}_{Bi}$ have more interface coordinates than can be represented by a linear combination of rigid body displacements. The matrices are of the form

$$\begin{bmatrix} m_{qi}^{II} & m_{qi}^{IO} \\ m_{qi}^{OI} & m_{qi}^{OO} \end{bmatrix}, \begin{bmatrix} c_{qi}^{II} & c_{qi}^{IO} \\ c_{qi}^{OI} & c_{qi}^{OO} \end{bmatrix}, \text{ and } \begin{bmatrix} k_{qi}^{II} & k_{qi}^{IO} \\ k_{qi}^{OI} & k_{qi}^{OO} \end{bmatrix} \quad (17)$$

where superscripts

I = interface motion

O = other than interface motion

Equation (16) is a special form of Eq. (17).

J. Equation of Motion of Total Structure

If each substructure is considered as a finite element, they can be combined with the

bus in a way similar to Eqs. (2) and (4). The results are

$$[\mathbf{M}] \begin{pmatrix} \{\ddot{u}\}_R \\ \{\ddot{u}\}_B \\ \vdots \\ \{\ddot{q}\}_i \end{pmatrix} + [\mathbf{C}] \begin{pmatrix} \{\dot{u}\}_R \\ \{\dot{u}\}_B \\ \vdots \\ \{\dot{q}\}_i \end{pmatrix} + [\mathbf{K}] \begin{pmatrix} \{u\}_R \\ \{u\}_B \\ \vdots \\ \{q\}_i \end{pmatrix} = \{0\} \quad (18)$$

$$\{P\}_B = [\mathbf{S}] \{u\}_B$$

$$\{P\}_i = [\mathbf{S}] [\phi]_i \{u\}_i$$

where

$\{u\}_R$ = rigid body degrees of freedom of the V-S/C or the motions at the V-S/C/Centaur interface

$[\phi]_i$ = displacement function of i^{th} substructure

$\{u\}_i$ = real displacements of i^{th} substructure

$\{P\}_B$ = member forces in the bus

$\{P\}_i$ = member forces in i^{th} substructure

The eigenvalues and eigenvectors of Eq. (18) with terms associated with $[\mathbf{C}]$ and $\{u\}_R$ removed are $[\omega^2]$ and $[\phi]$. Substitution of the transformation

$$\begin{pmatrix} \{u\}_B \\ \{\dot{q}\}_1 \\ \vdots \\ \{\dot{q}\}_i \end{pmatrix} = [\phi] \{x\} \quad (19)$$

into Eq. (18) and premultiplication by $[\phi]^T$ results in

$$[\mathbf{M}] \begin{pmatrix} \{\ddot{u}\}_R \\ \{\ddot{x}\} \end{pmatrix} + [\mathbf{C}] \begin{pmatrix} \{\dot{u}\}_R \\ \{\dot{x}\} \end{pmatrix} + [\mathbf{K}] \begin{pmatrix} \{u\}_R \\ \{x\} \end{pmatrix} = \{0\} \quad (20)$$

where

$$[\bar{\mathbf{M}}] = \begin{bmatrix} \bar{\mathbf{M}}^{RR} & \bar{\mathbf{M}}^{RE} \\ \bar{\mathbf{M}}^{ER} & \bar{\mathbf{M}}^{EE} \end{bmatrix}$$

$$[\bar{\mathbf{M}}^{EE}] = [\phi]^T [\mathbf{M}] [\phi]$$

$$[\bar{\mathbf{C}}] = \begin{bmatrix} 0 & 0 \\ 0 & \bar{\mathbf{C}}^{EE} \end{bmatrix}$$

(21)

$$[\bar{\mathbf{C}}^{EE}] = \begin{bmatrix} 2 \rho_i \sqrt{\bar{\mathbf{M}}^{EE} \bar{\mathbf{K}}^{EE}} \end{bmatrix}$$

where ρ_i is the critical viscous damping ratio,

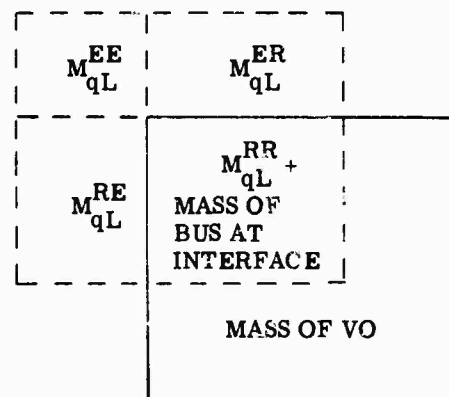
$$[\bar{\mathbf{K}}] = \begin{bmatrix} 0 & 0 \\ 0 & \bar{\mathbf{K}}^{EE} \end{bmatrix}$$

$$[\bar{\mathbf{K}}^{EE}] = [\phi]^T [\mathbf{K}] [\phi] = [\bar{\mathbf{M}}^{EE} \omega^2]$$

The significance of the rigid VLC is illustrated. Since the VLC attachment to the VO is statically determinant, from Eq. (15)

$$\begin{bmatrix} \mathbf{M}_{qL}^{RR} & \mathbf{M}_{qL}^{RE} \\ \mathbf{M}_{qL}^{ER} & \mathbf{M}_{qL}^{EE} \end{bmatrix}, \begin{bmatrix} 0 & 0 \\ 0 & \mathbf{C}_{qL}^{EE} \end{bmatrix}, \text{ and } \begin{bmatrix} 0 & 0 \\ 0 & \mathbf{K}_{qL}^{EE} \end{bmatrix}$$

where $i = L$ is the symbol used for the VLC. Combination of the mass matrix of the VLC with the bus can be shown as



The damping and stiffness matrices do not couple. Thus the physical addition of the rigid VLC is equivalent to adding $[m_{RL}]$ to the mass matrix of the VO. No other VLC parameters are included in the VO analysis.

The equations are derived for a system with small damping where the eigenvectors of the undamped equation can be assumed to diagonalize the original damping matrix. This is assumed for VO although discrete viscous dampers exist. See Ref. (6) for treatment of viscous dampers.

K. Size of the Problem

The approximate size of the VO dynamic model used for Load Analysis is summarized in Table 3.

SUBSTRUCTURE TESTS AND ANALYSIS CORRELATION

During the program, information on substructures, structural components, and parameters related to dynamics were obtained during the development test program. The tests were run to

- (1) Directly obtain dynamic data.
- (2) Establish feasibility of future tests.

The principal objectives of many tests were other than obtaining data to verify models.

Two tests to be discussed illustrate the procedure used in correlating the mathematical model with the test data.

A. Propulsion Module Modal Test

Figure 4 shows the propulsion module modal test setup. The objectives of the test were to:

- (1) Establish the difficulty of performing a modal test with ullage in the tanks. (Both a zero ullage and ullage conditions were tested.)
- (2) Establish nonlinearity of the system with excitation force.
- (3) Establish the influence of the tank pressure on its dynamic characteristics.
- (4) Measure the eigenvectors and eigenvalues.
- (5) Indirectly measure the constraint modes.
- (6) Measure the modal force transformations.

The changes in the model as a result of the test are shown in Tables 4, 5, and 6.

TABLE 3
Size of VO Dynamic Model

Substructure	Elastic DOF	Dynamic DOF	Interface DOF	Normal Modes
Rigid lander and bus	1,720	153	75	0
Scan platform	580	84	14	3
Solar panels	3,444	452	28	20
Cable trough	192	153	20	0
Propulsion module	695	78	16	12
3-hole tab	20,000	0	192	0
Mickey mouse tab	3,400	0	24	0
Siamese tab	1,760	0	22	0
CTA/VTA	42	0	36	0

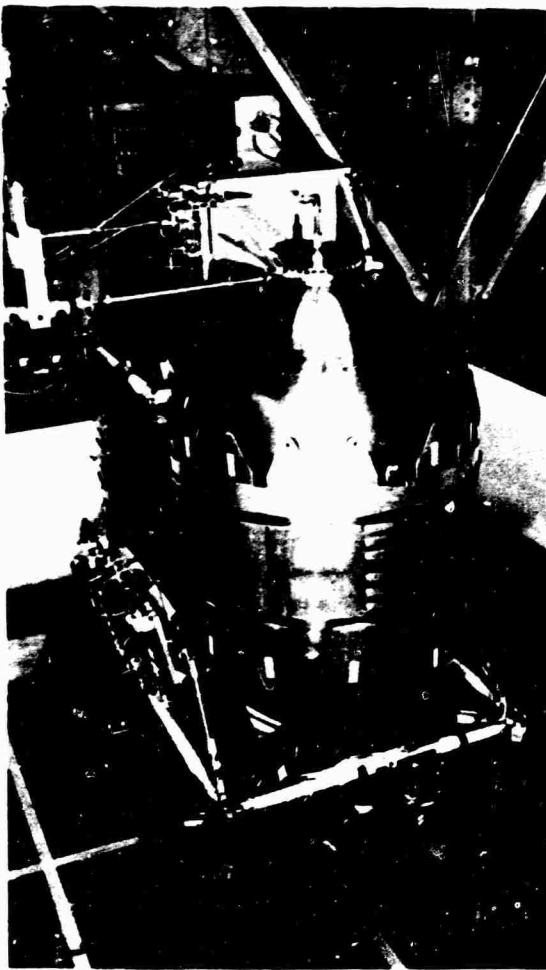


Fig. 4 - Propulsion module modal test

B. Solar Panel Modal Test

Figure 5 shows the solar panel modal test setup. A brief description of the results is shown in Table 7.

Since the mode shapes of the analysis and the test compared well, only the frequencies of the modes were changed. Extraneous modes from the analysis were eliminated. The modal test was performed on the solar panel with the relay antenna. The solar panel model result without the relay antenna was obtained analytically using the model with the relay antenna adjusted to the test data.

SYSTEM MODAL TEST AND ANALYSIS CORRELATION

A. Modal Test Configuration

As illustrated in Fig. 2, the VO system modal test configuration did not duplicate the

flight configuration. The objective was to verify as many significant substructures and their interactions as feasible. The modal test configuration is represented by the equations

$$\begin{aligned}
 [0] = & [M]_{T,A} \begin{Bmatrix} \{\ddot{u}\}_R \\ \{\ddot{u}\}_B \\ \{\ddot{q}\}_{P,T} \\ \{\ddot{q}\}_{S,T} \\ \{\ddot{q}\}_C \end{Bmatrix} + [C]_{T,A} \begin{Bmatrix} \{\dot{u}\}_R \\ \{\dot{u}\}_B \\ \{\dot{q}\}_{P,T} \\ \{\dot{q}\}_{S,T} \\ \{\dot{q}\}_C \end{Bmatrix} \\
 & + [K]_{T,A} \begin{Bmatrix} \{u\}_R \\ \{u\}_B \\ \{q\}_{P,T} \\ \{q\}_{S,T} \\ \{q\}_C \end{Bmatrix}
 \end{aligned} \quad (22)$$

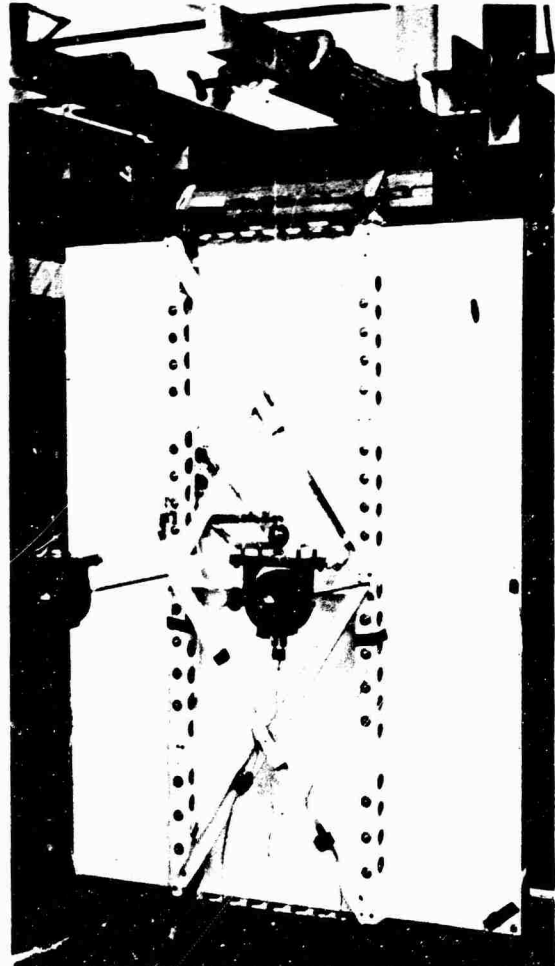


Fig. 5 - Solar panel modal test

TABLE 4
Frequency Change and Damping of Propulsion Subsystem Modal Test

Mode No.	Pretest Model (Hz)	Modal Test (Hz)	Posttest Model (Hz)	Mode Description	Damping Ratio
1	12.11	12.95	12.95	Oxidizer and fuel tanks in Y direction (in phase)	0.010
2	14.90	17.66	16.36	Oxidizer tank in Z direction	0.0049
3	19.24	20.80	19.83	Oxidizer and fuel tanks in Z direction	0.0084
	22.43			Local thrust plate	
4	25.76	22.97	26.70	Oxidizer and fuel tank in Y direction (out of phase)	
5	27.50	28.33	28.30	Fuel tank in Z direction	0.0074
	35.57			Local PCA	
6	38.67	32.76	34.25	Pressurant tank in θ_Y direction*	0.0106
7		42.80 [†]	45.75	Local PCA in X direction [†]	
8	41.62	50.67	49.69	Pressurant tank in Y direction	0.0078
12	50.54	65.38	65.67	PCA in θ_Y direction	0.0107

* θ_Y is rotation in radians

[†] MMA test data

$$\{P\}_B = [S] \{u\}_B$$

$$\{P\}_i = [S] [\phi]_i \{u\}_i$$

where

T, A = subscript representing analytical estimate of the modal test configuration

$\{u\}_R$ = rigid body displacement

$\{u\}_B$ = displacement of bus

$\{q\}_{P,T}$ = generalized coordinate of propulsion module with test propellant mass (see Table 2)

$\{q\}_{S,T}$ = generalized coordinate of the scan platform in test configuration; joints are not allowed to slip along the serration

$\{q\}_C$ = generalized coordinate of the cable trough

In steps identical to obtaining Eqs. (19) through (21), one obtains from Eq. (22):

eigenvalues,

$$[\omega^2]_{T,A} \quad (22a)$$

eigenvectors,

$$[\phi]_{T,A} \quad (22b)$$

TABLE 5
Kinetic Energy Distribution of Propulsion Module Modal Test

Mode		Pretest Analysis (%)	Modal Test (%)	Posttest Analysis (%)
12.95 Hz	Oxidizer tank	X		
		Y	63.38	76.76
		Z		68.17
	Fuel tank	X		
		Y	21.41	18.04
		Z		24.27
17.66 Hz	Oxidizer tank	X	33.11	23.63
		Y		34.02
		Z	25.39	50.09
	Fuel tank	X	15.65	13.81
		Y		16.72
		Z	2.89	0.71
20.80 Hz	Oxidizer tank	X	13.83	26.96
		Y		19.27
		Z	58.56	38.83
	Fuel tank	X	2.33	6.22
		Y		3.52
		Z	19.03	22.34
22.97 Hz	Oxidizer tank	X		
		Y	22.14	21.82
		Z		23.26
	Fuel tank	X	0.84	0.02
		Y	50.75	64.18
		Z	3.27	0.09
28.33 Hz	Oxidizer tank	X	11.60	11.72
		Y	1.65	0.37
		Z	5.22	3.54
	Fuel tank	X	6.78	8.35
		Y	2.74	0.83
		Z	57.10	58.92
				56.58

TABLE 6
Modal Forces of Propulsion Subsystem Modal Test .

Member No.	Mode 1 (lb)	Mode 2 (lb)	Mode 3 (lb)	Mode 4 (lb)	Mode 5 (lb)
4	Pretest	-627.5	133.9	-220.4	-12.99
	Test	-568.2	77.1	-266.1	-53.3
	Posttest	-572.9	112.9	-237.3	-110.5
3	Pretest	-70.8	-130.3	63.2	135.7
	Test	-66.8	-87.1	85.3	90.5
	Posttest	-73.8	-109.7	72.7	124.1
41	Pretest	469.7	-241.9	-179.2	231.6
	Test	476.6	-252.5	-109.6	188.0
	Posttest	427.2	-244.3	-147.8	183.4
40	Pretest	237.6	158.6	110.2	44.7
	Test	205.9	144.7	82.1	56.5
	Posttest	249.2	143.7	95.6	40.4
12	Pretest	596.2	124.0	-286.5	62.6
	Test	497.7	82.6	-294.7	43.1
	Posttest	549.1	95.8	-290.9	62.9
11	Pretest	144.7	-125.9	48.6	-46.5
	Test	151.4	-99.4	79.9	-98.4
	Posttest	152.6	-108.3	58.1	-38.2
36	Pretest	-530.9	-220.4	-152.2	170.6
	Test	-452.6	-266.1	-91.7	172.4
	Posttest	-489.0	-220.8	-126.0	134.6
37	Pretest	-124.0	171.5	118.9	110.5
	Test	-197.7	120.8	89.0	-67.8
	Posttest	-130.7	157.1	101.3	-105.3
18	Pretest	273.8	-25.9	-127.3	-52.4
	Test	264.9	-33.0	-121.5	-39.5
	Posttest	309.1	-30.7	-126.5	-48.9
8	Pretest	-299.0	-17.9	-104.4	43.5
	Test	-292.1	38.6	-115.3	25.7
	Posttest	-302.4	23.4	-100.0	70.5

TABLE 7
Frequency Change and Damping of Solar Panel Modal Test

Mode No.	Pretest Math Model (Hz)	Modal Test (Hz)	Adjusted Posttest Math Model (Hz)	Damping Ratio
1	37.0	22.4	22.4	0.023
2	31.56	26.8	26.8	0.017
3	34.55	31.0	31.0	0.030
4	40.11	—	—	—
5	45.17	38.5	38.5	0.030
6	59.70	57.5	59.70	0.030
7	62.32	64.9	—	—

transformation,

$$\begin{Bmatrix} \{\ddot{u}\}_B \\ \{\ddot{q}\}_{P,T} \\ \{\ddot{q}\}_{S,T} \\ \{\ddot{q}\}_C \end{Bmatrix} = [\phi]_{T,A} \{x\}_{T,A} \quad (22c)$$

equation of motion,

$$[\bar{M}]_{T,A} \begin{Bmatrix} \{\ddot{u}\}_R \\ \{\ddot{x}\}_{T,A} \end{Bmatrix} + [\bar{C}]_{T,A} \begin{Bmatrix} \{\dot{u}\}_R \\ \{\dot{x}\}_{T,A} \end{Bmatrix} + [\bar{K}]_{T,A} \begin{Bmatrix} \{u\}_R \\ \{x\}_{T,A} \end{Bmatrix} = \{0\} \quad (22d)$$

and force transformations,

$$\{P\}_B = [S][\phi]_{T,A} \{x\}_{T,A} \quad (22e)$$

$$\{P\}_i = [S][\phi]_i [\phi]_{T,A} \{x\}_{T,A} \quad (22f)$$

The above values are the analytical predictions of the modal test configuration.

The $[\bar{M}]_{T,A}$ term of Eq. (22d) can be expressed similarly to Eq. (21) as

$$[\bar{M}]_{T,A} = \begin{bmatrix} \bar{M}_{T,A}^{LR} & \bar{M}_{T,A}^{RE} \\ \bar{M}_{T,A}^{ER} & [\bar{M}_{T,A}^{EE}] \end{bmatrix} \quad (22g)$$

$$[\bar{M}_{T,A}^{EE}] = [\phi]_{T,A}^T [\bar{M}]_{T,A} [\phi]_{T,A} \quad (22h)$$

B. Correlation

The objective of the correlation of modal test data and analysis is to verify the mathematical model as shown in Eq. (22). However, this mathematical model is in a hybrid system, i.e., some degrees of freedom are expressed in the physical coordinates and others are in the generalized coordinates. The hybrid system is a result of the modal coupling technique used in the analysis. For a direct comparison, the solutions of Eq. (22) must be expressed in the form compatible to the measured test results. For this purpose, the normal modes obtained from Eq. (22) are transformed into the accelerometer locations.

$$[\phi']_{T,A} = [T][\phi]_{T,A} \quad (23)$$

where

$[\phi']_{T,A}$ = analytical mode expressed at accelerometer locations

$[\phi]_{T,A}$ = normal mode solution of Eq. (22)

$[T]$ = transformation matrix

In Eq. (22), 1773 degrees of freedom exist in the hybrid coordinates, whereas $[\phi']_{T,A}$ involves only 153 degrees of freedom. Because the accelerometer locations often do not coincide with the analytical node points, Eq. (23) is an approximation.

For the modal test, a test mass matrix $[M]_T$ was constructed based upon physical mass distribution and corresponded to the experimental accelerometer measurements. Throughout the correlation, the analytical predictions reduced to the accelerometer degrees of freedom [Eq. (23)] and the $[M]_T$ are used. The use of the $[M]_{T,A}$ of Eq. (22) is complicated because it contains masses corresponding to hybrid coordinates and the degrees of freedom of the test modes must be matched to correspond to the analytical degrees of freedom. The validity of $[M]_T$ is verified with the solution of Eq. (22) by the mixed orthogonality check.

$$[\phi]_{T,A}^T [M]_T [\phi]_{T,A} = [\bar{M}']_{T,A} \quad (24)$$

Ideally $[\bar{M}']_{T,A}$ is a diagonal matrix, however, as shown in Table 8, there are off-diagonal terms. In general for the first twelve modes, the off-diagonal terms are very small (less than 5%). This indicates that $[M]_T$ is indeed a valid mass matrix representing the total structural system for the first 12 modes. Additionally the magnitude of the off-diagonal terms indicates the best accuracy one can expect in an orthogonality check of the test modes with the $[M]_T$. Since a more detailed mass distribution was used in the analysis than in the

modal test data reduction program, the orthogonality of $[\bar{M}']_{T,A}$ deteriorates for the higher frequency modes.

The test modal data together with analytical prediction $[\phi']_{T,A}$ and $[M]_T$ are read into the computer file for processing. The correlation work is automated.

C. Mode Identification

Prior to any correlation, the identification of test modes to the corresponding analytical modes is required. This task is achieved by the following criteria:

$$|\bar{M}'|_T = [\phi']_{T,A} [M]_T \{ \phi_j \}_T \quad (25)$$

Here the j^{th} test mode is checked with all the analytical modes $[\phi']_{T,A}$. The j^{th} test mode corresponds to the analytical mode related to the largest k^{th} term in $\{M\}_T$. A perfect correlation exists when the k^{th} term is unity with all the other terms zero. After the identification of a test mode to an analytical mode, the correlation program calculates the necessary information required for a detailed comparison between the test and analysis. Table 9 shows the cross-orthogonality check between the test mode 701 and the first 30 analytical modes. For this case, the test mode 701 corresponds to the third analytical mode.

TABLE 8
Mixed Orthogonality -- Model VIII

Frequency (Hz)												Mode
1	2	3	4	5	6	7	8	9	10	11	12	
100	0.9	-0.3	-0.2	0.8	-0.9	1.4	1.6	-1.7	-0.3	-0.9	0.4	1
100	-0.2	-0.2	0.3	0.1	-0.1	0.2	-3.1	0.4	-2.2	-0.4		2
100	1.3	-1.6	1.1	-1.7	-1.4	0	-2.1	-1.2	0.7			3
100	-0.4	1.2	-0.2	-0.3	-2.7	1.7	-0.3	1.1				4
100		1.0	0.8	1.1	-0.6	2.2	-0.2	1.1				5
100		0.4	-0.7	0.8	0.9	-0.9	1.8					6
100		-1.8	0	0.2	-2.3	0.9						7
100		-0.2	-1.4	1.2	-0.2							8
100		-0.9	0.7	-1.4								9
100		-1.0	0.2									10
100		-2.3										11
		100										12

TABLE 9
Cross Orthogonality - Orthogonality of Test
Mode No. 701, Run Name DTA701 at
Frequency 7.48 Hz with Respect to
All Analytical Modes

Analytical- Mode No.	Freq	Ortho
1	4.35	-0.011
2	4.40	-0.015
3	7.48	-0.997
4	7.83	-0.015
5	10.92	-0.003
6	13.36	-0.015
7	14.64	-0.016
8	17.95	-0.023
9	18.81	-0.003
10	23.42	-0.006
11	24.28	-0.011
12	26.18	-0.008
13	28.12	-0.001
14	29.98	-0.011
15	31.36	-0.020
16	33.54	-0.009
17	34.68	-0.004
18	35.80	-0.003
19	36.95	-0.111
20	38.43	-0.002
21	39.11	-0.088
22	40.58	-0.051
23	42.65	-0.015
24	43.15	-0.013
25	45.32	-0.004
26	45.80	-0.011
27	51.80	-0.003
28	52.40	-0.007
29	53.15	-0.008
30	59.44	-0.010

CORRELATION CHOICE 1
ANALYTICAL MODE 3 FREQUENCY 7.48

D. Modal Test Equation

The mathematical equation governing the modal test structural system is:

$$\{f\}_T e^{i\omega t} = [M]_T \{\ddot{u}\}_T + [C]_T \{\dot{u}\}_T + [K]_T \{u\}_T \quad (26)$$

where

$\{u\}_T$ = displacement vector for each DOF associated with accelerometer measurement

$[M]_T$ = test mass matrix

$[C]_T$ = test damping matrix

$[K]_T$ = stiffness matrix

$\{f\}_T$ = force vector from the shaker

In contrast to the modal analysis as shown by the homogeneous Eq. (22), Eq. (26) is a forced response equation. The external harmonic excitation is provided by the shakers used in the modal test. The solution of Eq. (26) can be expressed in terms of generalized coordinates as follows:

$$\{u\}_T = [\phi]_T \{q\}_T \quad (27)$$

where $[\phi]_T$ is the normal mode matrix, which is the eigenvectors of the test configuration measured at accelerometer locations. Substitution of Eq. (27) into Eq. (26) and premultiplication by $[\phi]_T^T$ result in

$$\begin{aligned} [\phi]_T^T \{f\}_T e^{i\omega t} &= [-\bar{M}]_T \{\ddot{q}\}_T + [-\bar{C}]_T \{\dot{q}\}_T \\ &+ [-\bar{K}]_T \{q\}_T \end{aligned} \quad (28)$$

where

$$\begin{aligned} [-\bar{M}]_T &= [\phi]_T^T [M]_T [\phi]_T \\ &\text{generalized mass} \end{aligned} \quad (28a)$$

$$\begin{aligned} [-\bar{K}]_T &= [\phi]_T^T [K]_T [\phi]_T \\ &\text{generalized stiffness} \end{aligned} \quad (28b)$$

$$\begin{aligned} [-\bar{C}]_T &= [\phi]_T^T [C]_T [\phi]_T \\ &\text{generalized damping} \end{aligned} \quad (28c)$$

$$\begin{aligned} \omega_n &= \sqrt{\bar{K}_n / \bar{M}_n} \\ &\text{n}^{\text{th}} \text{ eigenvalue} \end{aligned} \quad (28d)$$

The accelerometer measurements obtained during the test are the response from the shaker force instead of the normal modes. The response is expressed as:

$$\{u\}_T = [\phi]_T [-H_n(\omega)] [\phi]_T^T \{f\}_T e^{i\omega t} \quad (29)$$

where

$$H_n(\omega) = \frac{\omega_n^2 / \bar{K}_n}{(\omega_n^2 - \omega^2) + i 2 \rho_n \omega \omega_n}$$

When the shaker frequency ω is tuned to one of the natural frequencies ω_n , only one term in the $[H_n(\omega)]$ dominates if ρ_n , the percentage of critical damping, is very small and all the natural frequencies are well separated. Thus the following approximation may be obtained:

$$\{u\}_T \approx \{\phi\}_n$$

A relatively "clean" normal mode can be measured when damping is small and the natural frequencies of the structure are well separated. In general, the damping of the structure is indeed very small but not all the natural frequencies are well separated. Hence, errors are expected when two normal mode frequencies are not well separated.

E. Modal Test Output

The output of the modal test is eigenvector,

$$[\phi]_T \quad (30a)$$

eigenvalue,

$$[\omega^2]_T \quad (30b)$$

and modal force coefficients

$$\{P\}_T \quad (30c)$$

Evaluating the generalized mass matrix similarly to Eq. (22g), including the masses corresponding to the rigid body displacements, results in

$$[\bar{M}]_T = \begin{bmatrix} \bar{M}_T^{RR} & \bar{M}_T^{RE} \\ \bar{M}_T^{ER} & [\bar{M}_T^{EE}] \end{bmatrix} \quad (30d)$$

where

$$[\bar{M}_T^{EE}] = [\bar{M}]_T \quad (30e)$$

of Eq. (28a). Equations (30a) through (30e) are compared to Eqs. (22a), (22b), and (22e) through (22h).

F. Frequency

The first data correlated are the natural frequencies. Table 10 lists the natural frequencies from analysis and corresponding test frequencies together with the mode description for the first twelve modes. Except for the eleventh mode, which is a scan platform mode, all the frequencies match fairly well.

G. Orthogonality

The generalized mass, Eq. (28a), is normalized to a unit matrix by proper normalization of each individual mode. Ideally,

$$[\bar{M}]_T = [\phi]_T^T [M]_T [\phi]_T = [I] \quad (31)$$

Any errors in the mode shape measurement or mass data produce finite off-diagonal terms in the generalized mass matrix. If all off-diagonal terms are small, the measured normal modes are orthogonal to each other with respect to the mass matrix. Therefore, the orthogonality check serves as an indication of the accuracy of the measured test modes and test mass matrix. The orthogonality check of the first twelve test modes is in Table 11. The off-diagonal terms are indeed small and are within the 10% goal established for the test. The largest term occurs between the first and second modes. Since Table 10 indicates the natural frequencies of the first two modes to be almost identical, accurate mode shape measurements for these two modes are difficult to obtain.

H. Effective Mass (Ref. ?)

In principle, the number of independent normal modes in a structural system is equal to the number of degrees of freedom. Obviously some of these modes are highly localized and of minor importance as far as the load analysis is concerned. With a limited number of modes obtained in the modal test, criteria are required to establish that the measured modes include the significant structural modes. For this purpose, the generalized rigid-body mass is used in the following way. In the analysis, the generalized rigid-body mass is defined, as in Eq. (22g), as $[\bar{M}^{RR}]_{T,A}$ or

$$[\bar{M}^{RR}]_{T,A} = [\{u\}_R]^T [M]_{T,A} [\{u\}_R] \quad (32a)$$

TABLE 10
Modal Frequency Comparison

Mode	Frequency (Hz)			Description
	Analysis	Test	Error (%)	
1	4.35	4.51	3.5	Bending in X
2	4.40	4.63	5.0	Bending in Y
3	7.48	7.87	5.0	Lander in θ_Z
4	7.83	8.30	5.7	Lander in Y
5	10.92	11.51	5.1	Lander in X
6	13.36	14.09	5.2	Lander in θ_Y
7	14.64	15.35	4.6	Oxidizer tank in Z
8	17.95	19.49	7.9	Fuel tank in Z
9	18.81	19.83	5.1	Lander in θ_X
10	23.42	24.85	5.8	Fuel tank in Y
11	26.18	29.54	11.4	Scan platform in θ_Y
12	24.28	26.49	8.3	Lander in Z

TABLE 11
Orthogonality

Mode	1	2	3	4	5	6	7	8	9	10	11	12
1	100.0	6.2	-0.2	1.1	-0.3	1.1	-2.3	-0.6	-1.7	0.6	-2.4	0.0
2		100.0	0.1	-1.2	-4.1	-3.0	-0.9	-2.5	1.0	1.2	3.4	-1.5
3			100.0	0.4	0.8	1.6	-0.2	3.5	-1.5	-0.5	-0.7	0.4
4				100.0	1.0	1.3	1.2	-0.1	-1.8	1.2	1.1	-0.5
5					100.0	0.6	0.8	4.6	-1.0	0.2	1.7	-0.4
6						100.0	0.4	-0.5	1.3	4.4	-0.6	1.6
7							100.0	-0.2	-0.1	3.6	-0.1	-1.3
8								100.0	-1.1	-1.9	-0.2	-1.5
9									100.0	5.9	-2.9	2.7
10										100.0	1.0	-3.4
11											100.0	2.5
12												100.0

From the modal test results of Eq. (36d),

$$[\bar{\mathbf{M}}^{RR}]_T = [\{u\}_R]^T [\mathbf{M}]_T [\{u\}_R] \quad (32b)$$

An experimental generalized rigid-body-mass derived from $[\bar{\mathbf{M}}^{RE}]_T$ is defined as

$$[\bar{\mathbf{M}}^{RR}]_T = [\bar{\mathbf{M}}^{RE}]_T [\mathbf{I}] [\bar{\mathbf{M}}^{ER}]_T \quad (33)$$

where

$$[\bar{\mathbf{M}}^{RE}]_T = [\{u\}_R]^T [\mathbf{M}]_T [\phi]_T \quad (34)$$

$$[\bar{\mathbf{M}}^{ER}]_T = [\bar{\mathbf{M}}^{RE}]_T^T \quad (35)$$

If all the experimental modes are obtained, it can be proven that

$$[\bar{\mathbf{M}}^{RR}]_T = [\bar{\mathbf{M}}^{RR}]_T \approx [\bar{\mathbf{M}}^{RR}]_{T,A} \quad (36)$$

Another check is $[\bar{\mathbf{M}}^{RR}]_T$ must be equal to the rigid body inertia property of the test configuration.

In the modal test, a limited number of measured modes was used to calculate the $[\bar{\mathbf{M}}^{RR}]_T$, now defined as effective mass. The comparison of $[\bar{\mathbf{M}}^{RR}]_T$ and $[\bar{\mathbf{M}}^{RR}]_T$ indicates whether the major modes were effectively surveyed. If $[\bar{\mathbf{M}}^{RR}]_T$ is close to $[\bar{\mathbf{M}}^{RR}]_T$, the major important modes with respect to the restrained point were obtained. Table 12 shows the summary of the effective mass of the first twelve test modes and corresponding analytical modes. The first twelve modes represent over 90% of the effective mass with respect to the base of the VTA/CTA.

TABLE 12
Effective Mass in Percentage

Mode	Mass					
	X (%)	Y (%)	Z (%)	θ_x (%)	θ_y (%)	θ_z (%)
1 Analysis	96.42	1.76	0.01	1.34	85.20	0.14
Test	89.51	7.97	0.03	6.12	78.23	0.88
2 Analysis	1.67	87.47	0.0	63.66	1.49	1.09
Test	3.30	86.49	0.03	64.45	3.15	1.13
3 Analysis	0.95	0.28	0.0	1.75	0.02	55.21
Test	0.89	0.35	0.01	1.88	0.02	56.91
4 Analysis	0.06	5.60	0.03	28.95	0.01	1.94
Test	0.10	4.81	0.10	27.51	0.0	1.66
5 Analysis	0.05	0.06	0.56	0.10	6.40	19.58
Test	0.0	0.11	0.58	0.19	7.80	20.43
6 Analysis	0.20	0.06	5.63	0.10	4.77	9.83
Test	0.38	0.01	6.67	0.01	5.65	7.39
7 Analysis	0.0	0.01	49.02	0.01	0.40	0.25
Test	0.01	0.0	51.80	0.0	0.63	0.24
8 Analysis	0.02	0.01	12.98	0.01	0.04	0.07
Test	0.02	0.0	12.52	0.01	0.0	0.15
9 Analysis	0.0	0.06	0.45	0.06	0.0	0.41
Test	0.0	0.05	0.90	0.02	0.0	0.09

TABLE 12
Effective Mass in Percentage (contd)

Mode	Mass					
	X (%)	Y (%)	Z (%)	θ_x (%)	θ_y (%)	θ_z (%)
10 Analysis	0.0	0.02	3.15	0.03	0.0	0.0
Test	0.0	0.01	0.58	0.03	0.01	0.04
11 Analysis	0.0	0.02	13.60	0.07	0.0	0.23
Test	0.0	0.01	11.57	0.02	0.0	0.06
12 Analysis	0.0	0.02	5.02	0.06	0.0	0.0
Test	0.0	0.07	22.17	0.20	0.0	0.06
Total	Analysis	99.37	95.37	90.45	96.12	98.33
Test	94.39	100.24	95.96	100.20	95.89	89.15

I. Mode Shape

The eigenvectors or mode shapes are important in the load analysis. The mode shape is expressed in the form of modal deflections of each degree of freedom (DOF). In the mathematical model, each DOF is assigned to a number shown in Fig. 2, the ODTM modal test configuration. The direction of the modal

deflection is indicated by the last digit in the DOF. Translation in X, Y, and Z are 1, 2, and 3 respectively. For example, 1013 represents the motion of node 101 in the Z direction. The modal deflection of each DOF is expressed in their own local coordinate system, which is shown in Figs. 6 to 10.

The maximum amplitudes of the modal deflection are normalized to unity. The analysis and test are compared and the difference at each DOF is expressed as a weighted deviation (WD) defined as

$$WD = \left[[\phi]_{T,A} - [\phi]_T \right] \text{ normalized} \quad (37a)$$

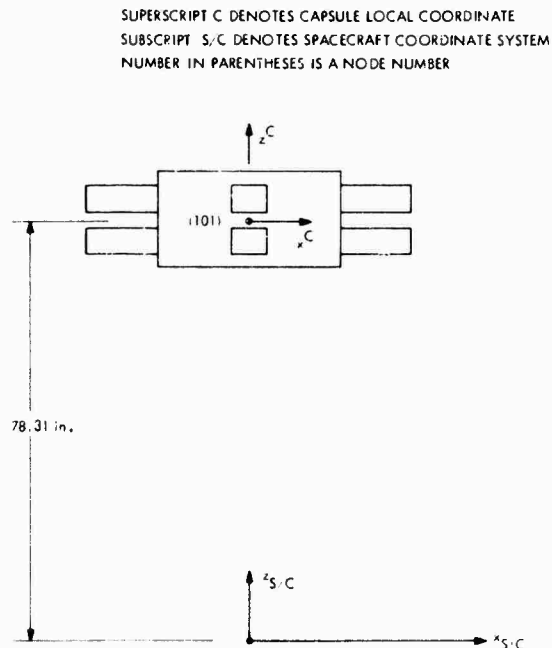


Fig. 6 - Local coordinate of VLC

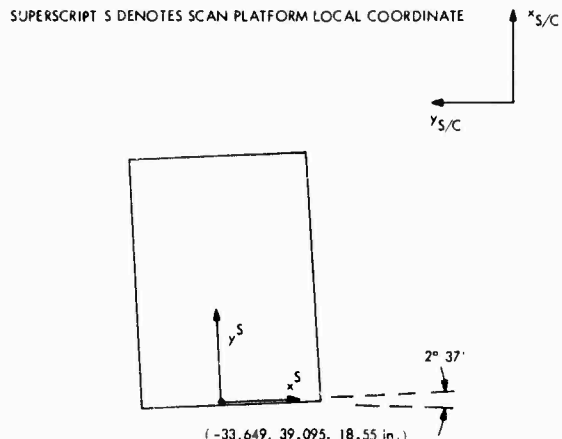


Fig. 7 - Local coordinate of scan platform

SUPERSCRIPT B DENOTES BUS LOCAL COORDINATE
NUMBERS IN PARENTHESES ARE NODE OR BAY NUMBERS

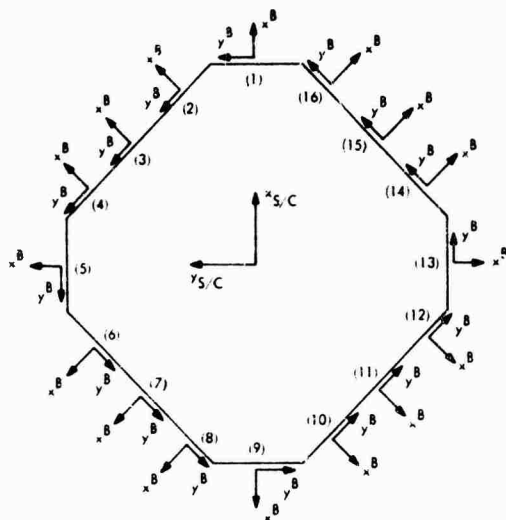


Fig. 8 - Local coordinate of bus

SUPERSCRIPT D DENOTES CABLE THROUGH LOCAL COORDINATE
NUMBERS IN PARENTHESES ARE NODE NUMBERS

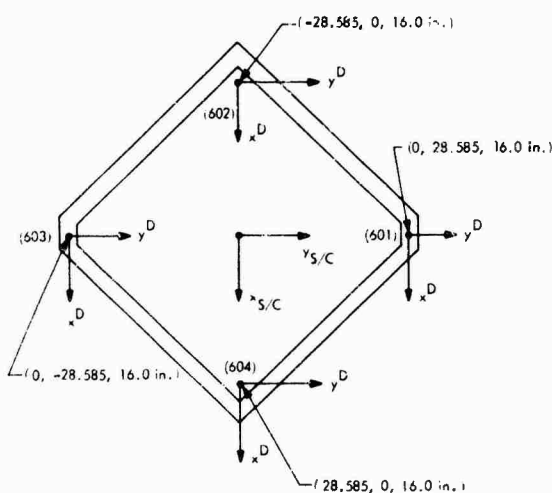


Fig. 9 - Local coordinate of cable trough

Also, for each mode the standard deviation (RSS) is calculated as

$$RSS = \left[\frac{1}{N} \sum_{i=1}^N (WD_i)^2 \right]^{1/2} \quad (37b)$$

SUPERSCRIPT P DENOTES PROPULSION LOCAL COORDINATE
NUMBERS IN PARENTHESES ARE NODE NUMBERS

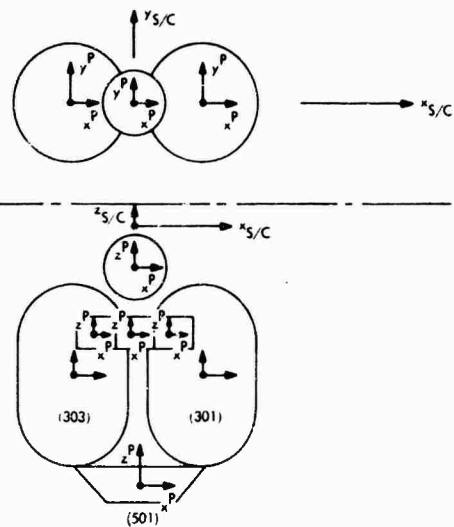


Fig. 10 - Local coordinate of propulsion module
where

N = number of DOF

$(WD)_i$ = weighted deviation of i^{th} DOF

In Tables 13 and 14, a typical mode shape comparison of a mode and the summary comparison of the first few modes, with only the important DOF and the standard deviations, are given.

TABLE 13
Modal Comparison - Analytical Mode 3 vs
Experimental Mode 701

DOF	Analysis	Test	Weighted Deviation
11	.346+00	.370+00	-.247-01
12	.666+00	.655+00	.109-01
13	.784-01	.490+01	.295-01
14	-.418-02	-.319+02	-.994-03
15	-.417-02	-.225+02	-.192-02
16	.101-01	.119-01	-.181-02
21	.505+00	.542+00	-.369-01
22	.284+00	.279+00	.568-02
23	.314-01	.459-01	-.145-01
24	-.260-02	.213+03	-.282-02
25	-.389-02	.254+02	-.643-02
26	.608-02	.958-02	-.351-02
31	.268+00	.286+00	-.178-01
32	.272+00	.226+00	.452-01
33	.747-01	.636-01	-.111-01

TABLE 13
Modal Comparison – Analytical Mode 3 vs
Experimental Mode 701 (contd)

DOF	Analysis	Test	Weighted Deviation
34	-0.314-02	-0.112-02	-0.202-02
35	0.968-02	0.570-02	0.399-02
36	0.707-02	0.162-01	-0.913-02
41	-0.914-02	-0.189-01	0.972-02
42	0.314-00	0.299-00	0.147-01
43	0.696-01	0.755-01	-0.593-02
44	-0.895-03	0.263-02	-0.353-02
45	-0.115-01	-0.171-02	-0.981-02
46	0.748-02	0.129-01	-0.538-02
51	-0.106-00	-0.110-00	0.312-02
52	0.353-00	0.325-00	0.281-01
53	0.140-00	0.121-00	0.187-01
54	-0.923-03	0.282-02	-0.375-02
55	-0.143-01	-0.889-02	-0.544-02
56	0.820-02	0.133-01	-0.506-02
61	-0.847-01	-0.966-01	0.119-01
62	0.403-00	0.322-00	0.804-01
63	0.135-00	0.113-00	0.229-01
64	-0.854-02	-0.347-02	-0.507-02
65	-0.976-02	-0.824-02	-0.152-02
66	0.139-01	0.158-01	-0.184-02
71	-0.309-00	-0.397-00	0.870-01
72	0.474-00	0.507-00	-0.328-01
73	0.707-01	0.137-00	-0.665-01
74	-0.364-02	-0.447-02	0.827-03
75	0.496-02	-0.124-01	0.173-01
76	0.145-02	0.146-01	-0.132-01
81	-0.561-00	-0.551-00	0.980-02
82	0.399-00	0.366-00	0.327-01
83	0.346-01	-0.388-01	0.734-01
84	-0.982-02	-0.216-02	-0.766-02
95	-0.119-01	-0.917-02	-0.270-02
86	0.115-01	0.155-01	-0.396-02
91	-0.297-00	-0.291-00	-0.617-02
92	0.806-00	0.816-00	-0.967-02
93	-0.756-01	-0.999-01	0.243-01
94	-0.976-02	-0.669-02	-0.307-02
95	-0.121-02	-0.782-02	0.662-02
96	0.100-01	0.520-02	0.482-02
101	0.186-00	0.167-00	0.195-01
102	0.851-00	0.931-00	-0.800-01
103	-0.161-00	-0.819-01	0.786-01
104	0.816-03	-0.629-02	0.711-02
105	-0.856-03	0.230-02	-0.315-02
106	-0.208-02	-0.172-02	-0.351-03
111	-0.949-01	-0.106-00	0.108-01
112	0.864-00	0.824-00	0.409-01
113	-0.124-00	-0.312-02	-0.121-00
114	-0.108-01	-0.352-03	0.104-01
115	0.195-01	0.227-01	0.326-02
116	0.103-01	0.913-02	0.118-02
121	-0.409-00	-0.361-00	-0.488-01
122	0.953-00	0.100-01	0.468-01
123	-0.187-00	-0.985-01	-0.889-01
124	-0.166-02	0.239-02	-0.405-02
125	-0.475-02	0.382-01	0.429-01
126	0.401-02	0.452-01	-0.412-01
131	0.287-01	0.327-01	-0.397-02

TABLE 13
Modal Comparison – Analytical Mode 3 vs
Experimental Mode 701 (contd)

DOF	Analysis	Test	Weighted Deviation
132	0.100+01	0.951+00	0.491-01
133	-0.140+00	-0.111+00	-0.287-01
134	0.323-02	0.513-02	-0.191-02
135	-0.120-01	0.656-02	-0.185-01
136	0.915-02	0.225-01	-0.133-01
141	0.460+00	0.459+00	0.825-03
142	0.790+00	0.691+00	0.994-01
143	-0.268-01	-0.246-01	-0.215-02
144	-0.263-03	0.662-02	-0.688-02
145	-0.106-01	-0.128-02	-0.935-02
146	0.138-01	0.195-01	-0.570-02
151	0.197+00	0.210+00	-0.129-01
152	0.795+00	0.744+00	0.504-01
153	0.500-01	-0.142-01	0.643-01
154	0.308-02	-0.193-03	0.327-02
155	0.141-03	-0.911-02	0.926-02
156	0.589-02	0.158-01	-0.994-02
161	-0.101-01	0.228-01	-0.329-01
162	0.784+00	0.770+00	0.142-01
163	0.690-01	0.215-01	0.476-01
164	-0.731-03	0.296-02	-0.369-02
165	-0.757-02	-0.831-02	0.738-03
166	0.152-01	0.111-01	0.408-02
1011	-0.464+00	-0.460+00	-0.392-02
1012	-0.374+00	-0.394+00	0.202-01
1013	-0.151-01	-0.206-01	0.547-02
1014	0.426-02	0.429-02	-0.389-04
1015	0.170-01	0.165-01	0.462-03
1016	0.398-01	0.426-01	-0.279-02
3011	0.470+00	0.467+00	0.239-02
3012	0.419+00	0.433+00	-0.146-01
3013	0.340-01	0.175-01	0.165-01
3014	0.499-02	0.512-02	-0.126-03
3015	-0.289-02	-0.343-02	0.541-03
3016	0.164-01	0.171-01	-0.742-03
3031	0.458+00	0.452+00	0.608-C2
3032	-0.165+00	-0.196+00	0.313-01
3033	-0.191-01	-0.426-01	0.236-01
3034	0.428-02	0.331-02	0.969-03
3035	-0.267-02	-0.364-02	0.978-03
3036	0.160-01	0.168-01	-0.798-03
4011	0.387+00	0.375+00	0.121-01
4012	-0.704-01	-0.598-01	-0.106-01
4013	0.756-02	-0.286-01	0.362-01
4014	0.373-02	0.689-02	-0.317-02
4015	0.289-02	-0.499-03	0.339-02
4016	0.181-01	0.192-01	-0.112-02
5011	0.551+00	0.566+00	0.148-01
5012	0.244+00	0.269+00	-0.245-01
5013	0.115-01	-0.225-01	0.346-01
5014	0.340-02	0.274-02	0.652-03
5015	-0.223-02	-0.713-03	0.151-02
5016	0.173-01	0.204-01	-0.313-02
2011	0.687+00	0.616+00	0.701-01
2012	-0.186+00	-0.407+00	0.217-01
2013	0.204+00	0.102+00	0.102-00
2014	-0.425-02	0.293-02	-0.718-02
2015	0.106-01	0.231-01	-0.126-01

TABLE 13
Modal Comparison – Analytical Mode 3 vs
Experimental Mode 701 (contd)

DOF	Analysis	Test	Weighted Deviation
2016	.147*01	.198*01	-.516*02
4021	.473*00	.743*00	-.698*01
4022	.120*00	.159*00	-.390*01
4023	-.75*01	-.324*01	-.432*01
4031	.673*00	.818*00	-.144*00
4032	.477*01	.833*01	-.354*01
4033	-.848*01	-.122*00	-.371*01
4041	.673*00	.734*00	-.603*01
4042	-.338*01	-.465*01	.127*01
4043	-.756*01	-.120*00	.449*01
6011	-.338*00	-.266*00	-.717*01
6012	-.268*00	-.259*00	-.934*02
6013	-.600*02	.341*01	-.401*01

TABLE 13
Modal Comparison – Analytical Mode 3 vs
Experimental Mode 701 (contd)

DOF	Analysis	Test	Weighted Deviation
6021	.379*00	.398*00	-.193*01
6022	-.848*00	-.852*00	.437*02
6023	.600*01	-.395*01	.996*01
6031	-.190*00	-.135*00	-.551*01
6032	.120*00	.120*01	.108*00
6033	.301*01	-.596*01	.897*01
6041	.239*00	.267*00	-.280*01
6042	.673*00	.649*00	.243*01
6043	-.379*01	.125*01	-.503*01
MAX EXPERIMENTAL AT 68 MAX ANALYTICAL AT 79 RSS ERROR = , .153*00			

TABLE 14
Summary of Mode Shape Comparison

Hardware	Mode 1		Mode 2		Mode 3		Mode 4		Mode 5		Mode 6		Direction
	Analysis	Test	Analysis	Test	Analysis	Test	Analysis	Test	Analysis	Test	Analysis	Test	
Lander	1.00 0.10	1.00 -0.23 -0.01	-0.09 0.45 0.01	0.14 0.50 0.02	0.46 0.37 0.02	0.46 0.39 0.02	-0.11 -1.00 -0.06	0.10 -1.00 -0.07	-0.81 -0.04 0.01	-0.80 -0.07 0.01	0.15 -0.02 -0.06	0.19 -0.08 -0.07	X Y Z
Scan platform	-0.06 0.83 -0.01	0.23 0.85 -0.12	-0.52 -0.08 0.10	-0.48 0.12 0.18	-0.69 0.19 -0.20	-0.62 0.21 -0.10	0.09 -0.01 0.29	0.08 -0.02 0.30	-0.51 0.85 -0.12	-0.45 0.75 -0.07	-0.30 0.92 0.31	-0.35 0.94 0.40	X Y Z
Bus	0.83 0.11 0.01	0.88 -0.34 0.02	-0.08 0.56 0.0	0.16 0.63 -0.08	-0.35 -0.67 -0.05	-0.37 -0.66 -0.05	-0.10 -0.17 -0.05	-0.10 -0.15 -0.02	0.20 -0.72 0.37	0.20 -0.63 0.31	0.13 -0.59 -0.29	0.14 -0.63 -0.31	X Y Z
Oxid tank	0.92 0.17 0.04	0.94 -0.35 -0.02	-0.07 0.78 0.0	0.12 0.84 0.01	-0.47 -0.42 -0.03	-0.47 -0.43 -0.02	-0.10 0.48 0.01	-0.10 0.50 0.0	0.67 -0.24 0.25	0.61 -0.27 0.25	-0.17 -0.28 -0.42	-0.18 -0.33 -0.52	X Y Z
Fuel tank	0.91 0.16 -0.04	0.94 -0.32 -0.04	-0.09 0.78 0.01	0.09 0.79 0.0	-0.46 0.17 0.02	-0.45 0.20 0.04	-0.09 0.48 0.02	-0.10 0.50 0.02	0.61 0.38 -0.15	0.60 0.41 -0.16	-0.16 0.39 0.04	-0.18 0.49 0.05	X Y Z
Press tank	0.79 0.11 0.0	0.86 -0.27 -0.04	-0.08 0.51 0.0	0.07 0.55 0.01	-0.39 0.07 -0.01	-0.38 0.06 0.03	-0.08 -0.05 0.02	-0.07 0.05 0.02	0.22 0.06 0.04	0.12 0.07 0.05	0.38 0.85 -0.20	0.47 0.79 -0.26	X Y Z
RSS	0.325		0.240		0.15		0.13		0.18		0.15		

J. Local Kinetic Energy

The generalized mass as shown in Eqs. (22h) and (28a) is expressed in the tensorial form as

$$\bar{M}_{ij}^{EE} = \sum_{l=1}^N \sum_{k=1}^N \Phi_{ik} M_{kl} \Phi_{lj} \quad (38)$$

If the normal modes Φ_{ij} are in the form of velocity, \bar{M}_{ij}^{EE} is in the form of kinetic energy

(see Eq. (5)). Then each term in Eq. (38) represents the modal kinetic energy associated with that particular DOF. In essence, this is an itemized generalized mass. The comparison of each individual term in Eq. (38) between the test and analysis provides detailed information about the mass associated with each DOF and the modal amplitude of that DOF. This is especially valuable for those degrees of freedom where the mass is questionable, such as the propellant tanks. The standard deviation (RSS) for the local kinetic energy comparison for each mode is calculated similarly to the mode shape comparison. In Table 15, a typical mode is selected for the kinetic energy comparison. Also, in Table 16, a summary comparison of the first few modes and the standard deviation of the kinetic energy comparison is given.

TABLE 15
Kinetic Energy Comparison – Analytical
Mode 3 vs Test Mode 701

DOF	Analysis	Experimental
11	.08	.09
12	.31	.27
13	.00	.00
14	.00	.00
15	.00	.00
16	.00	.00
21	.20	.21
22	.06	.05
23	.00	.00
24	.00	.00
25	.00	.00
26	.00	.00
31	.05	.05
32	.05	.03
33	.00	.00
34	.00	.00
35	.00	.00
36	.00	.01
41	.00	.00
42	.06	.05

TABLE 15
Kinetic Energy Comparison – Analytical
Mode 3 vs Test Mode 701 (contd)

DOF	Analysis	Experimental
43	.00	.00
44	.00	.00
45	.00	.00
46	.00	.00
51	.01	.01
52	.10	.08
53	.02	.01
54	.00	.00
55	.01	.00
56	.00	.00
61	.01	.01
62	.11	.07
63	.01	.01
64	.00	.00
65	.00	.00
66	.00	.01
71	.06	.08
72	.13	.14
73	.00	.01
74	.00	.00
75	.00	.01
76	.00	.01
81	.16	.14
82	.08	.06
83	.05	.00
84	.00	.00
85	.00	.00
86	.00	.01
91	.09	.08
92	.66	.62
93	.01	.01
94	.00	.00
95	.00	.00
96	.00	.00
101	.02	.02
102	.50	.54
103	.02	.00
104	.00	.00
105	.00	.00
106	.00	.00
111	.01	.01
112	.51	.42
113	.01	.00
114	.01	.00
115	.01	.02
116	.00	.00
121	.16	.11
122	.84	.84
123	.03	.01
124	.00	.00
125	.00	.06
126	.00	.05
131	.00	.00
132	.02	.04
133	.02	.01
134	.00	.00
135	.00	.00
136	.00	.01
141	.12	.11

TABLE 15
Kinetic Energy Comparison - Analytical
Mode 3 vs Test Mode 701 (contd)

DOF	Analysis	Experimental
142	.35	.24
143	.00	.00
144	.00	.00
145	.00	.00
146	.00	.00
151	.02	.02
152	.39	.31
153	.00	.00
154	.00	.00
155	.00	.00
156	.00	.01
161	.00	.00
162	.51	.45
163	.00	.00
164	.00	.00
165	.00	.00
166	.01	.00
1011	5.39	4.75
1012	3.98	4.03
1013	.01	.02
1014	.43	.40
1015	7.59	6.56
1016	62.20	64.90
3011	4.55	4.10
3012	3.60	3.51
3013	.03	.01
3014	.02	.02
3015	.00	.00
3016	.11	.11
3031	2.63	2.34
3032	.33	.43
3033	.01	.02
3034	.02	.01
3035	.02	.03
3036	.10	.10
4011	.14	.12
4012	.00	.00
4013	.00	.00
4014	.00	.00

The local kinetic energy information is also valuable in identifying the mode shapes by describing the items with the largest kinetic energy. The data are also used in defining the system damping from the substructure damping measurements.

K. Modal Force

In the analysis, the modal forces of the truss members are calculated for each mode. During the test, strain gauge data were taken at these truss members from which the test modal forces are obtained. The calculated modal forces from the analysis and measured member forces from the test are compared.

TABLE 15
Kinetic Energy Comparison - Analytical
Mode 3 vs Test Mode 701 (contd)

DOF	Analysis	Experimental
4015	.00	.00
4016	.03	.03
5011	.19	.16
5012	.04	.04
5013	.00	.00
5014	.00	.00
5015	.00	.00
5016	.02	.02
2011	.95	.78
2012	.06	.10
2013	.07	.03
2014	-.02	.02
2015	.24	.60
2016	-.03	.09
4021	.05	.05
4022	.00	.00
4023	.00	.00
4031	.05	.07
4032	.00	.00
4033	.00	.00
4041	.05	.05
4042	.00	.00
4043	.00	.00
6011	.02	.01
6012	.01	.01
6013	.00	.00
6021	-.02	.02
6022	.10	.09
6023	.00	.00
6031	.01	.00
6032	.00	.00
6033	.00	.00
6041	.01	.01
6042	.07	.06
6043	.00	.00

RSS ERROR = .247400

Since the magnitudes of the analytical modal forces are arbitrary, a normalization factor is found to multiply the analytical value to make a meaningful comparison. This normalization factor is calculated as follows:

$$\alpha = \frac{\sum_{i=1}^N (P_i^A P_i^T)}{\sum_{i=1}^N (P_i^A P_i^A)} \quad (39)$$

TABLE 16
Summary of Kinetic Energy Comparison

Mode DOF		1	2	3	4	5	6
Bus (%)	A*	11.45	11.23	6.87	1.98	13.76	17.82
	T†	11.38	11.43	6.25	1.54	11.90	14.41
Lander (%)	A	42.75	19.22	79.61	77.35	42.72	43.65
	T	40.58	21.88	80.65	77.35	44.25	42.51
Oxidizer tank (%)	A	25.64	39.35	8.32	11.16	23.81	21.05
	T	26.42	39.80	7.75	11.64	22.51	24.04
Fuel tank (%)	A	15.26	24.53	3.10	7.08	14.34	7.66
	T	16.01	21.22	2.93	7.52	15.46	9.18
Pressure tank (%)	A	0.84	0.79	0.18	0.05	0.23	0.73
	T	0.97	0.78	0.16	0.05	0.18	0.86
Engine (%)	A	0.93	2.00	0.25	1.02	1.31	0.84
	T	0.92	1.78	0.25	1.14	1.39	0.85
Scan platform (%)	A	2.08	1.92	1.27	0.64	3.22	7.30
	T	2.01	2.09	1.63	0.59	3.80	7.40
RSS (%)		0.452	0.319	0.247	0.208	0.233	0.330

*Analysis.
†Test.

where

α = normalization factor

N = number of members

P_i^A = analytical modal force of the i^{th} member

P_i^T = test modal force of the i^{th} member

The factor α minimizes the difference between the analytical value and test value in the least-square sense. The analytical member forces are multiplied by α and compared with the test value. Table 17 shows this comparison

together with the ratio of the comparison for a typical mode. The truss member identification is defined in Ref. (8). Only the axial forces are used in the comparison. The bending forces are not included in the comparison.

The discrepancies between the test and analysis are thought to be from two sources. One is the inherent disadvantage of using strain gauges that were setup for high strain reading from the static test. Since low levels of strain were recorded in the modal test, the accuracy of the reading is in question. The other source of discrepancy is the difference between the analysis and test mode shape. The modal forces are very sensitive to local differences in the mode shape.

TABLE 17
Axial Force Comparison – Factor = 6.076

Member	P (test) Mode 701 Freq = 7.840 Hz	P (analysis) Mode 3 Freq = 7.480 Hz	Ratio <u>P (analysis)</u> <u>P (test)</u>
TECFRAME			
BUS654	-0.2318+02	-0.2736+02	.1190+01
BUS661	.4773+01	.5932+01	.1222+01
BUS662	.2578+02	.3009+02	.1167+01
BUS664	-0.4597+00	-0.4137+01	.4311+01
SPACECRAFT TRUSS			
BUS646	-0.4931+02	-0.4710+02	.9437+00
BUS687	.1795+02	.1788+02	.1002+01
BUS639	.6992+02	.6230+02	.9052+00
BUS699	-0.1110+03	-0.1096+03	.9787+00
BUS690	-0.5990+02	-0.5524+02	.1089+01
BUS691	.2747+01	.2310+01	.8409+00
BUS692	-0.1106+02	-0.9632+01	.9703+00
BUS693	.6297+02	.6660+02	.1159+01
BUS694	.2033+03	.1338+03	.9806+00
BUS695	-0.1613+03	-0.1533+03	.9514+00
BUS696	-0.1849+02	-0.1939+02	.1049+01
BUS697	.6590+02	.5952+02	.9980+00
UPPER FLANGE TRUSS			
BUS726	-0.5537+02	-0.4972+02	.3793+00
BUS727	.6018+02	.6321+02	.1051+01
BUS729	-0.9699+01	-0.1255+02	.1294+01
BUS730	-0.2076+02	-0.2027+02	.1265+01
BUS732	.7329+01	.9957+01	.1359+01
BUS742	.1023+03	.9305+02	.3190+00
BUS746	-0.1095+03	-0.9234+02	.9557+01
LANDER TRUSS			
BUS750	.1195+01	.6561+01	.5491+01
BUS751	-0.1671+03	-0.1615+03	.9667+00
BUS752	.9808+02	.9439+02	.9524+00
BUS753	-0.1791+03	-0.1794+03	.1001+01
BUS754	.2112+03	.2227+03	.1055+01
BUS755	.4500+02	.5093+02	.1130+01
BUS MAIN LONGRDN			
BUS80F	.3042+02	.3031+02	.1194+01
BUS910	.1692+02	.1527+02	.9073+00
BUS811	.5996+01	.1418+02	.2365+01
BUS813	-0.1721+02	-0.1519+02	.3923+00
BUS81F	-0.1381+03	-0.1515+03	.1097+01
BUS818	-0.1525+03	-0.1313+03	.9611+00
BUS820	.4821+01	.5156+01	.1069+01
BUS823	-0.1863+02	-0.1906+02	.9663+00
BUS82E	.2078+03	.2228+03	.1072+01
BUS937	.1413+00	.9304+01	.6549+02

TABLE 17
Axial Force Comparison – Factor = 6.076 (contd)

Member	P (test) Mode 701 Freq = 7.840 Hz	P (analysis) Mode 3 Freq = 7.480 Hz	Ratio P (analysis) P (test)
EUS831	-.3867*02	-.3952*02	.1022*01
BUS932	.5C98*02	.4794*02	.9384*00
EUS933	-.1038*03	-.1C59*03	.1C2L*01
BUS939	-.4313*01	-.1563*01	.3625*00
EUS840	.1417*02	.1782*02	.1257*01
BUS941	-.2594*02	-.2123*02	.9184*00
PROPULSION SUBSYSTEM			
FFF003	.7637*01	.3336*01	.4369*00
FFF004	-.5652*01	.9120*01	-.1614*01
FFF008	.2962*01	.1560*02	.1747*01
FFF011	.1276*02	.1552*02	.1216*01
FFF012	-.6929*02	-.6563*02	.961L*00
FFF019	-.1608*01	-.1349*02	.9391*01
FFF028	.0454*00	.2003*01	.2753*01
FFF036	.5470*02	.436L*02	.7970*00
FFF037	.2029*02	.8557*01	.4217*00
FFF040	-.2423*02	-.2961*02	.1213*01
FFF041	.1876*02	.2142*02	.1172*01
FFF043	.5946*01	.6036*01	.1C15*01
FFF047	-.533L*01	-.3F19*01	.570L*00
FFF092	.2706*00	-.2533*01	-.9351*01
R.S.S. ERROR OF TEST VS ANALYSIS COMPARISON OF AXIAL FORCES			
		NORMALIZATION FACTOR	RSS ERROR OF FORCES
INPUT FACTOR		.000	.000
CALCULATED FACTOR		6.076	6.037
C.E. =	.5462*00		
W.E. =	.1692*00		

Several methods are used to establish a measure of error. They are:

Description	Relation	Reason
Least square error (LSE)	$\left[\frac{1}{N} \sum_{i=1}^N \left(P_i^T - P_i^A \right)^2 \right]^{1/2}$	No weight

Description	Relation	Reason
Weighted least square error (WLSE)	$\left[\frac{1}{N} \sum_{i=1}^N \left(\frac{\epsilon_T}{\epsilon_{FS}} \right) (P_i^T - P_i^A)^2 \right]^{1/2}$	Weighted readings with higher strain
Composite error (CE)	$\left[\frac{\sum_{i=1}^N \left P_i^T \right \left[\frac{(P_i^T - P_i^A)^2}{P_i^A} \right]}{\sum_{i=1}^N \left P_i^T \right } \right]^{1/2}$	Weighted readings with higher forces

where

ϵ_T = test strain gauge reading

ϵ_{FS} = full scale strain gauge reading

The results of the various weighting methods are in Table 18. Also the composite error is applied only to the Viking lander capsule adapter (VLCA) and V-S/C-A as shown in Table 19 to compare the data with the proof launch spacecraft Modal test (Ref. 9).

TABLE 18
Modal Force Comparison Errors

Mode		Least Square Error (lb)	Weighted Least Square Error (lb)	Composite Error (%)
Analysis	Test			
1	708	53.01	2.09	74.82
2	703	32.28	0.90	50.62
3	701	6.94	0.94	54.62
4	702	17.69	0.030	19.40
5	704	9.19	0.015	19.89
6	705	6.38	0.086	21.94
7	711	28.41	1.16	35.54
8	717	42.66	1.37	75.13
9	712	45.87	1.73	72.12
10	707	2.26	0.0035	51.87
11	714	22.39	0.29	101.3
12	713	52.71	1.61	98.83

TABLE 19
Composite Error of VLCA and V-S/C-A

Mode		VLCA (%)	V-S/C-A (%)
Analysis	Test		
1	708	55.75	46.81
2	703	54.56	41.67
3	701	18.81	12.06
4	702	5.37	7.19
5	704	8.20	17.52
6	705	25.46	8.53
7	711	21.82	14.89
8	717	49.18	51.88
9	712	79.37	82.52
10	707	29.95	59.40
11	714	102.0	108.6
12	713	62.99	21.99

To help resolve the source of discrepancy, test force coefficients are checked using the modal acceleration data. The truss loads resulting from the modal acceleration times the mass applied as a static load are compared to the modal force coefficient. The comparison for the VLCA members is shown in Table 20. The good correlation indicates the error to be the result of the difference in the analytical and test modes.

TABLE 20
Comparison of Modal Force by Inertia Load –
Mode 713, Frequency 26.49 Hz

Member No.	Test (lb)	Inertia (lb)	Analysis (lb)
750	161	175	134
751	53	47	-20
752	262	299	166
753	279	291	290
754	116	131	-44
755	104	130	157
LSE		20.92	85.41
CE		12.76	62.99

Future efforts will be to obtain the force coefficient throughout the structure by application of the modal acceleration times the mass as an external load.

L. Strain Energy

Strain energy (SE) of a mode is a significant parameter in the description of a mode shape, especially when modal forces are of interest. Equation (5) directly relates strain energy to the stiffness matrix.

For a mode, strain energy values describe the member or sets of members with the largest forces and deformations whereas kinetic energy (KE) describes the masses with the largest inertial motion. The significant difference is the SE of the system is directly related to relative displacements at the ends of the members whereas KE is directly related to the absolute displacement.

The axial strain energy of the i^{th} member monitored during the modal test is

$$(SE)_i = \frac{1}{2} \frac{F_i^2 L_i}{A_i E_i} \quad (40)$$

where

$(SE)_i$ = strain energy of the i^{th} member

F_i = force in the i^{th} member

L_i = length of the i^{th} member

A_i = cross-sectional area of the i^{th} member

E_i = modulus of elasticity of the i^{th} member

The SE of each axial member for both analysis and test is listed in the order of its magnitude. Also the SE of each member group is listed to help identify the characteristics of the mode shape. Table 21 shows the strain energy of each member and the comparison between test and analysis of a typical mode both in its magnitude and percentage. Table 22 shows the comparison of the same mode listed in the order of magnitude. Table 23 shows the percentage SE of each member group for the first twelve modes.

TABLE 21
Strain Energy Comparison – Analytical Mode 3 vs Test Mode 701

Member	Test (in.-lb)	Analysis (in.-lb)	Tcst (%)	Analysis (%)
TEC FRAME				
BUS559	.4564-02	.6497-02	.2716-02	.3875-02
BUS600	.2777-03	.4145-03	.1618-03	.2472-03
BUS602	.5556-02	.7705-02	.3294-02	.4596-02
BUS604	.1115-04	.2679-03	.0511-03	.1239-03
TOTAL:	.1061-01	.1492-01	.179-02	.9942-02
SPACECRAFT TRUSS				
BUS606	.1435-01	.1273-01	.8755-02	.7621-02
BUS607	.2637-02	.2646-02	.1539-02	.1578-02
BUS608	.3074-01	.2519-01	.1790-01	.1903-01
BUS609	.7540-01	.7318-01	.4449-01	.4365-01
BUS60C	.3551-01	.4213-01	.2068-01	.2513-01
BUS601	.4129-04	.2913-04	.2404-04	.1741-04
BUS607	.6894-03	.5077-03	.3998-03	.3028-03
BUS603	.3192-01	.3592-01	.1952-01	.2136-01
BUS606	.2807+00	.2410+00	.1460+00	.1438+00
BUS605	.154F+00	.1337+00	.3003-01	.8330-01
BUS60F	.336F-02	.3705-02	.1960-02	.2210-02
BUS607	.2347-01	.1351-01	.1367-01	.1104-01
TOTAL:	.6244+00	.5952+00	.3436+00	.3550+00
UPPER FLANGE TRUSS				
BUS726	.9999-02	.7741-02	.1922-02	.4817-02
BUS727	.1133-01	.1251-01	.6810-02	.7459-02
BUS728	.2151-03	.3607-03	.1253-03	.2149-03
BUS730	.1617-02	.2583-02	.5793-03	.1541-02
BUS732	.1233-03	.2285-03	.7208-04	.1353-03
SUS742	.819F-01	.6791-01	.4773-01	.4L45-01
BUS748	.1056+00	.7729-01	.6147-01	.4610-01
TOTAL:	.2108+00	.1685+00	.1228+00	.1L05+00
LANDER TRUSS				
BUS750	.1087-04	.3265-03	.6309-05	.1948-03
BUS751	.2261+00	.2113+00	.1717+00	.1160+01
BUS752	.5158-01	.4777-01	.3804-01	.2350-01
BUS753	.16L8+00	.1613+00	.976F-01	.9619-01
BUS754	.3617+00	.4619+00	.2104+00	.2397+00
BUS755	.1647-01	.2101-01	.6592-02	.1253-01
TOTAL:	.8167+00	.3435+00	.4753+00	.5L31+00
BUS MATN LONGITRON				
BUS90F	.2185-03	.3113-03	.1272-03	.1257-03
BUS910	.4135-03	.3409-03	.2409-03	.2L33-03
BUS911	.1799-04	.9597-04	.1041-04	.5903-04
BUS917	.5177-03	.4630-03	.3015-03	.2404-03
BUS918	.4413-02	.5312-02	.2570-02	.3169-02
BUS919	.5739-02	.3995-02	.3139-02	.2393-02
BUS920	.321F-04	.3677-04	.1872-04	.2193-04
BUS923	.6257-03	.5343-03	.3644-03	.3495-03
BUS92F	.1637-01	.1187-01	.8015-02	.7L81-02

TABLE 21
Strain Energy Comparison – Analytical Mode 3 vs Test Mode 701 (contd)

Member	Test (in.-lb)	Analysis (in.-lb)	Test (%)	Analysis (%)
EUS930	.3011-07	.1331-L3	.1753-07	.7937-04
EUS931	.3941-02	.4110-L2	.2295-L2	.2455-02
3US932	.4339-C2	.4262-L2	.2913-C2	.2542-02
4US933	.2548-L2	.2650-02	.1487-L2	.1581-02
3US934	.2664-C4	.3500-05	.1551-04	.2699-05
EUS848	.4822-L3	.7590-L3	.2790-03	.4527-03
3US941	.1170-C2	.7835-L3	.6912-03	.4573-03
TOTAL=	.3498-01	.3560-L1	.2638-L1	.2127-L1
PROPULSION SUBSYSTEM				
PPP003	.1049-03	.2002-04	.9109-04	.1194-04
FFF004	.6654-L4	.1733-L3	.3975-04	.1034-03
PPP009	.4594-03	.1402-02	.2675-C3	.9353-C3
FFF011	.3571-C3	.5280-L3	.2180-L2	.3149-03
PPP012	.9433-02	.3711-02	.5493-02	.5196-02
FFF018	.8424-L5	.9311-L3	.4906-05	.3538-03
PPP029	.2150-05	.1630-L4	.1252-05	.9721-05
FFF038	.6637-02	.4212-L2	.3963-02	.2513-L2
PPP037	.7346-C3	.1413-03	.4627-03	.3430-04
PPP040	.1657-L2	.1570-L2	.6154-C3	.9365-03
PPP041	.7524-03	.1036-02	.4382-03	.6177-03
FFF047	.2921-L3	.2917-L3	.1648-L3	.1740-L3
PPP053	.2297-03	.1054-03	.1332-03	.6239-04
FFF082	.2134-L6	.1870-L4	.1243-L6	.1115-L4
TOTAL=	.2010-01	.1892-L1	.1175-01	.1123-01
TOTAL=	.1717-01	.1677-L1	.1000-01	.1000-01
R.S.S. ERROR OF TEST VS ANALYSIS COMPARISON OF STRAIN ENERGY				
		NORMALIZATION FACTOR	RSS ERROR OF FORCES	
INPUT FACTOR		6.076	6.937	
CALCULATED FACTOR		.933	.001	

TABLE 22
Strain Energy in Order of Magnitude – Analytical Mode 3 vs Test Mode 701

Member	Strain Energy (Test) (in.-lb)	Member	Strain Energy (Analysis) (in.-lb)
EUS754	.2104+00	EUS754	.2397+00
EUS694	.1461+00	EUS694	.1438+00
SUS751	.1317+00	SUS751	.1200+00
EUS753	.9365-01	EUS753	.9619-L1
EUS695	.9003-C1	EUS695	.9330-01
EUS746	.6147-01	EUS746	.4610-L1
BUS742	.4773-L1	BUS699	.4365-01
EUS689	.4449-C1	BUS742	.4045-L1
BUS752	.3004-C1	BUS752	.2950-01
EUS690	.2068-01	EUS690	.2513-L1

TABLE 22
Strain Energy in Order of Magnitude – Analytical Mode 3 vs Test Mode 701 (contd)

Member	Strain Energy (Test) (in.-lb)	Member	Strain Energy (Analysis) (in.-lb)
PUS693	.1359-C1	BUSC93	.2136-L1
PUS698	.1700-C1	BUSF98	.1503-L1
BUS697	.1367-C1	BUS755	.1253-C1
BUS755	.1592-C2	BUS697	.1104-C1
BUS595	.0355-C2	BUS695	.7621-C2
BUS727	.0001-C2	BUS727	.7459-L2
BUS385	.0015-C2	BUS925	.7031-L2
EUS720	.0022-C2	FFF012	.5196-C2
PPPO12	.0487-C2	BUS726	.4517-S2
FFFC30	.0963-C2	BUS662	.4596-C2
BUS662	.3294-C2	BUS553	.3375-C2
EUS818	.7138-C2	BUS816	.3169-L2
BUS932	.2919-C2	BUS932	.2542-L2
EUS659	.2710-C2	FFF036	.2513-L2
BUS915	.2570-C2	BUS931	.2455-S2
EUS831	.2295-C2	BUS819	.2383-L2
BUS695	.1360-C2	BUS696	.2210-C2
EUS687	.1530-C2	BUS835	.1581-L2
BUS935	.1492-C2	BUS587	.1579-C2
EUS730	.9393-C3	BUS730	.1541-L2
BUS341	.0812-C3	FFP040	.9365-C3
PPPO40	.0154-C3	FFF009	.9363-C3
PPPO37	.0627-C3	PPPO41	.6177-C3
FFFC41	.0792-C3	EUS941	.4673-C3
BUS692	.3999-C3	BUS340	.4527-C3
BUS823	.3644-C3	FFP018	.3538-C3
BUS313	.3015-C3	BUS323	.3485-C3
EUS940	.2796-C3	FFP011	.3149-L3
PPPO09	.2575-C3	BUS582	.3028-C3
EUS810	.2409-C3	BUS660	.2472-L3
PPPO11	.2080-C3	BUS913	.2404-C3
FFFC43	.1640-C3	BUS728	.2149-L3
BUS660	.1516-C3	BUS910	.2033-C3
FFP053	.1332-C3	BUS750	.1348-C3
BUS906	.1272-C3	BUS806	.1957-L3
BUS728	.1257-C3	FFP043	.1740-L3
BUS732	.7208-C4	BUS732	.1363-C3
FFP003	.0109-C4	BUS664	.1239-C3
PPPO04	.3375-C4	PPPO04	.1034-C3
FUS691	.2404-C4	FFP037	.8430-L4

M. Reaction Forces

The calculation of reaction forces at the base of the VTA/CTA by the modal forces from the V-S/C-A strain gages and the modal accelerations provides a check on the test data.

The $[\bar{M}RE]_T$ matrix from Eq. (30d) represents the reaction forces from the modal accelerations. The reaction forces calculated from the V-S/C-A modal member force data are compared to $[\bar{M}RE]_T$. The comparison of the data are in Table 24.

N. Generalized Mass from Modal Damping

The generalized mass terms $[\bar{M}^{EE}]$ from Eq. (30d) are checked by the following relationship. At a normal mode, the damping values are offset by the force values. From Eq. (28),

$$[\bar{C}]_T \{ \dot{q} \}_T = [\Phi]_T^T \{ f \}_T \quad (41)$$

for the n^{th} mode. Since

TABLE 23
Strain Energy Distribution Comparison

Mode	Bedframe (%)	V-S/C Truss (%)	Upper Plane Truss (%)	Lander Truss (%)	Bus Main Longeron (%)	Propulsion Subsystem (%)
1 A*	0.01	0.86	0.03	0.09	0.04	0.02
1 T†	0.01	0.84	0.03	0.08	0.04	0.03
2 A	0.09	0.73	0.03	0.04	0.01	0.10
2 T	0.06	0.78	0.02	0.04	0.01	0.09
3 A	0.09	0.36	0.10	0.50	0.02	0.01
3 T	0.06	0.36	0.12	0.48	0.02	0.01
4 A	0.10	0.35	0.03	0.42	0.04	0.06
4 T	0.07	0.40	0.03	0.40	0.04	0.06
5 A	0.0	0.54	0.03	0.30	0.04	0.09
5 T	0.0	0.55	0.04	0.26	0.04	0.12
6 A	0.05	0.43	0.05	0.31	0.04	0.13
6 T	0.04	0.47	0.07	0.24	0.04	0.15
7 A	0.26	0.22	0.05	0.11	0.06	0.35
7 T	0.20	0.24	0.08	0.11	0.07	0.38
8 A	0.36	0.09	0.01	0.09	0.02	0.44
8 T	0.26	0.11	0.02	0.25	0.03	0.34
9 A	0.20	0.05	0.05	0.44	0.03	0.23
9 T	0.20	0.05	0.04	0.38	0.04	0.29
10 A	0.01	0.08	0.02	0.57	0.02	0.30
10 T	0.04	0.07	0.02	0.58	0.03	0.28
11 A	0.10	0.22	0.06	0.46	0.02	0.13
11 T	0.04	0.22	0.27	0.58	0.01	0.08
12 A	0.06	0.08	0.10	0.63	0.02	0.11
12 T	0.10	0.23	0.03	0.51	0.03	0.12

* Analysis.

† Test.

TABLE 24
Comparison of Reaction Force

Mode	Reaction Force: Accelerometer (Strain Gage) ^a					
	F_X (lb)	F_Y (lb)	F_Z (lb)	M_X (in.-lb)	M_Y (in.-lb)	M_Z (in.-lb)
708	401 (517)	-120 (-169)	-8 (54)	16700 (15587)	60000 (52441)	-1270 (-1565)
703	75 (78)	383 (391)	8 (-102)	-52400 (-33728)	11600 (6802)	1394 (1926)
701	45 (50)	-28 (-36)	-4 (-10)	10300 (9540)	1110 (-1398)	11400 (12847)
702	19 (14)	131 (138)	19 (-22)	-49300 (-44093)	59 (-1311)	2440 (2374)
704	-2 (-1)	19 (-1)	-44 (-50)	-3900 (-1585)	23700 (25842)	8060 (9087)
705	25 (22)	-4 (5)	-107 (-119)	684 (62)	15000 (14108)	-3440 (-4483)
711	12 (5)	-2 (-2)	1080 (1106)	241 (974)	18100 (18207)	-2240 (-3388)
717	17 (28)	-6 (-40)	444 (465)	1810 (3392)	833 (762)	-1490 (-557)
712	2 (17)	28 (81)	125 (97)	2600 (-6375)	-438 (248)	1200 (920)

^aNumbers in parentheses refer to strain gage measurements.

$$\bar{C}_{nn} = 2\rho_n \bar{M}_{nn} \omega_n \quad (42)$$

then

$$\bar{M}_{nn} = \frac{[\Phi_{ij}]}{2\rho_n \omega_n q_n} \{f\} \quad (43)$$

Each generalized mass term \bar{M}_{nn} is calculated from Eq. (43) by measuring the modal damping, frequency, velocity of the participation factor, shaker force, and displacement in the force direction. The comparison is in Table 25. Since the modal damping ρ_n varied, the \bar{M}_{nn} varied accordingly. As noted, the \bar{M}_{nn} is within the range of the damping measured; however, because of the variation in ρ_n , \bar{M}_{nn} cannot be accurately measured by this method.

TABLE 25
Generalized Mass Comparison

Mode	Based on Damping			Based on Mode Shape
	High	Aver-age	Low	
708	0.065	0.141	1.021	0.261
703	0.111	0.179	0.617	0.252
701	0.130	0.227	0.833	0.290
702	0.063	0.091	0.410	0.364
704	0.133	0.290	0.785	0.344
705	0.056	0.081	0.330	0.244
711	0.902	1.499	3.037	0.881
712	1.111	2.043	5.557	0.776
707	0.011	0.024	0.060	0.083
714	0.171	0.376	3.141	0.397
713	1.292	2.179	6.692	1.101

FINAL DYNAMIC MODEL

The final VO dynamic model is a combination of the modal test configuration and sub-structure characteristics verified by substructure tests. Since Eq. (22) representing the modal test configuration was verified by test, the parameters are accurate. Modifications are made to update the parameters to the V-S/C Mission B configuration. The subscript FB denotes Mission B configuration. The changes are:

CHANGES	REASON
$[M]_{T,A}$ to $[M]_{FB}$	The mass of the propellant is changed to the Mission B configuration; see Table 2.
$\{q\}_{P,T}$ to $\{q\}_{P,FB}$	The dynamic characteristics of the propulsion module changes
$\{q\}_{S,T}$ to $\{q\}_{S,FB}$	The dynamic characteristic of the scan platform changes since its joint is allowed to move along the serrations

The parameters verified by the modal test and updated to represent Mission B are combined with the remainder of the substructures. Each substructure is verified by a modal test. The combined equation of motion represented by Eq. (18) becomes

\hat{t}_{IR}^0	\hat{t}_{IR}^0	\hat{t}_{IR}^0
\hat{t}_{FB}^0	\hat{t}_{FB}^0	\hat{t}_{FB}^0
\hat{t}_{IP}^0	\hat{t}_{IP}^0	\hat{t}_{IP}^0
\hat{t}_{IS}^0	\hat{t}_{IS}^0	\hat{t}_{IS}^0
$[\mathbf{M}]_{\text{FB}}$	\hat{t}_{FC}^0	$[\mathbf{c}]_{\text{FB}}$
	\hat{t}_{FC}^0	\hat{t}_{FC}^0
	\hat{t}_{IP}^0	$[\mathbf{K}]_{\text{FB}}$
	\hat{t}_{IP}^0	\hat{t}_{FC}^0
	\hat{t}_{SPA}^0	$[\mathbf{e}]_{\text{FB}}$
	\hat{t}_{SPA}^0	\hat{t}_{SPA}^0
	\hat{t}_{SP1}^0	\hat{t}_{SP1}^0
	\hat{t}_{SP1}^0	\hat{t}_{SP1}^0
	\hat{t}_{SP2}^0	\hat{t}_{SP2}^0
	\hat{t}_{SP2}^0	\hat{t}_{SP2}^0
	\hat{t}_{SP3}^0	\hat{t}_{SP3}^0
	\hat{t}_{SP3}^0	\hat{t}_{SP3}^0
FB	FB	FB

$$\{P\}_B = [S]\{u\}_B \quad (45)$$

$$\{P\}_i = [S][\phi]_i \{u\}_i \quad (46)$$

Table (26) summarizes the various parameters verified by the corresponding tests.

TABLE 26
Test Verified Models

Parameter	Description	Test for Verification
$[M]_{FB}$	Mission B mass matrix	All the modal tests and the propellant effective weight tests
$\{U_R\}$	Rigid body mode	Calculations \bar{M}_{FB}^{RR} should check with the rigid inertia properties of the V-S/C/CTA/CTA at its base
$\{U_B\}$	Model of bus with CTA/VTA	Static test on the bus and system modal test; the CTA/VTA only included in the system modal test
$\{q\}_P$	Displacement function of propulsion	Modal and static test of propulsion module and system modal test with referee fluid
$\{q\}_S$	Displacement function of scan platform	Modal Test of scan platform and system modal test without joint slippage; the joint slippage was included for load analysis since higher forces would result in joint slippage
$\{q\}_C$	Displacement function of cable trough	Modal Test of cable trough and system modal test
$\{q\}_{SPA}$	Displacement function of solar panel with relay antenna	Modal and static solar panel tests with a relay antenna
$\{q\}_{SPi}$ ($i = 1, 3$)	Displacement function of solar panel	Based upon a mathematical model of the solar panel with a relay antenna; the relay antenna was removed from the math model for this configuration
$[C]_{FB}$	Damping matrix for Mission B configuration	Data based upon modal tests where available; the damping matrix was diagonalized at each transformation; the kinetic energy evaluation of the modes was used as a guide to estimate damping; solar panel viscous dampers were not included but estimated as a modal damping
$[K]_{FB}$	Stiffness matrix for Mission B configuration	Substructure modal and static tests; system modal tests
$[s]$	Load matrix	Substructure modal and static tests; system modal tests

The real eigenvalues and eigenvectors of Eq. (44) with $[C]_{FB} = 0$, results in

$$\left\{ \begin{array}{l} \{u\}_R \\ \{u\}_B \\ \{q\}_P \\ \{q\}_S \\ \{q\}_C \\ \{q\}_{SPA} \\ \{q\}_{SP1} \\ \{q\}_{SP2} \\ \{q\}_{SP3} \end{array} \right\}_{FB} = [\Phi]_{FB} \left\{ \begin{array}{l} \{u\}_R \\ \{x\}_{FB} \end{array} \right\} \quad (47)$$

Substitution of Eq. (47) with Eq. (44) and pre-multiplication of $[\Phi]_{FB}^T$ results in

$$\begin{bmatrix} M_{FB}^{RR} & M_{FB}^{RE} \\ M_{FB}^{ER} & \begin{bmatrix} M_{FB}^{EE} \end{bmatrix} \end{bmatrix} \left\{ \begin{array}{l} \{\dot{u}\}_R \\ \{\dot{x}\}_{FB} \end{array} \right\} + \begin{bmatrix} 0 & 0 \\ 0 & \begin{bmatrix} C_{FB}^{EE} \end{bmatrix} \end{bmatrix} \left\{ \begin{array}{l} \{\dot{u}\}_R \\ \{\dot{x}\}_{FB} \end{array} \right\} = [0] \quad (48)$$

$$+ \begin{bmatrix} 0 & 0 \\ 0 & \begin{bmatrix} K_{FB}^{EE} \end{bmatrix} \end{bmatrix} \left\{ \begin{array}{l} \{u\}_R \\ \{x\}_{FB} \end{array} \right\} = [0]$$

$$\{P\}_B = [S][\Phi]_{FB} \{x\}_{FB} \quad (49)$$

$$\{P\}_i = [S][\Phi]_i [\Phi]_{FB} \{x\}_{FB} \quad (50)$$

The procedure to obtain the flight model was not complicated. The effort required to obtain $[C]_{FB}^{EE}$ was based upon engineering judgement. Since damping for most substructures is measured or estimated, the system damping matrix was based upon the kinetic energy contribution of the substructures to the system mode.

The data represented by Eqs. (48) through (50) was transmitted to MMA to couple the VLC on the VO to obtain the V-S/C mathematical model.

CONCLUSION

Highlights of the steps leading to the VO dynamic model are summarized with the mathematical equations and data. The success is attributed to substructure modal coupling concepts where each substructure is experimentally verified. The degree of correlation is dependent on the use of the dynamic model. The mode shapes and frequencies of the system correlated well but some difficulty exists in correlating modal forces. A measure to establish the degree of correlation is still required.

An overall structures and dynamics program integrating the substructure analysis, hardware availability, and test will result in a successful dynamic model. Overall system modal tests may not be required.

REFERENCES

1. W. C. Hurty, Dynamic Analyses of Structural Systems by Component Mode Synthesis, Technical Report 32-530. Jet Propulsion Laboratory, Pasadena, California, January 1964.
2. L. Leppert, R. Miyakawa, and B. Wada, "Modal Test Results of the Viking Orbiter," paper presented at the 44th Shock and Vibration Symposium, Dec. 4-7, 1973, Houston, Texas.
3. B. K. Wada, "Viking Orbiter-Dynamics Overview," paper presented at the 44th Shock and Vibration Symposium, Dec. 4-7, 1973, Houston, Texas.

4. W. A. Benfield and R. F. Hruda, "Vibration Analyses of Structures by Component Mode Substitution," presented at AIAA/ASME 11th Structures, Structural Dynamics, and Materials Conference, Denver, Colorado, April 22-24, 1970. Also published in AIAA J. Vol. 9, No. 7, July 1971, pp. 1255-1261.
5. R. M. Bamford, A Modal Combination Program for Dynamic Analysis of Structures, Technical Memorandum 33-290. Jet Propulsion Laboratory, Pasadena, California, August 1966.
6. R. Bamford, B. K. Wada, J. A. Garba, and J. Chisholm, "Dynamic Analysis of Large Structural Systems," presented at the Winter Annual Meeting of the ASME, Washington, D.C., Nov. 30, 1971. Also published in Synthesis of Vibrating Systems, ASME, New York, 1971, pp. 57-71.
7. R. M. Bamford, B. K. Wada, and W. H. Gayman, Equivalent Spring-Mass System for Normal Modes, Technical Memorandum 33-380. Jet Propulsion Laboratory, Pasadena, California, February 1971.
8. E. Leppert, "VO'75 Test Plan, CDTM with VTA/CTA Modal Test," Project Document 611-59. Jet Propulsion Laboratory, Pasadena, California, May 9, 1973 (JPL internal document).
9. A. Leondis, "Viking Dynamic Simulator Modal Test Report," SD-73-096. General Dynamics/Convair Astronautics, San Diego, Calif., August 31, 1973.

MODAL TEST RESULTS OF THE VIKING ORBITER*

E. L. Léppert and B. K. Wada
Jet Propulsion Laboratory
Pasadena, California

and

R. Miyakawa
Martin-Marietta Aerospace
Denver, Colorado
(assigned to the Jet Propulsion Laboratory)

A modal test of the Orbiter Development Test Model (ODTM) has been conducted to verify, or update, the mathematical model used for load analysis. The approach used to assure the quality and validity of the experimental data is defined, the modal test is described, and test results are presented and compared with analysis results. Good correlation between the analyses and the test data assures an acceptable model for incorporation into the mathematical model of the launch system.

INTRODUCTION

The Jet Propulsion Laboratory is responsible for the Viking Orbiter System (VOS), which is part of the overall Viking Project managed for the National Aeronautics and Space Administration by the Viking Project Office at Langley Research Center. Two Viking spacecraft will be individually launched on a new Titan IIIE/Centaur D-1T launch vehicle in August 1975.

The analysis process used to define design loads utilizes mathematical models of the launch system and of the Viking spacecraft. The information is in the form of modal characteristics and requires the use of modal coupling techniques for solution with present computers [1]. Experimental verification of the dynamic characteristics is necessary to provide confidence that the analysis model adequately represents the actual structure.

The major objectives of the test [2] were to determine the dynamic characteristics and to evaluate the dynamic load paths of the ODTM configuration. Special efforts were made to ensure that the accelerometer measurements would provide valid dynamic information.

Strain gage measurements were desired at the highest feasible excitation level consistent with constraints to limit the accumulation of fatigue damage.

Before the tests reported in this paper were conducted, modal tests had been made on major and minor substructures of the VOS. Some of these tests were conducted to provide improved dynamic predictions for the mathematical model of the modal test configuration. These included tests of the propellant tank ("slosh" test), propulsion module, scan platform, and cable trough. Additional tests were conducted on the solar panels and the high-gain antenna to provide experimentally updated characteristics for inclusion in the final mathematical model of the VOS.

The general techniques described below for obtaining valid data and for data evaluation and correlation for the modal test configuration were also used in the substructure tests. In some cases, improvements were made in the test operation as a result of the substructure test experience.

Each test contributed to better definition of the dynamic characteristics of the modal

*This paper presents the results of one phase of research carried out at the Jet Propulsion Laboratory, California Institute of Technology, under Contract No. NAS 7-100, sponsored by the National Aeronautics and Space Administration.

test configuration and thus to improved confidence in the modal test predictions.

The planned approach to assure the quality and validity of the test results included computer programs especially written for pre-test and post-test calculations, and data checks made during the tests. The computer program outputs provided information for conducting the tests, for evaluating and correlating the test results with analysis predictions [3], and for delineating the source of differences.

MATHEMATICAL SUMMARY

A brief description of the mathematical operations and terminology used in this test is provided below, primarily in the form of definitions. (Complete development can be found in [3], [4], and [5].

$[m]_A, [m]_T$ mass matrix; analytical, test

$[\phi]_A, [\phi]_T$ normalized mode shape matrix (vectors)

$[\phi]_R$ rigid-body vectors

$$[\phi]_A^T [m]_T [\phi]_A \stackrel{?}{=} [m]_T \quad \text{test for validity of } [m]_T \quad (1)$$

$$[\phi]_T^T [m]_T [\phi]_T \stackrel{?}{=} [m_{ee}]_T \quad \text{orthogonality, test} \quad (2)$$

$[m^{rr}]$ rigid-body mass matrix

$[m^{er}]$ rigid-elastic inertial coupling

$$\begin{bmatrix} m^{rr} & m^{re} \\ m^{er} & m^{ee} \end{bmatrix} \quad \text{total elastic and rigid-body matrix}$$

$$[m^{er}] [m_{ee}]^{-1} [m^{re}] = [m_{eff}^{rr}] \quad \text{effective mass} \quad (3)$$

$$[m^{rr}] - [m_{eff}^{rr}] = [m_{res}] \quad \text{residual mass matrix} \quad (4)$$

Note that the normalization for the orthogonality matrices is such that each diagonal term is 100%. The effective mass terms for each mode are also presented in terms of percent of the total rigid-body value.

TEST CONFIGURATION

The configuration selected for the modal test (Fig. 1) included a rigid simulation of the Viking lander capsule (VLCA), the Viking lander capsule adapter (VLCA), the Viking Orbiter, the Viking spacecraft adapter, and the two adapters connecting the spacecraft to the

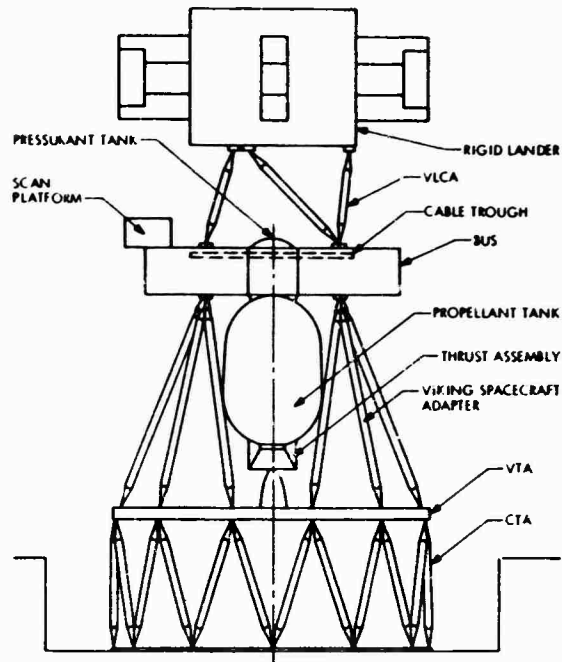


Fig. 1 - Modal test configuration

Centaur booster (the Viking transition adapter (VTA) and the Centaur truss adapter (CTA)). The Viking Orbiter included the bus, propulsion module, scan platform, and cable trough. Specifically excluded were the solar panels and the high- and low-gain antennas, which had been tested earlier. The thermal blankets were also excluded from the test article.

The rationale for selecting the components of the test configuration included the necessity to provide good analytical interfaces between the test article and both the flexible lander and the Centaur booster, and the requirement for obtaining accurate information on the dynamic characteristics of the major components of the VOS.

The inclusion of the rigid lander and the VTA/CTA trusses provided good mathematical interfaces, and the ability to attach shakers and to position accelerometers took precedence over inclusion of some of the less important components.

DETERMINATION OF INERTIAL PROPERTIES

The inertial properties of each item of the test article were experimentally determined or were calculated using measured weights and a detailed (estimated) weight distribution of the item. In particular, the properties of each bus bay were obtained by using measured values of the contents of the bay, supplemented by calculation of the bus structure contribution. Similar weight

calculations were made for other items; the resulting weights were used in both analysis and test prediction and in correlation calculations.

The propellant tanks were filled to the flight ullage condition with referee fluids (liquid Freon and isopropyl alcohol) and pressurized to 100 psi above ambient. The "effective" weight parameters were obtained from the results of the "slosh" and propulsion module tests.

The total weight of the test article was 7456 lb, of which 3235 lb (43%) was liquid.

The breakdown into weight items was coordinated with accelerometer positions so that the contribution of each portion of the structure to the total kinetic energy was correctly accounted for. For each weight item, a transformation for relating the accelerometer readings to the 6 degrees of motion of the lumped mass was generated and was inverted to prove its validity.

Meaningful comparisons between experimental and analytical results (such as orthogonality) are not possible if the inertial properties for each are not realistic and compatible. The difficulty arises in part because the analysis uses a more detailed distribution

and generates mode shapes at many structural node points, whereas the experimental distribution uses larger "lumped" masses and measures motion with a limited number of accelerometers. To determine that there was equivalence, a transformation of the analysis mode shapes to accelerometer readings was made and was used with the experimental mass matrix to obtain an "orthogonality" matrix (see Table 1 and Eq. 1). The close approach to being diagonal indicates the validity of the experimental distribution.

TEST FACILITY AND INSTRUMENTATION

The test was conducted in a special test facility consisting of a seismic base and a test tower. The test tower provided sets of beams and cranes for pendulous support of electrodynamic shakers, as well as catwalks and ladders for adjusting the cranes and for access to the test article (Fig. 2).

The test article was instrumented with 125 accelerometers and 290 strain gages distributed as shown in Table 2.

The accelerometer data acquisition system utilized a scanner to acquire the acceleration signals sequentially in a preselected order. The output of each scanned accelerometer signal and of a reference accelerometer signal

TABLE 1
Orthogonality of Analytical Modes and Test Mass Matrix^a

4.35	4.40	7.48	7.83	10.92	13.36	14.64	17.95	18.81	23.42	24.28	26.18	Frequency, Hz
1	2	3	4	5	6	7	8	9	10	11	12	Mode
100	0.9	-0.3	-0.2	0.8	-0.9	1.4	1.6	-1.7	-0.3	-0.9	0.4	1
100	-0.2	-0.2	0.3	0.1	-0.1	0.2	-3.1	0.4	-2.2	-0.4	1.1	2
100	1.3	-1.6	1.1	-1.7	-1.4	0	-2.1	-1.2	0.7	0.7	1.1	3
100	-0.4	1.2	-0.2	-0.3	-2.7	1.7	-0.3	1.1	1.1	1.1	1.1	4
100	1.0	0.8	1.1	-0.6	2.2	-0.2	1.1	-0.9	1.8	1.8	1.8	5
100	0.4	-0.7	0.8	0.9	-0.9	-0.7	0.9	-0.9	1.0	1.0	1.0	6
100	-1.8	0	0.2	-2.3	0.2	-1.8	0	-2.3	0.9	0.9	0.9	7
100	-0.2	-1.4	1.2	-0.2	-1.4	-0.2	-0.2	1.2	-0.2	-0.2	-0.2	8
100	-0.9	0.7	-1.4	0.7	-1.4	-0.9	0.7	-1.4	-1.4	-1.4	-1.4	9
100	-1.0	-1.0	0.2	-1.0	0.2	-1.0	-1.0	0.2	-1.0	-1.0	-1.0	10
100	-2.3	100	-2.3	100	-2.3	100	-2.3	100	-2.3	-2.3	-2.3	11
100	100	100	100	100	100	100	100	100	100	100	100	12

^aSee Eq. (1).

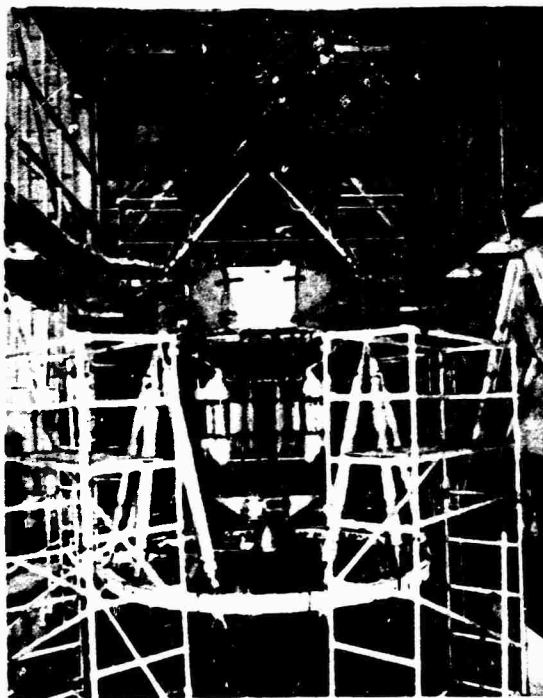


Fig. 2 - Modal test setup

TABLE 2
Instrumentation Distribution

Substructure	Accelerometers	Strain Gages
Rigid lander	6	
VLCA		18
Bus (16 bays)	72	163
Cable trough	8	
Scan platform	6	
Attitude control support		4
Viking space-craft adapter		36
Propulsion module	33	69
Total	125	290

(selected for each mode) was fed through matched tracking filters to a gain-phase meter, where it was reduced to ratio and phase angle form and converted by a coupler and

teletypewriter to printed and punched tape output. The strain gage system procured data in a similar manner. Information to fully identify each run was manually inserted with the teletypewriter.

The equipment could operate in a "manual select" mode to allow examination of acceleration ratio and phase of any individual channel.

TEST OPERATIONS

The test article was excited by (up to) ten 25-lb peak force Ling shakers. The system provided separate power supplies for the field and armature current; an oscillator to control the frequency of excitation; meters, oscillographs, and oscilloscopes to monitor the operation; and a means to simultaneously open the armature circuits for decay measurement.

The physical operations used to find and isolate the "pure" modes of the test article followed a normal pattern of searching for a response peak, then adjusting shaker positions, forces, and phases until Lissajou figures of force and velocity closed. For a simple system with good frequency separation and little stiffness or inertia coupling, this is an adequate approach. Initial calculations of the dynamic characteristics of the test article indicated that this approach would probably not be completely adequate.

To supplement the approach, computer programs were formulated to provide tables of predicted frequencies and mode shapes in the form of normalized accelerometer readings, normal mode plots, and plots of residual weight.

Figure 3 is an example of a residual weight plot [4, 5] for the Z direction. The plot is a measure of the importance of the mode in that direction and of the number of modes remaining to be isolated. In conjunction with a typical plot of the mode shape (Fig. 4) and tables of local kinetic energy distribution (Table 3), the residual weight plot provided information for the placement, phase, and force levels required to excite each mode. Residual weight plots were provided for X, Y, and Z translations and for θ_x , θ_y , and θ_z rotations; the mode shape plots included two lateral views in addition to the plan form view shown. The tabulated mode shape data allowed selection of the reference accelerometer channel and, with the data acquisition system in the "manual mode," a means for checking the amplitude and phase readings of important accelerometers with the predicted values. If these comparisons were not satisfactory, additional adjustments of frequency and shakers were made.

When satisfactory isolation was obtained, the accelerometers and strain gages were recorded, and oscillograph decay records of

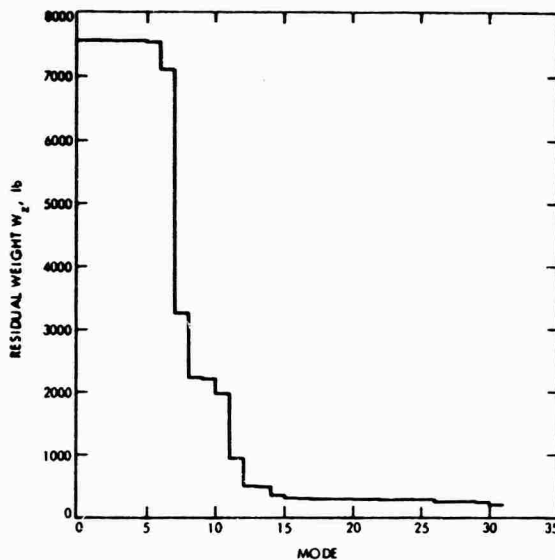


Fig. 3 - Analytical residual weight plot, W_z vs mode number (see Eq. 4)

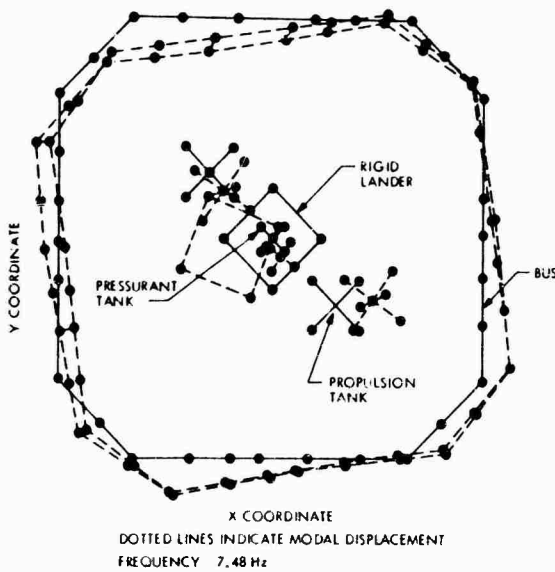


Fig. 4 - An analytical mode shape

selected accelerometers obtained. Additional recordings of each mode were obtained at higher levels with adjustment of frequency and shaker force, if required, to re-establish the mode. The higher-level tests were made to obtain more realistic damping and to establish the linearity characteristics of the test article.

As each recording was completed, the punched paper tapes were transmitted to storage in an 1108 computer and were processed by special data reduction and evaluation programs.

Three basic shaker setups were used — with major forces in the X, Y, and Z directions. After all the excitable modes for a given direction were obtained, sine sweeps were made to reveal possible additional modes. Routinely, a mode obtained early in a given shaker setup was reacquired before the setup was changed. In several cases, a mode was excited a second time by shakers in a different basic force direction.

DATA CHECKS

Prior to and during the test operations, planned checks were made to ensure that good strain gage and accelerometer data would be acquired. Additional checks were instituted as a result of anomalies encountered during the test.

During assembly and disassembly of the test article, and before and after each test period, static strains were recorded and processed. Before and after each test period, a scan of excitation voltage was taken. Good comparison of these readings to a standard set indicated that the data were valid. Any significant change was investigated to determine the cause of the discrepancy. A similar check on the gain-phase meter output was included when an intermittent error in output numbers was observed.

A series of checks on the accelerometer data provided comparisons between original and re-acquired modes, routine on-line comparison of modes at successively higher levels of excitation, and computer comparison of accelerometer levels to determine those gages with a consistently low output. A major accelerometer data error, caused by base sensitivity to stress (transmitted through a 1-1/4-in. micarta block) was detected by observing a distorted mode shape (Fig. 5).

RESULTS AND DISCUSSION

All important structural modes below 30 Hz were obtained, many at multiple levels of excitations. An initial set of data was at least partially invalidated by problems in strain gage readout and erroneous accelerometer readings, but adequate checks were developed to ensure the validity of the final measurements.

The most usually accepted measure of good modal data is the orthogonality of the modes as defined by Eq. (2). The pre-test criterion goal for off-diagonal terms was 10% or less. From Table 4, the maximum term is 6.2%, with only three terms equal to or greater than 5%.

Since the motion of the experimental mode is defined by a limited number of accelerometer positions, the mass matrix used cannot be considered exact. However, the orthogonality

TABLE 3
Analytical Local Kinetic Energy (Analysis Mode 701)^a

Node	Local Kinetic Energy Distribution, %						Sum
	X	Y	Z	θ_x	θ_y	θ_z	
1	0.08	0.31	0.00	0.00	0.00	0.00	0.40
2	0.20	0.06	0.00	0.00	0.00	0.00	0.26
3	0.05	0.05	0.00	0.00	0.00	0.00	0.11
4	0.00	0.06	0.00	0.00	0.00	0.00	0.06
5	0.01	0.10	0.02	0.00	0.01	0.00	0.13
6	0.01	0.11	0.01	0.00	0.00	0.00	0.14
7	0.06	0.13	0.00	0.00	0.00	0.00	0.19
8	0.16	0.08	0.00	0.00	0.00	0.00	0.24
9	0.09	0.66	0.01	0.00	0.00	0.00	0.77
10	0.02	0.50	0.02	0.00	0.00	0.00	0.54
11	0.01	0.51	0.01	0.01	0.01	0.00	0.55
12	0.16	0.84	0.03	0.00	0.00	0.00	1.03
13	0.00	1.02	0.02	0.00	0.00	0.00	1.05
14	0.12	0.35	0.00	0.00	0.00	0.00	0.48
15	0.02	0.39	0.00	0.00	0.00	0.00	0.41
16	0.00	0.51	0.00	0.00	0.00	0.01	0.53
101	5.39	3.98	0.01	0.43	7.59	62.20	79.61
301	4.55	3.60	0.03	0.02	0.00	0.11	8.32
303	2.63	0.33	0.01	0.02	0.02	0.10	3.10
401	0.14	0.00	0.00	0.00	0.00	0.03	0.18
501	0.19	0.04	0.00	0.00	0.00	0.02	0.25
201	0.95	0.06	0.07	-0.02	0.24	-0.03	1.27
402	0.05	0.00	0.00				0.05
403	0.05	0.00	0.00				0.05
404	0.05	0.00	0.00				0.05
601	0.02	0.01	0.00				0.03
602	0.02	0.10	0.00				0.12
603	0.01	0.00	0.00				0.01
604	<u>0.01</u>	<u>0.07</u>	<u>0.00</u>				<u>0.07</u>
	15.02	13.89	0.26	0.46	7.90	62.46	

^aFrequency = 7.48 Hz.

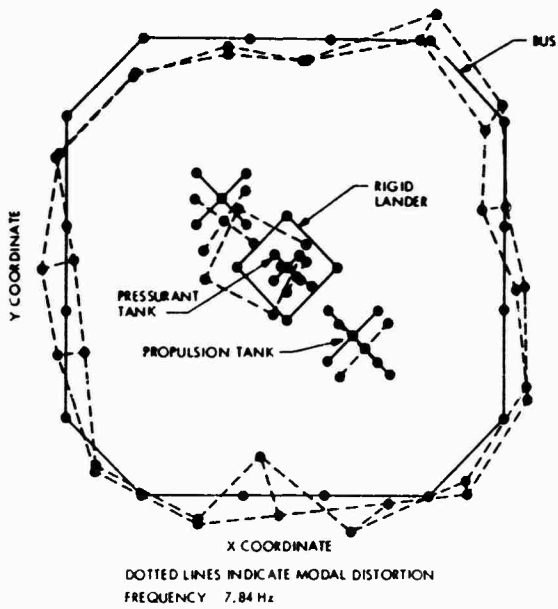


Fig. 5 - Distorted experimental mode shape

matrix of Table 1 indicates that an adequate representation has been used.

The experimental frequencies show good comparison with the analytical predictions (except for one mode) with an average increase of about 5.5% over the analytical (Table 5). Typical correspondence of the modes is shown by means of the effective mass (Table 6) and by modal plots (Figs. 4 and 6). In each case, the relationship between analytical and experimental data is good. Table 6 verifies that the major modes have been obtained when a minimum of 89% of the effective mass is accounted for. Additional good comparisons of "cross" orthogonality, mode shapes, and kinetic energies are shown in [3].

Although good comparison of the analytical and experimental results does not necessarily assure that the experimental data are good, when an analysis is updated by data obtained from modal tests of substructures, a good comparison tends to reinforce the validity of both.

TABLE 4
Orthogonality of Test Modes^a

4.51	4.65	7.84	8.30	11.51	14.19	15.35	19.61	19.82	24.85	26.49	29.34	Frequency, Hz
708	743	701	702	704	705	711	709	712	707	713	714	Mode
100	6.2	-0.2	-1.1	-0.3	1.1	-2.3	-1.9	-1.7	0.6	0	-0.6	708
100	0.1	-1.2	-4.1	3.0	-0.9	-2.4	1.0	-1.2	-1.5	-2.5		743
	100	0.4	0.8	1.6	-0.2	-0.7	-1.5	-0.5	0.4	3.5		701
		100	1.0	1.3	1.2	1.1	-1.8	1.2	-0.5	-0.1		702
			100	0.6	0.8	1.7	-1.0	0.2	-0.4	4.6		704
				100	0.4	-0.6	1.5	4.4	1.6	-5.0		705
					100	-0.1	-0.1	3.6	-1.3	-0.2		711
						100	-2.7	1.0	2.5	-0.2		709
							100	5.9	2.7	-1.1		712
								100	-3.4	-1.9		707
									100	-1.5		713
										100		714

^aSee Eq. (2).

TABLE 5
Analysis Prediction and Modal Test Frequencies

Analysis Mode	Analysis Frequency, Hz	Test Mode	Test Frequency, Hz	Percent Deviation
1	4.35	708	4.51	3.55
2	4.40	743	4.65	5.38
3	7.48	701	7.84	4.60
4	7.83	702	8.30	5.65
5	10.92	704	11.51	5.12
6	13.36	705	14.19	5.85
7	14.64	711	15.35	4.63
8	17.95	709	19.61	8.45
9	18.81	712	19.82	5.10
10	23.42	707	24.85	5.75
11	24.28	714	29.54	17.8
12	26.18	713	26.49	1.17

TABLE 6
Analytical and Experimental Effective Mass^a

Mode	X	Y	Z	θ_x	θ_y	θ_z
1	96.42 ^b (89.51) ^c	1.76 (7.97)	0.01 (0.03)	1.34 (6.12)	85.20 (78.23)	0.14 (0.88)
2	1.67 (3.30)	87.47 (86.49)	0.0 (0.03)	63.66 (64.45)	1.49 (3.15)	1.09 (1.13)
3	0.95 (0.89)	0.28 (0.35)	0.0 (0.01)	1.75 (1.88)	0.02 (0.02)	55.21 (56.91)
4	0.06 (0.10)	5.60 (4.81)	0.03 (0.10)	28.95 (27.51)	0.01 (0.0)	1.94 (1.66)
5	0.05 (0.0)	0.06 (0.11)	0.56 (0.58)	0.10 (0.19)	6.40 (7.80)	19.58 (20.43)
6	0.20 (0.38)	0.06 (0.01)	5.63 (6.67)	0.10 (0.01)	4.77 (5.65)	9.83 (7.39)
7	0.0 (0.01)	0.01 (0.0)	49.02 (51.80)	0.01 (0.0)	0.40 (0.63)	0.25 (0.24)
8	0.02 (0.02)	0.01 (0.0)	12.98 (12.52)	0.01 (0.01)	0.04 (0.0)	0.07 (0.15)
9	0.0 (0.0)	0.06 (0.05)	0.45 (0.90)	0.06 (0.02)	0.0 (0.0)	0.41 (0.09)
10	0.0 (0.0)	0.02 (0.01)	3.15 (0.58)	0.03 (0.03)	0.0 (0.01)	0.0 (0.04)
11	0.0 (0.0)	0.02 (0.01)	13.60 (11.57)	0.07 (0.02)	0.0 (0.0)	0.23 (0.06)
12	0.0 (0.0)	0.02 (0.07)	5.02 (22.17)	0.06 (0.20)	0.0 (0.0)	0.0 (0.06)
Total	99.37 (94.39)	95.37 (100.24)	90.45 (95.96)	96.12 (100.20)	98.33 (95.89)	88.75 (89.15)

^aSee Eq. (3).

^bAnalysis.

^cTest.

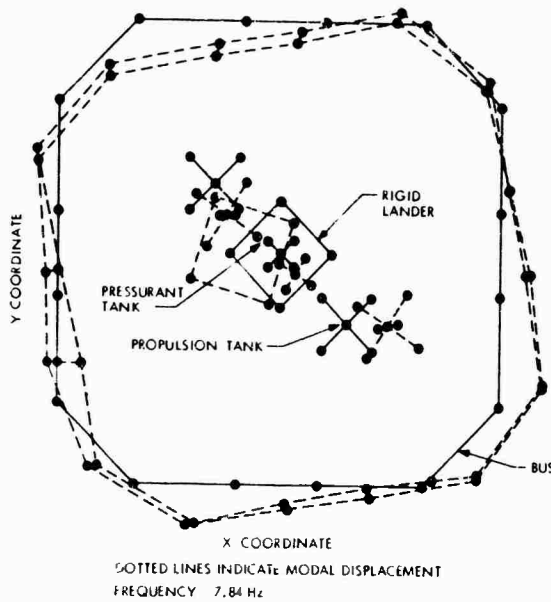


Fig. 6 - Valid experimental mode shape

The accuracy of modal strain is more difficult to establish. One representative mode is presented to help establish the accuracy as related to data scatter on strain magnitude. Figure 7 shows small scatter over a stress range approaching specified stress limits. (Since the limits were set to preclude possibility of fatigue damage, the member loads and strains are not large.)

Other methods were used to establish strain gage accuracy. The modal forces can be evaluated from strain gage or by a static

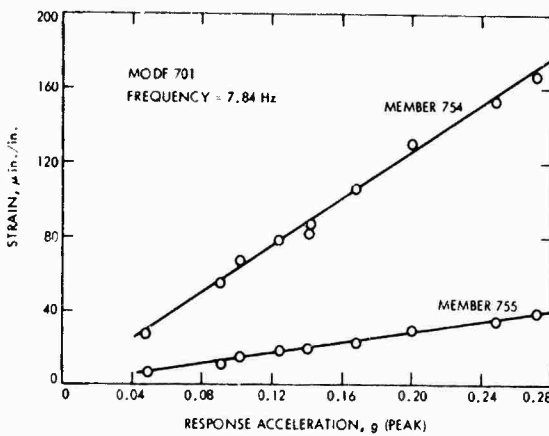


Fig. 7 - Strain vs response acceleration

solution of a structure with modal inertial forces. Table 7 shows the Viking lander capsule adapter results compared on this basis. Table 8 shows the Viking spacecraft adapter results based on the reactive forces from the VTA into the struts. A general observation is that the strain gage readings are accurate to within 25% if the magnitude of the strain is greater than $5 \mu\text{in./in.}$.

Damping was generally low, with the highest value (2% critical) corresponding to the two lowest frequencies where sloshing of the fluids was greatest. From Table 9, the lowest value was 0.4% for a mode which was dominantly rotation about the pitch axis for the rigid lander.

In general, the structure responded in a linear manner for the level of excitations achieved, as shown by the strain curves.

SUMMARY AND CONCLUSIONS

A modal test has been conducted on the ODTM configuration of the Viking spacecraft using a coordinated approach of analysis and test. Results from modal tests of substructures, conducted earlier, were used to provide data to improve the analytic model of the test article, from which high-confidence predictions of test characteristics were obtained.

The good correlation that was obtained between analyses and post-test data reductions reinforces the validity of both types of data and assures an acceptable model for incorporation into the analyses of the complete launch vehicle.

TABLE 7
Viking lander capsule adapter forces

Mode	Forces, ^a lb		Percent Error
	Strain Gage	Inertial Load	
750	161	175	8.70
751	53	47	11.30
752	262	299	14.20
753	279	291	4.20
754	116	131	12.80
755	104	130	24.60

^aFor mode 713, frequency = 26.49 Hz.

TABLE 8
Viking Spacecraft Adapter Base Reactions

Mode	Force, lb			Moment, lb-in. ²		
	F _x	F _y	F _z	M _x	M _y	M _z
708	401 ^a (517) ^b	-120 (-169)	-8 (54)	16700 (15587)	60000 (52441)	-1270 (-1565)
703	75 (78)	383 (391)	8 (-102)	-52400 (-33728)	11600 (6802)	1394 (1926)
701	45 (50)	-28 (-36)	-4 (-10)	10300 (9540)	1110 (-1398)	11400 (12847)
702	19 (14)	131 (138)	19 (-22)	-49300 (-44093)	59 (-1311)	2440 (2374)
704	-2 (-1)	19 (-1)	-44 (-50)	-3900 (-1585)	23700 (25842)	8060 (9087)
705	25 (22)	-4 (5)	-107 (-119)	684 (62)	15000 (14108)	-3440 (-4483)
711	12 (5)	-2 (-2)	1080 (1106)	241 (974)	18100 (18207)	-2240 (-3388)
717	17 (28)	-6 (-40)	444 (465)	1810 (3392)	833 (762)	-1490 (-557)
712	2 (17)	28 (81)	125 (97)	2600 (-6375)	-438 (248)	1200 (920)

^aValues from inertial loads.

^bValues from strain gages.

TABLE 9
Summary of High-Level Tests

Basic Mode	High-Level Mode	High-Level Freq, Hz	Ratio ^a	Member	Load, lb	Stress, psi	Damping $\rho = \frac{c}{c_{cr}}$
708	708	4.51	4.48	751	125	430	0.020
743	753	4.65	5.98	754	93.6	321	0.020
701	701	7.84	1.07	754	520	1780	0.007
702	732	8.29	1.56	752	360	1309	0.006
704	704	11.43	1.51	755	370	1280	0.005
705	705	13.95	1.41	752	398	1150	0.004
711	711	15.32	1.39	664	287	1848	0.007
709	709c	19.61	7.10	750	79	250	0.010
712	712	19.47	1.84	750	304	975	0.013
707	747	24.39	2.42	A-P47	—	2065	0.014
713	713	26.39	1.31	753	428	1311	0.007
714	714	29.44	3.12	754	180	629	0.009

^aRatio of specified limit
actual load

REFERENCES

1. B. K. Wada, "Viking Orbiter Dynamics," presented at the 44th Shock and Vibration Symposium, held at Houston, Texas, Dec. 4-7, 1973, sponsored by the Shock and Vibration Information Center, Washington, D.C.
2. E. Leppert, VO'75 Test Plan, ODTM with VTA/CT.1 Modal Test, JPL internal document PD 611-59, Jet Propulsion Laboratory, Pasadena, California, May 9, 1973.
3. B. K. Wada, J. Garba, and J. Chen, "Development and Correlation, Viking Orbiter Analytical Dynamic Model With
4. R. M. Bamford, B. K. Wada, and Gayman, W. H., Equivalent Spring-Mass System for Normal Modes, Technical Memorandum 33-380, Jet Propulsion Laboratory, Pasadena, California, Feb. 15, 1971.
5. B. K. Wada, R. Bamford, and J. Garba, "Equivalent Spring Mass: A Physical Interpretation," Shock and Vibration Bulletin 42, Jan. 1972.

DISCUSSION

Mr. Dorland: The last modal test I was involved in, linearity was a big bug-a-boo that we had to cope with. What would your strategy have been if the structure had not been linear?

Mr. Leppert: The structure here was linear but we have nonlinear components in our total vehicle. The solar panels are attached to the truss by means of viscous dampers. They also have attachments with a little bit of slop in them. This is one reason why they were left off. We needed to get a good definition of the basic structure of the airplane. The other modal test of the high gain antenna showed a nonlinearity with frequency also. That was the reason for leaving it off. However, I wouldn't really expect that, at the test levels used here, we would get into trouble. At higher levels there is, I think, a definite probability that, at 2 1/2 or 3 g levels on a piece of hardware like this that you will begin to bend. This is good, in a sense, because it's an indication that damping is going up, and you would like to have some damping.

Mr. Wada: Let me answer that question. The reason we went to such high levels as 1 to 2 g's, which are very high from the modal point of view, was to get as high a damping as possible in the flight type situation. (The commenter did not use the microphone and the balance of his answer was lost.)

Modal Test," presented at the 44th Shock and Vibration Symposium, held at Houston, Texas, Dec. 4-7, 1973, sponsored by the Shock and Vibration Information Center, Washington, D.C.

4. R. M. Bamford, B. K. Wada, and Gayman, W. H., Equivalent Spring-Mass System for Normal Modes, Technical Memorandum 33-380, Jet Propulsion Laboratory, Pasadena, California, Feb. 15, 1971.
5. B. K. Wada, R. Bamford, and J. Garba, "Equivalent Spring Mass: A Physical Interpretation," Shock and Vibration Bulletin 42, Jan. 1972.

Mr. Bamford: That is a reasonable strategy. I have one other question. I gather from the Schematic of the structure that it is full of pin joints & those trusses.

Mr. Wada: They were monobolts. (Other discussion lost.)

Mr. Dorland: That brings me to the last question I want to ask. With all those joints of that nature in the test article, did you find that the structure tended to work as you were running the survey. Did you find that the mode that you tuned on the last day of the survey came in on the same frequency as you tuned it on the first day of the survey?

Mr. Leppert: No, I had no problem setting up a mode at the same level that I had set it up before. However, there were two modes one of them which had some nonlinear characteristics. (Balance of discussion lost.)

IMPLEMENTATION OF INTERACTIVE GRAPHICS TO A TRANSIENT RESPONSE RING CODE

Robert W. Buchanan*, Thomas N. Vogel*, and Philip G. Underwood†
Lockheed Missiles & Space Company, Inc.
Sunnyvale, California

An interactive graphics approach to the implementation of a transient response ring code is described in detail, along with the requirements that led to its creation. The merits of this system are discussed including the ability of the analyst to selectively access any mode of operation and view or update any current system parameter. Finally, the system, which is fully operational at Lockheed Missiles & Space Co., Inc., is illustrated by an example from a production-analysis environment.

INTRODUCTION

The code developed as an extension of the work begun by P. G. Underwood [1, 2] to include various strain-rate and strain-hardening formulations and an interactive graphics capability. This paper reports on the work which was undertaken to determine the feasibility of employing interactive computer graphics for correlation studies involving experimental and calculated dynamic response data. Since the creation of the Hybrid Ring SHORE (HRS) code, the code has been utilized with great success in a production analysis environment in various departments throughout Lockheed. The visible potential of SHORE HRS has demanded rewriting of two additional codes to facilitate an interactive capability.

Though the authors feel the HRS code is an extremely economical and practical tool for the analysis of the transient response of rings, their primary goal in writing this paper was not to praise the code, but rather to indicate the enormous opportunities and capabilities available to the interactive user.

CODE SOLUTION METHOD

The plane stress ring version of the SHORE code (Shell of Revolution) is based on a one-dimensional simplification of the original two-dimensional code [1, 2]. In the ring version, the meridional displacement, its derivatives, and stress are assumed to be equal to zero. The subsequent text briefly describes the solution technique, and features of the code.

The shell equations solved by the SHORE code are derived by Sanders [3] with provisions for both linear and nonlinear kinematic solutions. The

loadings are initial radial velocity, initial step change in temperature, and surface pressure histories; all of these can be specified for each mesh point. The boundary conditions implemented through fictitious points include symmetry or antisymmetry at the starting angular location (0 deg) and at the terminal angular location.

Time integration is handled with the straight-forward second-order central-difference operator. Use of the formulation in terms of past- and post-displacement increments [2] produces a solution technique most compatible with incremental plasticity theory. The spatial derivatives are based on second-order three-point difference in conjunction with a half-spacing grid. This gridwork greatly simplifies the expressions for the various derivatives needed, and it also results in a more accurate solution than normally associated with second-order finite-difference expressions [4].

The plasticity formulations include perfect plasticity, and isotropic and kinematic linear strain hardening options. To obtain the stress resultants, the stresses are computed at five points through the thickness, and the integrations are performed using Simpson's method. For elastic solutions, algebraic expressions are used for the integration to save computer time; throughout the coding, algebraic forms are used wherever possible to avoid time-consuming numerical techniques.

The computational sequence is as follows. Starting with a new increment in time, the required boundary conditions for the displacement increments are set. The increments of strain and stress are computed first, then the total strain and stress, and then a check on yield conditions is made. If yielding has occurred, new total stresses are computed in the plasticity subroutine. Now, with the total stresses available, the resultants are computed, and their

*Research Engineer, Vulnerability & Hardening Studies.
†Research Scientist, Structural Mechanics Laboratory.

boundary conditions are set. Using the resultants and their derivatives in the equilibrium equations, the next increments in the two displacement quantities are computed, and once again the time loop commences.

EQUIPMENT

Lockheed's present scientifically oriented, interactive graphics capability consists of a Tektronics CRT Display Unit (Series 400) used in conjunction with a CDC 6400 Computer System. The CRT display system consists of two storage scopes, a tablet and stylus unit, and a hard copy output device. Interaction with the graphics system may be accomplished through the console keyboard or function keys, the tablet and stylus hardware or the joystick, which can be used to position points, lines, arcs, and alphanumeric characters on the scope. The hard copy unit is capable of producing 8-1/2-in. by 11-in. dry copies of any information displayed on either scope.

The CDC 6400 system features a 60-bit scientific computer with a 67,000-word, 100-nsec user available central memory. It also has an additional 8.4 million-word fixed-stack disk unit as secondary storage. The system is specifically designed for multi-job processing (seven CPU's) and therefore readily lends itself to interactive graphics applications. Figure 1 provides a view of the arrangement of the interactive graphics equipment.

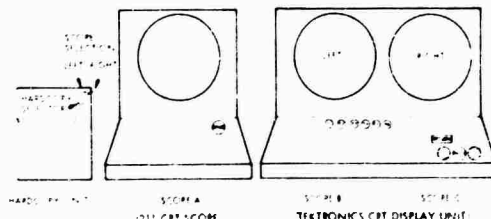


Fig. 1 - Equipment*

In addition, there is a CRT scope which monitors the program execution on the CDC 6400 (Scope A). Through this scope, commands may be input to the computer during execution. Also, it allows the user to view any core location or register of the computer. This is significant in permitting efficient, interactive debugging or updating of the basic computer code.

INTEGRATION OF GRAPHICS INTO CODE

The original transient response ring code, developed for the UNIVAC 1108 System, consists of a set of program modules or overlays whose interdependence is established by input parameters. Therefore, to implement the interactive graphics, one additional overlay was written to facilitate five basic modes of operation which, when used in the proper sequence, allows the analyst to:

- (1) Influence the program's execution by updating system parameters.
- (2) Overlay experimental and calculated graphs, overlay two calculated graphs, or selectively request printed and graphical output.
- (3) Update any input parameter or array value and then re-execute the code.
- (4) Execute multiple stacked decks of experimental or input data.
- (5) Pause or terminate program execution at any desired time.
- (6) Verify input decks prior to program execution.
- (7) Generate plot tapes for high speed, off-line plotting.

The CRT scopes are used for two distinct purposes. The first is to display output or input data. The output can be shown in graphical or printed form. The input consists of variables or arrays, both of which can be viewed and updated as desired. Secondly, the scopes are used to display questions which necessitate action by the analyst, or display the set of commands which are active in a given portion of the program. Figures 2 to 5 exemplify these displays.

The interactive portion of the code was designed for ease of operation by the analyst. Through displays on the CRT's or the 211 scope, the analyst is constantly able to monitor the program's execution, and he is cued as to which commands or program paths are currently available. Also, if the program encounters some difficulty, such as non-convergence, or non-compatibility between information requested or functions in the program, it does not error off. The problem is related to the analyst through the display, and several avenues of action are then made available to him. This type of interaction between the system and the analyst allows for almost on-site introduction and training on the equipment.

ILLUSTRATIVE EXAMPLE

Some discussion is merited on the type of project which precluded implementation of an interactive graphics capability to the existing transient response ring code.

Figure 6 illustrates the experimental configuration for the study. The pressure imparting device, or pusher plate, consists of an aluminum/mylar/aluminum layup preformed to the test specimen's outer radius. The pusher plate impacts the ring through an arc of -83 to +83 deg. The use of magnetic repulsive forces, which are proportional to the square of the current density applied across the pusher plate, supplies an easily determined and uniform pressure on the ring. From these tests, inner and outer surface strain gage data were collected for several angles.

UPDATE/RET KEY F1
 NEW VARIABLE KEY F2
 NEW CASE KEY F3
 END RUN KEY F4
 COMPARISON KEY F5

CALL MENU FIRST

KEY F1

Fig. 2 - Display of Command Module (CM) of program, denotes 5 major branches of code's logic

Fig. 3 - Allows for viewing and updating all input variables and array values

TO ALTER ONE VALUE, ENTER LINE NUMBER, A DELIMITER, THE NEW VALUE, DEPRESS RETURN.
 DEPRESS: PAGE TO UPDATE VALUES, TAB TO ROLL OUT, F4 FOR PROGRAMED OPTION.

SYSTEM PARAMETER MODIFICATION ROUTINE 1

1. NOT	18	21. S2	4.70000E+64
2. LATS	4	22. ALPHAT	-8.
3. KIMP	-1	23. SZ	4.20000E-04
4. JTEMP	0	24. H	2.90000E+05
5. IKI	8	25. INP	1
6. IKZ	9	26. S2C	1.60000E+05
7. JMS	1	27. S2T	5.70000E-04
8. NSL	1	28. ETA	0.
9. NON	-8	29. S2A	0.
10. KBC(1)	1	30. S2A	0.
11. KBC(2)	1	31. HA	0.
12. IV	1	32. INPA	0.
13. IST	1	33. S2C	2.
14. IEPt	1	34. S2AT	0.
15. IPZT	1	35. RHOA	0.
16. IPTT	1	36. TA	0.
17. RHO	6.67500E-02	37. IMP	-2.
18. THD	1.88923E+02	38. VB	-8.
19. LMD	-8.	39. PR	-8.
20. ET	4.40000E+07	40. DT	2.50000E-07

F1 EXECUTION OF PROC. F2 VALUES CHANGED CONT. F3 CALL MENU NUMBER 2
 F4 CALL COMMAND MODULE F5 VALUES CHANGED COMP. F6 INACTIVE

21 41 28

Fig. 4 - First of 2 displays of input variables

A particular study which utilized this code consisted of a one-layer beryllium ring which was subjected to transient pressure loadings imparted by the previously described pusher plate configuration. In such a study, the analyst might wish to consider many possible parameters and formulations in an effort to obtain correlation with the experimental results. In past studies, because of limitations on time and money (i.e., high computer costs, time in

de-bugging changes to the code, and the required one- to two-day turn-around time for graphical output), only a limited number of these variables were able to be considered.

The major goal of such a study is to enhance our capability of predicting experimental results, thus allowing for the proper placement of strain gage on specimens, and reducing the overall number of

DO YOU WANT TO GENERATE AN 1108 PLOT TAPE

IF YES TYPE RUN NO. AND RETURN

CALL CM TO RE-VIEW PLOTS, KEY F1

NEW CASE , NO PLOT TAPE GENERATED, KEY F2

Fig. 5 - Allows analyst to generate off-line plot tape

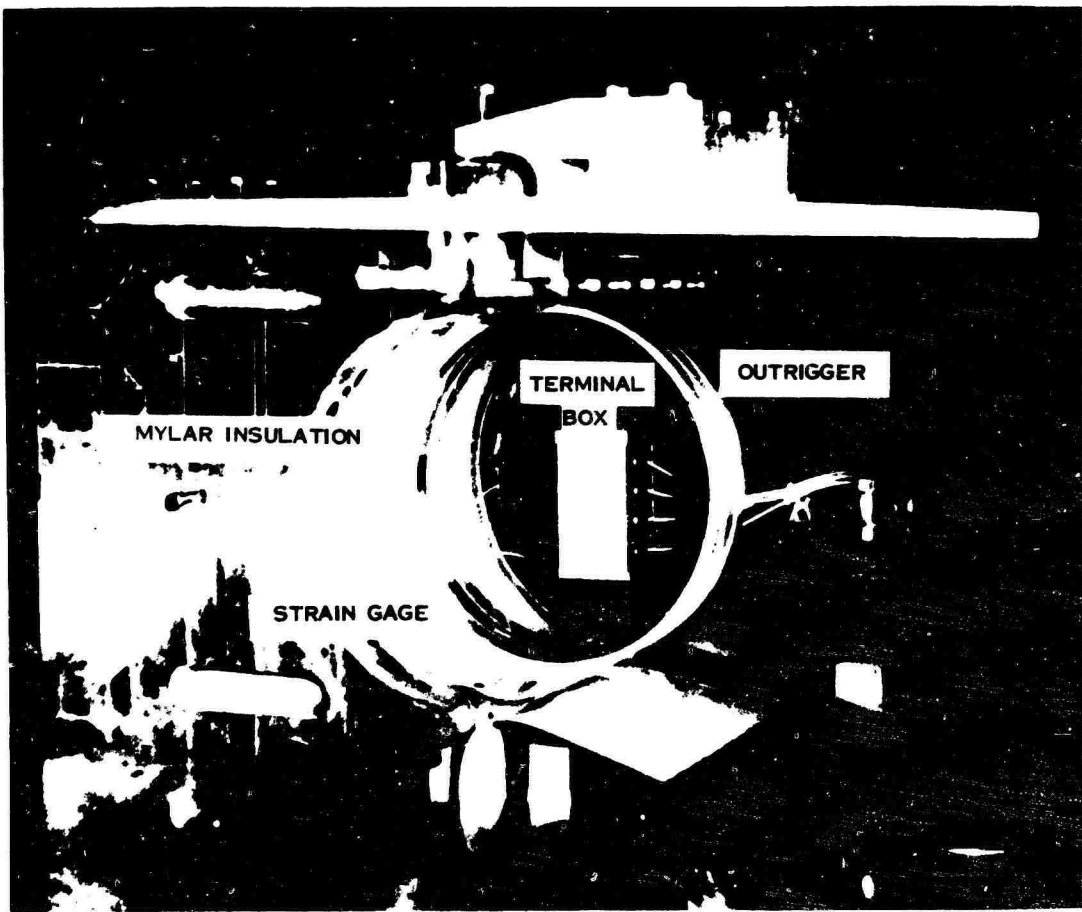


Fig. 6 - Test specimen installed in magnetic pusher assembly

costly experiments. With the speed and flexibility of the new code, it was anticipated that for the same expenditure in time and money, additional effort could be put forth to (1) improve, if necessary, the material model for beryllium (2) investigate the effects of different strain hardening and strain rate formulations or calculated results, and (3) obtain a better understanding of the interaction between the pusher plate and the test specimen. The study evolved into a process of making many short computer runs, and comparing the calculated data to the experimental data. After the model had compared favorably with the experimental results for early times, a run was made for the desired response time interval. The interactive graphics system lent itself favorably to this need because without wasting time, the analyst could make a run, view the results, change parameters and other system information, and re-execute. This alleviated the normal wait for the return of batch jobs and the ultimate hand plotting of experimental data on the calculated plots. The following paragraphs briefly describe the work performed, the results, and the role of the interactive graphics system.

Although the material properties for beryllium are generally well established, variances do exist in specimen properties because of the manufacturing methods [5]. Table 1 gives the final values used for the material model, and the bands over which such parameters as the yield stress, fracture stress, elastic modulus, and density were evaluated. A preliminary study conclusively showed that the ring's response, over the range of these parameters, is almost invariant. Also, note that the peak response values are identical (Fig. 7). Having determined the effect of the material properties on the response, the more difficult portion of the work was undertaken determining the proper plasticity formulation.

Two strain-hardening formulations (isotropic and kinematic), and two strain-rate effects were investigated. In past studies, only an isotropic formulation with no strain-rate effect was used. However, because of the characteristic reverse loading behavior of beryllium, as noted in other experiments and papers [5], it was believed that perhaps a kinematic

TABLE 1
Table of Values

Material Property	Range of Values Evaluated	Value Chosen for Study
Yield Stress	4.2E4 to 4.7E4 psi	4.7E4 psi
Fracture Stress	5.7E4 to 1.0E6 psi	5.7E4 psi
Tension		
Compression	1.0E5 to 1.0E6 psi	1.0E5 psi
Elastic Modulus	42E6 to 44E6 psi	4.4E7 psi
Density	6.675E-2 to 6.688E-2 lb/in. ²	6.675E-2 lb/in. ²
Strain Hardening Modulus	2.94E5 psi	2.94E5 psi

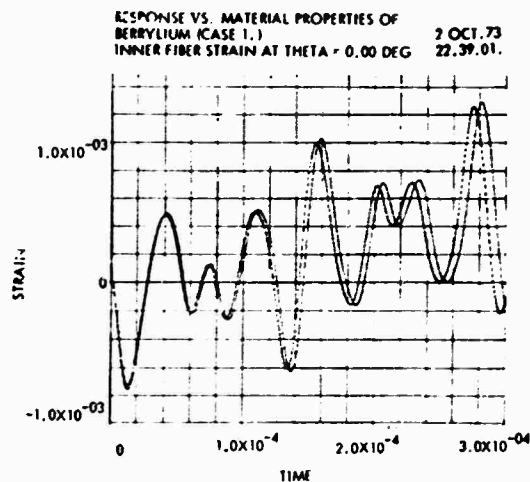


Fig. 7 - Shows programs capability of overlaying two calculated plots

strain-hardening formulation would more accurately describe the material response for the inelastic cases. Figures 8 and 9 show the results of the isotropic and kinematic formulations, respectively. The kinematic formulation exhibited greater strain relaxation (i.e., less permanent strain) than the experimental results because the difference between the yield stresses in compression and tension was kept constant, i.e., no Bauschinger effect was considered. This formulation afforded too much elastic deformation between the yield points. After further investigation, the isotropic formulation with 1 percent structural damping was chosen because it seemed to give the best approximation to the early time experimental peaks, and it also proved to give good results throughout the entire time interval of the response (Fig. 10).

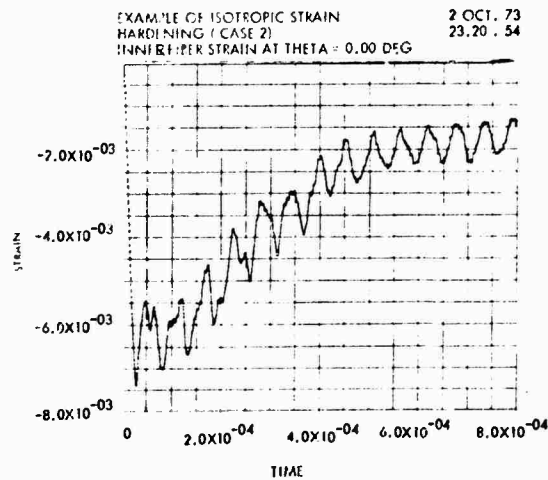


Fig. 8 - Example of isotropic strain hardening

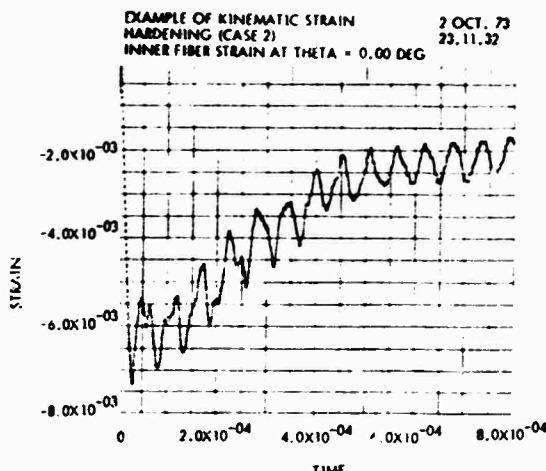


Fig. 9 - Example of kinematic strain hardening

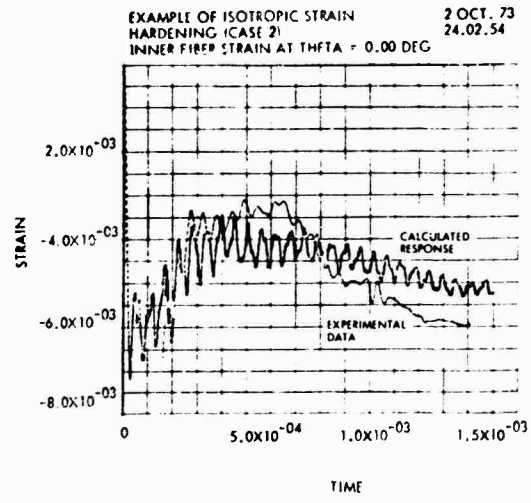


Fig. 10 - Experimental data (solid line) calculated response (dashed line)

Incorporating time-dependent strain-rate effects into the code proved very difficult because of the iterative scheme of the code, and entailed more time than it subsequently proved to be worth. Two formulations, one from Ref. [6] and the other derived by the authors were examined. Both however, produced excessively high yield values, thus allowing for large stresses which ultimately exceeded the specified fracture stress. Because dynamic fracture stresses are somewhat arbitrarily chosen and in the experiment the ring was known not to have failed, the fracture stress was increased to prevent fracturing (final value equaled 1.0 E6 psi). However, the resulting strains were then inappropriately small (the stresses still being very large) with respect to the experimental results. It should be noted that the interactive portion of the code proved extremely effective as

a debugging aid during this portion of the study. The 211 CRT scope was used to trace logic and data errors, thus allowing for the fast location and updating of the incorrectly coded areas.

The addition of the extra mass associated with the pusher plate also proved very important in achieving good correlation. The pusher remains in contact with the ring for a finite period of time (this time being a function of the initial pressure applied by the pusher). If the time is found to be a significant portion of the total response time, the added mass of the pusher must be considered in determining the ring's response. Because there is no constraint or bond between the pusher and the ring, the pusher was assumed to add only mass and not stiffness to the system. The interactive system was used to monitor the directional velocities of the nodal points to determine when the pusher flies off the ring. The fly-off time at each node therefore was determined so that the first peak of the experimental data was duplicated.

Figures 11 through 14 show the final results of this study for two cases with different pressure-time histories. The correlation between experimental and calculated results is very good; note that the maximum experimental values were always equaled or bounded by the calculated results. This indicates the capability to predict peak strains and stresses at various locations around the ring, and the approximate time of their occurrence.

CONCLUSION

As the illustrative example shows, these studies are quite extensive and predominately computer oriented. Consequently, it was a natural step to make the computer a direct tool of the analyst by an interactive graphics system, rather than a remote job processing system. The previous sections have discussed how the multiple capabilities of the system facilitate our present work. It is important that the

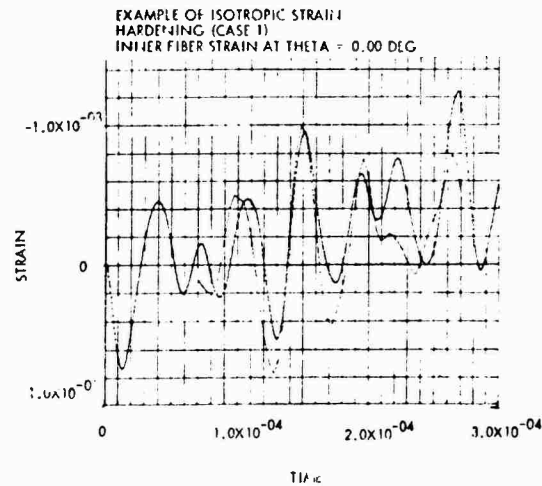


Fig. 11 - Experimental data (solid line) calculated response (dashed line)

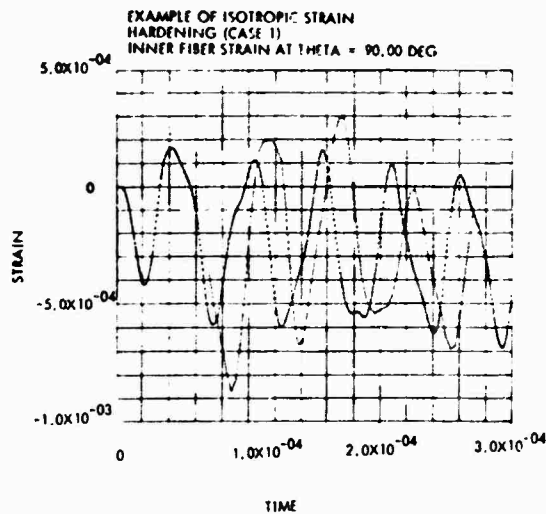


Fig. 12 - Experimental data (solid line) calculated response (dashed line)

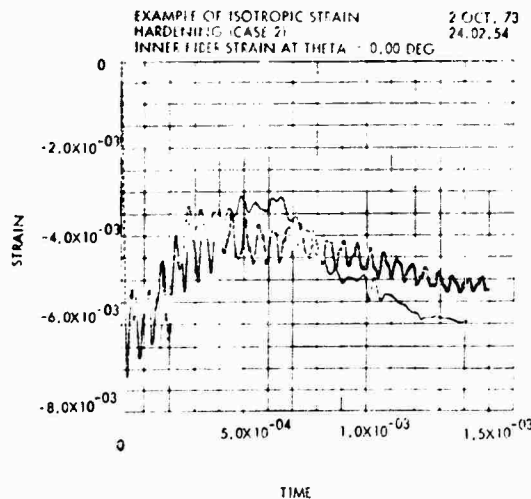


Fig. 13 - Experimental data (solid line) calculated response (dashed line)

system can perform the analysis successfully in a reasonable time, and it is also important that the complexity of the system has been held to a minimum. In all such system development, the analyst's ability to be able to understand and operate the system is vital; only when the analyst is fully aware of the system capabilities can he adapt the system to his needs. When this has been accomplished, the analyst will have a very powerful tool, which will not only allow him to receive direct feedback on the problem, but also will allow him to influence the analysis with respect to his interpretation and background of the problem.

It is difficult to state precisely the total saving in time and money achieved through this system. A cost study showed that for identical jobs on the

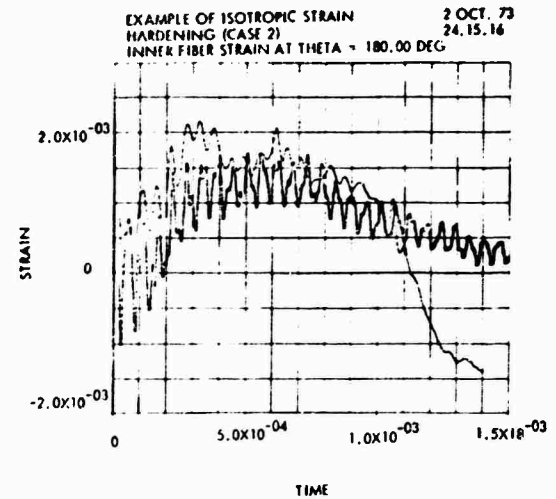


Fig. 14 - Experimental data (solid line) calculated response (dashed line)

interactive and batch system, the interactive system cost 25 to 27 percent less per run. However, this is just a portion of the total savings. The amount of time saved by the analyst who no longer has to wait overnight or longer for graphical output and no longer has to hand-plot much of the experimental data saves many manhours each month.

Most of the analysts who have used the system found it very easy to use and capable of fulfilling most of their needs.

This system was our first endeavor into interactive graphics, and proved to be a very beneficial learning process. Because of the initial success of the present code, two additional programs have been incorporated into the interactive graphics system. One, a lumped-mass dynamic response code is now in operation and the shell version of the present ring-code is currently being implemented.

It is reiterated that the most important aspects of this system are:

1. Flexibility
2. User orientation
3. Interactive nature

REFERENCES

- [1] Lockheed Missiles & Space Co., Inc., User's Guide to the SHORE Code, P. G. Underwood, LMSC-D244589, Palo Alto, Calif., Nov 1971
- [2] P. G. Underwood, "Transient Response of Inelastic Shells of Revolution," Journal of Computers and Structures, Vol. 2, 1972 pp. 975-989
- [3] J. L. Sanders, Sr., "Nonlinear Theories for Thin Shells," Quarterly Applied Mathematics, No. 21, 1963, pp. 22-36

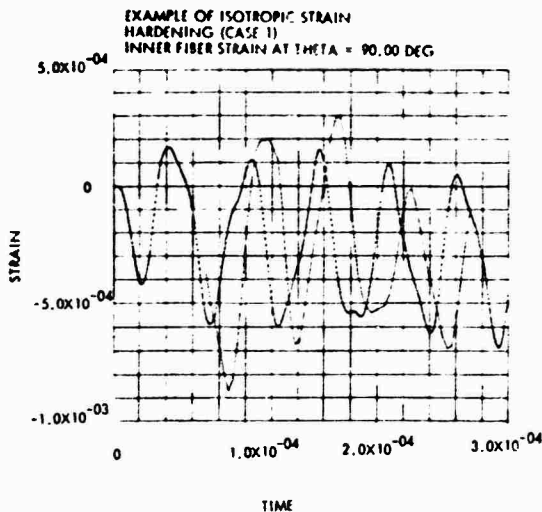


Fig. 12 - Experimental data (solid line) calculated response (dashed line)

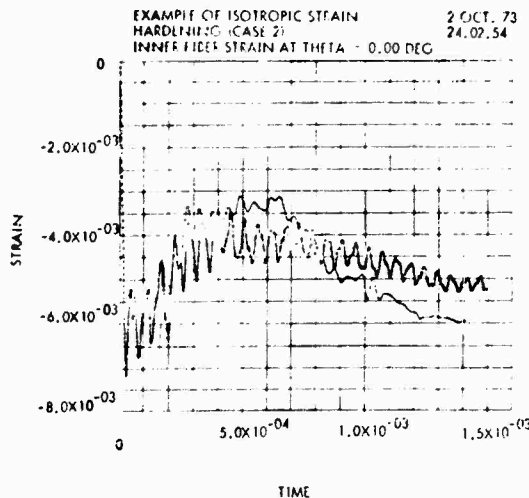


Fig. 13 - Experimental data (solid line) calculated response (dashed line)

system can perform the analysis successfully in a reasonable time, and it is also important that the complexity of the system has been held to a minimum. In all such system development, the analyst's ability to be able to understand and operate the system is vital; only when the analyst is fully aware of the system capabilities can he adapt the system to his needs. When this has been accomplished, the analyst will have a very powerful tool, which will not only allow him to receive direct feedback on the problem, but also will allow him to influence the analysis with respect to his interpretation and background of the problem.

It is difficult to state precisely the total saving in time and money achieved through this system. A cost study showed that for identical jobs on the

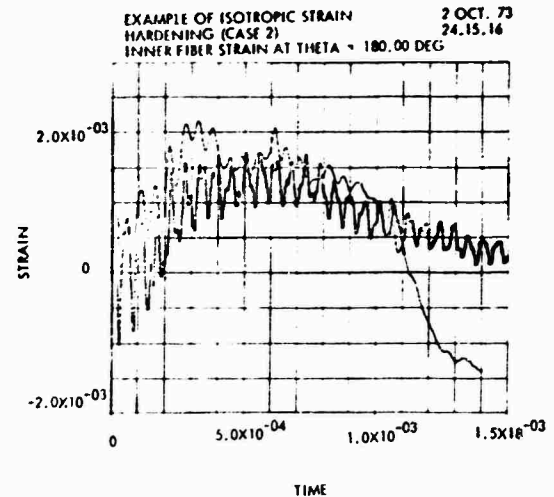


Fig. 14 - Experimental data (solid line) calculated response (dashed line)

interactive and batch system, the interactive system cost 25 to 27 percent less per run. However, this is just a portion of the total savings. The amount of time saved by the analyst who no longer has to wait overnight or longer for graphical output and no longer has to hand-plot much of the experimental data saves many manhours each month.

Most of the analysts who have used the system found it very easy to use and capable of fulfilling most of their needs.

This system was our first endeavor into interactive graphics, and proved to be a very beneficial learning process. Because of the initial success of the present code, two additional programs have been incorporated into the interactive graphics system. One, a lumped-mass dynamic response code is now in operation and the shell version of the present ring-code is currently being implemented.

It is reiterated that the most important aspects of this system are:

1. Flexibility
2. User orientation
3. Interactive nature

REFERENCES

- [1] Lockheed Missiles & Space Co., Inc., User's Guide to the SHORE Code, P. G. Underwood, LMSC-D244589, Palo Alto, Calif., Nov 1971
- [2] P. G. Underwood, "Transient Response of Inelastic Shells of Revolution," Journal of Computers and Structures, Vol. 2, 1972 pp. 975-989
- [3] J. L. Sanders, Sr., "Nonlinear Theories for Thin Shells," Quarterly Applied Mathematics, No. 21, 1963, pp. 22-36

COMPUTER GENERATED DISPLAYS OF STRUCTURES IN VIBRATION

Henry N. Christiansen
Brigham Young University
Provo, Utah

Computer generated continuous tone images are used to display the normal modes of vibration of finite element structural models. The existence of the mathematical model (and associated normal modes of vibration) is assumed, with the process being limited to the display process. The model is presented as a mosaic of triangular and quadrilateral elements on a raster driven cathode ray tube and recorded on film by a camera which is mounted in front of and facing the scope. Mode shape information (derived from the finite element structural model) is developed by adding appropriately magnified mode displacements to the node coordinates and/or coloring the model according to the level of displacement in a specified direction. Application of these procedures is shown for models of two unclassified United States Navy electro-mechanical sonar transducers.

INTRODUCTION

This paper is a result of a continuing computer graphics research project conducted by the author at the University of Utah under the sponsorship of the Department of the Navy and the Advanced Research Projects Agency. It grew out of earlier work on kinematic folded plate systems [1] and the display of displacement, and stress or strain functions for two dimensional finite element models [2]. This work introduced the concept of using computer generated continuous tone images to display the results of kinematic and elastic analyses of mathematical models.

It was apparent that similar display procedures could be utilized to produce realistic simulations of structures in vibration. An effort in this direction was spurred by the Naval Undersea Center, who had a requirement to display vibration results for three dimensional finite element models of sonar devices. Several displays of these transducers are included in the paper.

As the immediate application involved models for which the natural modes of vibration had already been calculated, the digital computer software

generated does not contain any elastic analysis capability. This is a departure from the previous programs which did contain kinematic and elastic analysis procedures.

COMPUTER GENERATED DISPLAYS

The past dozen years have seen the emergence of the field of computer graphics. The original work was concerned with the reduction of three dimensional data onto a plane. The problem of perspective was treated by Smith [3] and Johnson [4] and a significant advance was made by Roberts [5] with reasonable cost elimination of hidden lines. The last several years have seen the development of a number of structural applications using this basic line drawing technology. An early but sophisticated system was developed and reported by Batdorf [6] which emphasized the interactive nature of the man-machine environment and implications with respect to computer aided design.

Another important advance has come as a result of the creation of shaded pictures at the University of Utah (Romney [7], Warnock [8], and Watkins [9]), GE [10], and MAGI [11]. This paper,

among others, suggests the pattern portrayal capabilities inherent in this approach.

COMPUTER GENERATION OF CONTINUOUS TONE PICTURES

As mentioned previously, the mode of presentation in this paper is the continuous tone picture. This refers to the rendering of shaded objects by means of a raster driven cathode ray tube. The image produced is recorded on film by a camera mounted in front and pointing at the screen. As the picture is being computed and displayed one line at a time, the camera, with the shutter open, performs an integration function.

Just as the complete image is a sequence of lines, so an individual line is a sequence of dots (or groups of dots). The intensity of each dot must be computed and converted by a digital to analog device to a voltage which will in turn produce the desired intensity on the scope. The relationship between voltage and resulting intensity is non-linear and it becomes advisable to compensate for this effect. Each display shown in this paper contains 1024 lines, with each line containing 1024 dots. Thus, the picture is a mosaic of approximately one million dots, and the resolution of the scope is so good that it must be slightly defocused to avoid the appearance of these individual dots.

A scene is composed in terms of polygonal (in this case triangular and quadrilateral) elements. The hidden surface problem, which is analogous to the hidden line problem for line drawings, is solved as a result of comparisons of elements in a scene in order to determine which is in front of which. A simplification is obtained as a result of a perspective transformation which locates the observer at infinity in the direction of the Z axis, reducing the problem to a comparison of Z coordinates.

Systems have been written (Comba [12], Weiss [13], and Mahl [14]) which remove hidden components for curved surfaces by restricting the class of surfaces and/or accepting long execution times. In 1971, Gouraud [15], suggested a method which accepts a finite element approximation of the surface and shades the elements according to a linear function such that visual discontinuities between adjacent polygons disappear. The procedure suffers in that the derivatives of the intensity function are not continuous, however, the method is both general and efficient.

In 1972, Watkins was successful in reducing the hidden surface problem to hardware including the linear shading scheme. The computer generated pictures included in this paper were made using this equipment. The time required by the "Watkins Processor" is negligible and as other components of the system are improved, the total time required to produce a picture is being reduced.

To avoid the complication of shadows, the light source is located at the position of the observer and the intensity of the reflected light is made proportional to the cosine squared of the angle between the normal to the surface and the direction to the light source. When "flat" element shading is desired, an average normal for the element is utilized. However, when curved surface simulation is attempted, approximations for the normal to the surface at each node must be computed. The light intensity is then assumed to vary linearly between the nodes on the element outer edge. For the interior, this scheme results (except for triangles) in the shading being, somewhat, a function of the direction of the scan line across the element. This only becomes a serious consideration in the event that a single element is highly warped.

DISPLAY OF FINITE ELEMENT MODELS

In two dimensional finite element problems, the analyst will usually accept a one to one relationship between the structural elements and the display elements. However, in three dimensional problems each structural element has several surfaces, each of which may become one or more display elements. Therefore, it is normal (especially in large problems) to supply only those surfaces which will appear on the exterior in the display. Interior surfaces which might become visible in exploded views are also required.

The elements provided are grouped according to the "smooth" surface to which they belong. For example, to display a cube (from any orientation) requires six square display elements, each belonging to a separate group. On the other hand, to simulate a sphere one might use a large number of triangular and quadrilateral display elements, all belonging to the same group.

User control of the scene takes place at the element group level as well as for the total system. The option to

include or withhold a particular surface in a given display is made at the element group level, as is the specification of color and of a local translation vector for exploded views. Rotations, translations of the global coordinate axes, distance from the coordinate origin to the observer, scaling of the local translation vectors, and amplitude of the distortions (according to a selected mode shape), are all variables which are controlled at the total system level. The option of color requires the computation and display of three images. These images are the red, blue, and green component intensities for the prescribed element group and background colors. Prior to each pass, the appropriate color filter must be inserted between the scope and the camera.

Coloring the elements to indicate displacement levels proceeds according to

$$C_{ijk} = A_{ik} \cos^2 \theta + B_{ik} \sin^2 \theta$$

where: C_{ijk} is the intensity of the i^{th} color component at node j for surface k ;

A_{ik} is the intensity of the i^{th} color component specified (by the user) for surface k and displacement level δ_A ;

B_{ik} is the intensity of the i^{th} color component specified for surface k and displacement level δ_B ;

$$\theta = \frac{\pi}{2} \frac{(\delta - \delta_A)}{(\delta_B - \delta_A)}$$

$$\delta = \vec{u} \cdot \vec{u}_j$$

\vec{u} is a unit vector which indicated the specified direction for measuring displacements; and \vec{u}_j is the displacement vector for node j .

These intensities are also modified by multiplication with the cosine squared of the angle between the local normal and the direction to the light source.

MODEL DESCRIPTIONS AND DISPLAY EXAMPLES

Displays are presented for two finite element models of unclassified United States Navy electromechanical sonar transducers. Both structures were modeled with three dimensional (solid) finite elements taking advantage of geometrical symmetry.

The first device, shown in Figure 1, is a segmented piezoelectric cylinder. It is composed of 32 staves with alternating staves having opposite tangential polarization. Due to symmetry, it is necessary to model only the upper (or lower) half of two adjacent staves. This was done with four solid elements each having 20 nodal points (8 at the corners and 12 at the mid-points of the edges). Each nodal point has three displacement degrees of freedom and one electrical potential degree of freedom. By applying the appropriate boundary conditions it is possible to calculate various circular harmonic.

The display model, shown in Figure 2, contains 640 quadrilateral elements grouped into four surfaces. These display surfaces (the inner and outer cylinders and the top and bottom rings) describe only the exterior of the structural model. Figure 3 shows how the use of the curved surface simulation option smooths the cylindrical surfaces but still leaves a sharp edge between the cylinders and the top ring. Data for both the structural and display models were developed by personnel at the Naval Undersea Center (NUC), San Diego.

Figures 4 through 8 show the device distorted according to computed normal modes of vibration. The order of presentation is in agreement with ascending natural frequency. Figures 4, 6, and 8 illustrate flat shading, while Figures 5 and 7 show the effect of "smoothing."

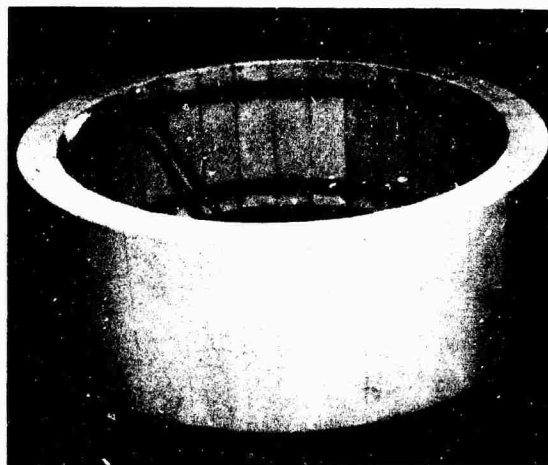


Figure 1. The Real Sonar Transducer

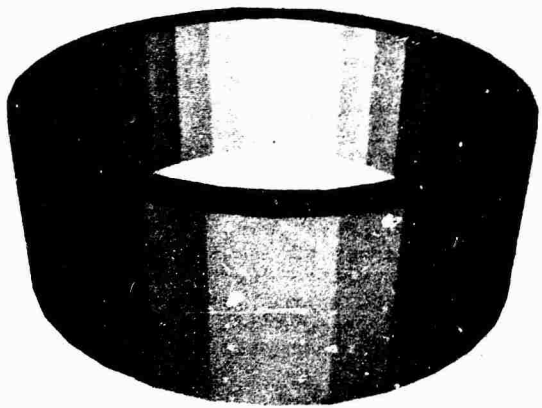


Figure 2. Display Model - "Flat" Format



Figure 5. Mode Shape #2

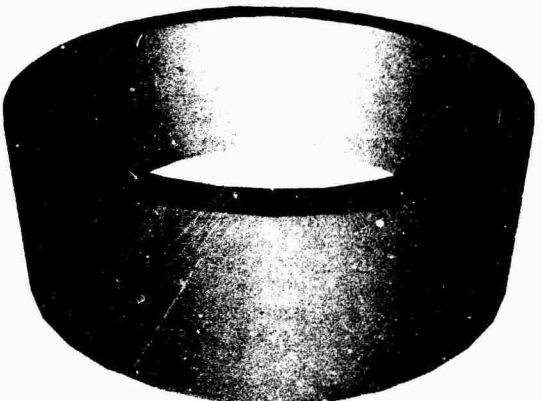


Figure 3. Display Model - "Smooth" Format



Figure 6. Mode Shape #3



Figure 4. Mode Shape #1

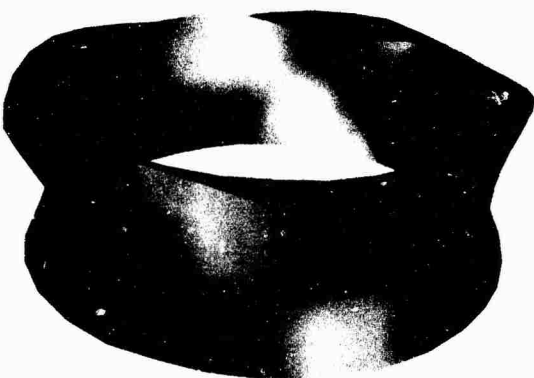


Figure 7. Mode Shape #4

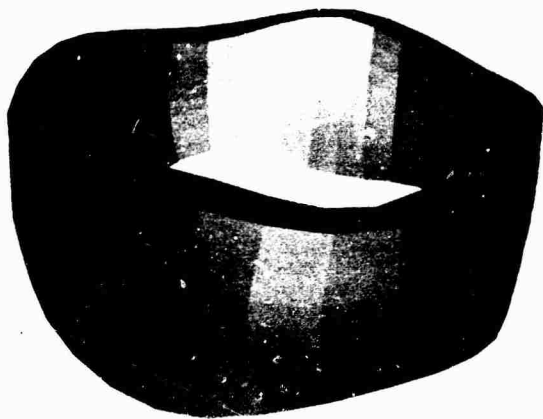


Figure 8. Mode Shape #5

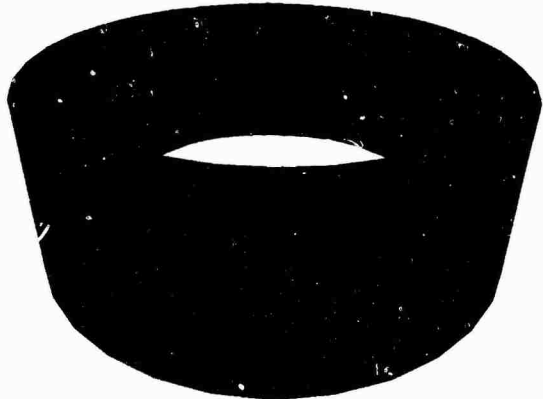


Figure 9. Displacement Shading - Mode Shape #1

Figure 9 illustrates the use of shading variations to indicate displacement levels in a user specified direction. This technique has been found most useful in the presentation of objects having irregular and unfamiliar shapes and when viewing a color display. When such techniques are applied to such familiar shapes as cylinders (for which the distorted shape is easily distinguished from the undistorted shape) and viewed in black and white, the value of the technique is reduced. In Figure 9, the model has been shaded according to the axial displacement component of the lowest natural frequency mode shape.

The second device, a T-shaped structure, is shown in Figure 10. This sonar element is composed of five main parts:

1. The radiating head (a solid piece of titanium);

2. A steel washer;
3. The active ceramic piezoelectric tube;
4. The tail mass (a solid piece of steel);
5. A steel stress rod.

The structural model which included all of these components, resulted in 1135 displacement degrees of freedom [16] for 1/4 of the device. The display model, as seen in an "exploded" view in Figure 11, includes:

1. The outer surface of the head (not including the surface covered by the washer);
2. The outer surface of the washer (grouped with the head in the "exploded" display);
3. The inner and outer surfaces of the ceramic tube including both ends;
4. The outer surfaces of the tail mass (not including the portion covered by the ceramic tube).

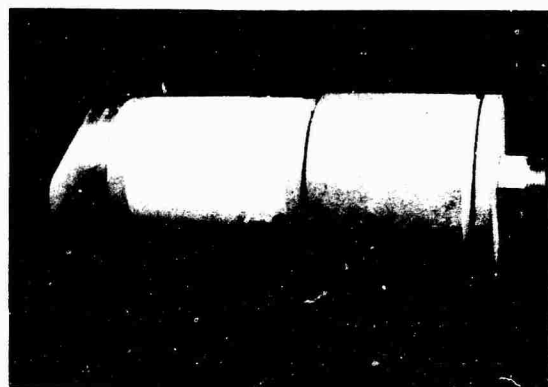


Figure 10. The Real Sonar Transducer

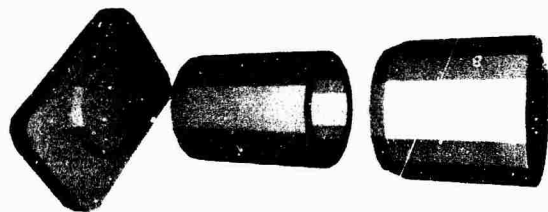


Figure 11. Display Model - "Exploded" View

Since the stress rod is, for the most part, inside the device, it is omitted from the display model. The four parts shown are represented by ten surfaces consisting of 452 elements. The structural model was developed at NUC in cooperation with the Electric Boat Division of General Dynamics, while the display data was generated at NUC. Figures 12 and 13 show "flat" and "smooth" versions of the assembled display model.

Figures 14, 15, and 16 illustrate the device distorted according to computed normal modes of vibration. Figure 14 is a lower frequency mode for which most of the motion occurs in the radiating head. Figure 15 illustrates an intermediate mode having relatively large displacements in the region of the ceramic tube. Figure 16 shows a higher frequency mode. Notice that the steel tail mass remains relatively undistorted in each mode. Figure 17 shows shading variation utilized to indicate the axial component of displacement for the high frequency mode shape.

RELATED EFFORTS

The contract with the Department of the Navy called for the production of a computer generated continuous tone movie of the T-shaped sonar transducer vibrating in the mode shapes shown in Figures 14, 15, and 16. Accordingly, the display program was modified to facilitate the specification of the desired animation, and a color movie was made using a new higher speed display system.

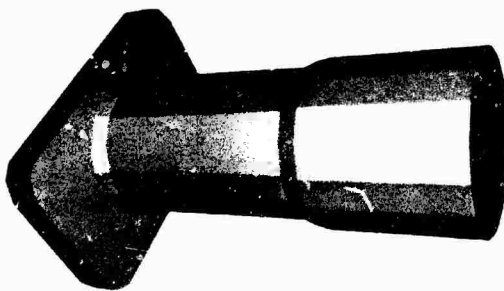


Figure 12. Display Model - Flat Format"

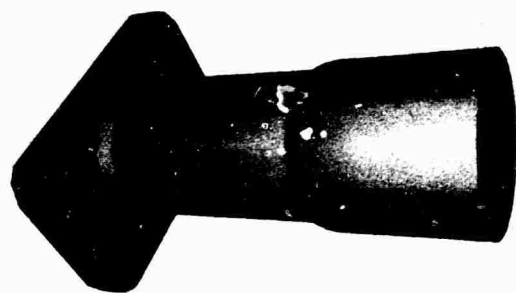


Figure 13. Display Model - "Smooth Format"

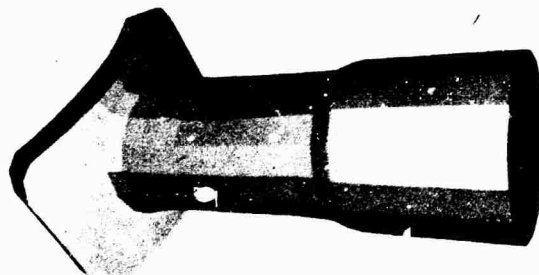


Figure 14. Lower Frequency Mode Shape

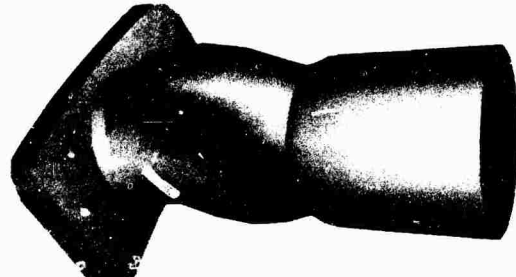


Figure 15. Intermediate Frequency Mode Shape

CONCLUDING COMMENTS

It is felt that computer generated continuous tone images (black and white and in color) are useful in presenting rather complex pattern information. For familiar objects, mode shape information is usually discernible by viewing distorted structures. For irregular, unfamiliar objects, shading according to displacement levels may be useful (especially in color). The production of movies of vibrating systems becomes justified as the complexity of the display increases. Movies have been found to be helpful in viewing rigid body components of the motion and in the display of wave propagation phenomena.

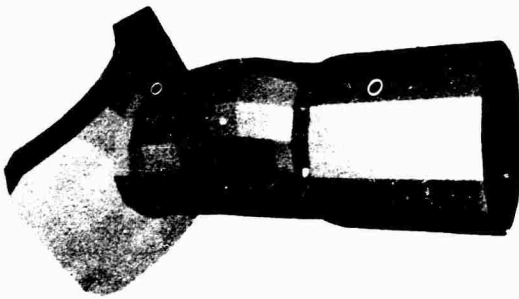


Figure 16. Higher Frequency Mode Shape

When using the movie production options, one may specify (in addition to the options available in the production of single frames):

1. The number of frames to be made under automatic control;
2. Frequency of vibration;
3. Smoothly accelerated motion for rigid body rotation and translation, "zooming," and "explosion" of selected surfaces;
4. The advancement of a "peel away" plane in space.

The "peel away" capability allows the viewing of interior or otherwise hidden surfaces by eliminating, from the display, elements (in specified surfaces) as they penetrate a user specified plane.

The software used to manipulate the data is almost entirely in FORTRAN. Due to the sponsorship of its development under federal funding, it is generally available upon request. While the program is hardware dependent, major portions have been converted to other configurations and used to generate line drawing movies. The hardware system is available for government related projects through contracts with the University of Utah. Due to the existence of government furnished equipment, it is not generally available for commercial work.

The author wishes to express his appreciation to Mike Milochik of the University of Utah for his time and talent in the processing of the photographs shown in this paper.

REFERENCES

1. R. D. Resch and H. N. Christiansen, "The Design and Analysis of Kinematic Folded Plate Systems," Proc. Symposium for Folded Plates and Prismatic Structures, International Assoc. for Shell Structures, Vienna, Austria, Oct. 1970.
2. H. N. Christiansen, "Displays of Kinematic and Elastic Systems," Proc. of the Third Conf. on Matrix Methods in Structural Mechanics, Wright-Patterson Air Force Base, Dayton, Ohio, Oct. 1971.
3. A. F. Smith, "Method for Computer Visualization," AMC Technical Report No. 8436-TM-2, Electronic Systems Laboratory, M.I.T., Sept. 1960.
4. T. E. Johnson, "Sketchpad III: Three Dimensional Graphical Communication with a Digital

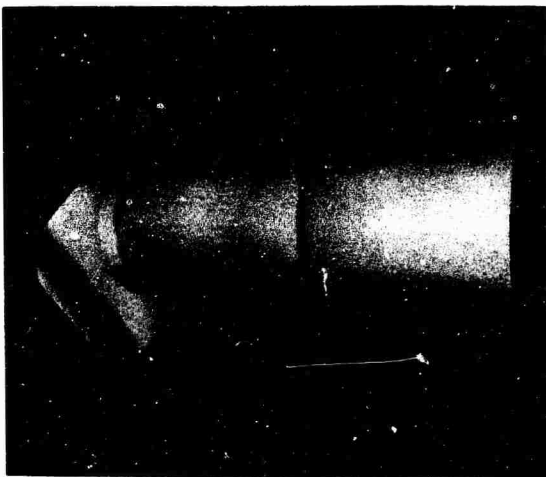


Figure 17. Displacement Shading

Computer," Report ESL-TM-173, Electronic Systems Laboratory, M.I.T., June 1963.

5. L. G. Roberts, "Machine Perception of Three-Dimensional Solids," Technical Report No. 315 Lincoln Laboratory, M.I.T., 22 May 1963.

6. W. J. Baudorf, S. S. Kapur, R. B. Sayer, "The Role of Computer Graphics in the Structural Design Process," Proc. of the Second Conf. on Matrix Methods in Structural Mechanics, Wright-Patterson Air Force Base, Dayton, Ohio, Oct. 1968.

7. G. W. Romney, "Computer Assisted Assembly and Rendering of Solids," Dept. Computer Science, Univ. of Utah, Salt Lake City, Tech. Rep. TR 4-20, 1970.

8. J. E. Warnock, "A Hidden Surface Algorithm for Computer Generated Halftone Pictures," Dept. Computer Science, Univ. of Utah, Salt Lake City, Tech. Rep. 4-15 June 1969.

9. G. S. Watkins, "A Real Time Visible Surface Algorithm," Dept. Computer Sci., Univ. of Utah, Salt Lake City, Tech. Rep. UTEC-CSc-70-101, July 1970.

10. R. S. Rougelot and R. Shoemaker, "G.E. Real Time Display," General Electric Co., Syracuse, N.Y., NASA Rep. NAS 9-3916.

11. MAGI, Mathematical Applications Group Inc., "3-D Simulated Graphics," Datamation, Vol. 14, Feb. 1968, p. 69.

12. P. G. Comba, "A Procedure for Detecting Intersections of Three Dimensional Objects," IBM New York Scientific Center, New York, N.Y., Rep. 39.020, Jan. 1967.

13. R. A. Weiss, "Be Vision, A Package of IBM 7090 Fortran Programs to Draw Orthographic Views of Combinations of Planes and Quadric Surfaces," Jour. Ass. Comput. Mach., Vol. 13, April 1966, pp. 194-204.

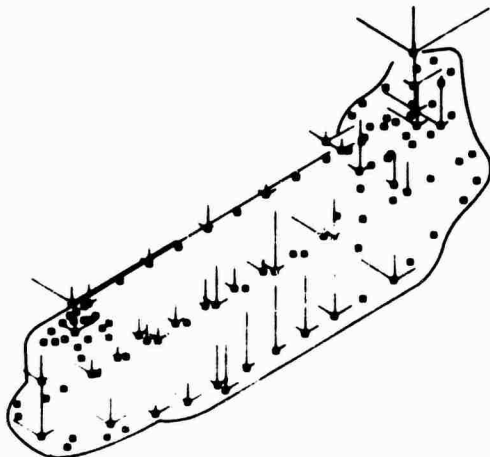
14. R. Mahl, "Visible Surface Algorithms for Quadric Patches," Dept. Computer Science, Univ. of Utah, Salt Lake City, Tech. Rep. UTEC-CSc-70-111, Dec. 1970.

15. H. Gouraud, "Computer Display of Curved Surfaces," Unpublished Ph.D. Thesis, Dept. Computer Science, Univ. of Utah, Salt Lake City,

June 1971.

16. J. T. Hunt, R. R. Smith, D. Barach, L. McCleary, C. Johnson, "Applications of the Finite Element Method and Computer Graphics. A Vibrational Analysis of a Sonar Projector Transducer Element." TP 321, Naval Undersea Center, San Diego, California.

VIBRATION REDUCTION BY USING BOTH THE FINITE ELEMENT STRAIN ENERGY DISTRIBUTION AND MOBILITY TECHNIQUES *



J. J. Sciarra
Boeing Vertol Company
Philadelphia, Pa.

Part of the design cycle for the development of a complex structure, subject to external oscillatory forces, must involve some means for vibration reduction. This complex structure could be a helicopter airframe in flight. Much of the reduction could be achieved by anti-vibration devices (such as dynamic absorbers) or by structural modification (detuning). The effectiveness of the former may be evaluated by impedance methods, and the effectiveness of the latter may be determined by strain energy techniques. Both these methods have been applied to the design of the Boeing Vertol Model 347 tandem rotor helicopter.

SUMMARY

In Reference (1), impedance methods utilizing the finite element method were developed to rapidly evaluate the effectiveness of anti-vibration devices attached to a complex airframe. Either test or calculated mobilities may be used in the analysis. This impedance methodology has been successfully applied to the design of absorbers for the new Boeing Model 347 tandem helicopter. The detuning of the 347 fuselage by

structural modification also resulted in an exceptionally low final vibration level throughout the entire flight envelope. The structure to be modified can be indicated by energy techniques. This paper presents and compares both methods.

Impedance methods in helicopter design may also be used to determine vibratory hub loads and moments acting in flight, or to decompose the vibration at a point due to remote multiple, phased exciting forces or moments into its vector components (Reference 2).

*The work presented in this paper was funded by the U.S. Army Research Office - Durham, North Carolina, under Contract DAHC04-71-C-0048. The paper was presented at the Impedance Seminar, Imperial College of Science and Technology, London, England, July 3, 1973.

The practical aspects of self-tuning Frahm type vibration absorbers are discussed in detail in Reference 3. The application in this reference was to further reduce vibration in the CH-47C Chinook.

The reduction of the vibration level of a helicopter can be accomplished in many ways. Only two of these ways associated with the airframe are considered and compared in this report. Another method that may be considered is the reduction of the vibratory aero-dynamic loading.

The first technique presented is local vibration reduction. This is accomplished by the use of a device, such as a dynamic absorber, a gyroscopic absorber, or a pendulum absorber, which is attached to an area of the complex structure. The proper tuning and design of the device allows a node to be generated on the structure, which reduces the vibration in its area. These local vibration reducers can be analyzed by using the impedance method in conjunction with the finite element method (Reference 1).

An attached absorber is shown in Figure 1.

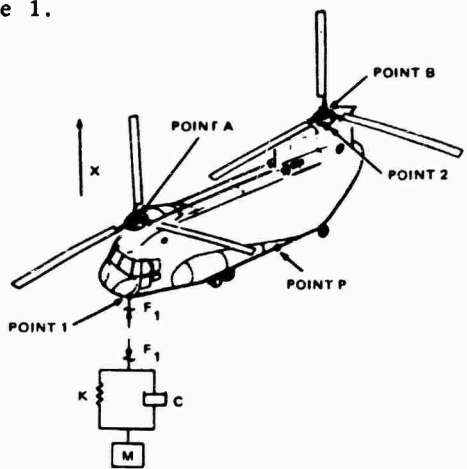


Figure 1. Fuselage with Absorber - Impedance Method.

The second technique presented is the lowering of the dynamic environment of a complex structure by structural modification. The structural modification employed should cause the movement of the natural frequency away from an exciting frequency. This is shown on the spectrum in Figure 2.

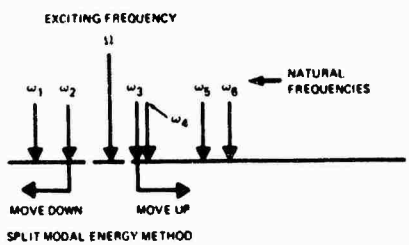


Figure 2. Split Modal Energy Method.

The obvious effect of this is to reduce the damped amplification factors.

Energy matrix methods are the type of analyses used to indicate which structural areas should be altered for optimum modification. Both impedance and energy methods are summarized in the next two sections. Their application to the Model 347 helicopter is presented in the last section.

IMPEDANCE METHOD

The current state-of-the-art in structural analysis dictates the use of the finite element method for complex structures.

First, a finite element mathematical model of the structure is generated. This model is then programmed into a computer in which a dynamic analysis is performed. Results are then obtained which give the damped response due to external exciting loads at given degrees of freedom.

This is termed "a normal mode analysis." The basic equation of motion in matrix form is:

$$[M]\{x\} + [C]\{x\} + [K]\{x\} = \{F_s\} \sin \Omega t + \{F_c\} \cos \Omega t. \quad (\text{Eq 1})$$

The solution to this is

$$\{x\} = \{x_s\} \sin \Omega t + \{x_c\} \cos \Omega t. \quad (\text{Eq 2})$$

In the above,

$[M]$ = mass matrix

$\{x\}$ = displacement (inches), or rotation (radians)

$[C]$ = damping matrix

$\{F_s\}\{F_c\}$ = sine or cosine components of the exciting loads, 'b', in.-lb

Ω = exciting frequency, rad/sec

$\{x_s\}\{x_c\}$ = sine or cosine components of the displacement (or rotation) of the nodes of one structural element, inches, radians

t = time, sec

A normal mode analysis may be used to find mobilities by mathematically exciting one degree of freedom and finding the response at all the degrees of freedom including the point of excitation.

For example, if the exciting force chosen is 1 lb which excites a node 5 in a vertical direction, then the response at some other node, say 3 vertically, is found using Equations 1 and 2.

The structural phase lag is determined by rewriting Equation 2 in amplitude-phase angle form.

Summarizing: $M_{3,5}$ = mobility

$= X_3/F_5$ = displacement and phase lag at 3 node vertically, caused by a force (=1 lb here) at 5 vertically

The external force or moment is usually real, but the mobility and displacement are complex numbers composed of an amplitude and modulus.

In general, mobility expressions for energy absorbing devices can be developed. The simplest is the mass-spring-damper system in Figure 3. The mobility of this device at point A is

$$\bar{M}_{AA} = [1/(K + i\zeta\omega C)] - (1/m\omega^2) = a + ib \quad (\text{Eq } 3)$$

where

$$a = (\Omega^2 - (\omega^2 + 4\zeta^2\Omega^2)) / (m\Omega^2(\omega^2 + 4\zeta^2\Omega^2)) \quad (\text{Eq } 4)$$

and

$$b = (-2\zeta\Omega) / (m\omega(\omega^2 + 4\zeta^2\Omega^2)) \quad (\text{Eq } 5)$$

with

$$\omega = (K/m)^{1/2} \quad (\text{Eq } 6)$$

and

$$\zeta = C/2m\omega. \quad (\text{Eq } 7)$$

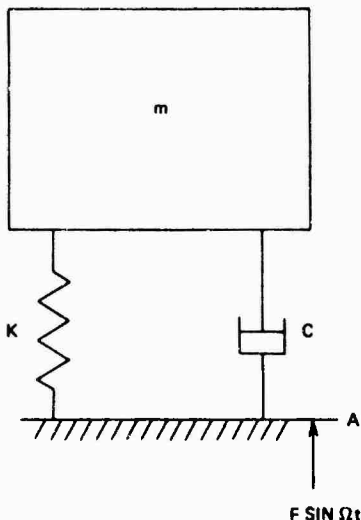


Figure 3. Absorber - Impedance Method.

Consider the complex structure in Figure 1. The displacement at point (1) is

$$X_1 = M_{1A}F_A + M_{11}F_1 \quad (\text{Eq } 8)$$

where M_{11} is the mobility at the point caused by a force or moment placed at the same location, F_1 is the force or moment at the same location, M_{1A} is the mobility at (1) due to F_A , a force at (A). The first term on the right in Equation (8) is the original displacement; the second term would correspond to the displacement caused by an external attached device. The force caused by an absorber is

$$F_1 = -\bar{F}_1 \quad (\text{Eq } 9)$$

but

$$\bar{F}_1 = X_1 \bar{M}_{11} \quad (\text{Eq } 10)$$

where \bar{M}_{11} is the mobility of the absorber from Equation (3).

So

$$\{1 + (M_{11}/\bar{M}_{11})\} X_1 = M_{1A}F_A \quad (\text{Eq } 11)$$

For two absorbers at points (1) and (2)

$$X_1 = M_{1A}F_A + M_{11}F_1 + M_{12}F_2$$

$$X_2 = M_{2A}F_A + M_{21}F_1 + M_{22}F_2 \quad (\text{Eq } 12)$$

or

$$\left. \begin{aligned} \{1 + (M_{11}/\bar{M}_{11})\} X_1 + (M_{12}/\bar{M}_{22}) X_2 &= M_{1A}F_A \\ (M_{21}/\bar{M}_{11}) X_1 + \{1 + (M_{22}/\bar{M}_{22})\} X_2 &= M_{2A}F_A \end{aligned} \right\} \quad (\text{Eq } 13)$$

Equations (11) and (13) are complex simultaneous equations.

For n absorbers:

$$\sum_{k=1}^n \{(\delta_{ik} + M_{ik}/\bar{M}_{kk}) X_k\} = M_{iA}F_A \quad (i = 1, 2, \dots, n) \quad (\text{Eq } 14)$$

where $\delta_{ik} = 1$, if $i = k$ and is zero if $i \neq k$.

If the external exciting force is phased, F_A may be written as $F \cosine \theta + iF \sin \theta$. This automatically considers the phase angle. If more than one force or moment acts on the complex structure, their total effect is obtained by solving Equation (14) for each, and then summing the displacements (superposition).

ENERGY METHOD

Two energy methods are presented in this section. The first is a modal method, and the second is a damped forced response method.

In the modal method, the natural frequency immediately above the exciting frequency is increased (this is referred to as "beefing-up"). One could also reduce the natural frequency immediately below the exciting frequency, if it is possible structurally.

In order to accomplish these effectively, a finite element analysis is first employed to yield a dynamic solution. The eigenvectors (mode shapes) are obtained, and then the modal strain energy distribution throughout the structure is found for a given mode shape whose natural frequency is to be modified. After the strain energies for each structural element have been obtained, they are then tabulated from the highest to lowest.

The structural elements in the highest strain would be the best candidates for modification of the natural frequency. This follows intuitively from the almost-invariance of the mode shapes and from Raleigh's Quotient. Theory (Reference 4) also substantiates this.

The procedure is more optimal from a weight point of view if the strain densities (strain energy/volume) are used rather than strain energy alone. An iterative loop could also be employed.

The second energy method involves the use of the damped forced response (DFR) in place of a mode shape. This methodology is currently being studied at Vertol under Contract DAHC04-71-C-0048 to the Army Research Office at Durham, North Carolina.

As in the modal method, the strain energies as determined by the steady state response for some load condition are calculated for all the structural elements. The strain energy is basically:

$$2S.E. = \mathbf{x}^T \begin{bmatrix} \mathbf{K}_e \end{bmatrix} \{ \mathbf{x} \} \quad (Eq. 15)$$

where \mathbf{K}_e is the stiffness matrix of a structural element and $\{ \mathbf{x} \}$ is the end displacements or rotations.

However, from Equation (2), the energy content of each structural ele-

ment varies with time; so it is necessary to find the maximum value within one cycle for each element. By considering Equations (2) and (15), and using simple calculus, the maximum vibratory strain energy (S.E.) of each structural element is:

2S.E. =

$$\mathbf{x}_s^T \mathbf{K}_e \mathbf{x}_s + \mathbf{x}_c^T \mathbf{K}_e \mathbf{x}_c + \sqrt{(\mathbf{x}_c^T \mathbf{K}_e \mathbf{x}_c - \mathbf{x}_s^T \mathbf{K}_e \mathbf{x}_s)^2 + (\mathbf{x}_s^T \mathbf{K}_e \mathbf{x}_c + \mathbf{x}_c^T \mathbf{K}_e \mathbf{x}_s)^2} \quad (Eq. 16)$$

which occurs when:

$$\Omega_e = \frac{1}{2} \tan^{-1} \frac{\mathbf{x}_c^T \mathbf{K}_e \mathbf{x}_s + \mathbf{x}_s^T \mathbf{K}_e \mathbf{x}_c}{\mathbf{x}_c^T \mathbf{K}_e \mathbf{x}_c - \mathbf{x}_s^T \mathbf{K}_e \mathbf{x}_s} \quad (Eq. 17)$$

The modifications may be done for a minimum weight penalty by considering strain density rather than energy. This method can also be put into an iterative loop to obtain an absolute optimal dynamic structure if a weight limitation is applied.

One method of resizing the structural elements in each cycle is shown in Reference 4 and is given as:

$$\Delta t_i = \frac{\alpha (S.D.)}{(S.D.)_{MAX OF ALL ELEMENTS}} \quad (Eq. 18)$$

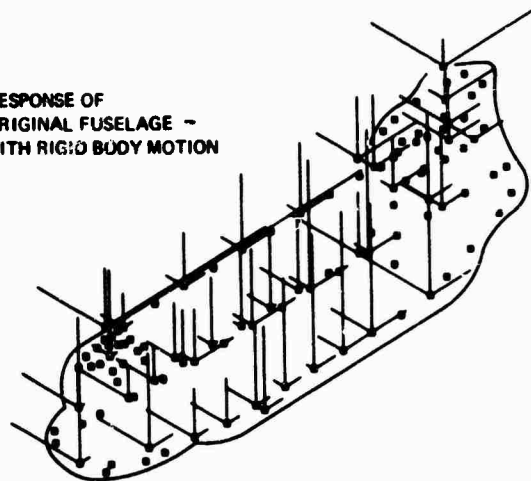
where "i" refers to the i th structural element, Δt is the change in a parameter (area, thickness, moment of inertia), α is an arbitrary constant (e.g. 1 or 2), and S.D. is the strain density. The weight penalty allowable would dictate the value of α .

This energy procedure was applied to a helicopter in forward flight (140 knots). Figures 4 and 5 summarize the results of this study. Figure 4 includes six degrees of freedom (mode shapes) for rigid body bending. Figure 5 includes elastic bending modes only. A total of six forces with sine and cosine components excited the craft at forward and aft hubs.

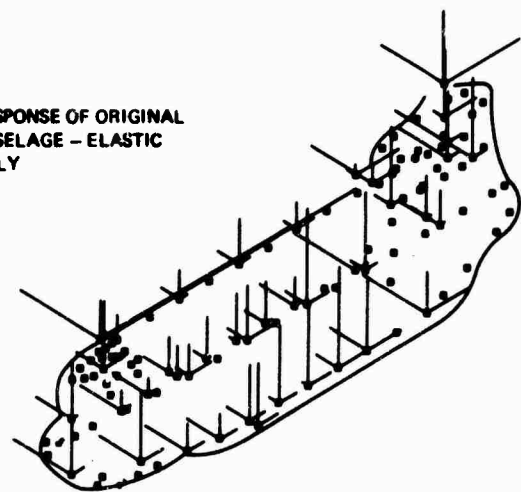
The original vibratory level is shown in the top figure. The middle fuselage represents the vibration level with 13 structural members doubled (1.2% weight penalty).

In the bottom figure, Equation 18 was used to scale the thickness of the 13 members (1.4% weight penalty). No iteration was used. It is seen from these figures that the vibration level was significantly reduced by structural detuning using the damped forced response (Reference 5).

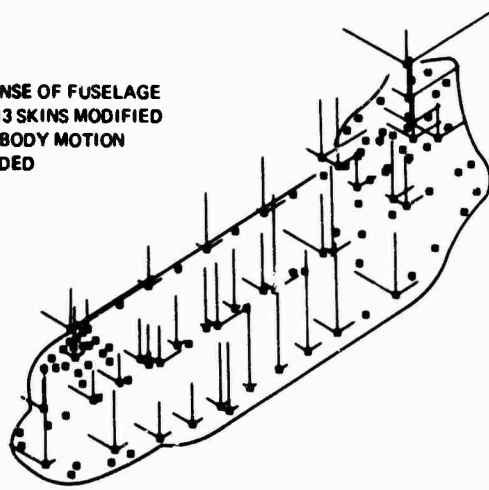
RESPONSE OF
ORIGINAL FUSELAGE -
WITH RIGID BODY MOTION



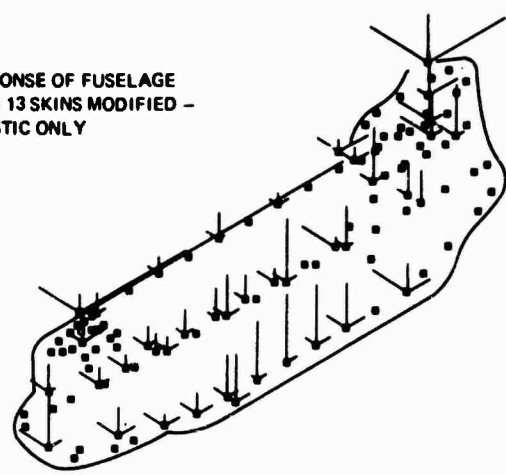
RESPONSE OF ORIGINAL
FUSELAGE - ELASTIC
ONLY



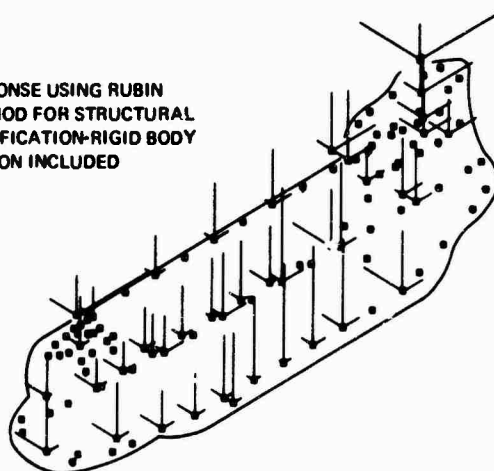
RESPONSE OF FUSELAGE
WITH 13 SKINS MODIFIED
RIGID BODY MOTION
INCLUDED



RESPONSE OF FUSELAGE
WITH 13 SKINS MODIFIED -
ELASTIC ONLY



RESPONSE USING RUBIN
METHOD FOR STRUCTURAL
MODIFICATION-RIGID BODY
MOTION INCLUDED



RESPONSE USING RUBIN
METHOD FOR STRUCTURAL
MODIFICATION - NO RIGID
BODY MOTION

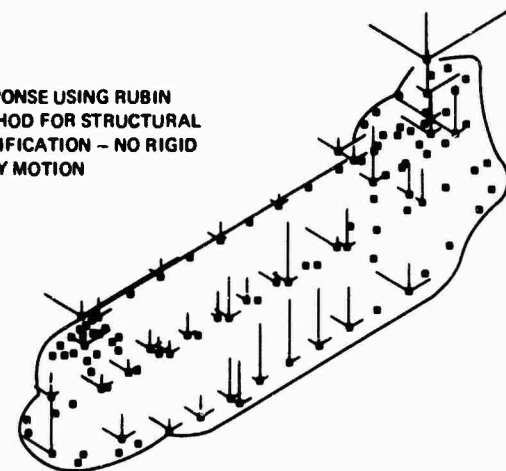


Figure 4. Vibration Reduction Through
Structural Modification,
Energy Method. Rigid Body
Motion Included.

Figure 5. Vibration Reduction Through
Structural Modification,
Energy Method. Elastic Modes
Only.

THE MODEL 347 HELICOPTER

The dynamic objectives for the design of a rotary aircraft are to attain low vibratory response levels. This is to assure crew comfort and insure structural integrity.

The block diagram below (Figure 6) shows one flow of analysis needed to accomplish the goal of minimization of n per revolution (n = number of blades) airframe vibration.

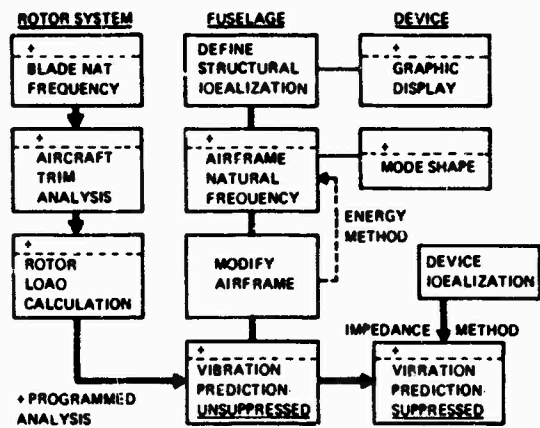


Figure 6. Airframe Vibration Reduction, Overall Scheme.

The combination of self-tuning vibration absorbers and airframe natural frequency alteration by structural modification as indicated in the above block diagram was successfully applied in the design of the new Boeing Model 347 helicopter. This helicopter is a growth version of the CH-47A Chinook. The fuselage was lengthened, the aft pylon was heightened, and wings were added.

Other means were also employed on the 347 to reduce vibration. These were use of a 4-bladed rotor, stiffening of the cockpit floor, and removal of cargo isolation in the cabin floor. All these are shown in Figure 7.

From the impedance study, six absorbers were finally used. For detuning, a door was added on the left hand side of the forward pylon cabin.

In the optimal design study for the inclusion of STVA's (self-tuning vibration absorbers), the impedance method was used exclusively. Because of the speed of the analysis on the computer, many variations were studied. The variations included location, weight, damping and number of STVA's.

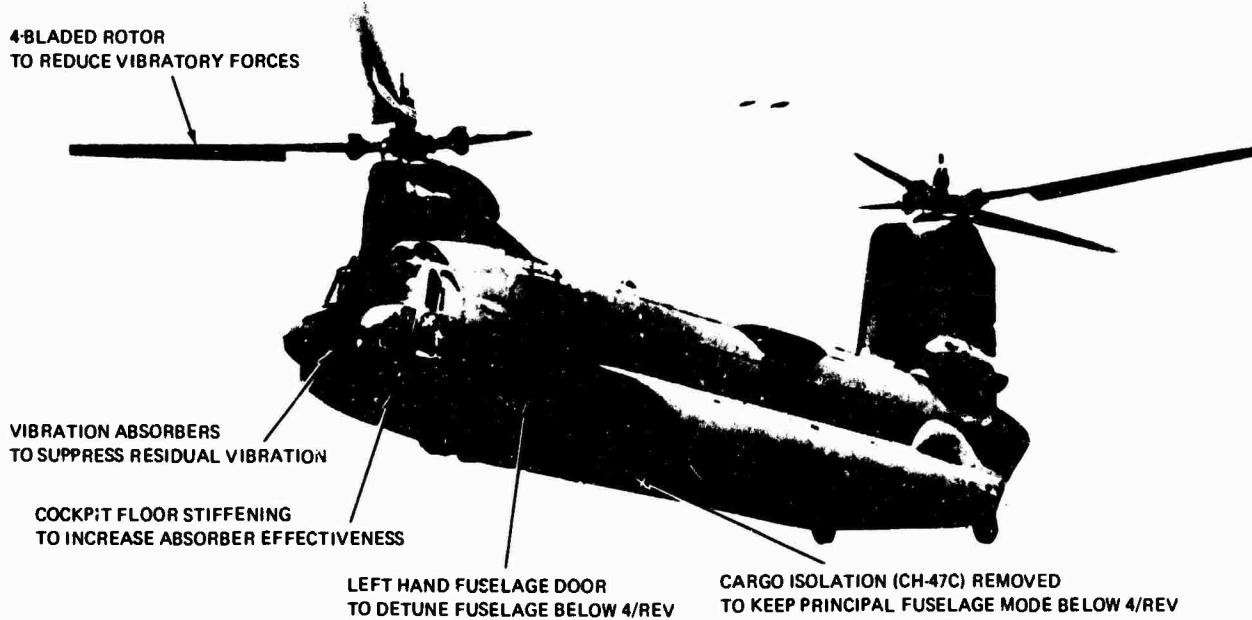


Figure 7. Methods Used to Reduce Vibration in the Boeing Vertol Model 347.

Figure 8 shows the airframe 4 per revolution vertical acceleration for the various fuselage stations. The unsuppressed fuselage results are compared to the results with 7 STVA's at various locations. The analysis allowed for 5 vibratory phased loads per hub. Each analysis required only 10 seconds or less of CPU time. The structural damping of each absorber was assumed to be .0025; their weight was 90 lbs each and they were tuned to 87 rad/sec.

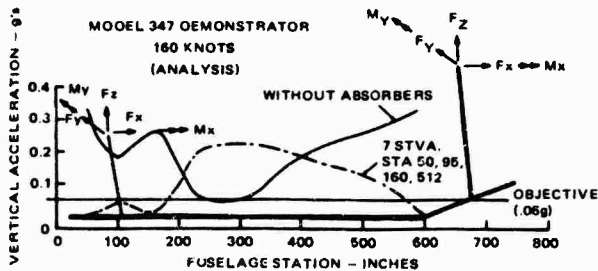


Figure 8. Airframe 4 per Revolution Vertical Acceleration Versus Fuselage Station.

The mobilities were all obtained analytically using the finite element normal mode method.

In Figure 9, test results for no absorbers are compared to results of a finite element analysis for the cockpit vertical vibration.

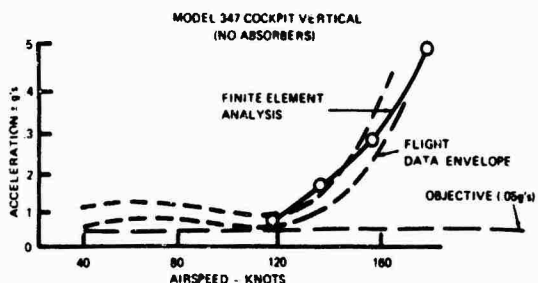


Figure 9. Correlation of Normal Mode Analysis with Flight Test.

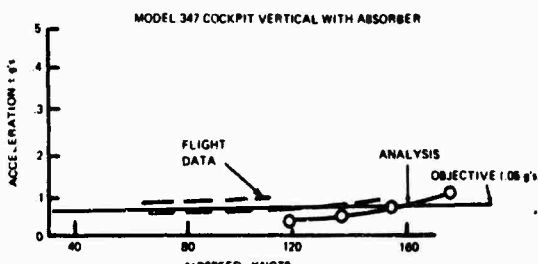


Figure 10. Correlation of Impedance Method Analysis with Flight Test.

In Figure 10, correlation of flight test with results of impedance methodology (Equation 14) is shown. It is seen that both the finite element and impedance methods provide good correlation with test.

CONCLUSIONS

1. Significant vibration reduction of a complex structure acting under exciting loads can be achieved by adding absorbers and through structural detuning.
2. Correlation of analysis with test is obtainable by utilizing the finite element and impedance methods.

ACKNOWLEDGEMENT

The correlation for the Boeing Model 347 was achieved by J.J. O'Leary, Chief of Dynamics at Boeing/Vertol.

REFERENCES

1. J.J. Sciarra, "Application of a Combined Direct Stiffness and Mobility Method to Vibration, Absorber Studies," ASME/MDD Vibrations Conference, Paper 67-VIBR-65 (March, 1967).
2. J.J. Sciarra, "Helicopter Fuselage Vibration Prediction by Stiffness/Mobility Methods," 37th Shock & Vibration Symposium, Orlando, Florida (October, 1967).
3. J.J. O'Leary, "Reduction in Vibration of the CH-47C Helicopter Using A Variable Tuning Vibration Absorber," 40th Shock & Vibration Symposium, Hampton, Virginia (December, 1969).
4. C.P. Rubin, "Dynamic Optimization of Complex Structures," AIAA Dynamics and Aeroelasticity Specialists Conference, New Orleans, La (April, 1969).
5. J.J. Sciarra, "Use of the Finite Element Damped Forced Response Strain Energy Distribution for Vibration Reduction," presented at ARO-D Military Theme Review, The Helicopter and V/STOL aircraft Research Conference, U.S. Army Research Office, NASA-Ames Research Center, Moffett Field, California, AD-751809 (September, 1972).

INFLUENCE OF ELASTIC SUPPORTS ON
NATURAL FREQUENCIES OF CANTILEVER BEAMS

Ruell F. Solberg, Jr.
Southwest Research Institute
San Antonio, Texas 78284

Nonuniform cantilever (clamped-free) beams, excited by sinusoidal motion at their clamped ends, were investigated analytically and experimentally. The investigation was motivated by requirements to design, fabricate, and test complex radio frequency direction finding antennas which attach to the top of surface ship masts. The requirements included design to withstand and test for vibration per MIL-STD-167 and design to withstand the high impact shock tests per MIL-S-901.

A general lumped-parameter (finite element) beam, forced-vibration, computer program was used to aid the analyses and optimize the design. Many structural parts of the antenna were mathematically modeled and approximated as nonuniform cantilever beams. The influence of deficient semi-infinite rigid supports at the clamped end of nonuniform cantilever beams on the lateral natural frequencies are presented for these structures. Representative measured results are compared to calculated results. Imperfect cantilever boundary conditions of typical linear and rotatory stiffnesses are shown to reduce severely the lateral natural frequencies. The classical assumption of semi-infinite rigid supports at the clamped end is shown to possibly produce large errors with possible catastrophic effects.

INTRODUCTION

A previous project required designing and fabricating an antenna assembly to MIL-SPEC and MIL-STD requirements from the breadboard phase, omitting the development phase. This antenna was designed for mounting at the top of a U. S. Navy ship mast. Although many of the requirements were the same or similar to previous projects, experience with these particular vibration [1] and shock [2] requirements was limited.

Efforts to obtain information and documents to aid the design for the shock requirements were unsuccessful in the available time. Therefore, the design requirements for the equipment were to withstand static

loads equivalent to 100 g. This resulted in a conservative design for some of the equipment with the penalty of excessive weight.

The vibration excitation frequencies were low with the upper frequency of the bandwidth at 33 Hz. For a narrow bandwidth of frequency excitation a practical method of vibration control is to design for structural resonances outside the bandwidth. The structural complexity was such that computer-aided analyses were performed so the individual major structural elements and their assembly could be designed such that the fundamental lateral natural frequencies would be slightly above the upper excitation frequency.

NOMENCLATURE

A	= cross sectional area, in. ²	r	= radius of fillet at junction of support and cantilever beam, in.
E	= modulus of elasticity, lb/in. ²	V	= shear load per unit width at support, lb/in.
g	= acceleration due to gravity, ft/sec ²	W	= load, lb.
h	= depth of cantilever, in.	x, y	= coordinate system, in.
h'	= effective depth of load distribution at support, in.	Δ	= static deflection, in.
k	= linear spring rate, lb/in.	δ	= deflection of cantilever in y-direction for linear spring only, in.
k_x	= linear spring rate, lb/in.	δ_θ	= deflection of cantilever in y-direction for torsional (rotatory) spring only, in.
k_θ	= rotatory spring rate, lb-in./rad	ν	= Poisson's ratio
L	= length, in.	ω	= circular natural frequency, rad/sec
M	= moment per unit width at support, lb-in./in.		

The antenna assembly is shown in Figure 1. The antenna assembly is essentially composed of three bays of antenna elements bolted to a vertical mast with electronic packages inside the mast. Numerous parts, including the assembly, were analyzed as cantilever (clamped-free) beams. Cantilever structures are undesirable for shock and vibration environments, but these types of structures were necessary for optimum electromagnetic performance of the antennas.

Some unexpected results were obtained when the antenna assembly was vibration tested. The fundamental lateral natural frequencies were approximately one-half of their theoretical values, with some then within the vibration excitation bandwidth. These errors resulted from using the classical analysis technique of assuming a semi-infinite support with infinite rigidity at the fixed end of a cantilever beam. Although a small shift of natural frequencies was anticipated because of finite rigidity, the frequency differences between the classical assumptions and the real situations were not expected and could have been catastrophic. The consequence of these experiences was an endeavor to better understand the effects of finitely rigid supports and to more accurately design for them.

in the future. The purpose of this paper is to present and discuss some of this investigation and the results.

Examples of the effects of elastic boundary conditions are presented for two structures which are analyzed as nonuniform cantilever beams. The lower bay of the antenna assembly, shown in Figure 1, is composed of eight individual antenna elements which are bolted to the mast, the vertical cylindrical structure. An individual element is one of the structures whose analysis is presented. Each antenna element weighs approximately 12 lb (5.4 kg), is a welded aluminum alloy structure, and is 23.75 in. (603.2 mm) long. A tapered beam effect was obtained for the booms of these elements by varying the vertical distance between two pieces of tubing such that the cross sectional moment of inertia and weight per unit length vary along the boom length. Calculation complexity for accurate natural frequencies caused by the varying moment of inertia and varying mass per unit length was greatly reduced by computer-aided analyses. The elements are welded to each other at their outer ends, which effectively gives high fundamental horizontal lateral natural frequencies. The elements, then,

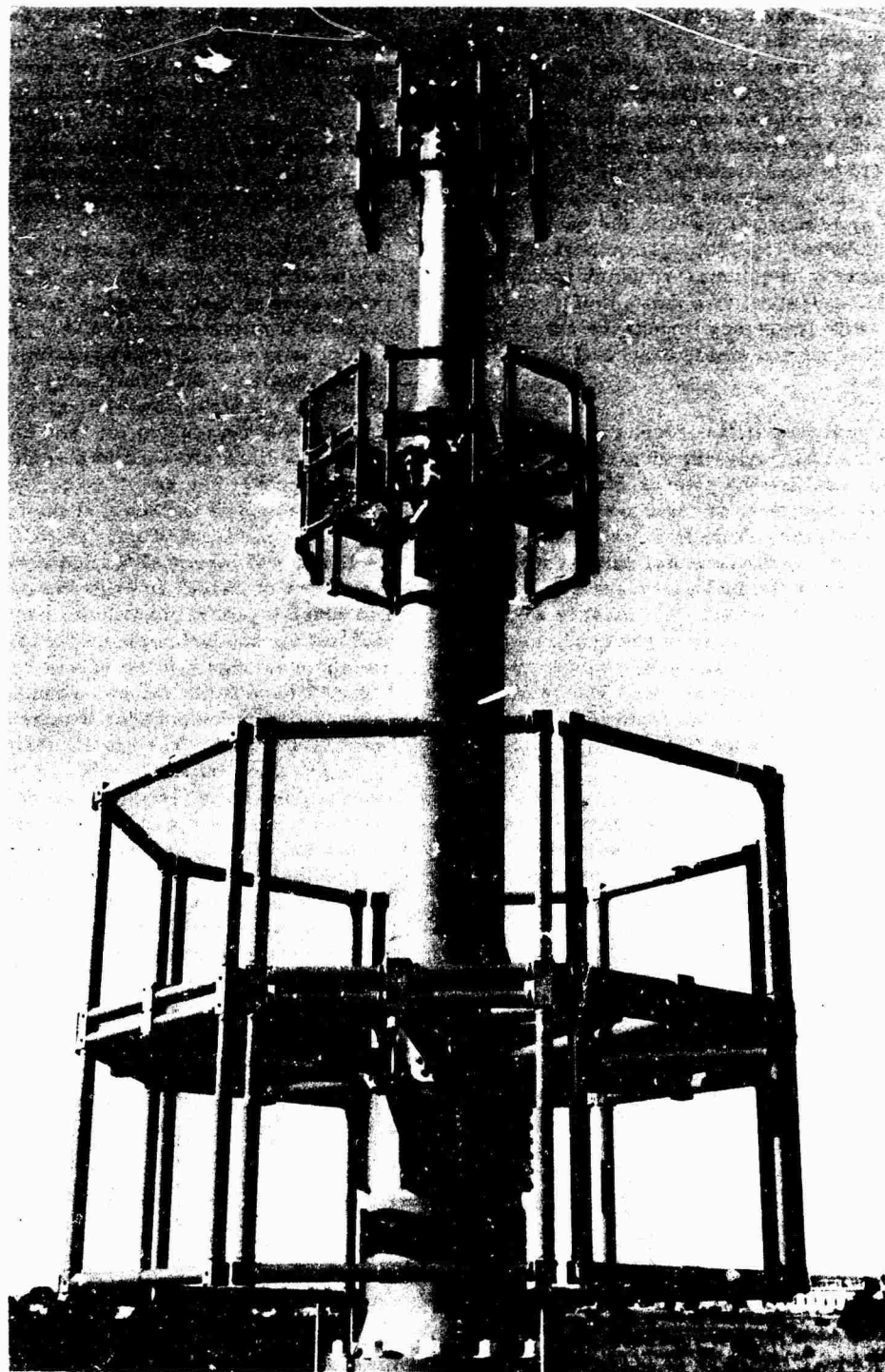


FIGURE 1: ANTENNA ASSEMBLY

only have vertical lateral natural frequencies of practical design concern.

The assembly of all the bays of the antenna elements, the mast, and electronic packages and other items inside the mast is the second structure considered in this paper. The assembly weighed approximately 375 lb (170 kg) with approximate envelope dimensions of 62 in. (1570 mm) diameter by 128 in. (3250 mm) high. The assembly was fabricated primarily of aluminum alloys with the parts welded and bolted together. An important electromagnetic requirement, which influenced the structural design, was that a uniform, very low radio frequency impedance exist between almost all structural parts and to electrical ground.

The analyses of the antenna assembly was simplified by analyzing individual major structures, such as the antenna elements, and then considering these as rigid bodies for the assembly analyses. This is a practical assumption when the fundamental natural frequencies of the individual parts are high compared to that of the mast. The mast is a complex structure because of the requirements for holes, flats, flanges, changes of diameter (including tapers), etc. The outside diameter of the mast varies from 21 in. (530 mm) at the bottom flange to 6.62 in. (168 mm) near the top.

Only lateral or transverse natural frequencies are of concern here because the longitudinal natural frequencies were at much higher values than the vibration excitation frequencies.

THEORETICAL ANALYSIS

This section discusses some fundamental concepts for the analysis and presents the results of some calculations for the structures as they are theoretically anticipated, as opposed to experimental test and verification results in a later section. It is not the intent to present significant new theory in this section. Also, the paper emphasizes computer results rather than computer program details.

Proper design of structures subjected to vibration and shock environments require anticipation of their natural frequencies, particularly if minimum weight is important and development testing is not possible for cut-and-try design. Classical natural frequency equations and stress and deflection analyses of cantilever beams are for the condition of the clamped end attached to a semi-infinite rigid support. The result is zero deflection and zero slope of the beam at the clamped end, i.e., the equivalent of infinite stiffness for the linear and torsional (called rotatory in remainder of paper) springs shown in Figure 2 in which a general cantilever beam with end load has its support replaced by idealized massless springs. If the spring rates for Figure 2 have finite values, simulation of general elastic support for the cantilever beam is obtained. The spring designated by k_x is assumed infinitely stiff for this paper since it does not affect the transverse deflections or transverse natural frequencies of the beams. The k_x spring affects only the longitudinal natural frequencies of the beam, which are not discussed in this paper. Hence, the linear spring will be the one designated by k from this point on.

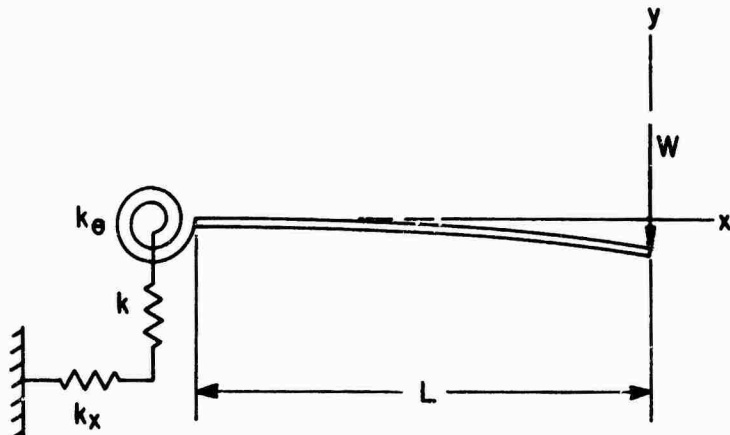


Figure 2: Schematic of Cantilever Beam with General Elastic Support

W. J. O'Donnell [3] gives the static deflection, in addition to that caused by bending and shear in the beam itself, of the neutral axis of uniform cantilever beams as a result of rotatory elasticity of the support. Rotatory elasticity allows rotation of the fixed end of the beam. Amplification and generalization of this work is given in a later paper [4]. The additional deflection, as a function of the distance x along the beam from the support, allowed by rotational compliance is

$$\delta_\theta = \frac{16.67 Mx}{\pi E(h')^2} + \frac{(1-\nu) Vx}{Eh'} \quad (1)$$

$$\text{where } h' = h + 1.5r. \quad (2)$$

This equation is for plane stress with a similar equation given for plane strain.

R. B. Hopkins [5] has additional discussions of flexibly supported cantilevers with examples, but vibration analysis is considered too extensive to be discussed in his treatise. Jacobson and Ayre discuss multi-story buildings in which the buildings are considered as rigid bodies in an elastic soil and as shear buildings in an elastic soil for which the rotational stiffness of the ground is infinite and the linear stiffness is finite [6].

Additional literature sources are given [7-10]; however, they are not strictly applicable to the structures considered here. For instance, only uniform cross-section beams are considered, which greatly simplifies analysis, but gives inefficient designs when weight and size are important.

O'Donnell was not concerned with the linear elasticity of the support and canceled its effect in his investigations. The equation for the additional deflection for the linear elasticity at the support of Figure 2 in terms of the linear spring stiffness is simply

$$\delta = \frac{V}{k}. \quad (3)$$

From the static deflection method for fundamental natural frequency

$$\omega^2 = \frac{g}{\Delta}, \quad (4)$$

which gives the natural circular frequency as a function of static deflection. It is obvious from equations (3) and (4) that the additional deflection allowed by an elastic support reduces the natural frequency.

The theoretical investigation of the effect of elastic boundary conditions at the fixed end for the antennas was obtained with a computer program. The program is used primarily for calculation of transverse natural frequencies and eigenvectors of general lumped-parameter (finite element) beams. In addition to other calculations, the program was developed to aid the analyses of cantilever structures under forced, steady-state sinusoidal excitation at the fixed end, i.e., aid in determining the effects of forcefully vibrating cantilever structures through a frequency bandwidth which may include resonant frequencies.

Variations of the moment of inertia and mass per unit length (cross-section variations) are handled by stepwise approximation, or by dividing the beam length into segments within each of which the cross-section is constant or varies only a small amount. The distributed mass in each segment is then lumped at the segment ends, or joints. The computations included rotary inertia in the plane of bending and structural damping for forced vibration. Bending moments were calculated by the computer at each joint for one-g static loading and for forced response. The one-g static bending stresses could be multiplied by a dynamic conversion factor to obtain approximate dynamic, or transient, stresses for the design shock spectrum although this method is sometimes not preferred [11, 12]. The multiplication factor is a function of the shock pulse length and magnitude, the structural natural frequencies, and the weight of the structure. As discussed earlier, the requirement here was that a multiplication factor of 100 be used.

The forced response maximum bending moments could be simply divided by the section modulus to obtain the dynamic bending stresses for steady state vibration. The computer program also determined each mode shape, but they are not discussed here and were generally of much less practical importance than the natural frequencies.

The effect of finite stiffness of the support on the antenna parts and assembly was analyzed theoretically by varying the rotational and linear stiffness values in the input data to the computer. The stiffnesses were varied with all other input data remaining constant, and the computer calculated the lateral natural frequencies, eigenvectors,

momenta at each joint for forced vibration, etc. The one-g moments did not change for different support stiffness values.

The large variation of natural frequencies theoretically possible is indicated by the semilogarithmic graph of Figure 3. The graphical representation of the fundamental natural frequency as a function of the rotatory stiffness, represented by the torsional spring of Figure 2, is for a mathematical model of a single antenna element of the lower bay of Figure 1. The linear spring rate is constant at 1,000,000 lb/in. (1,786,000 kg/mm) for Figure 3. The absolute value of the funda-

menta approach values asymptotically at their upper and lower ends, 126.09 Hz and 0.00 Hz for Figure 3.

A variation of the translatory spring rate for particular rotatory spring rates gives an indication of this effect on the transverse natural frequencies of these structures. The graphs for absolute values of natural frequencies are very similar to Figure 3, so normalized values for the first four modes of the same antenna element are plotted in Figure 4. The relative change for the modes is more obvious when the frequencies are normalized. Figure 4 is for a rotationally rigid support for

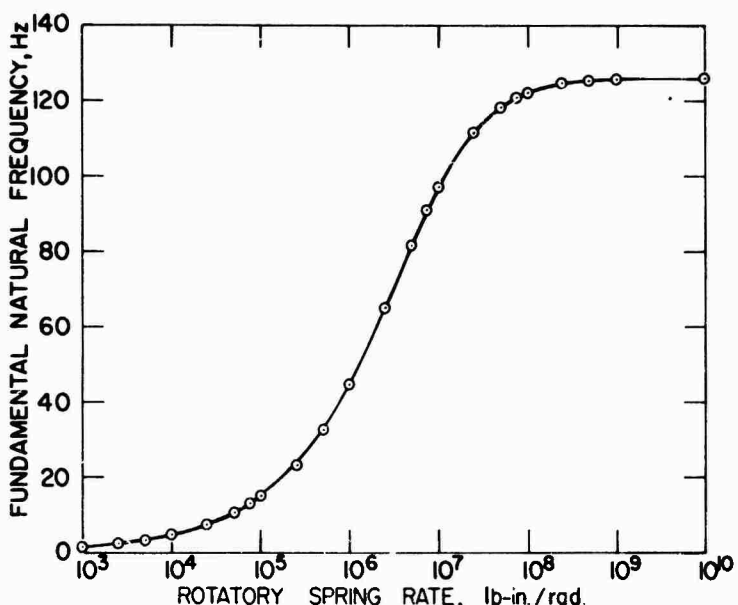


FIGURE 3: EFFECT OF ROTATORY SPRING RATE ON FUNDAMENTAL TRANSVERSE NATURAL FREQUENCY OF ANTENNA ELEMENT

mental transverse natural frequency varies from 126.05 Hz to 1.504 Hz for rotatory spring rates of 10,000,000,000 lb-in./rad (115,210,000,000 kg-mm/rad) and 1,000 lb-in./rad (11,521 kg-mm/rad), respectively. This range of rotatory stiffness is quite large; however, if a realistic value of stiffness for this structure is 1,000,000 lb-in./rad (11,521,000 kg-mm/rad) instead of ten times that, the fundamental natural frequency differs by more than 55 percent. The difference is even greater when compared to an infinitely stiff rotatory support, or if the true rotatory stiffness is lower. All of the graphs are of this general "S" shape for variations of rotatory or linear spring rates. The graphs

the antenna element, which was mathematically obtained by forcing the slope of the cantilever beam at the support to be zero. Similar families of graphs were obtained for various finite rotatory spring rates.

Much smaller numerical values of the linear spring rate, in comparison to the rotatory spring rate, were required for large variation of the fundamental natural frequency. Using the following equation for linear stiffness of a uniform bar under axial load

$$k = \frac{AE}{L} , \quad (5)$$

the linear spring stiffness of the support for

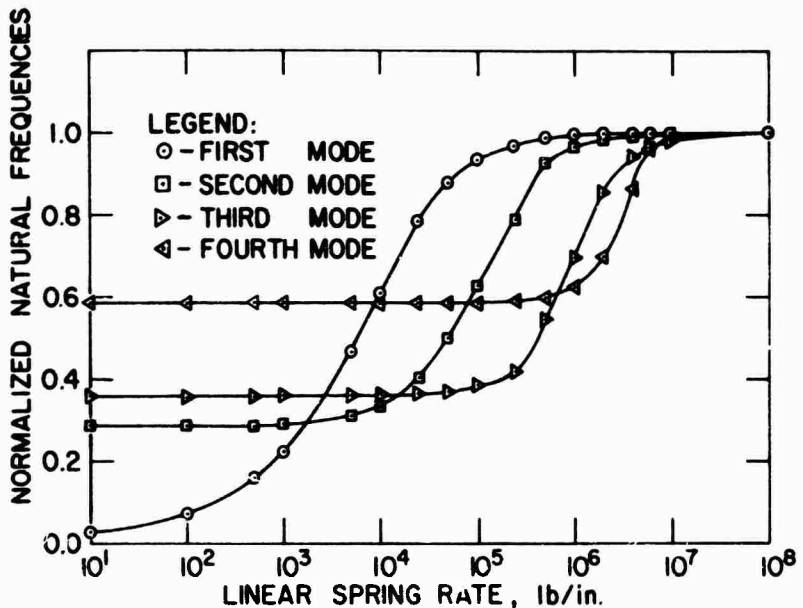


FIGURE 4: EFFECT OF LINEAR SPRING RATE ON TRANSVERSE NATURAL FREQUENCIES OF ANTENNA ELEMENT

the antenna element is on the order of 10,000,000 lb/in. (17,860,000 kg/mm). After checking Figure 4 for this value it is obvious that the translational spring rate is not of significant practical concern for the antenna element, particularly for the first two modes. In general, the rotatory spring rate has been of much more practical concern than the linear spring rate for all of the antenna structures. For this reason, the linear spring rate was largely ignored for most of the antenna element and assembly analyses. For other types of structures or for very accurate analysis the linear spring rate may be important.

An interesting pattern of the graphs of Figure 4 is that each higher mode has its natural frequency affected more drastically at higher spring rate values with each natural frequency changed less, relatively, for low spring rates than the preceding modes. However, this pattern did not continue for all higher modes. The relative change of the natural frequencies was quite varied for different modes, but in general, the relative effect was less, with most of the effect at higher spring rates, as the modes increased. Similar computer-aided analyses were performed on the antenna assembly.

The mast of the ship to which the antenna is attached should be part of the assembly analyses; however, adequate information

for this inclusion was not available, and only the antenna assembly, as shown in Figure 1, is analyzed. As mentioned earlier, the antenna elements for the three bays, the electronics packages, and some other parts are treated as rigid bodies for the assembly analyses; however, their rotary inertias and mass loadings were used for the computer calculations.

The antenna mast is effectively a tapered beam. Portions of its length are tapered with the diameters partly being determined by the size of parts attached to it or assembled inside of it.

Indication of the effects of rotational stiffness on the transverse natural frequencies of the antenna assembly is given by Figure 5. Again, the frequencies are normalized to indicate the relative effects for the first four modes of vibration. The linear spring rate for these graphs is 10^{20} lb/in. (1.79×10^{20} kg/mm), which for practical purposes is a translatory rigid support. Therefore, effects of the rotatory spring rate, only, are indicated by the graphs.

For a rotatory stiffness of 10,000 lb-in./rad (115,210 kg-mm/rad) the fundamental natural frequency is reduced to 2.1 percent of its value for infinite stiffness, the assumption for classical analysis. Obviously, from Figures 4 and 5 the frequencies for all modes

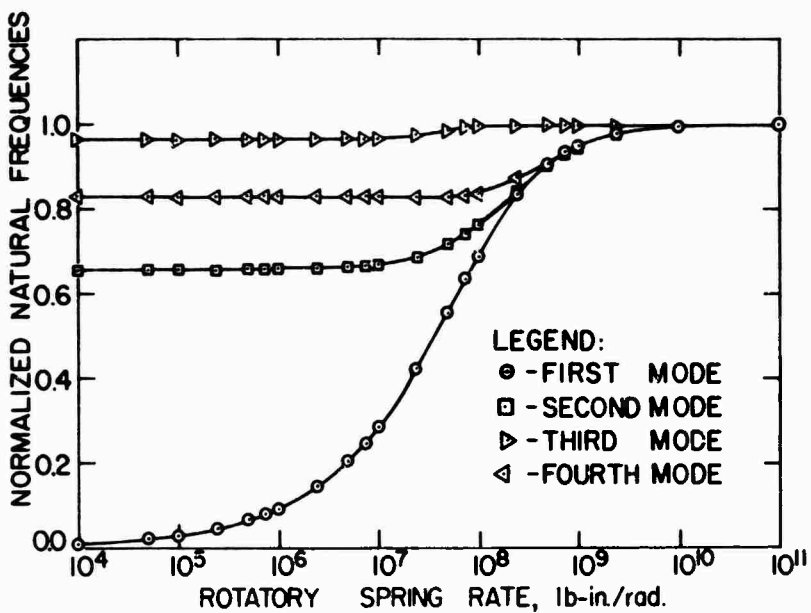


FIGURE 5: EFFECT OF ROTATORY SPRING RATE ON TRANSVERSE NATURAL FREQUENCIES OF ANTENNA ASSEMBLY

are not affected uniformly in a relative manner, and also from the data not in an absolute manner. The second mode of Figure 5 is affected less, relatively, than the first; but, in contrast to Figure 4, the fourth is affected more than the third. Of academic interest, the relative change was greater, for example, for the thirty-seventh mode than for the third. The frequencies for all of the modes approach asymptotic values at high and low rotatory spring rate values.

This mathematical model of the antenna assembly had 42 modes of vibration (42 degrees of freedom), and generally the natural frequency of each mode asymptotically approached values which did not cross the values of the next higher and lower modes. In other words, some modes, like the nineteenth, approached and equalled, but did not become less than, the frequency for infinite stiffness of the eighteenth mode. The frequency is highest for infinite stiffness. Similarly, the frequency for the nineteenth mode was never greater than the smallest value of the twentieth mode. In general, this was correct for all of the analyzed structures, but exceptions did occur. Also, some of the higher modes reached their lower asymptotic limits at very high spring rates, while a few did not change as a function of spring rate. In general, the higher modes approached their lower limits at higher spring rates, although this did not always occur.

Another example of the small effect of the linear spring rate on the fundamental resonance of these structures will be given. For the mathematical model of the antenna assembly and a reasonable value of rotatory spring rate of 25,000,000 lb-in./rad (288,000,000 kg-mm/rad) the fundamental frequency for an infinitely stiff linear spring was 12.988 Hz. For a linear spring rate of 5,000,000 lb/in. (8,950,000 kg/mm), the frequency decreased to only 12.983 Hz, or less than 0.04 percent change. For a decrease of the linear spring rate to one-fiftieth of the last example, or 100,000 lb/in. (179,000 kg/mm), the frequency change was less than two percent; however, the frequency change for the second mode was about 20 percent. The effect of the linear stiffness typically was much greater for several higher modes than it was for the first or second mode.

EXPERIMENTAL ANALYSIS

The cantilever structures analyzed theoretically in the previous section were vibration tested and an antenna element was shock tested.* Some of the testing was in excess of the requirements to obtain additional information as an aid for future structural design.

* The tests were for Type I of the vibration standard [1] and Grade A of the shock specification [2].

A spare antenna element for the lower bay of the antenna assembly was tested for vibration and shock effects. The high impact shock tests were conducted before vibration testing for scheduling purposes. The light-weight shock test machine, for items weighing approximately 250 lb (113 kg) or less, was used to apply the prescribed shock, and instrumentation was used for monitoring the acceleration. The antenna element was tested more severely than required, including under-simulation of the weight of the antenna assembly, to gain additional design information. Ballast was used to simulate antenna assembly weights of approximately 215 lb (97.5 kg) and 15 lb (6.8 kg). The drop height of the 400 lb (180 kg) hammer was increased in small increments so that the shock severity at which failure occurred could be more accurately determined.

The welds were examined visually after most shock impacts and radiographically before, during, and after shock testing. Also, certain dimensions and electromagnetic characteristics of the element were determined before, during, and after testing. The boom portion of the element was more resistant to the shock tests than was anticipated, and efforts to increase the shock severity included adding up to 15 lb (6.8 kg) of lead ingots at the end of the boom. The additional weight at the end of the boom did not contribute to more severe shock because the effect was to lower the transverse natural frequency sufficiently such that the maximum dynamic stresses did not change significantly.

The antenna element was shocked vertically for the orientation shown in Figure 1 and along the axis of the element boom. Shock along the third orthogonal axis was not performed because the attachment of the adjoining elements at their outboard ends was not simulated, and the test would not have been realistic. There were no observed changes in the electromagnetic characteristics of the element. Slight material yielding in the loop structure occurred at a particular shock along the boom axis. After yielding was observed, shock testing along the boom axis was discontinued. Excessive misalignment of the antenna parts severely reduces the electromagnetic performance of the antenna, so yielding of certain mechanical parts of the antenna assembly was considered as failure.

The severity of the vertical shock tests was much greater than for those applied

along the boom axis with the structure apparently capable of withstanding much more than was applied. However, shock severity for surface ship equipment is typically greater for vertical than for fore-and-aft and athwartship directions.

Vibration characteristics of the antenna element were then investigated alone and as part of the antenna assembly. The element was bolted to a thick aluminum plate which was attached to a concrete floor. A small vibration exciter, or shaker, was attached at various locations of the antenna element loop and at the end of the boom to determine approximate mode shapes, natural frequencies, and damping characteristics. The fundamental vertical transverse natural frequency was 100 Hz, and the damping ratio by logarithmic decrement techniques at this frequency was approximately 0.002, which is quite low. Additional vibration information of the antenna element was obtained when the antenna assembly was vibration tested.

Some of the vibration characteristics of the antenna assembly were first obtained with it bolted to a 1-in. (25 mm) thick aluminum alloy plate which was attached to a concrete floor. A small shaker was used to drive the assembly. The fundamental lateral natural frequency of the assembly in the athwartship direction was 21.3 Hz with the system damping ratio being approximately 0.005. The base of the mast and the aluminum plate were rotating sufficiently that elastic boundary conditions at the floor were visually obvious. The frequency for the second mode of vibration of the mast was 73.4 Hz. The damping ratio was slightly less than that determined at the fundamental resonance.

With the shaker attached to the end of the boom of an antenna element in the lower bay of Figure 1, the fundamental vertical lateral natural frequency of the element was 69.6 Hz with the damping ratio slightly less than 0.001.

Strain gages and accelerometers were used to determine approximate values of the rotatory stiffness of the boundary of the mast. At the frequencies for the first and second modes of vibration the rotatory spring rate of the support was approximately 220,000,000 lb-in./rad (2,535,000,000 kg-mm/rad) and 150,000,000 lb-in./rad (1,728,000,000 kg-mm/rad), respectively.

The antenna assembly was also

mounted to a fixture attached to a slip table, or oil-film slider table, which was driven by a much larger electrodynamic shaker. The fundamental lateral natural frequency of the assembly then was 16.8 Hz with a much broader peak, indicating much higher damping. The damping ratio at this frequency increased to 0.1. Although the slip table was modified to increase the rotatory spring rate, rotation was still visually observable. The rotatory spring rate was approximately 35,000,000 lb-in./rad (403,000,000 kg-mm/rad) at this frequency. Therefore, the decrease in the rotatory spring rate from the previous setup correctly produced a decrease in the natural frequency. The damping ratio of the slip table-shaker, without the antenna, was essentially the same as with the antenna, as was expected. Also, the damping ratio for the fundamental lateral resonance of the lower bay antenna elements increased to 0.04 from 0.001.

Although the mast was unsymmetric, primarily because of required access holes, the fore-aft natural frequencies at the first two modes of the mast differed from the athwartship direction by only 1.4 and 0.8 percent.

DISCUSSION AND CONCLUSIONS

The theoretical analyses and experimental investigations of the cantilever structures considered here indicate that the transverse natural frequencies are very much dependent upon the stiffness of their supports. The theoretical and experimental results of these structures did not closely agree, but the finite stiffness considerations provided much better agreement than do infinitely stiff supports, which is the classical and common assumption for analyses.

Theoretical natural frequencies of the antenna assembly for the first and second modes of vibration with rotatory spring rates equal to the measured values with the assembly attached to the concrete floor differed from the measured frequencies by 17 and 25 percent, respectively. When the antenna was attached to the slip table, the differences were 11 and 5 percent. The inertial effect of the supports would probably account largely for the lack of correlation of these theoretical to experimental values because it was not included in the theoretical analyses.

Decreases of natural frequencies for decreased rotatory stiffness at the support

were obvious experimentally as the fundamental decreased from 100 Hz for the single antenna element fastened to a thick plate which was attached to a concrete floor to 69.6 Hz when the element was attached to the mast. It was apparent that the local rotatory stiffness of the mast was less than the other mounting arrangement. The first two mode frequencies of the antenna assembly decreased from 21.3 Hz to 16.7 Hz and 73.4 Hz to 71.7 Hz for decreased support stiffness when the assembly was moved from the concrete floor mounting to the slip table.

The theoretical natural frequencies were affected greatest for certain ranges of the rotatory and translatory stiffness values. Most of the variation of the fundamental natural frequency for these two structures was for 10,000 lb-in./rad (115,000 kg-mm/rad) $\leq k_0 \leq$ 1,000,000,000 lb-in./rad (11,500,000,000 kg-mm/rad) and 100 lb/in. (179 kg/mm) $\leq k \leq$ 100,000 lb/in. (179,000 kg/mm). In general, for higher modes, the range of stiffness values for major effects to the natural frequencies increased.

For these structures the linear spring constant was essentially unimportant compared to the rotatory spring rate for effects on the fundamental transverse natural frequencies. For other types of structures, for very accurate analysis, or for investigation of the higher modes of vibration the linear spring rate may be important.

The work presented in this paper was not intended to be all inclusive nor extremely rigorous. The paper is an effort to share some of the information determined by computation and test and to stimulate others. Much of the work required practical answers quickly for design of subsequent structures in which weight was of much greater importance and for which the development phases were again omitted. Although the analyses and investigations of the subsequent structures are not yet to a stage for adequate discussion, the information presented in this paper was very meaningful for their structural design.

The possible significant effects of elastic boundary conditions at the fixed end of cantilever beams on the transverse natural frequencies has been demonstrated for some realistic structures. Typical cantilever beams with elastic supports as illustrated here are evident in many structures. Obviously, if infinite stiffness at the support is assumed and low safety factors are used to conserve

weight and size, large calculation errors may result with possible catastrophic results, particularly when structures are designed to have their natural frequencies only slightly higher than vibration environment or test excitation frequencies. Reductions of fundamental frequencies of 90 percent would not be unreasonable.

ACKNOWLEDGMENT

The author is indebted to several people at Southwest Research Institute for their help with this work and this paper, but especially acknowledges Dr. Dana Young, P. A. Cox, and A. F. Muller for their computer programming assistance.

REFERENCES

1. "Military Standard, Mechanical Vibrations of Shipboard Equipment," MIL-STD-167 (SHIPS), Department of the Navy, Washington, D.C., Dec. 20, 1954.
2. "Military Specification. Shock Tests, HI[High-Impact]; Shipboard Machinery, Equipment, and Systems, Requirements for," MIL-S-901C (NAVY), Department of the Navy, Washington, D.C., Jan. 15, 1963.
3. O'Donnell, W. J., "The Additional Deflection of a Cantilever Due to the Elasticity of the Support," Journal of Applied Mechanics, Vol. 27, No. 3, TRANS. ASME, Vol. 82, Series E, Sept. 1960, pp. 461-464.
4. O'Donnell, W. J., "Stresses and Deflections in Built-In Beams," Journal of Engineering for Industry, TRANS. ASME, Series B, Vol. 85, No. 3, Aug. 1963, pp. 265-273.
5. Hopkins, R. Bruce, Design Analysis of Shafts and Beams, McGraw-Hill, New York, 1970, pp. 177-188.
6. Jacobsen, L. S., and Ayre, R. S., Engineering Vibrations, McGraw-Hill, New York, 1958, pp. 110-112, 480-481.
7. Egle, D. M., "The Influence of Changing End Conditions on the Resonant Response of Beams and Plates," NASA CR-1736, University of Oklahoma, Norman, Oklahoma, Mar. 1971.
8. Cooper, H. F., Jr., "Vibrations of a Cantilever Beam Considering a Non-Rigid Wall Support," The Shock and Vibration Bulletin, Bulletin 34, Part 2, Dec. 1964, pp. 69-83.
9. Chun, K. R., "Free Vibration of a Beam with One End Spring-Hinged and the Other Free," Journal of Applied Mechanics, Vol. 39, TRANS. ASME, Series E, Vol. 94, Dec. 1972, pp. 1154-1155.
10. Cobble, M. H., and Fang, P. C., "Finite Transform Solution of the Damped Cantilever Beam Equation Having Distributed Load, Elastic Support, and the Wall Edge Elastically Restrained Against Rotation," Journal of Sound and Vibration, Vol. 6, No. 2, Sept. 1967, pp. 187-198.
11. "Shock Design of Shipboard Equipment, Dynamic Design-Analysis Method," NAVSHIPS 250-423-30, Department of the Navy, Washington, D.C., May 1961.
12. Clements, E. W., "Shipboard Shock and Navy Devices for its Simulation," NRL Report 7396, Naval Research Laboratory, Washington, D.C., July 14, 1972.